Infrared dynamics of non-Abelian gauge theories out of equilibrium

A Dissertation presented

by

Mark Mace

to

The Graduate School

in Partial Fulfillment of the

Requirements

for the Degree of

Doctor of Philosophy

in

Physics

Stony Brook University

August 2018

Stony Brook University

The Graduate School

Mark Mace

We, the dissertation committee for the above candidate for the

Doctor of Philosophy degree, hereby recommend

acceptance of this dissertation

Dmitri Kharzeev - Dissertation co-Advisor
Professor, Department of Physics and Astronomy
Senior Scientist, Physics Department, Brookhaven National Laboratory

Raju Venugopalan - Dissertation co-Advisor
Senior Scientist, Physics Department, Brookhaven National Laboratory
Adjunct Professor, Department of Physics and Astronomy

Axel Drees - Chairperson of Defense
Professor, Department of Physics and Astronomy

Derek Teaney
Associate Professor, Department of Physics and Astronomy

Adrian Dumitru
Professor of Physics, Department of Natural Sciences, Baruch College
and The Graduate School and University Center, The City University of New York

This dissertation is accepted by the Graduate School

Dean of the Graduate School

Abstract of the Dissertation

Infrared dynamics of non-Abelian gauge theories out of equilibrium

by

Mark Mace

Doctor of Philosophy

in

Physics

Stony Brook University

2018

The initial moments after an ultrarelativistic nuclear collision present a unique opportunity to study the many-body dynamics of Quantum Chromodynamics (QCD) out of equilibrium. This system is highly occupied with gluons up to an emergent semi-hard scale, Q_s, the saturation momentum. Because the coupling at early times is weak, systematic studies are possible using an effective theory of QCD, the Color Glass Condensate effective field theory (CGC EFT). In this dissertation, we use the CGC EFT to probe novel features of the infrared regime of far-from-equilibrium QCD systems.

The prospect of detecting the Chiral Magnetic Effect (CME) in ultrarelativistic heavy-ion collisions has generated great interest in real-time topological transitions, called sphaleron transitions, in QCD. Here chiral charge, anomalously produced by sphaleron transitions, generates an electric current when in the presence of the strong, but short-lived magnetic field created by the passing heavy-ions. This current can imprint itself on the detected hadrons: the search for this signal is a major focus of current and planned heavy-ion collision experiments at the Relativistic Heavy-Ion Collider (RHIC) at Brookhaven National Lab and the Large Hadron Collider (LHC) at CERN. Using first-principles-based real-time classical-statistical lattice gauge theory simulations, we demonstrate for the first time that sphaleron transitions occur in QCD out of equilibrium. By determining the time evolution of the characteristic scales in the system, we show that the rate of sphaleron transitions is controlled by the infrared screening scale. We then conclude that the rate of sphaleron transitions at early times is favorable for the generation of the CME. With the novel addition of chiral lattice fermions and a magnetic field, we investigate the real-time dynamics of anomalous transport phenomena, like the CME and the gapless excitation known as the Chiral Magnetic Wave (CMW), microscopically. Insights necessary for model building and phenomenology related to the search for the CME and the CMW are then discussed.

Long-range-in-rapidity correlations probe the early-time dynamics after the collision due to causality. In small systems, where final state effects are likely small, the study of such

correlations potentially offers a unique opportunity to directly access the early-time infrared dynamics of the system. First, we present a proof-of-principle parton model for proton–heavy-ion collisions. With this simple model, we qualitatively reproduce many of the multi-particle correlations observed experimentally, which are often ascribed to final state collective flow. This serves as a clear demonstration that such correlations can be generated without a final state hydrodynamic medium. Next, we develop an event-by-event framework to study initial correlations of gluons in light–heavy-ion collisions. We show that key systematics in the observed two-particle correlations at RHIC and the LHC can be quantitatively reproduced with this framework. This suggests that the observed correlations may arise, at least in part, from the earliest times after the collision. If this bears out, it would imply that the long-range-in-rapidity correlations measured in small systems are a direct result of the infrared dynamics of far-from-equilibrium QCD.

Dedication Page

To my parents.

Frontispiece

"So we beat on, boats against the current, borne back ceaselessly into the past."
— F. Scott Fitzgerald, *The Great Gatsby*

Table of Contents

List of Figures

List of Tables

Acknowledgements

The first time I realized I wanted to be a physicist was during my sophomore high school physics course. However, it was not because of the lectures. It really started because one day when we had a substitute teacher who, in lieu of teaching a new subject, put on an episode of the television show Numb3rs for the class to watch. While now I realize that many of the premises of the show are certainly far fetched, I was fascinated by the use of sophisticated mathematics to solve complex problems, with directly testable results. This realization sparked my interest in physics and mathematics. During the remainder of the semester, I read our textbook cover-to-cover (*Conceptual Physics* by Paul G. Hewitt) and could not get enough. So, first, I would like to thank the creators of the show Numb3rs and Paul G. Hewitt for sparking my interests in physics and mathematics.

However, this journey to becoming a physicist would have never been possible had it not been for my parents, Cathy and Ken. They have been incredibly self-less, showing me through example the value of hard work and dedication, and have given me so much support and encouragement, which has enabled me to pursue my dreams. I love you both and hope that I have made you proud.

Next, I would like to thank my advisors, Dima and Raju. Before coming to Stony Brook, I made a list of potential advisors, with these two topping the list; as luck would have it, they agreed to jointly advise my PhD studies. I consider myself very privileged to have had these two brilliant and influential physicists, with their own unique styles and interests, as role models, mentors, and collaborators. I would also like to thank both of them for allowing me a great amount of freedom in my work and for their unwavering support. Additionally, I have been very lucky to have traveled so much during my PhD, across the entirety of the US and Europe, and would like to thank them for enabling and encouraging this.

The physics in this thesis is the product of collaboration, so I am indebted to my long list of collaborators. First, I would like to thank Sören Schlichting, who has had to deal with me since my first moments as a PhD student and has taught me nearly everything I know about real-time simulations of gauge theories; thanks for your patience, constant energy, and sharing with me your excitement for the physics that makes up this thesis. I would like to thank Niklas Mueller, both for his great collaboration and for all of the times we spent together being dumb PhD students toiling in our confusion; thanks also for being a good friend and beer drinking colleague. I would like to thank Sayantan Sharma, for, among other things, showing me the beauty of overlap fermions, as well as for his constant encouragement to seek knowledge and truth and not take shortcuts; I hope to one day come visit you in India and see all of the beautiful places you told me about. Next, I would like to thank Kevin Dusling, who patiently taught a lot about small-x physics and small systems, as well as the art of perseverance in the face of a hard problem. I would like to thank Vladi Skokov for sharing his "crazy ideas" and enthusiasm for physics and life in general. I would like to thank Prithwish Tribedy for always reminding me to have real (experimental) physics in mind, and always being someone good with whom to discuss. I would like to thank Yuji Hirono, for having so much patience with me as an officemate, as well as for teaching me

a lot about (magneto)hydrodynamics, and with whom I think I have started more projects with than anyone on this list; I look forward to finally putting out some of the things we have discussed over the years.

Being a PhD student at Stony Brook and BNL, as well as spending time at the ITP in Heidelberg, has enabled me to share close quarters with many great people. I would like to thank Adith, Aleksas, Moshe, Rasmus, and the rest of the Stony Brook crew for making our window-less office not so dreary. I would like to thank the Nuclear Theory Group at Stony Brook for many amusing seminars and lunch time discussions. I would like to thank the many current and past staff, post-docs, and visitors at the BNL Nuclear Theory Group, where I spent a lot of my PhD studies, with whom I have been able to discuss physics and eat lunch, and who have generally made my life as a physicist-in-training better. In particular, I would like to thank Björn Schenke and Rob Pisarski for many insightful discussions (physics and otherwise). Additionally, I spent five very fruitful months in Heidelberg, Germany and would like to thank Jürgen Berges for his guidance and for enabling my trips to Heidelberg, which were very important in my development as a PhD student, as well as his collaboration. I would like to thank Alexander Rothkopf and Valentin Kasper for engaging physics discussions and camaraderie. I would like to thank Oscar (Carlos) García-Montero, both for always making my journeys to Germany and around Europe amusing (even when it involved sharing a flat in a sketchy part of town) and for great physics discussions. I would like to thank Abigail Tyrell, Kaushik Roy, and Niklas Mueller for very helpful comments on sections of this thesis.

My life as a PhD student would have been infinitely harder had it not been for all of the the administrative help and guidance from Don Sheehan, Dorothy Davis, Marlene Vera-Viteri, and Sara Lutterbie. Thanks so much for everything you do!

I would like to acknowledge the many great friends I made at Stony Brook and at the ad-hoc grad student fraternity of the NoCo house and thank them for making my life outside of physics truly enjoyable: Adith, Ashley, Ben, Eric, Fernando, Lucy, Matt, Morgan, Melissa, Mike, Nick, Rachel, and Sheridan (sorry if I forgot anyone!!). I also want to thank Melissa Hoffman for donating her amazing art skills with the ship illustration used for the frontispiece of this thesis. I also want to thank Bryn, Jeff, and Zach, for being there since day one; Rog for President.

Last, but certainly not least, I would like to thank Abby, for her love and support, as well as for inspiring me every day to be a better scientist as well as a better person. I love you and can't wait to see what the future holds for us.

The material in this dissertation is based on work supported in part by the U.S. Department of Energy, Office of Science, Office of Nuclear Physics, under Contracts No. DE-SC0012704 and DE-FG02-88ER40388. I would also like to thank the BEST Collaboration for support.

Publications

This thesis is based on and uses figures and text from the following publications, which the author was a co-author and contributed significantly to all of the calculations, interpretations, and preparation of original manuscripts. All rights for the publishers and co-authors are reserved.

1. M. Mace, S. Schlichting, R. Venugopalan. *Off-equilibrium sphaleron transitions in the Glasma.* Phys.Rev. D93, 074036 (2016); arXiv:1601.07342 [hep-ph]. Copyright (2016) by the American Physical Society

2. M. Mace, N. Mueller, S. Schlichting, S. Sharma. *Non-equilibrium study of the Chiral Magnetic Effect from real-time simulations with dynamical fermions.* Phys. Rev. D 95, 036023 (2017); arXiv:1612.02477 [hep-lat]. Copyright (2017) by the American Physical Society

3. J. Berges, M. Mace, S. Schlichting. *Universal self-similar scaling of spatial Wilson loops out of equilibrium.* Phys. Rev. Lett. 118, 192005 (2017); arXiv:1703.00697 [hep-th].

4. K. Dusling, M. Mace, R. Venugopalan. *Multiparticle collectivity from initial state correlations in high energy proton-nucleus collisions.* Phys. Rev. Lett. 120, 042002 (2018); arXiv:1705.00745 [hep-ph]. Copyright (2018) by the American Physical Society

5. K. Dusling, M. Mace, R. Venugopalan. *Parton model description of multiparticle azimuthal correlations in pA collisions.* Phys. Rev. D 97, 016014 (2018); arXiv:1706.06260 [hep-ph]. Copyright (2018) by the American Physical Society

6. K. Dusling, M. Mace, R. Venugopalan. *What does the matter created in high multiplicity proton-nucleus collisions teach us about the 3-D structure of the proton?* PoS QCDEV2017 (2018) 039; arXiv:1801.09704 [hep-ph]. Copyright (2018) the authors

7. M. Mace, V. Skokov, P. Tribedy, R. Venugopalan. *Hierarchy of azimuthal anisotropy harmonics in collisions of small systems from the Color Glass Condensate.* Phys. Rev. Lett. 121, 052301 (2018); arXiv:1805.09342 [hep-ph]. Copyright (2018) by the American Physical Society

8. M. Mace, V. Skokov, P. Tribedy, R. Venugopalan. *Systematics of azimuthal anisotropy harmonics in proton-nucleus collisions at the LHC from the Color Glass Condensate* arXiv:1807.00825 [hep-ph].

Chapter 1

Introduction

Moments after the Big Bang, the universe was extremely hot, dense, and rapidly expanding. While impossible to recreate the exact conditions of the Big Bang in a laboratory, high energy heavy-ion collision experiments, currently conducted at the Relativistic Heavy-Ion Collider (RHIC) at Brookhaven National Lab (BNL) in the USA and the Large Hadron Collider (LHC) at CERN in Switzerland and France, allow for the study of a strongly correlated system of deconfined quarks and gluons, similar to the initial matter produced by the Big Bang. The matter created in these collisions is described by Quantum Chromodynamics (QCD), the fundamental theory of quarks and gluons interacting via the strong nuclear force. As the energy of a nuclei increases, the density of gluons in the nuclei grows dramatically. When two high energy nuclei collide, they form a far-from-equilibrium system highly occupied with gluons. This extreme gluon density gives rise to an emergent semi-hard scale, Q_s, the saturation momentum. This scale becomes the dominant scale of the problem, which allows for a weak coupling description of the system. An effective field theory of QCD, known as the Color Glass Condensate effective field theory (CGC EFT), has been developed to describe the dynamics of this exotic state of matter [9]. Thus, in order to understand the early-time dynamics, it is necessary to understand the properties of the infrared regime of out of equilibrium QCD – this is the primary focus of this dissertation. In particular, we will study real-time topological transitions, as well as long-range-in-rapidity correlations, both of which can be generated during these earliest times. As we will discuss, in larger systems, these topological transitions, which are controlled by infrared excitations, may give rise to observable anomalous transport phenomena. In smaller systems, the long-range-in-rapidity correlations detected at RHIC and the LHC may be a direct probe of the infrared dynamics of the initial state.

1.1 Overview

Ultrarelativistic heavy-ion collision experiments began as a means to study the high energy-density limit of nuclear matter, whereby the building blocks of the nuclei would reveal themselves [10, 11, 12, 13, 14]. At the time of the first relativistic heavy-ion collisions [15], the fundamental theory of the strong interaction, Quantum Chromodynamics (QCD), was still emerging. A large number of hadrons had been detected in collider experiments. To explain

their different properties, it was postulated that hadrons were composite objects, made up of so-called 'quarks' [16, 17]. This speculation was confirmed by deep inelastic electron-proton scattering experiments [18, 19], where it was determined that the proton is not point-like, but has point-like constituents. These constituents were originally termed 'partons' [20, 21][a], and later identified as the previously conjectured quarks. While these initial quark/parton models were able to describe many of the observed hadrons, an additional quantum number was needed to maintain the correct quantum statistics of the wavefunction under the Pauli Exclusion Principle: this is the *color* of the strong interaction. The quark model was then reformulated as a non-Abelian gauge theory of the group $SU(N_c = 3)$, with a gauge boson, the gluon. Thus QCD, the theory of quarks and gluons interacting via the strong force, was born.

However, two emergent features of QCD were needed for consistency with what was observed in experiment. The first is asymptotic freedom [22, 23]. This is the property that the coupling of QCD becomes asymptotically weak at either high energies or short distances, while the coupling becomes strong at low energies or long distances. The discovery of this property justified the use of perturbative methods for high energy/short distance physics. Perturbative QCD (pQCD) has been tremendously successful (c.f. Chapter 9 of [24] for a review and comparison of pQCD theory calculations to recent LHC measurements). The second feature is confinement. This is the statement that at low energies/long distances (set by the scale of QCD, $\Lambda_{QCD} \approx 200$ MeV [24]), free quarks and gluons cannot exist. Instead, the strong coupling of QCD dictates that they must be in bound states of two valence quarks (mesons) or three valence quarks (baryons) (states of four or five valence quarks are also postulated, the latter of which has been detected at the LHC [25]). When the coupling becomes strong, perturbative approaches break down.

The transition from a state of confined to asymptotically free quarks and gluons is what underlies the entire field of ultrarelativistic heavy-ion collisions. First principles lattice QCD simulations have confirmed this transition. At zero and low baryon densities, a cross-over phase transition has been observed [26, 27]. At larger baryon densities, it is believed that QCD undergoes a first-order phase transition which culminates at a critical point [28]. A conjectured phase diagram of QCD matter is shown in Fig. 1.1. With the current and planned low and medium energy heavy-ion collision experiments at RHIC, the Facility for Antiproton and Ion Research (FAIR) at GSI in Germany, and the Nuclotron-based Ion Collider fAcility (NICA) at the Joint Institute for Nuclear Research in Dubna, Russia, it may be possible to experimentally map the entire phase diagram.

With high enough temperatures, it was long speculated that a new state of matter, the Quark Gluon Plasma (QGP), would form in the deconfined region of the phase diagram [10, 11, 12, 13, 14]. This new phase of matter, consisting of deconfined, but strongly interacting quarks and gluons, was first discovered with ultrarelativistic heavy-ion collisions at RHIC [29], and subsequently confirmed at the LHC. However, the discovery of the QGP is only a starting point towards a complete understanding of the many-body QCD dynamics which occur during a heavy-ion collision. A salient questions is how does the QGP form? The picture of how this systems approaches thermal equilibrium has progressed significantly in recent years (the modern weak-coupling perspective is briefly reviewed in Sec. 1.4.1). Nev-

[a] In modern terminology, partons refer to both quark *and* gluons.

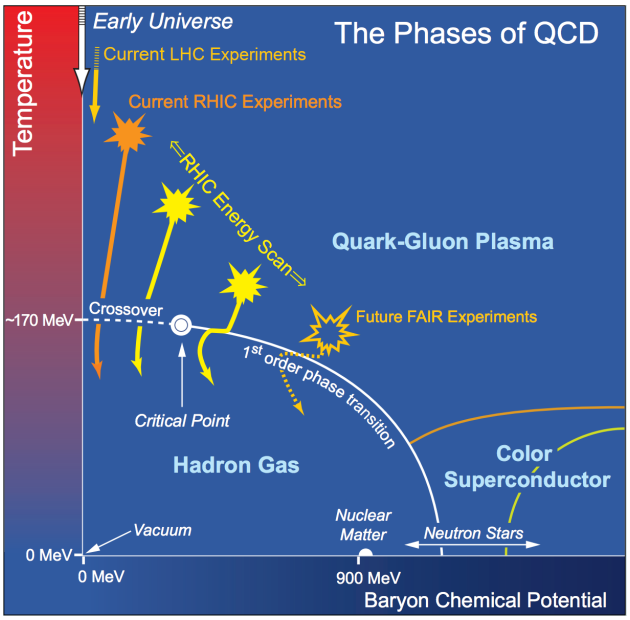

Figure 1.1: The conjectured phase diagram of QCD. Figure adapted from [1].

ertheless, there is still much to learn about the properties of the matter in the pre-equilibrium regime. In the first half of this thesis (Chapters 2 and 3), we will discuss novel real-time topological features related to infrared excitations which occur at the earliest times after a heavy-ion collision. These excitations may lead to observables signals at RHIC and the LHC, and are the subject of intense current search. However, to be able to directly probe the initial state and pre-equilibrium dynamics of the system, the QGP phase (so-called 'final state') would need to be small or not happen at all. An intriguing prospect for this is with smaller systems, like proton-lead collisions at the LHC and proton/deuteron/helium-3–gold collisions at RHIC. In Chapters 4 and 5, we will show that the long-range-in-rapidity correlations observed in these systems may offer a direct window into the initial state and the pre-equilibrium dynamics.

1.2 Outline

In the following sections of this introductory chapter, we will first give a very brief field-theoretical introduction to QCD. We then detail the basics of the lattice description of QCD, which will be used throughout Chapters 2 and 3. Then we will review the state-of-the-art in the modeling of ultrarelativistic heavy-ion collisions, including a discussion of the CGC EFT, which underlies the majority of the physics discussed in this thesis.

In Chapter 2, we perform simulations which verify the existence of real-time topological transitions, so-called sphaleron transitions, for the first time in an off-equilibrium QCD system. Sphaleron transitions have garnered much recent interest due to the proposal of the Chiral Magnetic Effect (CME) in heavy-ion collisions. A sphaleron transition will anomalously produce local domains of chiral charge. When the chiral charge is in the presence of the strong, but short-lived magnetic field created at the earliest moments after a heavy ion

collision, the CME generates an electric field. Thus, it is crucial for sphaleron transitions to occur during the pre-equilibrium stage of a heavy-ion collision in order for a detectable CME signal to form. In addition to the determination of the off-equilibrium sphaleron transition rate, properties of the dynamical scales which form in an off-equilibrium non-Abelian plasma are studied.

In Chapter 3, we develop a first-principles-based real-time lattice field theory description of fermion production, including the first ever implementation of real-time chiral lattice fermions. We first study the out-of-equilibrium production of chiral fermions resulting from a sphaleron transition. Then, with the addition of an external magnetic field, we investigate the real-time dynamics of the CME and related anomalous transport phenomena microscopically. We discuss both the fermion mass and magnetic field dependence on the produced currents, which may have implications for modeling and phenomenology of present and future experiments.

In Chapter 4, we detail a proof-of-principle parton model for multiparticle correlations. In this model of proton–heavy-ion collisions, we consider eikonal quarks scattering off a dense nuclear target. Strikingly, we demonstrate that many of the observed multiparticle correlations, believed to signify collectivity and hydrodynamic behavior, can be qualitatively reproduced without any medium or final state interactions. Additionally, we use this simple model to elucidate general features of the correlations calculated in initial state models.

In Chapter 5, we develop an event-by-event framework for calculating initial gluon correlations for light-ion–heavy-ion collisions using the CGC EFT. Employing this framework, we first show that the systematics observed for proton/deuteron/helium-3–gold collisions at RHIC can be reproduced by initial state gluon correlations. We then demonstrate that this framework can also describe the multiplicity dependence for proton-lead collisions at the LHC. This establishes that correlations generated by the initial state can be significant and in line with the experimental data, challenging the hydrodynamic paradigm for small systems. While further study is needed to resolve this debate, if initial state correlations are found to be dominant in these small systems, this would allow for unprecedented access to the early-time, and thus infrared, dynamics of out-of-equilibrium QCD experimentally.

Finally, in Chapter 6, we summarize the findings in this thesis, and give an outlook to future studies to further address the topics discussed in this thesis. A number of Appendices then follow the main body of this dissertation.

Throughout this thesis we will always work in natural units, $\hbar = c = 1$, where all quantities are given either in terms of GeV or fm (such that $1 = 0.197\ \text{GeV} \cdot \text{fm}$), unless explicitly noted otherwise. We adopt the covariant Minkowski metric tensor with mostly negative signature, $\text{diag}(g_{\alpha\beta}) = (1, -1, -1, -1)$.

1.3 Basics of Quantum Chromodynamics

As previously mentioned, QCD is the fundamental theory of the strong force. It is a non-Abelian gauge theory with the group $\text{SU}(\text{N}_\text{c} = 3)$, however what follows will be for general N_c; in Chapters 2 and 3 we will study SU(2)-QCD for computational simplicity. The matter fields are composed of spin-1/2 fermions in the fundamental representation, the quarks, which come in 6 'flavors' and N_c colors. The quarks are represented by the field spinor ψ_i,

where $i = 1, 2, .., N_c$ is the fundamental color index. There are also corresponding anti-quarks, denoted by the Hermitian conjugate, $\psi^\dagger$. The gauge bosons are the gluons, which are spin-1 and are in the adjoint representation. They are represented by the gauge field A^a_μ, where $a = 1, ..., N_c^2 - 1$ is the adjoint color index, and $\mu = 0, ..., 3$ is the spacetime (Lorentz) index. The Lagrangian is given by the Yang-Mills and Dirac terms respectively,

$$\mathcal{L} = -\frac{1}{4} F^a_{\mu\nu} F^{\mu\nu}_a + \sum_{\text{flavors} f} \bar{\psi}^{(f)}_i (i \not{D}^{ij} + m^{(f)} \delta^{ij}) \psi^{(f)}_j \,, \tag{1.1}$$

where repeated indices are summed over. Here

$$D^{ij}_\mu = \partial_\mu \delta^{ij} - ig(t^a)^{ij} A^a_\mu \tag{1.2}$$

is the gauge covariant derivative in the fundamental representation, where $\not{D} \equiv \gamma_\alpha D^\alpha$, where $\alpha = 0, 1, 2, 3$ are Dirac indices, γ_μ are the Dirac (gamma) matrices, and $\bar{\psi} = \psi^\dagger \gamma^0$. This gauge covariant derivative is given in terms of the generators t^a of the fundamental representation of Lie algebra $\mathfrak{su}(\mathrm{N_c})$ for the group $\mathrm{SU(N_c)}$. The fundamental representation generators t^a are $\mathrm{N_c} \times \mathrm{N_c}$ traceless, Hermitian matrices that are normalized as $tr[t^a t^b] = \delta^{ab}/2$. They obey the commutation relation $[t^a, t^b] = i f^{abc} t^c$, where f^{abc} is the $\mathrm{SU(N_c)}$ structure function. For SU(2), $t^a = \frac{\sigma^a}{2}$ where σ^a are the Pauli matrices, and for SU(3), $t^a = \frac{\lambda^a}{2}$ where λ^a are the Gell-Mann matrices. The non-Abelian field strength tensor is given by

$$F_{\mu\nu} = \frac{i}{g} [D_\mu, D_\nu] = \partial_\mu A_\nu - \partial_\nu A_\mu - ig[A_\mu, A_\nu] = F^a_{\mu\nu} t^a \,. \tag{1.3}$$

It is also possible to define the gauge covariant derivative in the adjoint representation,

$$D^{ab}_\mu = \partial_\mu \delta^{ab} - ig(\tilde{t}^d)^{ab} A^d_\mu \,, \tag{1.4}$$

where $(\tilde{t}^a)^{bc} = -i f^{abc}$ are the adjoint representation generators. The field strength tensor can then alternatively be written as

$$F^a_{\mu\nu} = \partial_\mu A^a_\nu - \partial_\nu A^a_\mu + g f^{abc} A^b_\mu A^c_\nu \,. \tag{1.5}$$

Here g is the gauge coupling of QCD; this coupling runs with the energy scale. Typically, the coupling is given in terms of the strong coupling constant, $\alpha_S = g^2/4\pi^2$. As previously mentioned, for high energies, g, and thus α_S, is small, while for low energies both become large. QCD being a gauge theory is invariant under the local gauge transformations,

$$\psi(x) \rightarrow \Omega(x)\psi(x) \tag{1.6}$$

$$\bar{\psi}(x) \rightarrow \bar{\psi}(x)\Omega^{-1}(x) \tag{1.7}$$

$$A_\mu(x) \rightarrow \Omega(x) A_\mu(x) \Omega^{-1}(x) - \frac{i}{g} [\partial_\mu \Omega(x)] \Omega^{-1}(x) \,, \tag{1.8}$$

where $\Omega(x)$ is an $\mathrm{SU(N_c)}$ matrix such that $\Omega^{-1} = \Omega^\dagger$. It is then straightforward to show that the QCD Lagrangian, Eq. (1.1), in gauge invariant. It is possible to make a specific choice of gauge; in many practical applications this is necessary. However, all physical quantities must be invariant of the chosen gauge.

To solve QCD from first principles, at very high energies (and low parton densities) perturbative methods can be employed. In the next section, we will discuss how to solve QCD when this is not the case.

1.3.1 Lattice QCD

In the regime where the inherently non-linear aspects of QCD become important, such as for many-body systems or for low-energy systems, perturbation theory is not applicable. To study this non-perturbative regime from first principles, so-called lattice formulations have been developed [30]. Particular examples will be discussed extensively in Chapter 2 and 3; we will only provide a basic introduction in what follows.

In these formulations, D-dimensional spacetime is discretized as a D-dimensional hypercubic grid, or lattice. Consider an isotropic lattice with N lattice sites for each of the D dimensions, with a spacing a between each site. The Lagrangian or Hamiltonian of the continuum gauge theory is then reformulated in terms of discrete fields which depend on discrete variables. To recovered the continuum theory, one must simultaneously take the number of sites N to infinity and the spacing between the sites a to zero. At finite lattice spacing and number of sites, the lattice formulation may break some of the symmetries of the continuum theory. There is some ambiguity in how the lattice formulation is done; different formulations may have different symmetry properties in the discretized version. Additionally, since in the lattice formulation both position and momentum space are finite, the theory is regulated in the IR and UV by the smallest and largest momentum scales possible, given in terms of the inverses of the size of the lattice, $L = Na$, and the lattice spacing, a, respectively.

Let us now consider QCD. First, we define our spatially-isotropic 3+1D Minkowski spacetime lattice as

$$\Lambda = \{n = (n_0, \mathbf{n}) |\ n_0 = 0, ..., N_t - 1;\ n_1, n_2, n_3 = 0, 1, ..., N_s - 1\}\,, \tag{1.9}$$

where the spacing between sites is a_t and a_s for the temporal and spatial directions respective. Starting with the QCD Lagrangian, Eq. (1.1), we will now define the our lattice field variables. The fermion fields then become $\psi(n)$ and $\bar{\psi}(n)$, where again they have Dirac, color, and flavor indices; however for notational simplicity we will not explicitly denote these. All contractions between indices remain unchanged in the lattice discretized formulation. Gauge transformations of the fermion fields are analogous to the continuum, Eq. (1.8), however the position is $x \to n$. Derivatives then take the form of finite difference equations, where we will employ a central difference scheme. Thus derivatives of any spacetime-dependent function $f(x)$ take the form

$$\partial_\mu f(x) \to \frac{1}{2a_\mu}(f(n + \hat{\mu}) - f(n - \hat{\mu}))\,, \tag{1.10}$$

where $\hat{\mu}$ denotes an increment of +1 unit on the lattice in the μ direction. In order to preserve gauge invariance for the Dirac term on the left hand side of Eq. (1.1), we cannot simply define the gauge fields with respect to lattice position n. Instead, we consider the gauge link, $U_\mu(n)$, which acts as a gauge transporter between a position n and $n + \hat{\mu}$ of the gauge field $A_\mu(n)$. Thus we define the gauge link as

$$U_\mu(n) = \exp(-iga_\mu A_\mu(n)) \tag{1.11}$$

where repeated indices here are not summed. A gauge transformation of the gauge link takes the form

$$U_\mu(n) \to \Omega(n) U_\mu(n) \Omega^\dagger(n + \hat{\mu})\,. \tag{1.12}$$

Noting that $U_{-\mu}(n) = U_\mu^\dagger(n-\hat{\mu})$, this allows us to see that by expanding the gauge link for small a_μ,

$$U_\mu(n) \approx \mathbb{1} - iga_\mu A_\mu(n) + \mathcal{O}(a_\mu^2), \qquad U_{-\mu}(n) \approx \mathbb{1} + iga_\mu A_\mu(n-\hat{\mu}) + \mathcal{O}(a_\mu^2)\,. \tag{1.13}$$

The *naïve* Dirac term of the lattice QCD Lagrangian then takes the form

$$\mathcal{L}_{lat}^F(n) = \bar{\psi}\left(\sum_{\mu=1}^{4} i\gamma^\mu \frac{U_\mu(n)\psi(n+\hat{\mu}) - U_{-\mu}(n)\psi(n-\hat{\mu})}{2a_\mu} + m\psi(n)\right) \tag{1.14}$$

where the continuum result can be readily obtained by expanding the gauge links by Eq. (1.13) and taking the $a_\mu \to 0$ limit. However, in formulating the lattice discretized Dirac term we have introduced spurious unphysical artifacts; these are the so-called lattice doublers. These extra fermion modes arise from the fact that the lattice inverse Dirac operator (the quark propagator) at finite lattice spacing has more poles than the physical fermion pole. It is possible to introduce a term which explicitly gives these unphysical fermion modes a large mass such that they will decouple from the physical fermion modes; this is the Wilson term [31]. We will introduce and demonstrate how to improve upon the Wilson term in detail in Sec. 3.1.1 of Chapter 3. While the Wilson term is the simplest solution to the fermion doubler problem, the addition of this extra term at finite lattice spacing explicitly breaks the chiral symmetry of QCD at the Lagrangian level. This symmetry will be retrieved in the continuum limit (albeit taking the chiral-continuum limit is an exponentially hard problem at strong coupling), however for certain problems of interest it is desirable to have chiral symmetry at finite lattice spacing. At present the only known lattice fermion discretization which explicitly preserves chiral symmetry is the so-called overlap formulation [32, 33][b]. In Chapter 3, we will formulate and then perform first ever studies with overlap fermions in Minkowski spacetime. A derivation of the overlap Hamiltonian is provided in Appendix D. We conclude by noting that a chiral, doubler-free formulation of a lattice gauge theory in even spacetime dimensions is non-trivial, and has deep connection to differential and algebraic topology [35, 36].

For the Yang-Mills term of the QCD Lagrangian, we must introduce the plaquette variable for gauge links, $U_{\square,\mu\nu}(n)$. This plaquette variable is a product of four nearest-neighbor gauge links which form a closed loop (in the shape of a square) starting at the position n and moving in the $+\hat{\mu}$ and $+\hat{\nu}$ directions. By construction it is gauge invariant. More explicitly,

$$\begin{aligned} U_{\square,\mu\nu}(n) &= U_\mu(n)U_\nu(n+\hat{\mu})U_{-\mu}(n+\hat{\mu}+\hat{\nu})U_{-\nu}(n+\hat{\nu}) \\ &= U_\mu(n)U_\nu(n+\hat{\mu})U_\mu^\dagger(n+\hat{\nu})U_\nu^\dagger(n)\,. \end{aligned} \tag{1.15}$$

The Yang-Mills term then takes the form of the Wilson gauge action,

$$\mathcal{L}_{lat}^G(n) = -\frac{2}{a_t a_s^3}\sum_{\mu<\nu} \mathrm{Re\ tr}\left[\mathbb{1} - U_{\square,\mu\nu}(n)\right]\,, \tag{1.16}$$

[b]There are also domain wall fermions [34], where one considers a similar setup to the Wilson formulation, but adds a fictitious fifth dimension. When the extent of this extra dimension is large, chiral symmetry breaking is exponentially suppressed. Even with this extra dimension, the computational cost compared to overlap is generally less. Because of this, the domain wall formulation is frequently used in Euclidean lattice gauge theory simulations. It can also be formally shown that when the extra dimension is taken to be infinitely large, the overlap operator is recovered.

where the inequality in the sum is over plaquettes ensures that only a single orientation is considered, avoiding double counting. Similar to the Dirac term, it is clear that by expanding the Wilson gauge action in terms of gauge fields A_μ, one retrieves the continuum result in the $a_\mu \to 0$ limit. Away from this limit, corrections are of order $\mathcal{O}(a_\mu^2)$.

For a complete pedagogical introduction, as well as many practical and interesting aspects of modern lattice field theory, see [37].

1.3.2 Semi-Classical Methods

To solve the full quantum theory, the lattice QCD path integral must be evaluated. As previously mentioned, at present, this can only be done in Euclidean spacetime, precluding the study of the real-time dynamics from first principles. However, in many of the situations we will consider in this thesis, a classical or semi-classical description can be justified (this approximation will be justified in the relevant sections where applied). It is straightforward to then derive the classical equations of motion from the principle of stationary action,

$$\frac{\delta S[A]}{\delta A^a_\mu(x)} = 0\,, \tag{1.17}$$

where the action is defined as $S = \int d^4x \mathcal{L}$. From this expression and Eq. (1.1), we arrive at the classical Yang-Mills (CYM) equations,

$$[D_\mu(x), F^{\mu\nu}] = J^\nu\,, \tag{1.18}$$

where J^ν is an matter field current (for full QCD given by $J^{\mu a} = g\bar{\psi}\gamma^\mu t^a \psi$) which is covariantly conserved, as $D_\mu J^\mu = 0$. This current vanishes identically for pure gauge theory. For the fermion fields, the equation of motion is the Dirac equation; we will postpone any further discussion until Chapter 3, where formulating and solving this equation non-perturbatively is the main focus.

Focusing on the pure gauge CYM equations, we fix some of the residual gauge freedom by taking temporal gauge, $A_0 = 0$. This is a particularly convenient choice for the lattice, as the temporal gauge links go to unity. The continuum equations of motion are then simply

$$\begin{aligned} \partial_t A_i &= E_i\,, \\ \partial_t E_i &= -D_j F_{ji}\,, \end{aligned} \tag{1.19}$$

where the conjugate momenta E^a_i are algebra valued fields, which we identify as the chromo-electric field. There is an additional constraint equation, the non-Abelian version of Gauss law $D_i E^i = 0$ (the right hand side will not be zero if we relax the pure gauge assumption).

Lattice versions of these equations of motion can be derived from the classical Yang-Mills Hamiltonian, first derived by Kogut and Susskind [38], or the Wilson gauge action [39, 40, 41]. Using the former method, we provide the lattice equations of motion and briefly discuss how these equations of motion are solved numerically in Chapter 2.

1.4 Standard Model of Heavy-Ion Collisions

Ultrarelativistic heavy-ion collisions allow for one of the only settings for the study of the many-body dynamics of the strong force. Currently, collisions are performed at RHIC with two gold (Au) ions at with top center-of-mass energy of 200 GeV, and at the LHC with two lead (Pb) ions at 2.76 TeV. Before the collision, the two nuclei are highly Lorentz contracted nuclei as they move at nearly the speed of light. Once a collision occurs, the colliding nucleons inside of the nuclei deposits a large amount of energy in the collision region. This then creates a medium, which rapidly expands, cools, and isotropizes until it reaches the so-called cross-over temperature, calculated from first principles lattice QCD simulations to be $T_c \simeq 155$ MeV $\approx 2 \cdot 10^{12}$ °C [26], whereby the quarks and gluons which were once liberated form hadrons. As previously mentioned, there now exists strong evidence that the medium created in these collision is a QGP [42].

For few-body systems, like the high energy collisions of leptons, the QCD dynamics of the system can be accurately described in terms of perturbative QCD. However, for the many-body problem found in heavy-ion collisions, at present, it is not known how to describe the entire evolution of the system in terms of the underlying theory of QCD. This is because current methods for exactly solving QCD are ill-suited for dynamical systems due to so-called sign problems [43][c]. It is likely that even if these problems were circumvented, the computational resources needed would be insurmountable even with fastest current supercomputers. Thus it is necessary to develop effective models for the evolution of the system, which can be validated by comparison to data. This modeling has progressed significantly over the past decade, with a few standard paradigms have been emerged, which we will now cover.

1.4.1 Initial dynamics: the Color Glass Condensate

A systematic QCD approach to describe the very early-time evolution of the matter in an ultrarelativistic heavy-ion collisions is through the Color Glass Condensate effective field theory (CGC EFT) [9]. The CGC EFT is formulated in the infinite momentum frame (with appropriate gauge choice) and relies on a separation of energy scales between hard and soft partons, which are primarily gluons. This is experimentally well justified, as demonstrated from parton distribution functions (PDFs) extracted from deep inelastic electron-proton scattering (DIS) experiments. Results from the HERA experiment [2] are shown in Fig. 1.2, where it is clear that at small Bjorken x [d], the gluons dominate the hadronic wavefunction. In the high energy (Regge-Gribov) limit, x becomes very small. Typical values of x at RHIC energies are $x \sim 10^{-2}$, while for the LHC $x \sim 10^{-3} - 10^{-4}$. This implies that it is reasonable to consider a high energy nucleus as being composed primarily of high density gluon matter.

However, the growth in the gluon density at small-x must be tamed in order for the cross-section to not violate the Froissart-Martin "black-disk" limit. Non-linear effects in

[c] A sign problem also exists for finite baryon density lattice QCD calculations, which would also need to be avoided in order to simulate the entire evolution of the heavy-ion collision.

[d] In DIS kinematics, $x = \frac{Q^2}{2P \cdot q}$, where P is the the hadron four-momentum, and $Q^2 = -q^2$ is the exchanged photon virtuality, where q is the space-like momentum of the photon. In the infinite momentum frame, this becomes equivalent to the partonic momentum fraction (neglecting hadron mass effects).

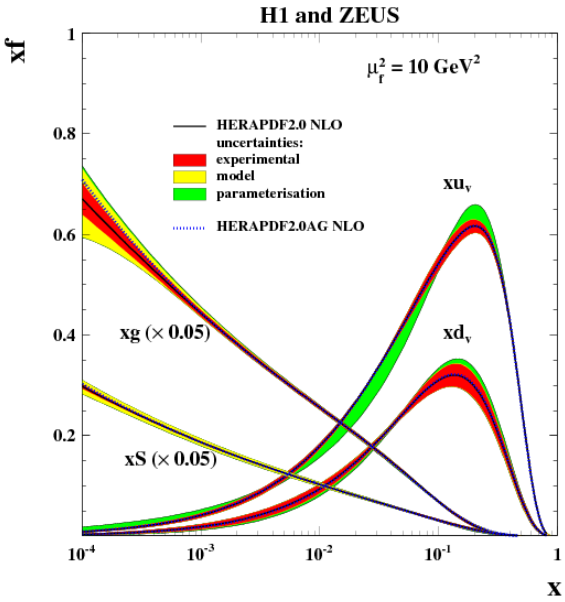

Figure 1.2: Parton distribution functions measured from the HERAPDF 2.0 collaboration at a fixed virtuality, Q^2, as a function of x. Figure from [2].

QCD, which can be understood as the emergence of a non-zero probability for gluons to recombine, coupled with shadowing effects, solve this problem: this is the phenomena of gluon saturation [44] (we refer the interested reader to [45] for a comprehensive review). In this high gluon density state, an intrinsic resolution scale, known as the saturation momentum scale, Q_s, emerges. The scale Q_s increases with energy (and thus momentum fraction x), as well as the number of nucleons, A; this allows for the parametric relation

$$Q_s^2 \sim A^{1/3}\left(\frac{1}{x}\right)^{\lambda}, \tag{1.20}$$

where $\lambda > 0$ [46]. The maximum momenta in the nuclear wavefunction where the gluon occupation is large is also set by Q_s. At sufficiently high energies (small x), or large enough nuclear size A, Q_s becomes a semi-hard scale such that $Q_s \gg \Lambda_{QCD}$; Q_s is then the dominant scale of the problem. By virtue of the asymptotic freedom of QCD, $\alpha_S(Q_s) \ll 1$, which permits the application of weak coupling methods to systematically compute quantities in this otherwise highly non-trivial many-body system. As we are in the nonlinear regime with small coupling g, the largest momentum is of the order $1/g$, as can be inferred from Eq. (1.5). Parametrically, the gluon occupation is then $f(k_\perp \leq Q_s) \sim \langle AA \rangle \sim \frac{1}{g^2} \sim \frac{1}{\alpha_S} \gg 1$.[e]

Consider now a hadron in the infinite-momentum frame with momentum $P^\mu = (P, 0, 0, P)$. In light-cone coordinates[f], this hadron has (only) large longitudinal momentum $P^+ = \sqrt{2}P$.

[e]This is the *condensate*-like quality of the CGC; however unlike a Bose-Einstein condensate where most of the photons are peaked around $k = 0$, here most of the gluons are peaked around $k = Q_s$.

[f]The light-cone coordinates for a general four-vector v^μ are defined as $v^\mu = (v^+, v^-, \mathbf{v}_\perp)$, where $v^\pm = \frac{1}{\sqrt{2}}(v^0 \pm v^3)$. Taking the inner product between momentum and position, $p \cdot x = p^+x^- + p^-x^- - \mathbf{p}_\perp \cdot \mathbf{x}_\perp$; thus when p^- has the interpretation as light-cone energy, x^+ can be understood as light-cone time. Similarly, when p^+ has the interpretation as longitudinal momentum, x^- can be interpreted as the longitudinal coordinate.

Fast (large-x) partons, typically the valence quarks, carry the majority of this light-cone longitudinal momentum. They then act as sources for soft partons ($q^+ \ll P^+$); from the HERA PDFs in Fig. 1.2, these will primarily be small-x gluons [47, 48, 49].

In high energy nuclear collisions at RHIC and the LHC, before the collision the nuclei are moving near the speed of light, thus we consider nuclei in a collision to move along the +/− light cones, as depicted in Fig. 1.3. As the large-x valence partons have a large light-cone momentum, we treat them eikonally, whereby their light-cone momentum doesn't change by emitting (or absorbing) a small-x gluon. There is however a separation of time scales due to different coherence lengths [48, 49] – the fast moving, large-x valence partons are seen as "frozen" with respect to the small-x partons[g]; as an eikonal current, they take the form $J^\pm \sim \delta(x^\mp)$. As there are presumably a large number of sources, we may additionally treat them classically. These sources are then simply represented as eikonal currents with classical color charge density ρ, of the form

$$J_a^\mu = \delta^{\pm\mu}\rho_a(x^\pm, \mathbf{x}_\perp)\delta(x^\mp)\,. \tag{1.21}$$

Gauge invariance is maintained as the sources ρ are stochastic variables[h] which have zero expectation value. From the viewpoint of the soft gluons, the fast moving valence partons are highly Lorentz contracted, so $\rho_a(x^\pm, \mathbf{x}_\perp) = \rho_a(\mathbf{x}_\perp)$ is generally assumed. Since we argued that the gluons in the nuclei are highly occupied, by the correspondence principle they can be treated as classical gauge fields, A^μ. We can then appeal to semi-classical methods; thus the equations of motion for the gluon fields are given by the classical Yang-Mills equations,

$$[D_\mu, F^{\mu\nu}] = J^\nu\,. \tag{1.22}$$

Expectation values of an operator $\mathcal{O}$ are taken as a classical-statistical average over ρ, given in terms of a weight functional of ρ, $W_{\Lambda^+}[\rho]$, as

$$\langle\mathcal{O}\rangle = \int [D\rho] W_{\Lambda^+}[\rho]\mathcal{O}[\rho]\,, \tag{1.23}$$

where $\mathcal{O}[\rho]$ is the expectation value for $\mathcal{O}$ for a given charge configuration ρ. Here Λ^+ is the scale which separates the fast moving ($k^+ > \Lambda^+$) valence charges and the soft fields ($k^+ < \Lambda^+$). Because we are dealing with colored objects, we must average over all possible configurations of charges to ensure gauge invariance.

Without detailed knowledge of how these color charges are distributed in the nucleus, a simple way to model the color charge densities is to assume that the effective color charge seen by a colored probe is a random walk. This is the McLerran-Venugopalan (MV) model [48, 49]. Thus, we assume that only two-point Gaussian correlations exist,

$$\langle\rho_a(x^\pm, \mathbf{x}_\perp)\rangle = 0\,, \qquad \langle\rho_a(x^\pm, \mathbf{x}_\perp)\rho_b(y^\pm, \mathbf{y}_\perp)\rangle = g^2\mu^2\delta_{ab}\delta(x^\pm - y^\pm)\delta^2(\mathbf{x}_\perp - \mathbf{y}_\perp)\,, \tag{1.24}$$

where μ^2 is the fluctuations in the color charge per unit area, which scales parametrically like $A^{1/3}$ for large nuclei. For the MV model, the weight functional is a Gaussian functional of ρ,

$$W_{\Lambda^+}[\rho] = \exp\left(-\int d^2\mathbf{x}_\perp \frac{\rho_a(\mathbf{x}_\perp)\rho_a(\mathbf{x}_\perp)}{2\mu^2}\right). \tag{1.25}$$

[g] This separation of characteristic timescales is a *glass*-like feature of the CGC.

[h] Additionally, because of the stochasticity of the sources, they are akin to a spin-*glass* [47].

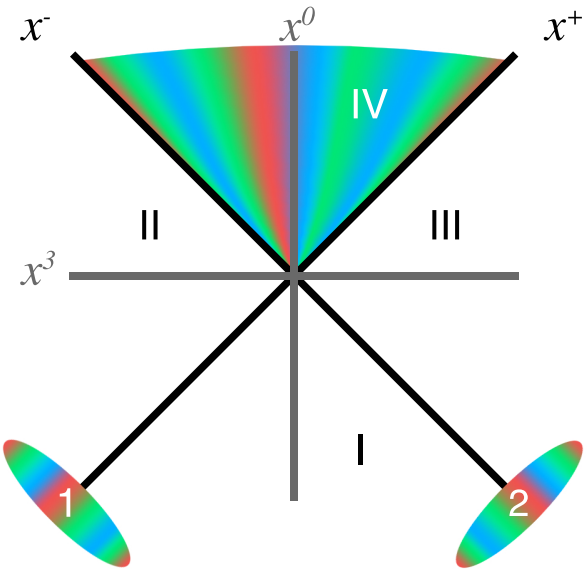

Figure 1.3: Cartoon depiction of an ultrarelativistic nuclear collision on the light cone.

The MV model is suitable for moderate values of $x \sim 10^{-2}$, however for smaller values of x, quantum evolution is needed – this is accomplished through the so-called JIMWLK [50, 51, 47, 52, 53] evolution equation. This Wilsonian renormalization group equation removes the dependence on Λ^+, which otherwise is logarithmic. Remarkably, this evolution equation can be formulated in terms of the weight functional $W_{\Lambda^+}[\rho]$, such that the equations of motion remain the classical Yang-Mills equations. The MV model is generally used as an initial condition for JIMWLK evolution, which is then solved numerically through reformulation as a Langevin equation [54]. In this thesis we will however neglect the effects of evolution.

Dense-dense

Returning to the classical Yang-Mills equation, following Fig. 1.3, we now set can solve this boundary value problem for the specific case of valence charge current

$$J^\mu = \delta^{+\mu}\rho_{(1)}(\mathbf{x}_\perp)\delta(x^-) + \delta^{-\mu}\rho_{(2)}(\mathbf{x}_\perp)\delta(x^+)\,. \tag{1.26}$$

We take Fock-Schwinger gauge, $x^+A^- + x^-A^+ = 0$, so $A^+_{(1)} = 0$ and $A^-_{(2)} = 0$ [55]. Trivially, in region I of Fig. 1.3, $A^\mu = 0$. From the current in Eq. (1.26), the isolated gauge fields in regions II and III of Fig. 1.3 are pure gauge transverse fields [48, 49],

$$A^\pm_m(\mathbf{x}_\perp) = 0\,, \tag{1.27}$$

$$A^i_{(m)}(\mathbf{x}_\perp) = \frac{i}{g}U_{(m)}(\mathbf{x}_\perp)\partial^i U^\dagger_{(m)}(\mathbf{x}_\perp)\,, \tag{1.28}$$

where $m = 1, 2$ referring to the $x^3 = +z$ and $-z$ moving nuclei respectively. Here the Wilson lines are given by

$$U_{(m)}(\mathbf{x}_\perp) = \exp\left(-ig\Phi_{(m)}(\mathbf{x}_\perp)\right)\,. \tag{1.29}$$

The field $\Phi_{(m)}$ is generated by the valence charges,

$$\partial_\perp^2 \Phi_{(m)} = g\rho_{(m)}(\mathbf{x}_\perp)\,, \tag{1.30}$$

which is determined using solutions to the classical Yang-Mills equations, $\partial_i A^i_{(m)} = g\rho_{(m)}(\mathbf{x}_\perp)$. The combined gauge field for regions I,II, and III is then

$$A^\pm = 0\,, \tag{1.31}$$
$$A^i = \theta(x^-)\theta(-x^+)A^i_{(1)}(\mathbf{x}_\perp) + \theta(x^+)\theta(-x^-)A^i_{(2)}(\mathbf{x}_\perp)\,. \tag{1.32}$$

In order to solve for the classical Yang-Mills equations inside the forward light cone, region IV, we first much match singularities on the light cone, i.e. at $\tau = 0$[i] [55, 56]. These singularities exist at $x^+ = 0$ and $x^- = 0$, at $x^+ = 0$ for $x^- > 0$, and at $x^- = 0$ for $x^+ > 0$. The result is well known [55], and most compactly written in $\tau - \eta$ coordinates (in the equivalent $A_\tau = 0$ gauge) as

$$A^i(\tau = 0, \mathbf{x}_\perp) = A^i_{(1)}(\mathbf{x}_\perp) + A^i_{(2)}(\mathbf{x}_\perp)\,, \tag{1.33}$$
$$A^\eta(\tau = 0, \mathbf{x}_\perp) = [A^i_{(1)}(\mathbf{x}_\perp), A^i_{(2)}(\mathbf{x}_\perp)]\,. \tag{1.34}$$

Given an initial configuration of $\rho_{(m)}$'s, the boundary conditions Eqns. 1.33 and 1.34 serve as an initial condition for further evolution of classical Yang-Mills evolution in the interior of the forward light cone. Despite the system being weakly coupled, it is highly correlated. Keeping all order in ρ's for both nuclei (this is the origin of the moniker 'dense-dense') precludes perturbative methods. This weakly coupled system can be solved exactly numerically, as it is well known how to solve classical Yang-Mills. Pioneering numerical work was performed in [57]. These studies generally are performed in a 2+1D boost invariant spacetime, and have been applied to a variety of problems, c.f. [58, 59, 60, 61, 62]. Recent progress has been made towards extending such simulations to 3+1D spacetime [63]. At present, the CGC initial conditions coupled with realistic nuclear color charge modeling and 2+1D classical Yang-Mills evolution are used as an initial condition for viscous hydrodynamics [5], with great phenomenological success [64, 65].

The Glasma

A striking observation can already be made from the boundary ($\tau = 0$) conditions, Eqns. 1.33 and 1.34 [55]: the strong color fields which exist in the pre-collision nuclei will produce very strong longitudinal chromoelectric and chromomagnetic fields already at the first instant of the collision, $\tau = 0$. By the approximate boost invariance, the fields are extended far in the longitudinal extent. As previously mentioned, the color charges are localized in the transverse plane to "domains" of extent $1/Q_s$. Thus, the localized parallel chromoelectric and chromomagnetic fields form so-called "glasma flux tubes" [66]. Such field configurations already have non-trivial properties, for instance they will have large topological charge, which may lead to anomalous fermion production via the chiral anomaly of QCD [66, 67].

[i] It is also common to formulate this problem in Bjorken coordinates (Milne metric), where $\tau = \sqrt{(x^0)^2 - (x^3)^2} = \sqrt{2x^+x^-}$ is the proper time and $\eta = \frac{1}{2}\ln(x^+/x^-)$ is the spacetime rapidity. In this case our gauge choice is easily understood as $A_\tau = x^+A^- + x^-A^+ = 0$.

These strong fields at $\tau = 0$ will also produce the matter that eventually becomes the QGP. The details of how this happens has slowly emerged over the past decade. First, as the initial glasma flux tubes are highly anisotropic, they are unstable in the presence of small vacuum fluctuations [68]. These fluctuations begin to break the approximate boost invariance of the system, which leads to plasma instabilities which breaks up the flux tubes structures. The plasma instabilities then cause exponential mode growth in the infrared, whereby the system becomes highly over-occupied for modes with $k < Q_s$[j] over a very short time. This forms the over-occupied state of matter which is referred to as the Glasma – the state of matter in between the CGC and the QGP. Using classical-statistical methods[k], it was observed that the system then begins to thermalize and isotropize through a turbulent cascade. The system then reaches a non-thermal fixed point via a universal attractor, whereby the results become insensitive to the details of the initial conditions [39, 70, 71]. Perhaps most remarkably, these simulations were able to numerically determine, from the universal scaling exponents of the distribution function, which thermalization scenario the classical Yang-Mills dynamics leads to [71].

The initially over-occupied gluons will however scatter, produce quarks, and in general become more dilute as the system expands. At the point in the evolution when the gluon occupation becomes parametrically of order $f \sim 1$, classical-statistical methods are no long applicable. Instead, an effective kinetic theory description can be applied [72]; however, there is a regime where classical-statistical and effective kinetic descriptions are simultaneously valid [73, 74]. As the system continues to move towards isotropy and thermal equilibrium, and the coupling increases, it has been shown that there is a smooth mapping between this effective kinetic theory description and hydrodynamics [75, 76]. In practice, simulations of heavy-ion collisions directly map the initial conditions to hydrodynamics, neglecting the kinetic regime. Very recently, an effective kinetic theory framework has been established to smoothly connect the initial CGC/Glasma dynamics to viscous hydrodynamics [77, 78]. Thus, from the weak coupling perspective, the bulk approach to equilibrium is now fairly well understood.

Dilute-dense

Let us now consider asymmetric systems, like proton–lead at the LHC or proton/deuteron /helium-3–gold at RHIC, generically called pA collisions. As previously mentioned, parametrically $Q_s^2 \sim A^{1/3}$. Hence, it is likely that in a pA collision, the projectile (p/d/^{3}He) has a smaller Q_s^2 than the target (Au/Pb) nucleus. In the CGC EFT, the relation $(Q_s^p)^2 \ll (Q_s^A)^2$ can be understood formally in terms of the respective ρ's. In this so-called dilute-dense limit [79, 80], ρ_p is assumed to be much less than ρ_A. This implies that the Wilson line of the projectile can be expanded, and truncated, in powers of ρ_p. Without loss of generality, let us assume that $\rho_{(1)} = \rho_p$ and $\rho_{(2)} = \rho_A$ from the discussion in the previous sub-section

[j]This result hold for a more general over-occupied system with characteristic momentum scale Q, and may have applications to other systems than heavy-ion collisions.

[k]Since this is an initial value problem for classical fields, it is possible to map the problem to a classical-statistical problem [69]. The effects of the first order quantum corrections are included by calculating observables using expectation values evaluated over an ensemble of classical configurations with a common stochastic initial condition which is representative of the quantum phase-space distribution.

around Fig. 1.3. This simplifies the fields in regions II and III, such that Eq. (1.28) takes the form

$$A_p^i(\mathbf{x}_\perp) = \partial^i \Phi_p - \frac{ig}{2}\left(\delta_{ij} - \frac{\partial_i \partial_j}{\partial_\perp^2}\right)\left[\partial^j \Phi_p(\mathbf{x}_\perp), \Phi_p(\mathbf{x}_\perp)\right] + \mathcal{O}(\Phi_p^3)\,, \tag{1.35}$$

$$A_A^i(\mathbf{x}_\perp) = \frac{i}{g} U_A(\mathbf{x}_\perp)\partial^i U_A^\dagger(\mathbf{x}_\perp)\,, \tag{1.36}$$

where $\Phi_p(\mathbf{x}_\perp) = \frac{g}{\partial_\perp^2}\rho_p(\mathbf{x}_\perp)$. Keeping terms of order Φ_p (order ρ_p) allows for a straightforward, albeit lengthy, solutions to the fields for region IV, the forward light cone. We will not reproduce these results here, but full expressions can be found, in multiple gauges, in [79, 80, 81].

Having an analytical solution then for $A^\mu(x^+, x^-, \mathbf{x}_\perp)$ allows us to define the single inclusive distribution using the Lehmann-Symanzik-Zimmermann (LSZ) reduction formula [79, 81]. A particularly clear exposition is given in [81], where it is explicitly shown that at this order only "surface" terms, i.e. production at $\tau = 0$, contribute. The final compact result, which we will use in Chap. 5, is

$$E_k \frac{dN}{d^3k} = \frac{1}{8\pi^3 k_\perp^2}\left(\delta_{ij}\delta_{lm} + \epsilon_{ij}\epsilon_{lm}\right)\Omega_{ij}^b(\mathbf{k}_\perp)\left[\Omega_{lm}^b(\mathbf{k}_\perp)\right]^*\,. \tag{1.37}$$

Here $\delta_{ij}(\epsilon_{ij})$ is the Kronecker delta (antisymmetric tensor), $\Omega_{ij}^b(\mathbf{k}_\perp)$ is the Fourier transform of

$$\Omega_{ij}(\mathbf{x}_\perp) = g\left[\frac{\partial_i}{\partial_\perp^2}\rho_p^a(\mathbf{x}_\perp)\right]\partial^j W_{ba}(\mathbf{x}_\perp)t^b\,, \tag{1.38}$$

and

$$W_{ba}(\mathbf{x}_\perp) = 2\mathrm{tr}\left(U^\dagger(\mathbf{x}_\perp)t_b U(\mathbf{x}_\perp)t_a\right) \tag{1.39}$$

is the adjoint Wilson line describing the target. The quantity Ω has a simple interpretation as the gauge field of the projectile being color-rotated by the Wilson line of the target.

However, this result is also manifestly symmetric for $\mathbf{k}_\perp \to -\mathbf{k}_\perp$. Thus at this order in ρ_p, the odd component of the double inclusive distribution, responsible for the generation of the Fourier harmonics $v_3\{2\}$ (we will introduce this quantity in detail in Chapter 4), is exactly zero [81]. Since v_3 has been experimentally observed in all pA systems, it is clear that the lowest order in the dilute-dense power counting does not account for all of the observed physics qualitatively. However, v_3 is non-zero in the dense-dense limit for proper times $\tau > 0$ [61, 62], so there must be some order in ρ_p which gives rise to a non-zero v_3. Recently, it was shown that by including ρ_p^2 contributions, the odd component of the double inclusive distribution, and thus v_3, does not vanish [81]. The result is rather cumbersome but is provided in Eq. (5.3). We note that the full computation of the order ρ_p^2 (Φ_p^2) contribution is still incomplete [82], and remains an outstanding challenge. Nevertheless, we see that by considering the leading non-trivial pieces of the dilute-dense limit, qualitative expectations of finite even and odd azimuthal harmonics are achieved.

We conclude by noting that there is a further perturbative limit, the so-called dilute-dilute limit, or Glasma graph approximation. In this limit, only a single gluon exchange

is considered in the amplitude. Valid for $k_\perp > Q_s$, this approximation has been successful in explaining "ridge" correlations at the LHC for pA and pp collisions [83, 84, 85, 86, 87, 88]. However, as we will show in Chap. 4 and Appendix G, it is insufficient to describe multiparticle correlations at RHIC or the LHC.

1.4.2 Bulk evolution and hadronization

Following the early-time non-equilibrium dynamics, the system created during a heavy-ion collision becomes inherently quantum mechanical and strongly coupled. At this stage, currently available QCD-based methods are insufficient to describe the system microscopically. One effective description of the system, originally proposed by Landau, is to consider a long-wavelength, low energy effective description of the system in terms of relativistic hydrodynamics. While progress has been made in understanding how to derive hydrodynamics as a long-wavelength effective theory of a quantum field theory (see e.g. [89] and references within), a formulation from QCD remains an open problem.

The modern description of hydrodynamics for heavy-ion collisions comes from more basic assumptions. Consider first a non-interacting system of particles. If the de Broglie wavelength, λ_{DB}, is much shorter than the mean free path (typical interaction length), ℓ_{mfp}, the particles can be treated effectively as being classical objects[1]. If we have a many-body system of such classical particles, then the overall system size L will be larger than ℓ_{mfp} (and λ_{DB}). Thus, the individual particle nature is lost and the dynamics of the system becomes that of a continuous medium, a fluid. However, in order to have a well-defined low energy effective theory (this description should only be valid for "soft" physics, $p_\perp \lesssim 2$ GeV), the assumption of local thermal equilibrium is needed to be able to define average quantities within a single fluid cell [90]. For a strongly interacting system like the QGP, this is believed to approximately be the case.

To formulate the equations of motion for hydrodynamics for heavy-ion collisions, we first consider the basic requirements of local conservation of energy, momentum, and local charge conservation (for instance baryon number or electric charge),

$$\partial_\mu T^{\mu\nu} = 0\,, \quad \partial_\mu j_i^\mu = 0 \tag{1.40}$$

where $T^{\mu\nu}$ is the energy-momentum tensor and j_i^μ is the local charge current for charge i. Additionally, we require that the second law of thermodynamics is preserved with respect to the entropy current S^μ,

$$\partial_\mu S^\mu \geq 0\,. \tag{1.41}$$

The quantities must however be formulated in terms of the hydrodynamic fluid four-velocity, u^μ, which we can generally define as the four velocity as $u^\mu = \gamma(1, \mathbf{v})$ such that $u_\mu u^\mu = 1$; here $\gamma = (1 - v^2)^{-1/2}$. Then the constitutive relations are determined using an expansion in gradients. To lowest order (ideal hydrodynamics), the different vector and tensor structures, $T^{\mu\nu}$, j_i^μ, and S^μ, can be defined in terms of $u^\mu(x)$ and the thermodynamic variables, $\epsilon(x)$,

[1] In the opposite limit, the wavefunctions non-trivially overlap and must be treated quantum mechanically.

the energy density, $P(x)$, the pressure, and $s(x)$, the local entropy density:

$$T^{\mu\nu} = (\epsilon + P)u^\mu u^\nu - Pg^{\mu\nu}\,, \tag{1.42}$$

$$j_i^\mu = n_i u^\mu\,, \tag{1.43}$$

$$S^\mu = su^\mu\,. \tag{1.44}$$

However, for modern heavy-ion collision phenomenology, it has been argued that dissipative effects, especially viscosity, are important [91, 92, 93, 94]. To include these effects and ensure causality [95], a second order expansion in gradients is needed [96, 97]. The exact form of second order viscous hydrodynamics is still a topic of active investigation (c.f. [98, 99]), the shear viscosity transport coefficient, η, has generated great interest recently. While η has long been expected to be large [91], the relevant ratio in the equations of motion, η/s, was found to very small in phenomenological studies using viscous hydrodynamics [94], of the orders 10^{-1}. Remarkably, this coincides with the lower bound calculated in $\mathcal{N} = 4$ Super Yang-Mills [100] of $\eta/s \geq 1/4\pi$. While first-principles QCD calculations of the transport coefficients remain elusive, recent progress has been made with lattice SU(3) Yang-Mills simulations [101, 102] and using functional methods for QCD [103]; the latter of which has even been applied to hydrodynamic modeling [104]. If the actual QCD plasma value for η/s turns out to be close to the phenomenological value, this would be the lowest η/s of any physical system– thus the QGP would be the most perfect liquid in nature.

Closing this system of equations requires an equation of state, relating the pressure, energy density, and the charge densities, $n_i = \sqrt{j_i^\mu k_{\mu,i}}$, which are defined in terms of the temperature T and any relevant chemical potentials. As previously mentioned, the equation of state has been calculated for QCD in thermal equilibrium at zero and small baryon chemical potential using first principles lattice QCD simulations [26, 27]. For ultrarelativistic heavy-ion collisions, the baryon number density is believed to be vanishingly small [m], and the plasma to be locally electrically neutral, so in practice the local conserved charges are not considered. However, when at lower energies or if including chiral effects, these currents need to be included.

Once the equations are determined, one has to supply an initial condition for quantities like $T^{\mu\nu}$ and u^μ. As mentioned in the previous section, the state-of-the-art of initial state modeling comes from combining Glauber-like [105] sampling of initial nucleon positions with CGC and Glasma dynamics [5]. The hydrodynamic description of deconfined, strongly interacting quark and gluon matter breaks down when the temperature or energy density reaches a low enough value such that the particles stop interacting collectively and must instead be treated as individual particles – this is the (kinetic) freeze-out. Due to confinement, it is assumed that there is an instantaneous hadronization. In practice, a single temperature or energy density is chosen whereby the matter in a given fluid cell freezes out and becomes part of the four-dimensional freeze-out hypersurface, Σ_μ. Once the freeze-out hypersurface has been determined, the standard method to calculate the momentum distribution of hadrons

[m] This vanishing baryon number density necessitates the use of the Landau (energy) frame – this choice of frame becomes important when we include viscous effects. For a more complete discussion on choices of frame, see e.g. [90].

is through the Cooper-Frye procedure [106], given by

$$\frac{d^3N}{d^2\mathbf{p}_\perp dy} = \int_\Sigma f(x,p)p^\mu d\Sigma_\mu \,, \tag{1.45}$$

where y is the rapidity, f is the distribution function for a particular species of hadrons (the equilibrium part is assume to be a Bose or Dirac distribution, however corrections from dissipative effects are also included for second order hydrodynamics), p^μ is the hadron four-momentum, and N is the number of hadrons. With this momentum distribution, it is possible to compute various observables. We conclude by noting that current state-of-the-art simulations generally include additional resonance decays, as well as hadronic rescatterings, before "detection". These effects are taken into account by using well-known packages like UrQMD [107, 108].

1.4.3 Wrap-up

As discussed, the standard model of heavy-ion collisions is a collection of effective descriptions, all matched together by simple physical considerations like conservation of energy. While seemingly ad-hoc, it has been shown to be compatible with a large variety of data in heavy-ion collisions at both RHIC and the LHC, ranging over a factor of ~ 100 in energy. This model has even become somewhat predictive; for a recent example of LHC Xe-Xe collisions, see [109].

However, in addition to understanding the regime of validity of this paradigm, we must understand where it breaks down. For the CGC EFT, it is clear that for lower energies, many of the approximations made require large corrections, likely requiring a completely new formalism. For low energy collisions, like what will be explored in the upcoming RHIC Beam Energy Scan II program, only phenomenologically motivated models for the initial state dynamics currently exist [110]. Additionally, in these low energy collisions, the pure hydrodynamic assumption becomes less reliable as some fluid cells will freeze out or may never become hydrodynamic in the first place.

Another regime where this paradigm may break down is in smaller systems, like proton–nucleus or proton–proton collisions. For these systems, it is unclear if the second order hydrodynamic formulation is enough, as gradients and viscous corrections can be very large, and cavitation (negative pressures) is possible, signaling a clear breakdown of the effective description [111, 112, 78]. However, the applicability of hydrodynamics has been a subject of intense recent study, with conceptual advances coming from the possibility of off-equilibrium attractors in QGP-like plasmas (see e.g. [113] and references within). Potentially a more pressing problem, however, is the fact that a key signature of the QGP, jet quenching, has not been observed experimentally in small systems [114]. As an alternative, in Chapters 4 and 5, we will discuss the possibility that these small systems can be described primarily in terms of the pre-equilibrium dynamics.

Chapter 2

Sphalerons and the approach to equilibrium

The following chapter is based off of

- M. Mace, S. Schlichting, R. Venugopalan. *Off-equilibrium sphaleron transitions in the Glasma.* Phys.Rev. D93, 074036 (2016). Copyright (2016) by the American Physical Society

- J. Berges, M. Mace, S. Schlichting. *Universal self-similar scaling of spatial Wilson loops out of equilibrium.* Phys. Rev. Lett. 118, 192005 (2017); arXiv:1703.00697 [hep-th]. Copyright (2017) by the American Physical Society

Topological transitions are ubiquitous in nature and believed to be responsible for a variety of phenomena across the most diverse energy scales. In the context of non-Abelian gauge theories, a prominent example are transitions between energy degenerate ground states of definite Chern-Simons number, mediated by unstable, spatially localized classical field configurations of finite energy called Sphalerons [115, 116, 117, 118, 119]. Interest in these so-called sphaleron transitions first arose in the context of electroweak baryogenesis [120, 121, 122]: the high temperatures make these transitions energetically favorable and may lead to the large violations in baryon number necessary to explain the matter-antimatter asymmetry of the universe [123].

Sphaleron transitions can also be significant in QCD at high temperatures and energy densities [124, 125]. In this case, there is no baryon number violation; however, due to the chiral anomaly and the Atiyah-Singer index theorem, these sphaleron transitions can generate significant amounts of axial charge. Because such transitions are governed by ultrasoft magnetic modes [121], their rate in a non-Abelian plasma at finite temperature can be computed by solving classical equations of motion in real time [126]. Hard quantum modes still play a role due to Landau damping effects [127]; nevertheless, their effect can be accounted for in the hard thermal loop effective theory [128] and the sphaleron transition rate can still be computed in a real time simulation non-perturbatively [129]. Estimates

now exist for an SU(3) gauge theory at high temperatures where weak coupling methods are justified [130].

A striking observation is that if the axial charge generated from sphaleron transitions is produced in the presence of a sufficiently strong external magnetic field, a net vector charge current can be produced in a hot QCD plasma [131, 132]. This phenomenon is the Chiral Magnetic Effect (CME), introduced previously in Chapter 1. This pheomena can be studied in ultra-relativistic heavy-ion collisions, where the magnetic fields in non-central collisions are very large at early times after the collision, and the energy densities are also sufficiently large that deconfined QCD matter is created. Experimental searches for the CME are ongoing at RHIC and the LHC, and intriguing hints suggestive of the CME and other anomalous transport effects have been seen [133, 134, 135, 136]. However conventional explanations for the observed signatures have also been put forward [137, 138, 139, 140, 141] and further progress relies in part on an improved theoretical understanding of the expected magnitude and features of the signal. A status report on theoretical models of the CME and on-going experimental searches can be found in Ref. [142].

A major complication for theoretical descriptions of the chiral magnetic effect in heavy-ion collisions is the very short lifetime of the external magnetic field at the highest RHIC and LHC energies. Computations suggest that the magnitude of the magnetic field becomes smaller than the values relevant for the CME ($eB \geq m_\pi^2$) on very short time scales of ~ 0.1 to $0.2\,\frac{fm}{c}$ of the LHC and RHIC collisions respectively [143] though in principle, very large electrical conductivities in the QGP can extend this time scale to slightly longer times [144]. Hence to understand whether the CME has observables consequences in heavy ion collisions, one needs to obtain an estimate of the sphaleron transition rate at very early times in the collision when the system is far off-equilibrium.

A systematic QCD approach to the very early time evolution in ultra-relativistic heavy ion collisions is obtained in the Color Glass Condensate (CGC) effective field theory [9], previously introduced in Chapter 1. In this description, very high occupancy gluons in the nuclear wavefunctions are released in the collision generating non-equilibrium matter called the Glasma [48, 55, 57, 66]. The dynamics of the Glasma is controlled by a saturation scale Q_s, which represents the hard momentum scale up to which gluons in the nuclear wavefunction have maximal occupancy. This saturation scale grows with the energy of the collision. When $Q_s \gg \Lambda_{\rm QCD}$, where $\Lambda_{\rm QCD}$ is the intrinsic QCD scale, the QCD coupling $\alpha_S(Q_s) << 1$ and weak coupling methods are applicable. Because the occupancy of gluons is parametrically of order $1/\alpha_S(Q_s) >> 1$ in the Glasma, the early time dynamics of this matter may be described by classical-statistical methods [58, 145, 146, 147, 70]. One therefore has a clean theoretical limit in QCD, whereby the properties of the non-perturbative Glasma can be computed systematically [148].

In this chapter we present a first real time non-perturbative computation of the far from equilibrium sphaleron transition rate in the Glasma. For simplicity, we shall consider sphaleron transitions in a fixed box rather than the realistic (but computationally far more challenging) longitudinally expanding case [a]. We will employ a numerical lattice imple-

[a] Fluctuations in the Chern-Simons number for the longitudinally expanding, albeit boost invariant, Glasma were considered previously in [59]. Because boost invariant gauge field configurations are 2+1-dimensional configurations, the second homotopy group of SU(2) is trivial. Thus in this case, non-zero integer valued topological transitions are not allowed; fractional values of topological charge can nevertheless

mentation of the classical-statistical dynamics and adapt techniques previously developed in the context of classical Yang-Mills simulations to extract the thermal sphaleron transition rate [149, 150, 3, 151], and in real-time studies of electroweak baryogenesis [152, 153, 154, 155, 156, 157, 158].

A deeper understanding of the rate of sphaleron transitions requires that one explore simultaneously the scales associated the hard modes as well as the softer electric and magnetic screening scales in the Glasma. How these scales develop with time has been discussed previously in the context of thermalization of the Glasma in both analytical [159, 160] and numerical approaches [39, 161, 162]. We will revisit this problem and demonstrate numerically that a clear separation of scales takes place with the temporal evolution of the Glasma.

In particular, we will compute the spatial Wilson loop which provides the scale determining magnetic screening in a hot plasma in equilibrium. Albeit the non-equilibrium temporal evolution of the spatial Wilson loop has been studied previously [39], we will go further and extract the scaling exponent that controls the temporal evolution of the corresponding string tension in the classical theory. We will show that the time evolution of the sphaleron transition rate is controlled by this string tension, scaling dimensionally as the string tension squared. Unlike the thermal case, topological transitions in the Glasma are determined by this magnetic scale alone and are robustly described by classical-statistical dynamics as long as occupancies are large.

The outline of this chapter is as follows: in Section 2.1, we will give a brief overview of sphaleron transitions, in and out of equilibrium. In Section 2.2, we discuss in some detail how we measure the Chern-Simons number on a real time numerical lattice. We shall outline two different approaches, a "slave field" approach and a "calibrated cooling" approach and demonstrate, as a warm-up, our technology in the well understood case of thermal equilibrium initial conditions. Then in Section 2.3, we will introduce our non-equilibrium initial conditions and compute physical hard and soft scales as well as the far from equilibrium sphaleron transition rate. We will compare and contrast our results to those obtained in thermal equilibrium. In Section 2.5, we will summarize our results, discuss their implications and outline future work. Some details of the numerical procedure and essential tests are described in two Appendices.

2.1 Sphaleron transitions and axial charge dynamics

In $SU(N_c)$ gauge theories with N_f light flavors of fundamental fermions, the conservation of the axial current associated with each quark species

$$j^{\mu}_{5,f} = \overline{q_f}\gamma^{\mu}\gamma_5 q_f \ , \tag{2.1}$$

is violated due to the axial anomaly as well as the explicit symmetry breaking introduced by the quark masses m_f

$$\partial_{\mu} j^{\mu}_{5,f} = 2m_f \overline{q}\gamma_5 q - \frac{g^2}{16\pi^2} F^a_{\mu\nu}\tilde{F}^{\mu\nu}_a \ , \tag{2.2}$$

be generated by fluctuations in the color electric and color magnetic fields.

where $F^a_{\mu\nu} = \partial_\mu A^a_\nu - \partial_\nu A^a_\mu + g f_{abc} A^b_\mu A^c_\nu$ denotes the non-Abelian field strength tensor and $\tilde{F}^{\mu\nu}_a = \frac{1}{2}\epsilon^{\mu\nu\alpha\beta} F^a_{\alpha\beta}$ is its dual [163]. Since in the high-temperature phase the explicit breaking due to the quark masses is usually neglected, we will denote the combined axial current of all light flavors as j^μ_5 in the following. In this limit, the anomaly equation takes the form

$$\partial_\mu j^\mu_5 = -\frac{g^2 N_f}{16\pi^2} F^a_{\mu\nu} \tilde{F}^{\mu\nu}_a \,, \tag{2.3}$$

and states that fluctuations of the $SU(N_c)$ gauge fields characterized by $F_{\mu\nu}\tilde{F}^{\mu\nu}$ can induce local imbalances of the axial charge density (j^0_5) as well as global imbalances of the net axial charge

$$J^0_5(t) = \int d^3x \; j^0_5(t,x) \,. \tag{2.4}$$

As noted previously, it was realized that in the presence of additional $U(1)$ electro-magnetic fields, such imbalances of axial charge densities (j^0_5) can lead to a variety of novel transport phenomena associated to the Chiral Magnetic (CME) [131, 132] and related effects [142].

Since the anomaly relation in Eq. (2.3) suggests that the fluctuations of axial charges are sourced by fluctuations of $F_{\mu\nu}\tilde{F}^{\mu\nu}$, basic features of the generation of an axial charge imbalance can be understood by investigating the non-Abelian dynamics of gauge fields[b]. Concentrating on the Yang-Mills sector from now on, it is convenient to express the right hand side of the anomaly equation in terms of the Chern-Simons current

$$K^\mu = \frac{g^2}{32\pi^2}\epsilon^{\mu\nu\rho\sigma}\left(A^a_\nu F^a_{\rho\sigma} - \frac{g}{3} f_{abc} A^a_\nu A^b_\rho A^c_\sigma\right) \,, \tag{2.5}$$

which satisfies the relation

$$\partial_\mu K^\mu = \frac{g^2}{32\pi^2} F^a_{\mu\nu} \tilde{F}^{\mu\nu}_a \,, \tag{2.6}$$

such that the overall difference of net axial charge is given by

$$J^0_5(t_2) - J^0_5(t_1) = -2N_f \int_{t_1}^{t_2} dt \int d^3x \; \partial_\mu K^\mu \,. \tag{2.7}$$

Since the spatial integral over the (four) divergence of the Chern-Simons current ($\int d^3x \, \partial_\mu K^\mu$) defines a total time derivative, the right hand side of Eq. (2.7) can be expressed in terms of the difference of two boundary terms

$$\int_{t_1}^{t_2} dt \int d^3x \; \partial_\mu K^\mu = N_{CS}(t_2) - N_{CS}(t_1) \,, \tag{2.8}$$

where N_{CS} denotes the Chern-Simons number

$$N_{CS}(t) = \int d^3x \; K^0(t,x) \,, \tag{2.9}$$

[b]We note that in general there is a nontrivial interplay between the dynamics of the gauge sector and previously existing imbalances of axial charges [164, 165, 166]. However, since we are mostly interested in the generation of such axial charge imbalances we will not consider these effects within this study.

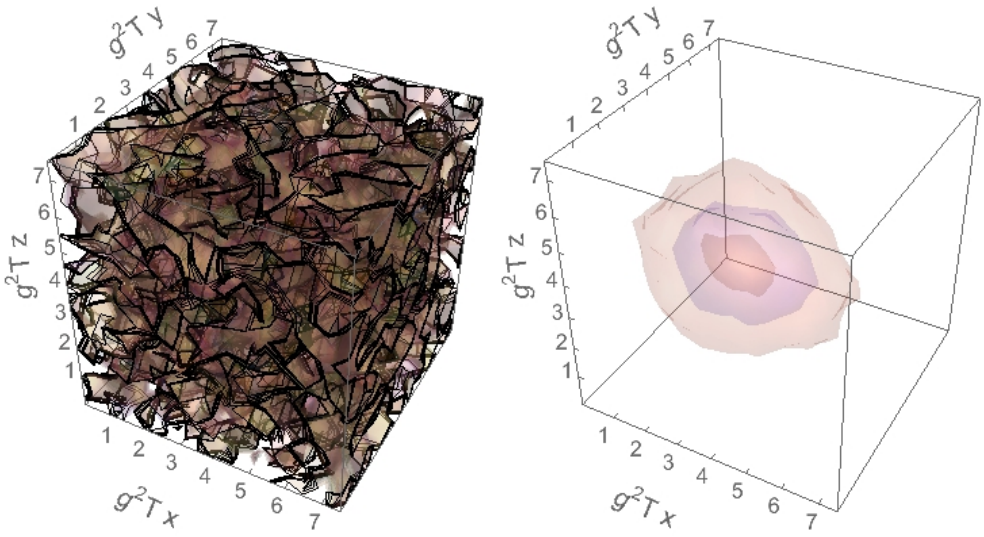

Figure 2.1: Spatial profile of $\frac{g^2}{8\pi^2}\ E_i^a(\mathbf{x})B_i^a(\mathbf{x})$ for a 3D Yang-Mills configuration in thermal equilibrium ($N = 16$, $\beta = 2$). Left: thermal field strength fluctuations contributing to $\vec{E}\cdot\vec{B}$ on all length scales. Right: spatial profile of $\vec{E}\cdot\vec{B}$ during a sphaleron transition after cooling to remove short distance fluctuations.

which is a unique property of the gauge field configuration at the boundary. When considering a vacuum state for instance, the Chern-Simons number N_{CS} can be associated with the homotopy class $Hom(G) \in \pi_3(SU(N_c)) \simeq \mathbb{Z}$ of the gauge transformation $G : \mathbb{R}^3 \cup \{\infty\} \to SU(N_c)$ that transforms the configuration to the topologically trivial vacuum state[c]. (See for example [167] for a comprehensive review.) Consequently, the Chern-Simons number of a vacuum state is an integer which distinguishes between energy degenerate but topologically inequivalent configurations.

When considering states of finite energy density, either in or out of thermal equilibrium – dynamical transitions between different topological sectors can occur [120] mediated by the sphaleron [115]. While sphaleron transitions manifest themselves in a change of the gauge field topology, the Chern-Simons number of an excited state configuration is – in contrast to vacuum states – no longer necessarily an integer. Instead, $N_{CS}(t)$ behaves as a continuous function of time whose derivative, according to Eqs. (2.8) and (2.6), satisfies the relation

$$\frac{dN_{CS}}{dt} = \frac{g^2}{8\pi^2}\int d^3x\ E_i^a(\mathbf{x})B_i^a(\mathbf{x})\ , \tag{2.10}$$

where we will express $\frac{1}{4}F^a_{\mu\nu}\tilde{F}^{\mu\nu a} = E_i^a B_i^a$ with $E_a^i = F_a^{0i}$ and $B^i = \frac{1}{2}\epsilon^{ijk}F_{jk}$ from now on. Clearly, the integrand in Eq. (2.10) receives contributions not only from topological transitions but also from ordinary fluctuations of the field strength that are unrelated to topology. This is illustrated in Fig. 2.1 where we show a snapshot of the integrand $\frac{g^2}{8\pi^2}E_i^a(\mathbf{x})B_i^a(\mathbf{x})$ for a thermal 3D Yang-Mills configuration. Thus from Eq. (2.3), both ordinary fluctuations and topological transitions contribute to the generation of an axial charge imbalance.

[c]While for gauge fields with periodic boundary conditions the gauge transformations map from the 3-torus $\mathbb{T}_3$ to the gauge group $SU(N_c)$, the set of homotopy classes of the map is still isomorphic to integers.

For Yang-Mills theories in thermal equilibrium, sphaleron transitions dominate the late time behavior of the Chern-Simons number [120, 121, 168] that is related to the generation of a net axial charge. Since individual sphaleron transitions are uncorrelated with each other, the long time behavior of the Chern-Simons number in thermal equilibrium can be characterized by an integer random walk between different topological sectors. Accordingly, the sphaleron transition rate can be defined from the N_{CS} auto-correlation function [169, 170]

$$\Gamma_{sph}^{eq} \equiv \lim_{\delta t \to \infty} \frac{\langle (N_{CS}(t+\delta t) - N_{CS}(t))^2 \rangle_{eq}}{V \delta t}, \tag{2.11}$$

in the spirit of a transport coefficient. Since the definition of Γ_{sph}^{eq} involves a real time correlation function, even in thermal equilibrium, this quantity is not accessible using first principles calculations in Euclidean lattice gauge theory. (See for instance [130] for a discussion.) Instead, calculations of the equilibrium sphaleron transition rate have been performed using either weak coupling numerical lattice techniques [126, 171] or by investigating theories with a holographic dual [172].

Parametric estimates of the sphaleron transition rate in weakly coupled plasmas in thermal equilibrium give

$$\Gamma_{sph}^{eq} = \kappa \, \alpha_S^5 T^4 \, , \tag{2.12}$$

where $\alpha_S = g^2/4\pi$ here denotes the coupling constant [127, 173, 174] and κ is a non-perturbative constant. This parametric estimate is based on the argument [120, 121, 168] that the typical spatial length scale corresponding to a sphaleron transitions is determined by modes with wavelengths on the order of the inverse magnetic screening scale $1/g^2T$. The time scale necessary to achieve a sphaleron transition turns out not to be $1/g^2T$ as previously argued [168], but a longer time scale $1/g^4T$, which accounts for the "Landau damping" of the transition time due to the interaction of the soft magnetic modes with hard modes on the scale of the temperature. This parametric scaling has also been confirmed independently by numerical simulations [175, 176, 177, 130] which extract [130] $\kappa = 0.21 \, N_c^3(N_c^2-1)(N_c g^2 T^2/m_D^2)$ within logarithmic accuracy in the coupling g; plugging in the value of the Debye mass m_D for very weak couplings, $N_f = 0$ and $N_c = 3$, one obtains $\kappa \sim 132 \pm 4$.

Our work here extends these studies to the case of an overoccupied non-Abelian plasma that is far off-equilibrium. Since such a system is dominated by classical dynamics, the sophisticated real time lattice techniques [149, 150, 3, 151] previously used to study sphaleron transitions in equilibrium can be straightforwardly adapted to the problem of interest here. However the problem in our case is simpler because, unlike the thermal case, hard quantum modes do not influence the sphaleron transition rate in the Glasma. The dynamics of non-equilibrium sphaleron transitions is entirely determined by the classical-statistical simulations; indeed, for the time scales studied, the sphaleron rate in the Glasma is governed by soft modes on the order of the magnetic screening scale determined from the spatial Wilson loop. Before we present these results, we will first review the real time numerical techniques that are essential to compute sphaleron transitions.

2.2 Topology measurement on the real time lattice

In this section, we will outline the numerical classical-statistical methods that have been developed for the real time simulations of topological transitions at high temperatures and adapt these for our non-equilibrium context. One first solves the classical Yang-Mills equations on the lattice; in this first study, for simplicity, we will consider only the case of an SU(2) gauge theory. While a lattice formulation of the problem is essential to describe non-perturbative real-time phenomena, the lattice discretization, as we shall discuss, poses problems for the extraction of topological information in the plasma. We will outline the sophisticated methods that have been devised to reliably extract Chern-Simons number on the lattice for non-Abelian plasmas in equilibrium. In particular, we will discuss the independent calibrated cooling and slave field methods and adapt these to the non-equilibrium Glasma case. As a benchmark for our computations, we will reproduce and discuss key features of the well known equilibrium results.

2.2.1 Classical-statistical lattice setup

We discretize the theory on a 3D spatial lattice with N sites and spacing a in each direction following the Hamiltonian formulation of lattice gauge theory in temporal axial gauge. We define the lattice gauge link variables $U_\mu(x)$ and electric field variables $E^\mu(x)$ such that they transform according to

$$\begin{aligned} E^\mu_{(G)}(x) &= G(x)E^\mu(x)G^\dagger(x)\,, \\ U^{(G)}_\mu(x) &= G(x)U_\mu(x)G^\dagger(x+\hat{\mu})\,, \end{aligned} \tag{2.13}$$

under time independent gauge transformations. Defining the variation of the lattice gauge links with respect to the gauge fields as

$$\frac{\delta U_\mu(x)}{\delta A^a_\nu(y)} = -iga\ \tau^a\ U_\mu(x)\ \delta_\mu{}^\nu \frac{\delta_{x,y}}{a^3}\,, \tag{2.14}$$

where τ^a denotes the fundamental generator of $SU(N_c)$, we solve the classical Hamilton equations of motion

$$\begin{aligned} \partial_t E^\mu_a(x) &= -\frac{\delta H}{\delta A^a_\mu(x)}\,, \\ \partial_t U_\mu(x) &= -iga\ \tau^a\ \frac{\delta H}{\delta E^\mu_a(x)} U_\mu(x)\,, \end{aligned} \tag{2.15}$$

derived from the lattice Hamiltonian

$$H = \frac{a^3}{2}\sum_{j,x} E^a_j(x)E^a_j(x) + \frac{2}{g^2 a}\sum_\Box \mathrm{ReTr}\Big[\mathbb{1} - U_\Box\Big]\,, \tag{2.16}$$

using a leap-frog updating scheme. Here $U_\Box$ is the plaquette variable, defined in Eq. (1.15). With the classical solutions in hand, we can subsequently extract the observables of interest from the lattice field configurations and perform an average over an ensemble of all field configurations.

2.2.2 Chern-Simons number measurement

While we are interested in the dynamics of topological transitions and the behavior of the Chern-Simons number over the course of the non-equilibrium evolution, there are several problems associated with the lattice definition of the corresponding observables–a clear discussion of these can be found in [151]. First of all, since the lattice is a discrete set of points, meaningful topological concepts can only be defined for i) sufficiently smooth configurations, for which gauge links are close to the identity and ii) slowly varying configurations, for which neighboring plaquettes are nearly identical. These are the gauge field configurations which effectively admit an interpolation between lattice sites. Further, there exists no local operator definition of the Chern-Simons current $K^0(t,x)$ such that the spatial integral $\int d^3x\ K^0(t,x)$ is a total time derivative for generic field configurations. Instead, local operator definitions of the Chern-Simons current can only be made approximately equal to a total derivative for sufficiently smooth and slowly varying field configurations.

Since these problems are particularly severe for classical-statistical simulations in thermal equilibrium, different techniques known as the "calibrated cooling" [149, 151] and the "slave field" [178, 3] method have been developed in this context to overcome this challenge on real time lattices. We will briefly summarize below the basic ideas behind both methods. More details on the technical implementation of both methods are given in the Appendices A and B.

Calibrated cooling

Problems with the lattice definition of the Chern-Simons current arise primarily due to ultraviolet fluctuations on the scale of the lattice spacing. However, fortuitously, the contribution of these ultraviolet modes to the sphaleron transition rate is suppressed because the sphaleron rate is dominated by the dynamics of modes on the order of the magnetic screening length [120, 121, 168]. Hence an efficient way to deal with the aforementioned problems is to suppress the effect of ultraviolet fluctuations on the topology measurement by use of a "calibrated cooling" technique [149, 151].

The most efficient way to remove ultraviolet fluctuations in a gauge invariant fashion is to follow the trajectory of the configuration along an additional "cooling time" direction τ along which the gauge links evolve according to the energy gradient flow[d]

$$\begin{aligned} \partial_\tau U_\mu(t,x;\tau) &= -iga\ \tau^a E^{\mu,a}_{cool}(t,x;\tau)\ U_\mu(t,x;\tau)\ , \\ E^{cool}_{\mu,a}(t,x;\tau) &= -\frac{\delta H}{\delta A^\mu_a(x)}\ . \end{aligned} \tag{2.17}$$

By this procedure, ultraviolet fluctuations are efficiently removed and one can then define

[d]While gradient flow techniques are also frequently used in Euclidean lattice gauge theory [179, 180, 181, 182, 183], we note that the calibrated cooling technique employed here differs in the following aspects. While in 4D Euclidean lattice gauge theory, the gradient flow follows the steepest descent of the 4D gauge action, the cooling trajectory of our gauge field configuration follows the steepest descent of the 3D lattice Hamiltonian, such that three dimensional gauge field configurations at different times are cooled independently of each other.

the Chern-Simons number by following the gradient flow (gf) all the way to the vacuum[e]

$$N_{CS}^{gf}(t) - N_{CS}^{vac}(t) = -\frac{g^2 a^3}{8\pi^2} \int_0^\infty d\tau \sum_x E_{i,a}^{\rm cool}(t,x;\tau)\ B_{i,a}^{\rm cool}(t,x;\tau)\ .$$

While the Chern-Simons number of the associated vacuum configuration $N_{CS}^{vac}(t)$ is an integer characterizing the topological properties of the gauge field configuration, the integral on the right hand side contains the fluctuations above the vacuum and can be evaluated using an $\mathcal{O}(a^2)$ improved operator definition of the chromo-electric and chromo-magnetic fields inside the integral as described in Appendix A. Typically the field configurations become smooth already after cooling to $\tau a^2 \sim 1$. Thus ultraviolet lattice effects on the Chern-Simons number expression from integrating Eq. (2.10) are small and the method is topological [151]. However the numerical cost of cooling all the way to the vacuum is too large for this definition to be practical and it is therefore useful to consider the following modifications instead.

Instead of cooling all the way to the vacuum ($\tau \to \infty$) it is sufficient to cool for a shorter depth τ_c to efficiently remove ultraviolet fluctuations on the scale of a single lattice spacing. For such cooled configurations, a local operator definition of the Chern-Simons current behaves approximately as a total derivative; one can therefore define the change in Chern-Simons number between two different times t_1 and t_2 by comparing the cooled images of the configurations,

$$N_{CS}(t_2) - N_{CS}(t_1) = \frac{g^2 a^3}{8\pi^2} \int_{t_1}^{t_2} dt' \sum_x E_{i,a}(t',x;\tau_c)\ B_{i,a}(t',x;\tau_c)\ ,$$

as described in detail in App. A. By varying the amount of cooling τ_c applied to the configuration, one in addition controls both the magnitude and typical wavelength of ordinary field strength fluctuations that contribute to the Chern-Simons number measurement. We shall investigate the dependence on the cooling depth τ_c in more detail below. We note that one can check whether the definition of the Chern-Simons current indeed behaves as a total derivative by adding occasional coolings all the way to the vacuum to compute N_{CS} (according to the previous definition in Eq. (2.18)). This measurement is re-calibrated to ensure that any residual lattice errors do not accumulate over time. An illustration of this calibrated cooling method is shown in Fig. 2.2.

In practice, we evolve the field configurations along the real-time axis t and perform cooling up to a variable length τ_c for every 0.5 lattice units in time. Based on the cooled images of the configurations, we then compute the change in Chern-Simons number according to Eq. (2.18), as described in detail in Appendix A. We re-calibrate this measurement by performing a cooling to the vacuum[f] for every 5 lattice units in time. When comparing the computations using respectively the definitions in Eqns. (2.18) and (2.18), we observed that the largest discrepancy was of the order of 0.1 (and typically much smaller than that). The close agreement indicates that the method employed is indeed topological.

[e]Cooling to the classical vacuum amounts to following the energy gradient flow in Eq. (2.17) up to the point where the magnetic energy density vanishes identically to machine precision.

[f]Since in practice the cooling to the vacuum is extremely costly, we use up to two steps of blocking [151] for our largest field configurations during this process. For more information, see Appendix A.

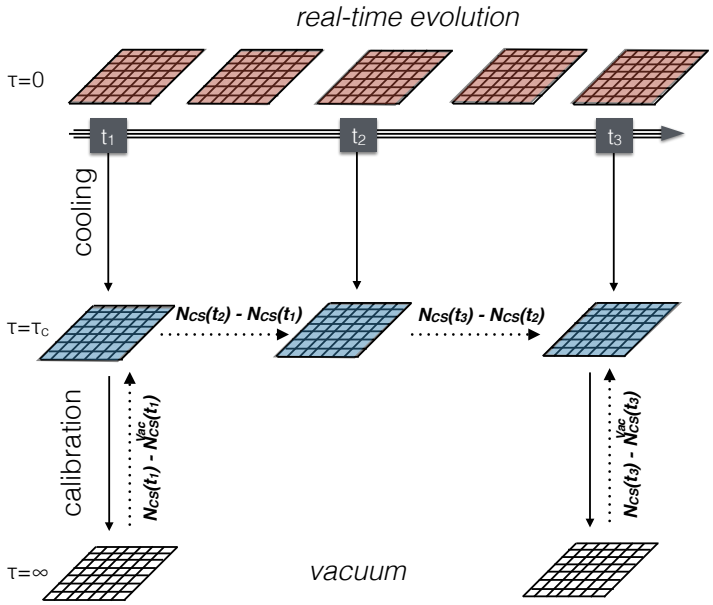

Figure 2.2: Illustration of the calibrated cooling method.

Slave Field Method

In the calibrated cooling method, ultraviolet fluctuations are removed explicitly to arrive at a topological definition of the Chern-Simons number. An alternative method referred to as the "slave field" method was proposed by Woit [178] and developed further by Moore and Turok [3]. The basic idea underlying this method is to extract the integer part of the Chern-Simons number (which, loosely speaking, corresponds to the integer part $N_{CS}^{vac}(t)$ in Eq. (2.18)) by measuring the winding number N_W of the gauge transformation $S(x)$ which transforms the configuration to the topologically trivial sector, setting

$$N_{CS}^{SF} = N_W \ , \tag{2.18}$$

where the acronym SF stands for Slave Field. Since the topological trivial sector of 3D Yang-Mills theory satisfies the (minimal) Coulomb gauge condition that

$$Q = \frac{1}{3N^3N_c} \sum_{j,x} \mathrm{ReTr}\Big[\mathbb{1} - U_j^{(S)}(x)\Big] \tag{2.19}$$

is minimal, finding the gauge transformation $S(x)$ is then equivalent to the problem of fixing Coulomb gauge on the real time lattice. As pointed out in [3], keeping track of this gauge transformation over the course of the Hamiltonian time evolution can be efficiently achieved using a sequence of small gauge transformations determined by an extended variant of the Los Alamos gauge fixing algorithm described in more detail in Appendix B.

At first sight, it may appear as if this procedure were completely free of the aforementioned ultraviolet problems. However these problems return in determining the winding

number of the gauge transformation. Indeed, a topologically meaningful definition of the winding number is only possible when $S(x)$ is sufficiently slowly varying[g]; when this is the case, the winding number can be extracted using the methodology of Woit [178]. Specifically, for the $SU(2)$ gauge group, the winding number is characterized by the degree of the map

$$N_W = deg\,(S) \tag{2.20}$$

and can be extracted in a straightforward way following [3]–the procedure is described in further detail in Appendix B. Similarly, in the case of $SU(N_c)$ with $N_c > 2$, one can extract the winding number by decomposition into $SU(2)$ sub-groups [184].

By fixing the Coulomb gauge condition at the initial time, the slave field $S(x)$ can initially be set to the identity such that it is slowly varying at that time. However, ensuring that the slave field $S(x)$ remains slowly varying over the course of the Hamiltonian evolution is a non-trivial task and generally requires a more careful tuning of the algorithm. The strategy devised in [3] is to monitor the roughness of the gauge transformation. This quality is quantified in terms of the peak stress defined as

$$PS = \sup_x \sum_j \mathrm{ReTr}\Big[\mathbb{1} - \frac{1}{2}\Big(U_j^{(S)}(x) + U_j^{\dagger,(S)}(x-\hat{j})\Big)\Big]\,, \tag{2.21}$$

and to apply the transformation to Coulomb gauge of the dynamical fields U, E and S

$$U_i(x) \to U_i^{(S)}(x)\,, \quad E_i(x) \to E_i^{(S)}(x)\,, \quad S(x) \to \mathbb{1}\,, \tag{2.22}$$

whenever the peak stress falls below a certain threshold [3]. Consequently, by restoring the Coulomb gauge condition dynamically, one ensures that the slave field remains slowly varying on large time scales and the extraction of the winding number is topological.

Despite the elegance of the slave field method, in practice, the underlying local gauge fixing algorithm is very inefficient on large lattices and performing the frequent gauge fixing required for the topology measurement becomes prohibitively expensive. We will therefore use this method primarily as a benchmark and cross-check of the calibrated cooling technique discussed previously.

2.2.3 Chern-Simons measurements & sphaleron transitions in thermal equilibrium

Before we apply the above methods to study sphaleron transitions in the Glasma, we will briefly discuss the application of these methods to $SU(2)$ Yang-Mills theory in thermal equilibrium. While the correct determination of the sphaleron rate at weak coupling requires a simultaneous description of the hard ($\sim T$) and soft ($\sim g^2 T$) excitations of the systems – as discussed earlier in Sec. 2.1 – our primary goal is to illustrate basic features of the evolution of the Chern-Simons number in thermal equilibrium. We will therefore neglect the effects

[g]The slave field $S(x)$ does not necessarily have to be close to the identity for this condition to be satisfied.

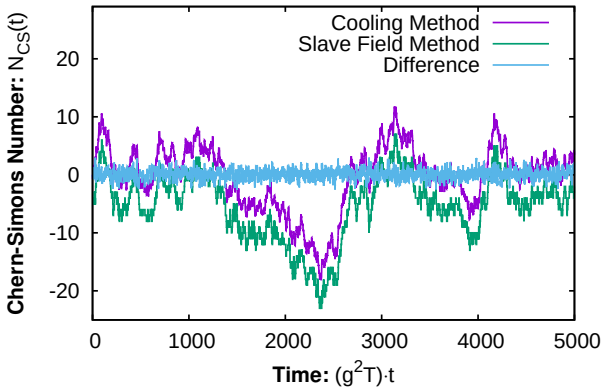

Figure 2.3: Comparison of Chern-Simons number measurements using the calibrated cooling ($\tau_c = 0.75\ (g^2T)^{-2}$) and slave field techniques for a single configuration in thermal equilibrium ($N = 24$, $\beta = 2$). Slave field results are shifted by 5 units for comparison purposes. The difference between the two methods is small over the course of the entire simulation.

of hard excitations in the thermal case and instead follow previous work that explored the behavior of soft ($\sim g^2T$) modes in 3D classical Yang-Mills theory.

We generate thermal configurations using the highly efficient thermalization algorithm developed by Moore [185]. Beginning with a cold start ($U_\mu = \mathbb{1}\ , E^\mu = 0$), we perform a series of iterations of the following steps:

1) Generate color electric fields according to a Gaussian distribution with

$$\langle E_a^i(x) E_b^j(y) \rangle = \beta_{lat}^{-1} \delta^{ij} \delta_{ab} \delta_{x,y}$$

where $\beta_{lat} = 1/(g^2Ta)$ is the lattice coupling in 3D Yang-Mills theory[h].

2) Project the color electric fields on the constraint surface where Gauss's law condition $D_\mu E^\mu = 0$ is satisfied using the algorithm described in [150].

3) Evolve the gauge links and electric fields according to Hamilton's equations of motion for some time t_{th} to allow energy to be exchanged between the electric and magnetic fields.

until the energy density settles to its equilibrium value[i]. We subsequently perform the real time evolution by solving Hamilton's equations of motion as described in Sec. 2.2.1 and measure the Chern-Simons number using the methods described in Sec. 2.2.2. Since our primary aim was to illustrate the time evolution of the Chern-Simons number in the equilibrium setup, we performed our thermal simulations on rather small $N = 24$ lattices with $\beta_{lat} = 2$ where comparisons to published results are available [3].

[h] Our normalization of the lattice coupling differs by a factor of 4 from the one used in earlier works [3].

[i] For a choice of $t_{th}a = 50$ we find that for a $N = 24$ lattice and β_{lat} values as discussed below, convergence is typically achieved in less than 20 iterations.

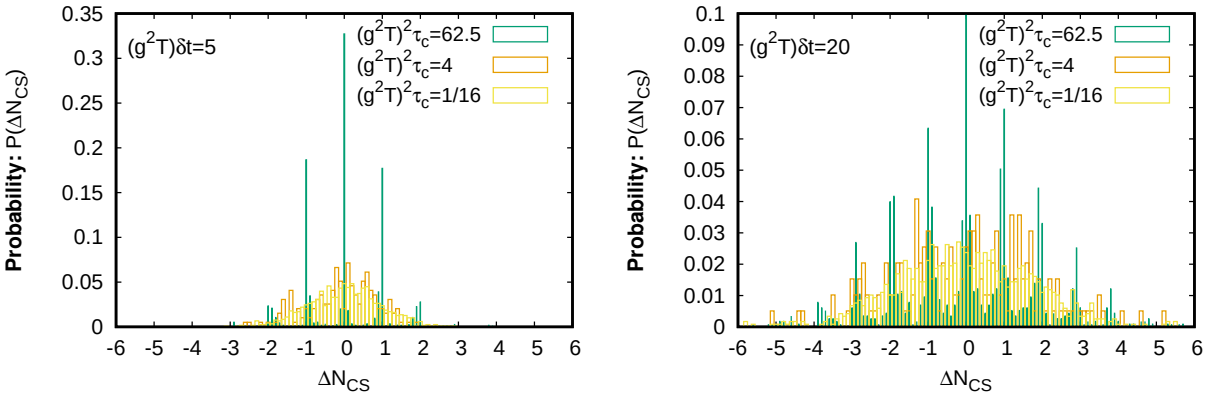

Figure 2.4: Histogram of the Chern-Simons number difference ΔN_{CS} for equilibrium configurations ($N = 24$, $\beta = 2$) separated by $\delta t = 5\ (g^2T)^{-1}$ (left panel) and respectively $\delta t = 20\ (g^2T)^{-1}$ (right panel) during the real time evolution. The different curves in each panel correspond to the results for different levels of cooling.

We first investigate the behavior of the Chern-Simons number over the course of the real time evolution for a single field configuration. Our results are shown in Fig. 2.3. The different curves correspond to the extraction of the Chern-Simons number using the calibrated cooling (purple) and slave field (green) techniques. Since the difference between the two measurements – also shown in Fig. 2.3 – is small, we have shifted the slave field measurement by 5 units for better comparison of the results.

The long time behavior of the correlation function in Fig. 2.3 is dominated by transitions between different topological sectors that are characterized in terms of approximately integer changes of the Chern-Simons number over a short amount of time. While thermal field strength fluctuations also contribute to the calibrated cooling measurement, the comparison with the slave field measurement – designed to measure the topological contribution only – shows that the effect of ordinary field strength fluctuations is small and does not significantly affect the long time behavior of the Chern-Simons number. We find, consistent with the results of [3, 151], that both methods agree within statistical white noise over the course of the entire simulation.

We can further quantify the time evolution of the Chern-Simons number by investigating the statistical properties of the Chern-Simons number difference

$$\Delta N_{CS}(t, \delta t) = N_{CS}(t + \delta t) - N_{CS}(t)\ , \tag{2.23}$$

during the real time evolution. In equilibrium, time translation invariance guarantees the result to be independent of t and we have verified this explicitly. Our results for the probability distribution $P(\Delta N_{CS})$ are shown in Fig. 2.4 based on the data sets in Tab. 2.1. Different panels in Fig. 2.4 show our results for two different separations in time $\delta t = 5\ (g^2T)^{-1}$ (left panel) and $\delta t = 20\ (g^2T)^{-1}$ (right panel), whereas different curves in each panel correspond to different choices of the cooling depth $\tau_c = 0.0625 - 62.5\ (g^2T)^{-2}$ employed in the measurement of the Chern-Simons number.

While a minimal amount of cooling is necessary to ensure that the Chern-Simons current

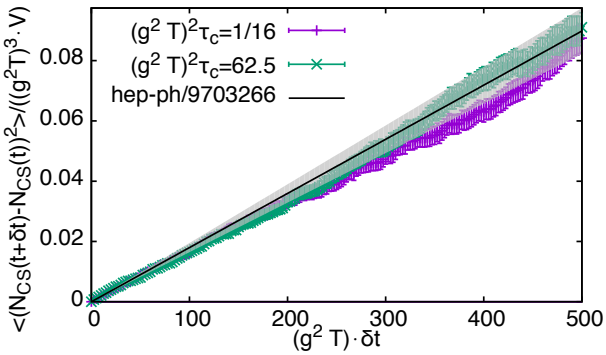

Figure 2.5: Auto-correlation function of the Chern-Simons number for equilibrium configurations ($N = 24$, $\beta = 2$) with two different cooling depths $(g^2T)^2\tau_c = 0.0625$ and 62.5. Our results are compared to the sphaleron rate from [3].

behaves at least approximately as a total time derivative[j], by cooling further one successively removes residual field strength fluctuations from the configurations and thereby reduces their contribution to the Chern-Simons number. After cooling down to $\tau_c = 62.5\ (g^2T)^{-2}$, the difference in Chern-Simons number is strongly peaked around integers as the measurement is completely dominated by transitions between different topological sectors[k]. Since more transitions occur over a larger time scale δt, the width of the distribution increases significantly, as is clear from the results shown in the upper and lower panels of Fig. 2.4. Even though this behavior is most prominent for the coolest configurations, it can also be clearly seen for modest cooling times relative to the behavior of the original field configurations.

We now compute the auto-correlation function of the Chern-Simons number,

$$C(t,\delta t) = \frac{1}{V}\Big\langle \big(N_{CS}(t+\delta t) - N_{CS}(t)\big)^2 \Big\rangle , \tag{2.24}$$

which, according to Eq. (2.11), can be used to define the sphaleron transition rate in the late time limit of the correlation function. Our results are shown in Fig. 2.5, where we present the auto-correlation function in Eq. (2.24) as a function of the temporal separation δt. We find that the auto-correlation function is approximately independent of the cooling depth τ_c indicating once again the dominance of topological transitions for the long-time behavior of the Chern-Simons number. One also observes from Fig. 2.5 that the N_{CS} auto-correlation function shows an approximately linear rise as a function of δt. This result is consistent with the expectation that consecutive sphaleron transitions have the Markovian property of being uncorrelated with each other on sufficiently long time scales. The long time behavior of the Chern-Simons number can therefore be approximated by an integer random walk with the diffusion constant given by the sphaleron transition rate,

$$\frac{1}{V}\Big\langle \Delta N_{CS}^2(\delta t)\Big\rangle_{eq} = \Gamma_{sph}^{eq}\,\delta t\ . \tag{2.25}$$

[j]The quality of this approximation can be checked explicitly during the calibration step [3]. We refer to Appendix A for a more detailed discussion.

[k]Small differences from integer values arise not only due to residual field strength fluctuations, but also due to (small) lattice discretization errors in the determination of the space-time integral of the Chern-Simons current in Eq. (2.18).

N	β_{lat}	g^2Ta	$(g^2T)^2$	$\tau_c N_{confs}$
24	2	1/2	0.0625	1152
24	2	1/2	4.0	196
24	2	1/2	62.5	1180

Table 2.1: Data sets for studying sphaleron transitions in 3D $SU(2)$ Yang-Mills theory in thermal equilibrium.

We compared our results for the sphaleron transition rate to the previous extraction by Moore [3]. The latter is represented by the black line with grey error bands in Fig. 2.5. Excellent agreement is obtained between the two calculations.

2.3 Sphaleron transitions in the Glasma

Now that we have demonstrated that we can reproduce established results in the literature for computing the sphaleron transition rate in non-Abelian plasmas in thermal equilibrium, we can apply these techniques to explore topological transitions in the Glasma. We will begin with discussing the initial conditions for the Glasma in weak coupling. We will for simplicity not consider the realistic case of a Glasma undergoing rapid longitudinal expansion but will restrict ourselves to an isotropic system in a static box. In agreement with previous studies, we will show that even if one starts with a one scale problem given by the initial hard scale, the saturation scale Q_s, a scale separation develops with time between the hard scale and the softer electric and magnetic screening scales. Of particular interest is the temporal evolution of the spatial string tension, which we will compute for the first time. We will then compute the Chern-Simons number in the Glasma and study its auto-correlation behavior. Finally, we will demonstrate that one can express the extracted sphaleron transition rate in terms of the magnetic screening scale in the system.

2.3.1 Initial conditions & Single particle spectra

We choose our initial conditions to mimic the physical situation in a weak coupling scenario of an ultra-relativistic heavy ion collision at very high energies [186, 70]. The defining feature of the non-equilibrium plasma, often called the Glasma, is an initial non-perturbatively large phase space occupancy $f(t_0, p) \sim 1/\alpha_S$ of gluon modes up to a saturation scale Q_s. As discussed previously, these initial conditions can be implemented in a simple quasi-particle picture where the initial gauge fields, and their momentum conjugate electric fields, are expressed as a superposition of transversely polarized gluons,

$$\begin{aligned} A^a_\mu(t_0, x) &= \not\int \frac{d^3k}{(2\pi)^2}\frac{1}{2k}\sqrt{f(t_0,k)}\left[c^a_k \xi^\lambda_\mu(k) e^{ikx} + c.c.\right] , \\ E^a_\mu(t_0, x) &= \not\int \frac{d^3k}{(2\pi)^2}\frac{1}{2k}\sqrt{f(t_0,k)}\left[c^a_k \dot{\xi}^\lambda_\mu(k) e^{ikx} + c.c.\right] , \end{aligned} \tag{2.26}$$

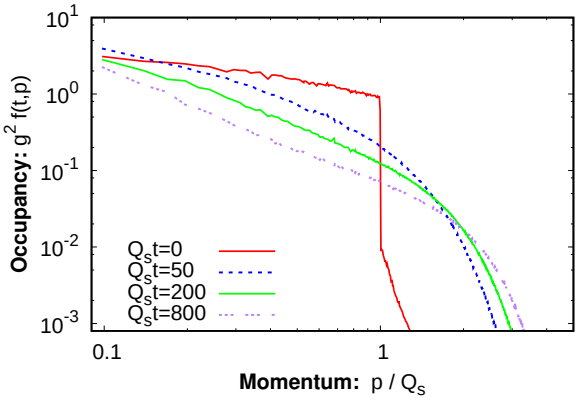

Figure 2.6: Single particle spectra extracted at different times $Q_s t = 0, 50, 200, 800$ of the non-equilibrium evolution on a $N = 128$ lattice with spacing $Q_s a = 0.5$.

where $\xi_\mu^\lambda(k)$ labels the transverse polarization vectors, the c's are complex Gaussian random numbers with zero mean and unit variance and $\not\int$ indicates a sum over polarizations and an integral over wavenumbers. The above initial conditions do not automatically satisfy the non-Abelian Gauss law $D_\mu E^\mu = 0$; we must therefore enforce this constraint using the methods described in [150]. Our initial gluon distribution $f(t_0, k)$ is chosen to be

$$f(t_0, k) = \frac{n_0}{2\pi N_c \alpha_S} \frac{Q_s}{\sqrt{k^2 + Q_s^2/10}} \theta(Q_s - k) \,, \tag{2.27}$$

where n_0 is a free parameter of order unity that can be used to vary the initial overoccupancy– if not stated otherwise, we choose $n_0 = 1$ as the default value.

While our choice of initial conditions may appear peculiar at first sight, previous studies [186, 161, 162] have demonstrated that the details of the initial conditions become irrelevant on a time scale $Q_s t \sim n_0^{-2}$, which corresponds parametrically to the inverse of the large angle scattering rate. Indeed, following the time evolution of the gluon spectrum[1] shown in Fig. 2.6, one observes a rapid change of the gluon distribution at early times $Q_s t \lesssim 50$. As first reported in [161, 162], the Glasma subsequently approaches a universal attractor solution characterized by an infrared power law with a rapid fall–off at high momenta. This evolution is shown for $Q_s t \leq 800$ in Fig. 2.6. In this regime, the dynamics is entirely characterized in terms of a self-similar scaling of the gluon distribution [186, 161, 162]

$$f(t, p) = (Q_s t)^\alpha f_S((Q_s t)^\beta p) \,. \tag{2.28}$$

The scaling exponents $\alpha = -4/7$ and $\beta = -1/7$ in this regime have been extracted to high accuracy from classical-statistical simulations [186, 161, 162] and can be understood from simple considerations in kinetic theory [160, 159]. As discussed in [187, 186] the self-similar scaling in Eq. (2.28) persists up to a timescale $Q_s t_{\rm Quantum} = \alpha_s^{-7/4}$, when the typical occupancy of hard modes becomes of order unity. Beyond $t_{\rm Quantum}$ a classical-statistical description is no longer accurate, as instead quantum effects become important and drive the system to thermal equilibrium [75].

[1]We extract the single particle spectrum from equal time correlation functions in Coulomb gauge as discussed in detail in [186].

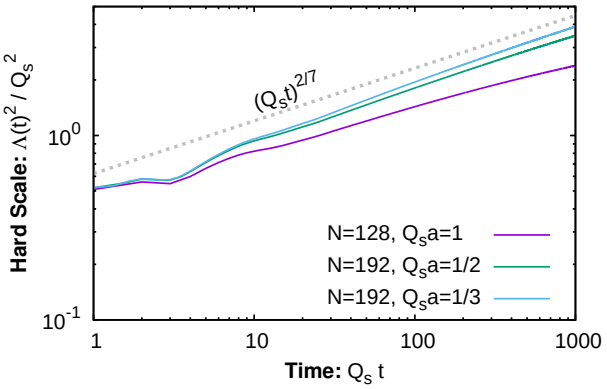

Figure 2.7: Evolution of the hard scale $\Lambda^2(t)$ for three different lattice spacings $Q_s a = 1, 1/2, 1/3$. The grey dashed line indicates a $(Q_s t)^{2/7}$ scaling behavior.

2.3.2 Evolution of characteristic scales

In a weakly coupled plasma in thermal equilibrium, the three scales are parametrically separated by powers of the coupling constant, with the hard scale $\sim T$ much larger than the electric screening scale $\sim gT$, much larger than the magnetic screening scale $\sim g^2T$. However in the Glasma, initially all scales are on the order of the saturation scale Q_s because of the non-perturbatively large occupancies $f \sim 1/\alpha_S$. Hence the hierarchy of scales characteristic of a weakly coupled plasma in equilibrium has to be developed dynamically during the thermalization process.

Even though the existence of a scale hierarchy is essential for the applicability of most weak coupling methods, and plays a crucial role for the theoretical understanding of the sphaleron transition rate in thermal equilibrium, we emphasize that the classical-statistical lattice approach does not explicitly rely on a separation of scales. We will therefore use this approach in the following to study the time evolution of the characteristic scales starting from the non-perturbative high occupancy regime.

Hard scale Λ

We first consider the time evolution of hard scale $\Lambda(t)$, describing the characteristic momentum scale of hard excitations in the plasma. Following the methodology of previous Yang-Mills studies [162, 186, 70], we determine this scale using the gauge invariant local operator definition

$$\Lambda^2(t) = \frac{\langle H(t)\rangle}{\langle \epsilon_B(t)\rangle}\,, \tag{2.29}$$

where the dimension six operator $H(t)$ corresponds to the trace of the squared covariant derivative of the field strength tensor

$$H(t) = \frac{1}{3V}\int d^3x\; D^{ab}_j(x)F^{ji}_b(x)\; D^{ac}_k(x)F^{ki}_c(x)\,. \tag{2.30}$$

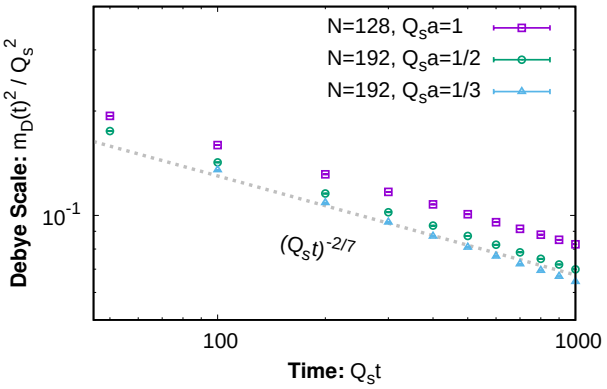

Figure 2.8: Evolution of the Debye scale $m_D^2(t)$ for three different lattice spacings $Q_s a = 1, 1/2, 1/3$. The grey dashed line indicates a $(Q_s t)^{-2/7}$ scaling behavior.

Here $\epsilon_B(t)$ denotes the magnetic energy density

$$\epsilon_B(t) = \frac{1}{4V} \int d^3x \; F_{ij}^a(x) F_{ij}^a(x) \,. \tag{2.31}$$

Summation over the color $a, b, c = 1, \cdots, N_c^2 - 1$ and spatial Lorentz indices $i, j, k = x, y, z$ is implied. This hard scale can be expressed in perturbation theory as the ratio of moments of the single particle distribution as (see for example [186])

$$\Lambda^2(t) = \frac{2}{3} \frac{\int d^3p \; p^3 \; f(t,p)}{\int d^3p \; p \; f(t,p)} \tag{2.32}$$

such that for a weakly coupled plasma in thermal equilibrium one has

$$\Lambda_{eq}^2 = \frac{80}{63} \pi^2 T^2 \,. \tag{2.33}$$

whereas initially

$$\Lambda_{init}^2 = c_\Lambda \; Q_s^2 \tag{2.34}$$

where $c_\Lambda = \frac{236 - 6\sqrt{11}}{525}$ up to higher order corrections for our choice of initial condition. Our results for the non-equilibrium evolution of the hard scale are shown in Fig. 2.7 for three different lattice spacing $Q_s a = 1, 1/2, 1/3$. Since the operator definition in Eq. (2.29) involves an ultraviolet sensitive dimension six operator, the result is only slowly convergent as a function of the lattice spacing. Moreover, since the physical hard scale Λ increase as a function of time, clear deviations from the continuum limit can be observed for coarser lattices at late times. However, for the finer lattices we find that the time evolution of of the hard scale converges towards a $\Lambda^2 \sim (Q_s t)^{2/7}$ scaling behavior as reported previously in [160, 186]. Indeed, this scaling is expected from the self-similar evolution of the single particle distribution in Eq. (2.28).

Debye scale m_D

We will now discuss the extraction of the Debye mass, which corresponds to the (static) electric screening scale in the plasma. Since we are unaware of a non-perturbative definition of the Debye mass in the context of classical-statistical real-time lattice simulations[m] we follow previous works [160, 186] and instead use the leading order perturbative definition of the Debye screening mass

$$m_D^2(t) = 4\, g^2 N_c \int \frac{d^3p}{(2\pi)^3} \frac{f(t,p)}{p} \,. \tag{2.35}$$

The corresponding lattice expression is obtained by replacing the momentum integral $\int \frac{d^3p}{(2\pi)^3}$ in this expression by the lattice sum over discrete momentum modes $\frac{1}{(Na)^3}\sum_p$. In a weakly coupled plasma in thermal equilibrium,

$$m_{D,eq}^2 = \frac{g^2 N_c T^2}{3} \,, \tag{2.36}$$

with the Debye scale is parametrically smaller than the typical hard momentum scale. In contrast, one finds initially in our non-equilibrium simulation that

$$m_{D,init}^2 = c_{m_D^2}\, n_0 Q_s^2 \,. \tag{2.37}$$

where $c_{m_D^2} = \sqrt{\frac{2}{5}}\frac{\sqrt{11}-1}{\pi^2}$ for our choice of initial condition. Comparing this expression to Eq. (2.34). we observe that there is no parametric separation of scales at the initial time even at arbitrarily weak coupling. Our results for the non-equilibrium temporal evolution of the Debye scale $m_D^2(t)$ are depicted in Fig. 2.8 for different lattice discretizations. We find that m_D^2 approaches an approximate $(Q_s t)^{-2/7}$ scaling behavior in the continuum limit, consistent with the expectation suggested by the scaling of the single particle distribution.

Spatial string tension σ

In thermal equilibrium, the sphaleron transition rate is controlled by the dynamics of modes with momenta on the order of the inverse magnetic screening length. It is therefore desirable to extract an equivalent quantity in our non-equilibrium setup and study its evolution in time. As in thermal equilibrium, one can investigate the behavior of spatial Wilson loop

$$\mathrm{W}(t,A) = \mathcal{P}\exp\Big(ig \oint dx^i A_i(x,t)\Big), \tag{2.38}$$

as a function of the area A enclosed by the loop. Since the large distance behavior of the Wilson loop in thermal equilibrium is characterized by an area law,

$$\Big\langle \mathrm{Tr}\ \mathrm{W}(A)\Big\rangle_{eq} \propto e^{-\sigma A}, \tag{2.39}$$

[m]For a discussion of the non-perturbative definition of the Debye mass in Euclidean lattice gauge theories, see for instance [188]. However it is not obvious how to adapt these concepts to our real time lattice simulations.

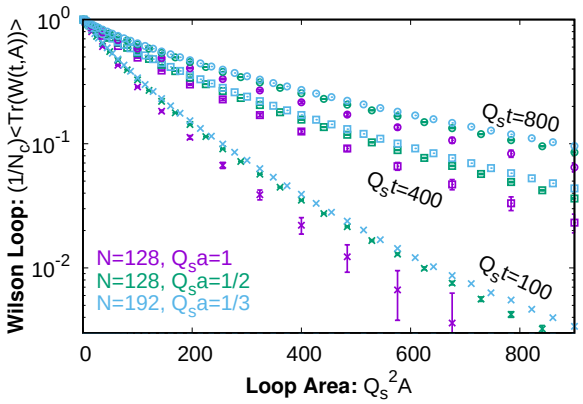

Figure 2.9: Expectation value of the trace of the spatial Wilson loop versus the area of the loop at times $Q_s t$ = 100, 400, 800 (bottom to top). The different colored curves for each time correspond to different lattice discretizations.

with the spatial string tension σ related to the magnetic screening scale parametrically as

$$\sigma \sim g^4 T^2 \,, \tag{2.40}$$

at weak coupling, we can similarly extract the spatial string tension σ in our non-equilibrium simulations and use $\sqrt{\sigma}$ as a proxy for the inverse magnetic screening length.

We first analyze the behavior of the spatial Wilson loop itself to establish the area law scaling in Eq. (2.39) for our non-equilibrium setup.[n] Our results for the (real-part of the) trace as a function of the area of the Wilson loop at three different times $Q_s t$ = 100, 400, 800 of the evolution are presented in Fig. 2.9. While for small areas the Wilson loops are close to the identity and do not exhibit scaling, convergence towards an area law scaling as in Eq. (2.39) can be observed for sufficiently large areas. Since the observation of such area law scaling in an out-of-equilibrium plasma is quite non-trivial, we briefly note that our results are in line with the findings reported in [39, 189]. Although area law scaling emerges clearly for all times shown in Fig. 2.9, extending our analysis to much earlier times is extremely challenging. This is because the values of the Wilson loop decrease rapidly as a function of area at very early times; accurately resolving values $\lesssim 10^{-3}$ requires enormous statistics, far exceeding the number of configurations N_{confs} = 4000 used in Fig. 2.9.

We can further quantify the long distance behavior of the Wilson loop in terms of the spatial string tension $\sigma(t)$, which can be extracted from the logarithmic derivative of the Wilson loop with respect to the area

$$\sigma(t) = -\left.\frac{\partial \ln \left\langle \mathrm{Tr}\ \mathrm{W}(t,A)\right\rangle}{\partial A}\right|_{Q_s^2 A \gg 1} . \tag{2.41}$$

[n] Our results presented in this section are obtained for so called on-axis Wilson loops, i.e. square loops with sides oriented along the lattice coordinate directions $(1,0,0),(0,1,0),(0,0,1)$. We have also investigated the behavior of so called off-axis Wilson loops where, instead of orienting the sides along the $(1,0,0),(0,1,0),(0,0,1)$ directions, the sides of the rectangle are oriented along any mutually orthogonal directions of lattice vectors (pointing for example in the $(2,1,0)$ and $(-1,2,0)$ directions). Within statistical errors the off-axis results agree with the on-axis measurements when expressed as a function of the area of the loop.

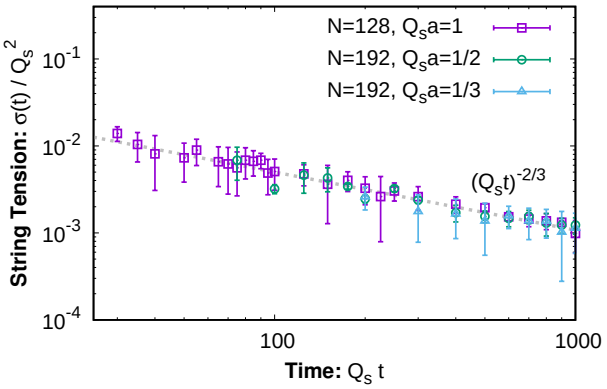

Figure 2.10: Time evolution of the spatial string tension $\sigma(t)$ extracted from the logarithmic area derivative of the Wilson loop.

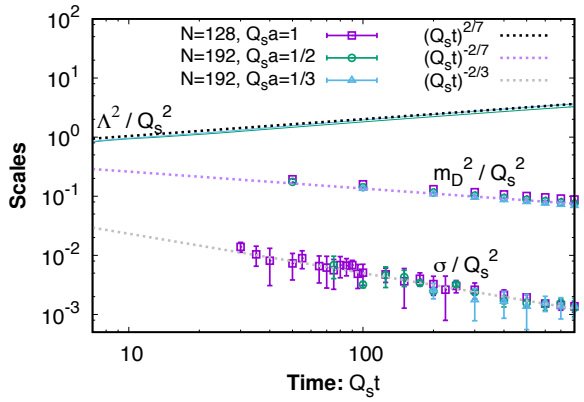

Figure 2.11: Time evolution of the hard scale (Λ^2), the electric screening scale (m_D^2), and the spatial string tension (σ). A clear separation of scales is established dynamically.

In practice, we compute the logarithmic derivative at different values of $Q_s^2 A$ by performing a fit involving three adjacent data points. Subsequently, we search for an area independent value at $Q_s^2 A \gg 1$ to extract the spatial string tension and include residual variations into our error estimate.

Our results for the string tension $\sigma(t)$ as a function of time are shown in Fig. 2.10. Here we combined data for different lattice discretizations. While the error bars for the string tension are significantly larger relative to the previous measurements, one clearly observes a rapid decrease of the string tension as a function of time. We find that the time dependence can be approximately described by a $(Q_s t)^{-2/3}$ scaling behavior. We caution however that the precision with which we extract the exponent is limited to the 10 % level – primarily by the large statistical uncertainties in the measurement of the Wilson loop. We also note that in contrast to the time evolution of the hard and electric screening scales which can be estimated from kinetic theory [159, 160], we are not aware of an analytic prediction of the time evolution of the non-perturbative magnetic screening scale.

N	n_0	$Q_s a$	$Q_s^2\ \tau_c$	N_{confs}	N	n_0	$Q_s a$	$Q_s^2\ \tau_c$	N_{confs}
64	0.5	1.0	12	256	96	1.0	1.0	250	2048
64	1.0	1.0	12	256	96	1.0	1.0	324	2048
64	1.0	1.0	324	1024	128	1.0	0.5	1	128
64	1.5	1.0	12	256	128	1.0	0.5	12	512
96	1.0	1.0	1	128	128	1.0	1.0	1	128
96	1.0	1.0	12	4096	128	1.0	1.0	12	2432
96	1.0	1.0	36	1024	192	1.0	0.5	12	512
96	1.0	1.0	108	1024	192	1.0	1.0	1	128
96	1.0	1.0	216	1024	192	1.0	1.0	12	512

Table 2.2: Data sets employed in the study of sphaleron transitions out-of-equilibrium.

Dynamical separation of scales

Our results for the time evolution of the different characteristic scales of the Glasma are compactly summarized in Fig. 2.11, where we plot the hard scale $\Lambda^2(t)$, the electric screening scale $m_D^2(t)$ and the spatial string tension $\sigma(t)$ (as a proxy for the magnetic screening scale) as a function of time. Initially all scales are of similar magnitude up to order one factors depending the details of the initial conditions. Subsequently a clear separation of scales emerges dynamically as a function of time. While the hard scale increases according to a power law in time, the electric and magnetic screening scales decrease and separate from each other as well due to the faster decrease of the string tension relative to the Debye mass. Since such a separation of scales is essential to the applicability of standard (perturbative) weak coupling methods (such as effective kinetic descriptions or hard-loop effective field theories), our non-perturbative lattice results provide clear evidence that these methods become applicable at sufficiently late times.

2.3.3 Sphaleron transitions & evolution of Chern-Simons number

With the estimates obtained of the time evolution of the characteristic hard and soft scales in the Glasma, we will now proceed to study sphaleron transitions and the evolution of Chern-Simons number. We first note that a crucial difference from the thermal case is that we can simultaneously resolve the dynamics of hard as well as soft excitations using a classical-statistical lattice description. In the thermal case, the typical occupancies of hard modes ($p \sim T$) are of order unity $f(p \sim T) \sim 1$ and a classical description does not apply to the hard modes. In contrast, in the Glasma, the hard modes ($p \sim \Lambda(t)$) are high occupied, $f(p \sim \Lambda(t)) \gg 1$, and therefore admit a classical description. Due to the noted complication, the study of sphaleron transitions in a weakly coupled plasma in thermal equilibrium proceeds via an effective field theory for soft ($p \sim g^2 T$) modes as discussed in Sec. 2.1. Since there is no such complication in the non-equilibrium case, we can directly study sphaleron dynamics in the Glasma using first principles lattice techniques.

This benefit is not without cost because for the Glasma all relevant scales have to be resolved simultaneously on the lattice. In addition, since the relevant scales are separating rapidly from each other with time, one typically requires very large lattices and the char-

acteristic scales are accessible only for a limited amount of time. A summary of the lattice parameters and data sets used in our study is provided in Tab. 2.2. If not stated otherwise, all results shown were obtained for $N = 96$ lattices with spacing $Q_s a = 1$.

Sphaleron transitions & Chern-Simons number

Since there are important conceptual differences of sphaleron dynamics in the Glasma relative to the thermal equilibrium case, we will begin by illustrating the time evolution of the Chern-Simons number and demonstrate our ability to successfully identify topological transitions. In Fig. 2.12, we show the time evolution of the Chern-Simons number for a short period of time during the non-equilibrium evolution of a single gauge field configuration. Different curves in Fig. 2.12 correspond to different extraction methods and can be characterized as follows.

In the first case we perform gradient flow cooling of the non-equilibrium field configuration all the way to the vacuum and measure the integral of the Chern-Simons current along the cooling trajectory, as in Eq. (2.18). In this way we obtain the green curve in Fig. 2.12, which exhibits clear discontinuities. The positions of these discontinuities are indicated by the vertical gray lines. Each discontinuity corresponds to a transitions between different topological sectors defined by the so-called "gradient flow separatrix" [151], which occurs when the gauge field configuration evolves from the basin of attraction of one vacuum state to the basin of attraction of another topologically inequivalent vacuum state.

By adding the Chern-Simons number $N_{CS}^{vac}(t)$ of the corresponding vacuum state, as in Eq. (2.18), we obtain the blue curve in Fig. 2.12 corresponding to the gradient flow definition N_{CS}^{gf} of the Chern-Simons number. One observes that N_{CS}^{gf} is a continuous function of time. In addition to the topological information, it also contains contributions from finite energy fluctuations of the chromo-electric and chromo-magnetic fields.

We have also compared our results from the gradient flow definition of the Chern-Simons number with the ones obtained from the calibrated cooling technique. When choosing a small cooling depth $Q_s^2\tau_c = 0.25$, we obtain the orange curve in Fig. 2.12, which closely follows the gradient flow definition. By choosing a larger value of $Q_s^2\tau_c = 250$ for the cooling depth, we can practically remove all field strength fluctuations above the vacuum and restrict the measurement of the Chern-Simons number to its topological content. Indeed one observes from the purple curve in Fig. 2.12, that for $Q_s^2\tau_c = 250$ the evolution is characterized by discontinuous transitions between different topological sectors, which nicely coincide with the crossings of the gradient flow separatrix.

Even though we can separate the topological content of the Chern-Simons number from the contribution of field-strength fluctuations at different length scales by varying the cooling depth, it is not a priori obvious which contributions to the Chern-Simons number are most relevant to the physics of the chiral magnetic effect. We will therefore vary the amount of cooling in the following and present results for different values of the cooling depth.

Statistical analysis of Chern-Simons number

Now that we have established that we are able to identify topological transitions out-of-equilibrium, we will proceed with a more detailed statistical analysis. In order to obtain a

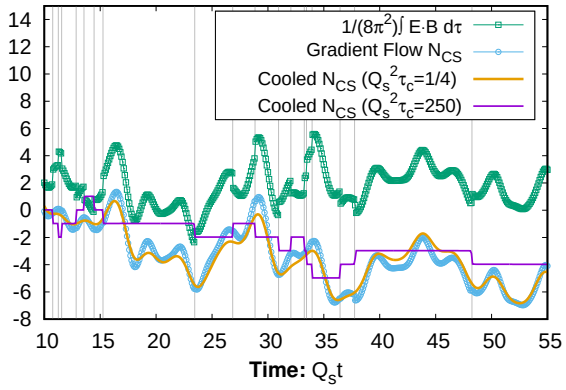

Figure 2.12: Evolution of the Chern-Simons number for a single non-equilibrium configuration on a $N = 96$ lattice with spacing $Q_s a = 1$. Different curves correspond to different extraction procedures and contain variable amounts of field strength fluctuations in addition to the topological contributions.

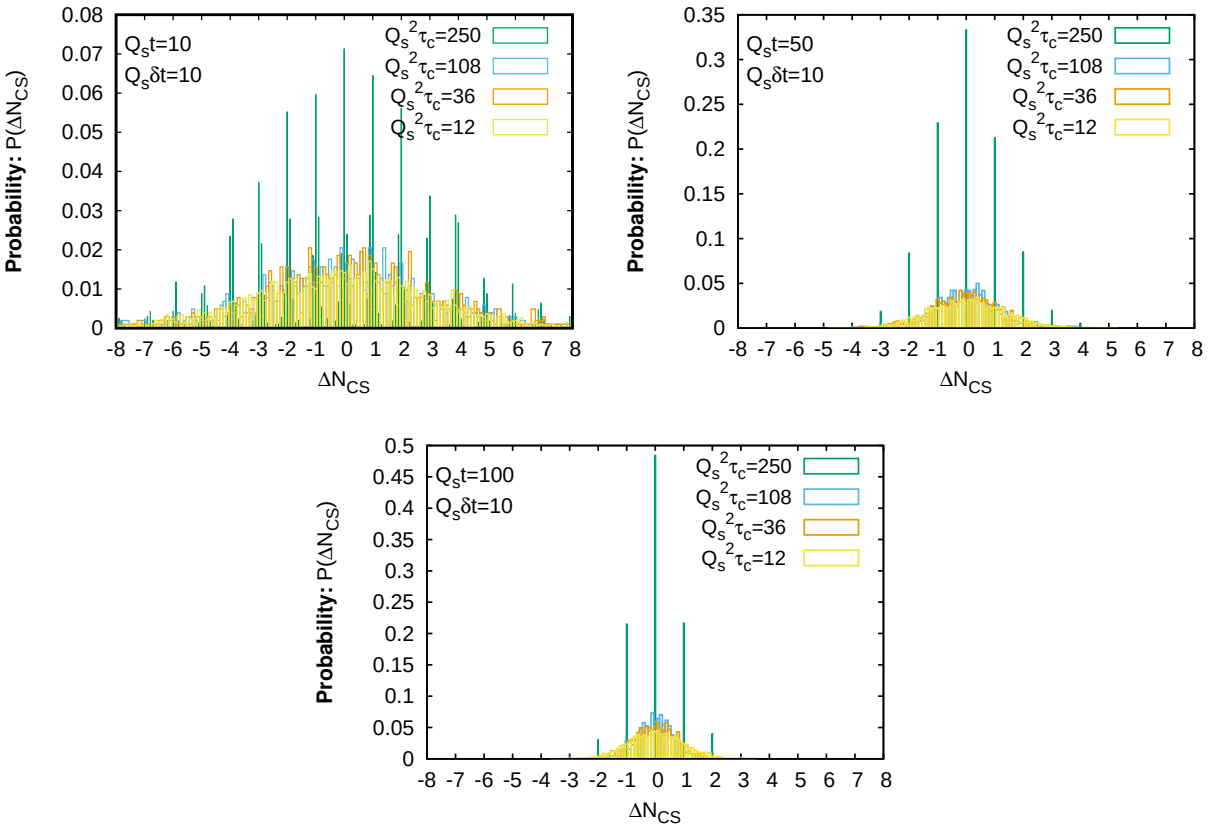

Figure 2.13: Histograms of the distribution of the Chern-Simons number difference ΔN_{CS} within $Q_s \delta t = 10$ units of time difference on a $N = 96$, $Q_s a = 1.0$ lattice. The different panels correspond to different reference times $Q_s t = 10,\ 50,\ 100$ (top left, top right, bottom) of the non-equilibrium evolution.

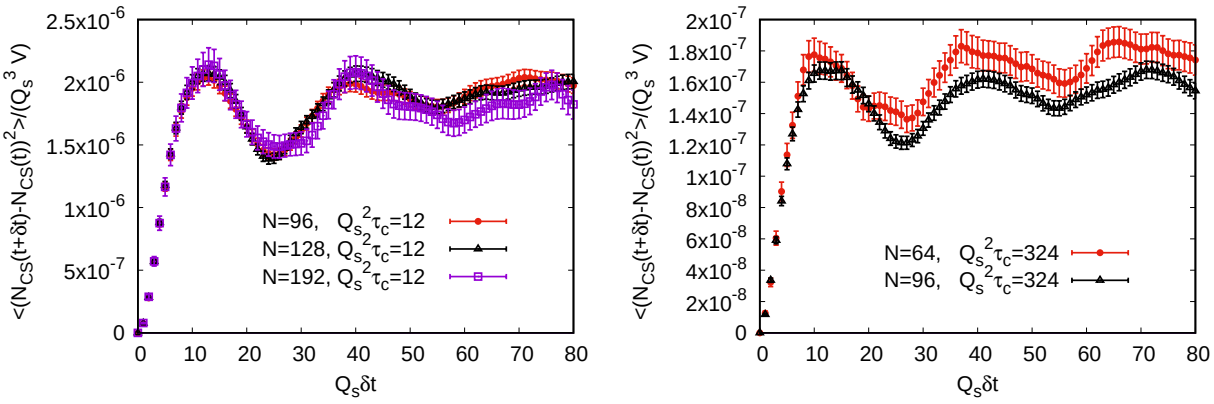

Figure 2.14: Chern-Simons number auto-correlation function $\frac{1}{Q_s^3 V}\langle (N_{CS}(t+\delta t)-N_{CS}(t))^2\rangle$ as a function of the temporal separation δt starting from $Q_s t = 50$ during the non-equilibrium evolution. Different curves in each panel correspond to different lattice volumes $Q_s^3 V = 96^3, 128^3, 196^3$ for cooling depth $Q_s^2\tau_c = 12$ (left) and $Q_s^3 V = 64^3, 96^3$ for $Q_s^2\tau_c = 324$ (right).

first estimate of the time dependence of the transition rate, we follow the methodology in Sec. 2.2.3 and first investigate the probability distribution of the difference ΔN_{CS} between the measurements of the Chern-Simons number at reference time t and subsequent time $t + \delta t$. (See the definition in Eq. (2.23).) Our results for three different reference times $Q_s t = 10,\ 50,\ 100$ during the non-equilibrium evolution and a common separation of $Q_s \delta t = 10$ are shown in Fig. 2.13. Irrespective of the amount of cooling, which primarily affects how narrowly the distributions are peaked around integer values, a clear difference between the different panels emerges. At early times of the non-equilibrium evolution, transitions between different topological sectors occur frequently resulting in a broad probability distribution for $Q_s t = 10$. At the later times $Q_s t = 50,\ 100$, the rate of transitions decreases rapidly as a function of time leading to much narrower distributions. Most prominently, starting at $Q_s t = 100$ one finds that after a time $Q_s \delta t = 10$ approximately half of the field configurations can still be found in the same topological sector. Most of the other half has merely transitioned to the neighboring topological sector. Very few configurations have $|\Delta N_{CS}| > 1$ when sufficient cooling ($Q_s^2\tau_c = 250$) is applied to isolate the topology at these late times.[o]

While a rapid decrease of the sphaleron transition rate may be expected based on our previous observation that the magnetic screening scale decreases significantly as a function of time during the non-equilibrium evolution, we would like to further quantify this effect and determine the physical scales associated with the rate. We follow the same methodology devised in the equilibrium case and study the auto-correlation functions of the Chern-Simons number. Our results for the auto-correlation function of the Chern-Simons number $C(t, \delta t)$ are summarized in Figs. 2.14 and 2.15.

Fig. 2.14 shows results for the auto-correlation function for a fixed reference time $Q_s t = 50$ during the non-equilibrium evolution. Starting with a rapid rise for small separations

[o]We emphasize that the detailed fractions depend on the physical volume determined by the lattice size $V = (Na)^3$. Most importantly, we will demonstrate shortly that the variance $\langle \Delta N_{CS}^2 \rangle$ of the distributions exhibits the expected volume scaling.

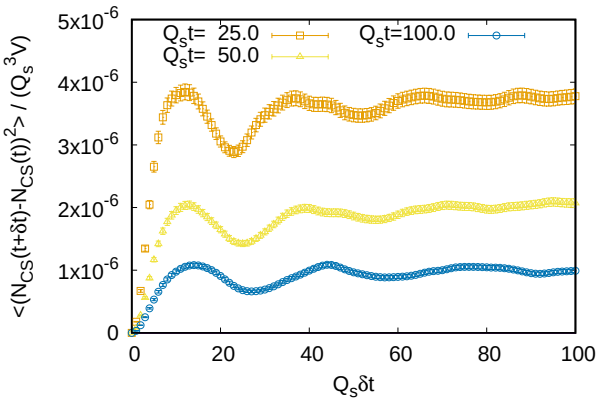

Figure 2.15: Chern-Simons number auto-correlation function $\frac{1}{Q_s^3 V}\langle (N_{CS}(t+\delta t) - N_{CS}(t))^2 \rangle$ as a function of the temporal separation δt, at three different times $Q_s t = 25,\ 50, 100$. Cooling depth is $Q_s^2 \tau_c = 12$ in all cases.

$Q_s \delta t \lesssim 10$, the growth of $\langle \Delta N_{CS}^2 \rangle$ slows down dramatically at larger δt and is superseded by pronounced oscillations. In fact the oscillations are so significant that for certain periods such as e.g. $Q_s \delta t \simeq 10 - 20$ the variance $\langle \Delta N_{CS}^2 \rangle$ decreases with increasing separation δt. We have verified that this oscillatory behavior persists even for deeper cooling, as can be observed from the lower panel of Fig. 2.14 where we show results for $Q_s^2 \tau_c = 324$. Most importantly, this behavior is robust under variations of the lattice volume as can be observed from the different curves in Fig. 2.14 which agree with each other within errors – indicating that our results are not significantly affected by finite volume effects.

We emphasize that the non-monotonic behavior observed in our non-equilibrium simulations is clearly different from the thermal case, shown in Fig. 2.5, where in contrast $\langle \Delta N_{CS}^2 \rangle$ increases monotonously as a function of the separation time. Moreover the non-monotonic behavior observed in Fig. 2.14 is inconsistent with the usual interpretation of the Chern-Simons number evolution as a Markovian process. This is the case even when a time-dependent transition rate is assumed. It instead points to the fact that essential features of the dynamics on these time scales are non-Markovian as the evolution of the Chern-Simons number exhibits pronounced memory effects.

While the non-monotonic behavior of the Chern-Simons number auto-correlation may come as a surprise, we find that it is a robust feature of the non-equilibrium evolution also at later times. This is seen in Fig. 2.15, where we plot the Chern-Simons auto-correlation function starting from three different reference times $Q_s t = 25, 50, 100$ during the non-equilibrium evolution. Even though a clear time dependence is seen in Fig. 2.15, the general oscillation pattern remains intact albeit a slight change in the oscillation frequency can be observed.

The most prominent feature of Fig. 2.15 though is the change in magnitude between different times $Q_s t = 25,\ 50,\ 100$. Clearly, the overall magnitude of $\langle \Delta N_{CS}^2 \rangle$ is significantly larger at earlier times and confirms our previous observation of a larger rate of topological transitions early on in the evolution of the Glasma. We will further quantify this statement below by extracting the rate of topological transitions associated with the initial rise of the auto-correlation function.

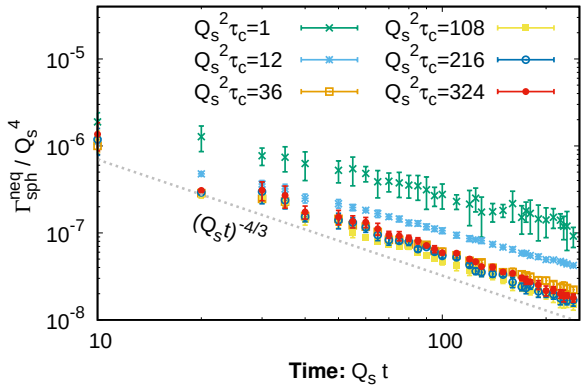

Figure 2.16: Non-equilibrium sphaleron transition rate $\Gamma^{neq}_{sph}(t)$ as a function of time $Q_s t$ for various different values of the cooling depth $Q_s^2\tau_c$.

2.3.4 Quantifying the rate of topological transitions

We established clearly that Chern-Simons number evolution in the Glasma is non-Markovian. The equilibrium definition of the sphaleron transition rate in Eq. (2.11) as the slope of the N_{CS} auto-correlation function in the late time limit is therefore not sufficient to quantify topological transitions in the Glasma. However, for short enough separations in time $Q_s\delta t \lesssim 10$, the auto-correlation function does exhibit a rapid and approximately linear rise. We will exploit this behavior to quantify the time dependence of the transition rate as

$$\Gamma^{neq}_{sph}(t) = \left\langle \frac{(N_{CS}(t+\delta t) - N_{CS}(t))^2}{V\ \delta t} \right\rangle_{Q_s\delta t<10} . \tag{2.42}$$

This definition of the rate does not by any means single out topological contributions; it potentially receives large contributions from fluctuations of the color-electric and color-magnetic strength on all scales. We will therefore further apply different levels of cooling τ_c to efficiently suppress field-strength fluctuations on short distance scales. In particular, by choosing $Q_s^2\tau_c \gg 1$ to cool almost all the way to the vacuum we can effectively suppress non-topological fluctuations and obtain a rate more closely related to the extraction of the sphaleron transition rate in thermal equilibrium[p].

Our results for the non-equilibrium sphaleron transition rate $\Gamma^{neq}_{sph}(t)$ as a function of time are presented in Fig. 2.16 for various levels of cooling. For small values of $Q_s^2\tau_c \sim \mathcal{O}(1)$, a significant dependence on the cooling depth is observed. This indicates large contributions to the rate from fluctuations of the color-electric and color-magnetic strength at short distance scales. In contrast, the results for large values of $Q_s^2\tau_c \gg 1$ appear to converge towards a single curve isolating the genuine contributions due to topological transitions.

Irrespective of the cooling depth, a clear time dependence of the rate can be observed. Starting from the largest values at early times, the rate rapidly decreases as a function of

[p]Similarly, we could also apply cooling to the vacuum and simply count the number of transitions defined by crossings of the gradient flow separatrix per unit time. However as some of the separatrix crossings do not affect the evolution on longer time scales, this measurement would differ by a "dynamical prefactor" [151] which potentially also depends on time.

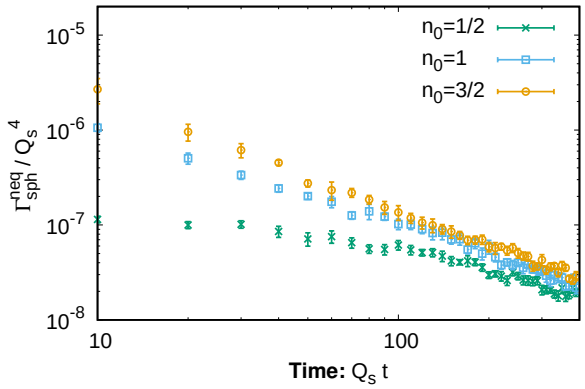

Figure 2.17: Non-equilibrium sphaleron transition rate $\Gamma^{neq}_{sph}(t)$ as a function of time $Q_s t$ for different initial over-occupancies n_0 = 3/2, 1, 1/2. All curves have a cooling depth of $Q_s^2 \tau_c$ = 12.

time and eventually approaches a power law behavior $(Q_s t)^{-\zeta}$ with an approximate scaling exponent $\zeta \simeq 4/3$. Albeit the early time behavior depends on the details of the initial conditions, we find that variations of the initial conditions do not affect the scaling behavior at later times. This is shown in Fig. 2.17 where the non-equilibrium sphaleron transition rate is plotted for different initial over-occupancies n_0; all the curves approach a common scaling behavior around $Q_s t \sim 100$. On the other hand, it is also clear that the sphaleron transition rate is by far the largest at early times and one should therefore expect a significant sensitivity to early time dynamics in time integrated quantities such as the axial charge density.

The time dependence of the sphaleron transition rate in the scaling regime can be compared to those of the characteristic scales of the Glasma. As we noted previously, the sphaleron transition rate in equilibrium is most sensitive to modes on the order of the magnetic screening scale. One can analogously express the corresponding rate in the Glasma in units of the spatial string tension previously extracted in Sec. 2.3.2. Our results for the dimensionless ratio $\Gamma^{neq}_{sph}(t)/\sigma^2(t)$ are presented in Fig. 2.18 as a function of time. While both the square of the spatial string tension as well as the non-equilibrium sphaleron rate change by an order of magnitude over the time scale shown in Fig. 2.18, the ratio of the two quantities remains approximately constant with $\Gamma^{neq}_{sph}/\sigma^2 = (2.2 \pm 0.4) \cdot 10^{-3}$ extracted from the result shown in Fig. 2.18. We interpret this result as clear evidence that the dynamics of sphaleron transitions off-equilibrium is fully determined by modes on the order of the inverse magnetic screening length in the Glasma.

2.4 Dynamical scales redux

In this section, we briefly detail a follow-up study to the dynamical scales in Sec. 2.3.2.

Strongly interacting gauge field theories, such as quantum chromodynamics (QCD), have elementary non-perturbative excitations described by Wilson loops [190, 30]. Such extended objects play an important role also in string theories [191] or suitable generalizations in formulations of quantum gravity [192]. In thermal equilibrium the Wilson loop of QCD pro-

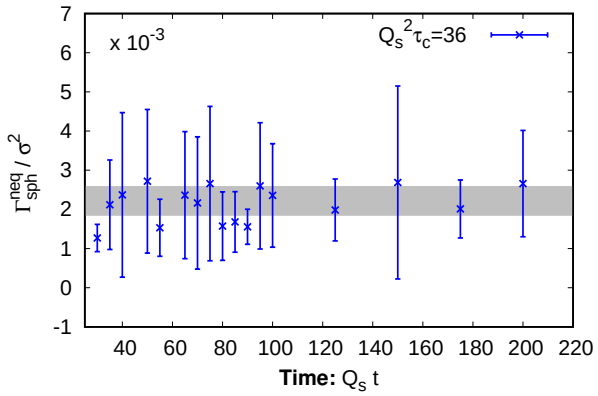

Figure 2.18: Non-equilibrium sphaleron transition rate normalized by square of the spatial string tension.

vides an important means to distinguish the confined "hadronic" phase from the deconfined "quark-gluon plasma" state [193]. Despite the well-established relevance of the Wilson loop for our understanding of fundamental problems in vacuum or thermal equilibrium, much less is known about its significance for dynamical situations out of equilibrium.

The main new result is the scaling property of the spatial Wilson loop that characterizes a universal state of QCD matter far from equilibrium. This state provides an important building block for our understanding of the early stages of ultra-relativistic heavy-ion collisions in the limit of sufficiently high energies. In such collisions a nonequilibrium plasma of highly occupied gluons is expected to form [66, 9], with transient scaling properties [70, 186, 76] characterizing the thermalization process of the non-Abelian plasma at weak gauge coupling. However, the notion of occupancies of individual gluons is not gauge invariant and becomes problematic beyond the perturbative high-momentum regime. Since the Wilson loop is gauge invariant, it allows the investigation of non-perturbative "infrared" properties of the strongly correlated nonequilibrium system in an unambiguous way [39, 189, 194].

Based on numerical simulations of the plasma's real-time dynamics in the highly excited regime, we establish a self-similar behavior for the time evolution of the spatial Wilson loop. The self-similarity can be fully characterized in terms of a universal scaling exponent and scaling function that are time independent. Such universality far from equilibrium is based on the existence of nonthermal fixed points [195], which represent nonequilibrium attractor solutions reached on a time scale much shorter than the asymptotic thermalization time. Since the scaling properties associated with the nonthermal fixed point are insensitive to details of the underlying model and initial conditions, our results provide an important missing piece for the determination of the nonthermal universality classes of non-Abelian gauge theories. We focus here on relativistic non-Abelian plasmas, however, there are important links to similar phenomena in a wide range of applications from cosmology to cold atoms [71].

While the relevant non-perturbative long-distance or infrared behavior of non-Abelian plasmas can be extracted from Wilson loops, the perturbative scaling properties at higher momenta are well described in terms of quasi-particle excitations and can be inferred from gauge-fixed correlations functions [39, 196, 161, 162, 194]. Combining both, we establish

the full nonthermal scaling properties of (statistically) homogenous and isotropic Yang-Mills plasmas from short to large distance scales. To this end, we also extend previous calculations for the $SU(2)$ gauge group to the case of an $SU(3)$ gauge symmetry underlying QCD. Our results reveal a rather large universality class that is even insensitive to the symmetry group of $SU(2)$ versus $SU(3)$.

2.4.1 Nonequilibrium Wilson loop

Wilson loop operators W transport a (color-) electrically charged particle all the way around a closed loop in space-time. Specifically, for a particle charge in the fundamental representation of the non-Abelian $SU(N_c)$ gauge group with N_c colors, the color-averaged transport along a closed line $\mathcal{C}$ is represented by the trace of a path-ordered ($\mathcal{P}$) exponential of the gauge field operator $\mathcal{A}_\mu(x)$ [30],

$$W = \frac{1}{N_c} \mathrm{Tr}\, \mathcal{P} e^{ig \oint_{\mathcal{C}} dx^\mu \mathcal{A}_\mu(x)} , \tag{2.43}$$

where g denotes the gauge coupling, and x^μ are the space-time coordinates with $\mu = 0$–4.

In vacuum or thermal equilibrium the closed curve C is either taken to include the time direction, in which case the time variable is analytically continued to imaginary values, or runs along spatial directions only. The latter is called a spatial Wilson loop. In general, out of equilibrium the time variable may not be continued to imaginary values and we will consider spatial Wilson loops only. The theory is then regularized on a lattice, where the Wilson loop involves products of lattice link variables describing the gauge degrees of freedom [30].

In equilibrium at zero temperature the expectation value of the Wilson loop $\langle W \rangle_{\mathrm{eq}}$ in the pure gauge theory (without dynamical quarks) decreases exponentially with the area A as

$$-\log \langle W \rangle_{\mathrm{eq}} = \sigma_{\mathrm{eq}} A \tag{2.44}$$

for sufficiently large A. Specifically, for the temporal-spatial Wilson loop with imaginary times such an *area-law* behavior characterizes confinement, and the associated equilibrium string tension σ_{eq} describes the linear rise of the static quark–anti-quark potential for large spatial separations. At zero temperature, spatial Wilson loops show the same area-law behavior as their temporal-spatial counterparts. However, for spatial Wilson loops this behavior persists even in the deconfined high-temperature phase, where it reflects non-perturbative gauge-field correlations [197].

Since thermal equilibrium is time-translation invariant, the expectation value $\langle W \rangle_{\mathrm{eq}}$ is a constant in time. In contrast, for the highly excited nonequilibrium plasma the expectation value $\langle W \rangle(t, A)$ explicitly depends on time $t \equiv x^0$ [39, 189, 194]. A self-similar behavior of the nonequilibrium spatial Wilson loop is described in terms of a universal scaling exponent ζ and scaling function w as

$$-\log \langle W \rangle(t, A) = w\left((t/t_0)^{-\zeta} A Q^2 \right) , \tag{2.45}$$

where t and A are measured in units of a suitable reference time scale t_0 and momentum scale Q, respectively. Instead of separately depending on time and spatial area of the loop,

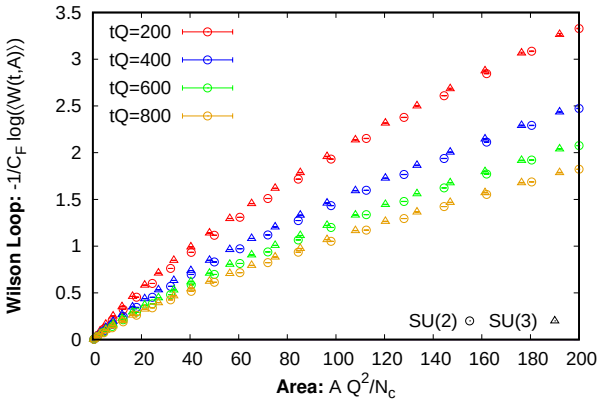

Figure 2.19: The logarithm of the spatial Wilson loop as a function of the area at different times for gauge groups $SU(N_c)$ with $N_c = 2$ (circles) and $N_c = 3$ (triangles). Rescaling with the Casimir color factor $-1/C_F(N_c)$ (see main text) leads to very similar results both for two and three colors.

in a self-similar regime the dynamics only depends on the product of the area and some (fractional) power of time. Such a non-trivial behavior requires a significant loss of information about the microscopic parameters of the underlying system, from which universality originates.

2.4.2 Self-similarity and area law scaling at large distances

Motivated by the Color Glass Condensate picture of nucleus-nucleus collisions, we consider as an initial condition a nonequilibrium state with energy density $\epsilon \sim Q^4/g^2$ describing an over-occupied gluonic state with characteristic momentum Q [66, 9][q]. Details of the initial conditions are found to become irrelevant on a short time scale $tQ \sim \mathcal{O}(1)$, as demonstrated previously in $SU(2)$ simulations of perturbative quantities in Refs. [161, 162, 194]. While Q is taken to be sufficiently large such that the "running" gauge coupling $g(Q)$ is weak due to the phenomenon of asymptotic freedom, the system is strongly correlated because of the non-perturbatively large energy density.

In this case the nonequilibrium quantum dynamics can be accurately mapped onto a classical-statistical problem, involving sampled solutions of classical Yang-Mills equations for inhomogeneous gauge fields. The latter can be rigorously solved using real-time lattice simulation techniques following Refs. [39, 196, 161, 162, 194] for the case of a non-expanding plasma [r]. The description reproduces the underlying quantum dynamics at sufficiently early times and breaks down at $tQ \sim g^{-7/2}$ [161, 162], when the occupation numbers of typical perturbative momentum modes become of order one such that genuine quantum corrections start playing an important role. Since the value of the gauge coupling drops out of the

[q] In the previous sections, this was identified with the saturation scale, Q_s. The scaling results do not explicitly depend on the interpretation of the scale Q, only that that the problem is characterized by a single dimension-ful scale

[r] All data shown are obtained on 128^3 lattices with spatial lattice spacing $Qa = 0.5$ and time step $tQ = 0.01$.

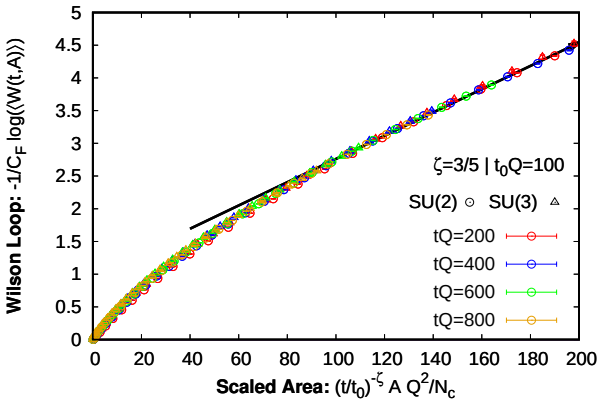

Figure 2.20: The same as in Fig. 2.19, however, now as a function of the time-rescaled area $\sim t^{\zeta}A$ with scaling exponent $\zeta = 3/5$. The collapse of the data onto a single curve demonstrates a remarkable level of self-similarity across times, areas, and gauge group.

classical-statistical dynamics, the precise value of g merely sets the time scale for the range of validity of our results [186].

By virtue of the short-distance expansion for small A,

$$W(t,A) \simeq 1 - \frac{g^2}{6N_c} A^2 \epsilon_B(t)\,, \tag{2.46}$$

where $\epsilon_B(t)$ denotes the (time-dependent) color-magnetic energy density [s], the Wilson loop is expected to approach unity for small enough areas. However, in the case of a possible area-law behavior for large areas $A \gg 1/Q^2$ and sufficiently late times $t \gg 1/Q$ the Wilson loop becomes significantly smaller than unity and decreases monotonically as a function of A such that $-\log\langle W\rangle(t,A) \sim A$.

In Fig. 2.19 we present results for the nonequilibrium Wilson loop at different times as a function of the spatial area. Shown is $-\log\langle W\rangle(t,A)$ which approaches zero for $A = 0$ and is seen to rise monotonically with the area for $A \gg 1/Q^2$. We display results for both $SU(2)$ and $SU(3)$ gauge groups. After taking into account the Casimir color factors, normalizing the data points with $C_F = (N_c^2 - 1)/2N_c$ discloses a very similar behavior for $N_c = 2$ and $N_c = 3$.

Fig. 2.20 shows the same data as Fig. 2.19, but now as a function of the *rescaled* spatial area $\sim t^{-\zeta}A$ with a time scaling exponent whose numerical fit value suggests $\zeta = 3/5$. Most remarkably, the various sets of data points at different times for $A \gg 1/Q^2$ are found to collapse onto a single curve to very good accuracy. This provides a striking demonstration of the self-similar scaling behavior (2.45).

Based on the self-similarity observed, we can obtain a precise estimate of the scaling exponent ζ in (2.45) using a statistical χ^2-analysis as described in Ref. [186]. Performing the

[s] In terms of the spatial components $i,j = 1,2,3$ of the field-strength tensor $F^a_{ij}[\mathcal{A}]$ with color index $a = 1,..,N_c^2 - 1$ the magnetic energy density is $\epsilon_B = \frac{1}{4}F^a_{ij}F^{ij}_a$ [30], where summation over repeated indices is implied.

analysis separately for $N_c = 2$ and $N_c = 3$, we obtain

$$\begin{aligned} SU(2): &\qquad \zeta = 0.603 \pm 0.005\ (\chi^2) \pm 0.004\ (sys.)\,, \\ SU(3): &\qquad \zeta = 0.604 \pm 0.004\ (\chi^2) \pm 0.005\ (sys.)\,, \end{aligned} \tag{2.47}$$

where the χ^2-error estimate in the first parentheses is associated to the quality of the scaling for a fixed range of areas and times, and the systematic uncertainties given in the second parentheses are estimated by varying the window in A and t in the analysis. Despite the different structure of the $SU(2)$ and $SU(3)$ gauge group, the respective infrared scaling exponents are found to agree well with each other within errors.

The behavior of the spatial Wilson loop for large areas reflects the long-distance or "infrared" properties of the strongly correlated system. Similar to the large-distance behavior of the spatial Wilson loop in a high-temperature equilibrium plasma [197], our data clearly indicates the approach to an area law, which is illustrated by the straight line in Fig. 2.20. However, since the area-law behavior occurs in the self-similar regime of the nonequilibrium evolution, we find that in this case a generalized scaling behavior

$$-\log\langle W\rangle(t, A) \sim t^{-\zeta} A \tag{2.48}$$

holds for a sufficiently large *ratio* of spatial area and fractional power of time. Since the scaling exponent ζ is positive, data points describing larger areas and later times map onto corresponding sets of data points for smaller areas and times. Stated differently, to observe an area law one has to probe larger and larger areas the later the time becomes. In this regime, we may also use (2.48) to define a time-dependent spatial string tension [39, 189, 194]

$$\sigma(t) = -\frac{\partial \log\langle W\rangle(t, A)}{\partial A} \sim t^{-\zeta} \tag{2.49}$$

that is consistent with a previous result [194] obtained in the context of sphaleron transitions out of equilibrium.

The area law of the nonequilibrium Wilson loop is only observed at sufficiently large ratio $\sim t^{-\zeta} A$, and Fig. 2.20 shows significant deviations to the corresponding straight line for smaller ratios. Since the area law is related to a non-perturbative infrared scale given by the spatial string tension σ, one may expect a different scaling behavior at shorter length scales where no string tension can be infered. However, Fig. 2.20 indicates that the self-similar scaling even holds somewhat beyond the area-law regime. We find that the same exponent ζ that characterizes the asymptotic scaling of the string tension describes the data well down to $(t/t_0)^{-\zeta} A Q^2/N_c \gtrsim 10$.

2.4.3 Self-similar scaling in the perturbative regime

We emphasize that for $AQ^2 \lesssim \mathcal{O}(1)$ there are clear deviations from the self-similar infrared scaling (2.45) observed, which is also expected from the expansion (2.46) of the Wilson loop for small areas. While the Wilson loop allows one to extract the relevant long-distance properties in a gauge-invariant way, it is less suitable to visualize the detailed short-distance

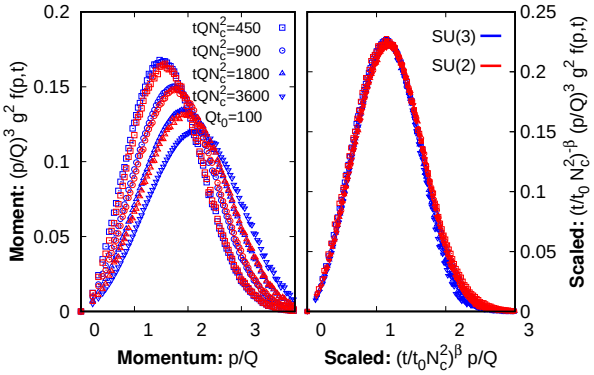

Figure 2.21: Left: The third moment of the single particle distribution $\sim p^3 f(p,t)$, which is sensitive to perturbative momenta, at different times $(t/t_0)N_c^2$ for $N_c = 2$ and $N_c = 3$. Right: The rescaled data for $\beta = -1/7$ collapses onto a single curve demonstrating self-similarity in the perturbative regime.

or ultraviolet properties. Besides gauge invariant observables, based e.g. on the energy-momentum tensor, also gauge-fixed quantities provide a valid description for the perturbative higher momenta at weak gauge coupling g. Since the gluon distribution function $f(t,p)$ as a function of spatial momentum p and time t has a direct correspondence in kinetic theory, it is typically employed to characterize perturbative scaling properties. The distribution can be extracted from equal-time correlation functions of the gauge fields $\langle \mathcal{A}^*_\nu(t,p)\mathcal{A}_\mu(t,p)\rangle$ projected on the transverse polarizations in Coulomb gauge [186].

Self-similarity of the distribution function at higher momenta amounts to

$$f(t,p) = (t/t_0)^{4\beta}\, f_S\left((t/t_0)^\beta p/Q\right)\,, \tag{2.50}$$

where the time-dependent normalization $\sim t^{4\beta}$ multiplying the time-independent scaling function f_S arises because of energy conservation, implying that the energy density $\epsilon \sim \int d^3p\, p f(t,p) = \text{const.}$ The universal scaling exponent β together with the fixed point distribution function f_S characterize the perturbative scaling regime.

The left panel of Fig. 2.21 shows data for the third moment $\sim p^3 f(t,p)$ of the distribution as a function of momentum p at different times $t/t_0 \gg 1$. The figure presents results for $N_c = 2$ and $N_c = 3$. One observes that the different data sets lie remarkably well on top of each other for given normalized times $N_c^2 t/t_0$. Moreover, if we rescale momenta according to (2.50) with $\beta = -1/7$ all data sets at different times collapse onto a single time-independent curve as demonstrated in the right panel of Fig. 2.21. For $N_c = 2$ the perturbative scaling behavior has been observed previously [161, 162] and the value $\beta = -1/7$ is taken from an effective kinetic theory analysis in the perturbative regime [73]. Performing the numerical analysis separately for $N_c = 2$ and $N_c = 3$, we obtain

$$\begin{aligned} SU(2): &\qquad \beta = -0.145 \pm 0.017\ (\chi^2) \pm 0.002\ (sys.)\,, \\ SU(3): &\qquad \beta = -0.141 \pm 0.020\ (\chi^2) \pm 0.002\ (sys.)\,. \end{aligned} \tag{2.51}$$

The fixed point distribution f_S has a universal shape, and the results indicate a rather large universality class that is also insensitive to the symmetry group of $SU(2)$ versus $SU(3)$.

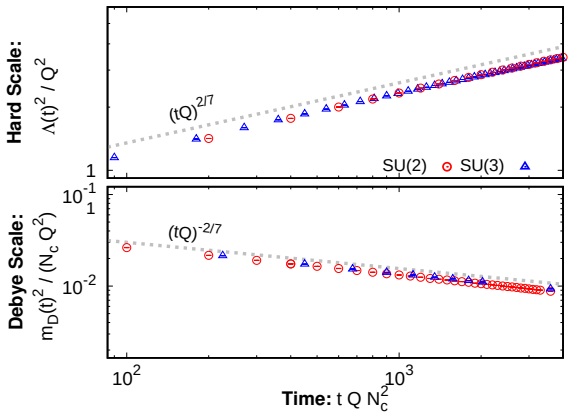

Figure 2.22: The perturbative hard scale (top) and Debye scale (bottom) as a function of time tQN_c^2 for $N_c = 2$ and $N_c = 3$. Both the two- and three-color cases clearly exhibit the same scaling $\Lambda^2(t) \sim t^{2\beta}$ and $m_D^2(t) \sim t^{-2\beta}$ for $\beta = -1/7$.

In the perturbative regime one expects a hierarchy of scales, which appear at different orders of the weak coupling g. In an equilibrium plasma at temperature T, the "hard" momenta are of order T, while the color electric and magnetic screening scales are of order gT and g^2T, respectively. In the nonequilibrium plasma, we characterize the typical momenta $\Lambda(t)$ of hard excitations in terms of a local gauge invariant operator definition constructed from a ratio of covariant derivatives of the field strength tensor and the field strength itself [186, 162]. Expressed perturbatively, the hard scale is defined as the ratio of moments of the single particle distribution [161, 162]

$$\Lambda^2(t) \simeq \frac{2}{3}\frac{\int d^3p\, p^3 f(t,p)}{\int d^3p\, p\, f(t,p)} \sim t^{-2\beta}\,, \tag{2.52}$$

which explicitly shows the scaling of this quantity with the exponent β. Here the last equality is obtained from inserting (2.50) into the momentum integral of (2.52). Numerical results are presented in the upper panel of Fig. 2.22, which clearly exhibits the same value of the scaling exponent β both for two and three colors.

At softer momenta, the Debye scale m_D is related to the electric screening scale in plasma. The leading perturbative contribution may be expressed in terms of the distribution function as [161, 162]

$$m_D^2(t) = 4g^2 N_c \int \frac{d^3p}{(2\pi)^3}\frac{f(t,p)}{p} \sim t^{2\beta}\,. \tag{2.53}$$

Its scaling behavior is demonstrated in the lower panel of Fig. 2.22.

Finally, the soft magnetic screening scale in the plasma may be related to the spatial string tension or $\sim \sqrt{\sigma}$. Following a naive power counting, one may be tempted to argue from (2.52) and (2.53) that $\sqrt{\sigma}$ should behave $\sim t^{3\beta}$. However, this scale concerns the deep infrared where typical occupancies are of order $f \sim 1/g^2$ in our case, such that a perturbative description is not valid in this regime. Instead, we find according to (2.49) that $\sqrt{\sigma} \sim t^{-\zeta/2}$. With the values (2.47) and (2.51) we note that -3β is more than 40% larger than $\zeta/2$, which is well beyond our statistical uncertainties.

Nonthermal fixed points provide an important means to classify and describe the dynamical evolution of strongly correlated systems out of equilibrium. While perturbative scaling properties at high momenta can be understood in terms of self-similar scaling of the single-particle distribution, the notion of quasi-particles with a well-defined momentum becomes inappropriate at soft momenta. Instead, the non-perturbative long-distance behavior is well captured by the elementary excitations of extended objects described by gauge-invariant Wilson loops. Combining both descriptions allows us to establish the full nonthermal scaling properties of the plasma from short to large distance scales. Performing an unprecedented numerical effort in this respect, we are able to characterize the self-similar scaling properties by two independent universal exponents, ζ in the non-perturbative infrared and β in the perturbative ultraviolet regime, and associated scaling functions. We find a remarkable universality between $SU(2)$ and $SU(3)$ Yang-Mills plasmas, which exhibit the same characteristic scaling behavior far from equilibrium even in the deep infrared. In view of the significant differences in their thermal equilibrium critical properties, where the $SU(2)$ symmetric theory exhibits long-distance scaling in the Ising universality class and the $SU(3)$ theory is discontinuous at the thermal phase transition, our results point to a rather large universality class for the nonequilibrium scaling phenomenon. Since universal properties are independent of the details of the underlying microscopic system, and the nonthermal behavior is to some extent even insensitive to the symmetry group, this opens the possibility of unexpected links between seemingly disparate physical systems far from equilibrium.

2.5 Conclusion & Outlook

We presented a first study of the dynamics of sphaleron transitions in the Glasma – the overoccupied and off-equilibrium non-Abelian plasma formed at early times in ultra-relativistic heavy ion collisions. For simplicity, we considered the Glasma dynamics for SU(2) gauge fields in a fixed box at the very weak couplings where classical-statistical dynamics captures its early time properties.

The Glasma at the earliest time in our simulation is characterized by a single hard scale Q_s, defined as the momentum up to which all modes in the Glasma have maximal occupancy of order $1/\alpha_S$; the occupancy falls sharply beyond Q_s. We showed that novel soft electric and magnetic scales develop in the Glasma and separate from each other and the hard scale dynamically with characteristic power laws in time that are independent of details of the initial conditions. Such a separation of scales is essential for the thermalization process since, in weak coupling, a clean hierarchy of these scales describes the equilibrium dynamics of a non-Abelian plasma.

In particular, we examined the temporal behavior of the spatial Wilson loop and demonstrated that it obeys an area law, with the scale set by a spatial string tension. We studied its temporal behavior in detail and extracted, for the first time, the power law that governs its decay with time. In analogy to the thermal case, the spatial string tension can be understood to determine the length scale for magnetic screening in the plasma.

We next explored the dynamics of Chern-Simons charge in the Glasma. By employing two different cooling techniques we demonstrated the existence of integer valued topological transitions and studied their temporal evolution. In analogy to the thermal case, we

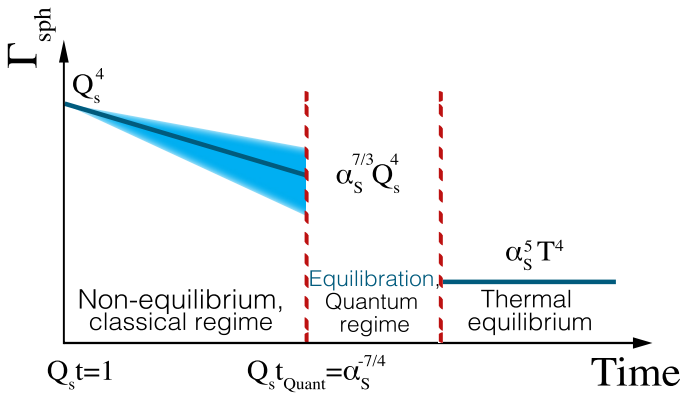

Figure 2.23: Sketch of the temporal evolution of the sphaleron transition rate in the non-expanding Glasma. Shaded band represents the uncertainty in our extraction of the scaling exponent. See text for details.

computed the auto-correlation of the Chern-Simons charge; in contrast to the former, the auto-correlation function in the Glasma is non-Markovian and even demonstrates oscillatory behavior with increasing auto-correlation time.

We argued that one can still identify a meaningful sphaleron transition rate for short auto-correlation times and studied the behavior of this rate with the evolution of the Glasma. Our first observation was that, with increasing cooling time, the Glasma sphaleron rate converges to a limiting value. This indicates that one is measuring the rate of genuine topological transitions at the maximal cooling times studied. Secondly, we found that while the sphaleron transition rate is sensitive to the initial occupancy at early times, it is insensitive to it at late times where it approaches a characteristic scaling behavior. Most strikingly, we find that the sphaleron transition rate, to a good approximation, scales with time as the string tension squared, or as the fourth power of the inverse magnetic screening length.

While in a weakly coupled plasma in thermal equilibrium the magnetic screening length l_{mag} is parametrically $\sim 1/\alpha_S T$, it is much smaller in the Glasma where initially l_{mag} is on the order of the inverse hard scale $1/Q_s$. As a consequence, the sphaleron transition rate in the Glasma is greatly enhanced compared to the equilibrium value of $\Gamma_{\rm eq} \sim \alpha_S^5 T^4$; in particular there is no parametric suppression of the sphaleron rate in the Glasma as $\Gamma_{\rm neq} \sim Q_s^4$.

As the Glasma evolves and begins to develop a separation of scales, the sphaleron transition rate decreases, as illustrated in Fig. 2.23. Within our classical-statistical framework we can follow this evolution up to a time scale $t_{\rm Quantum} \sim \alpha_S^{-7/4}\, Q_s^{-1}$ where the occupancy of hard modes in the plasma becomes of order unity and the classical description breaks down [186]. Employing our extraction of the time evolution of the string tension, we can estimate that by the time $t_{\rm Quantum}$ the sphaleron rate has dropped to $\Gamma_{\rm neq} \sim \alpha_S^{10/3} T^4$. In arriving at this estimate, we have equated the energy density of the Glasma to an equilibrium plasma with the same energy density, which gives us $T^4 \sim Q_s^4/\alpha_S$. Thus at $t_{\rm Quantum}$, $\Gamma_{\rm neq}$ is still parametrically $\alpha_S^{-5/3}$ larger than the equilibrium value.

There is non-trivial quantum dynamics at the end of the classical regime which prevents

our following the evolution of the sphaleron transition rate all the way to equilibrium. While there has been a lot of progress in understanding the equilibration of hard modes based on kinetic theory [75], it will be important to study the equilibration process of the sphaleron rate in this quantum regime.

From the perspective of computing the chiral magnetic effect, it is however the early time dynamics that matters the most. This is because the sphaleron transition rate is much larger at early times than the rate in thermal equilibrium. While this is encouraging, more work is required to understand the extrapolation of the weak coupling rates to realistic couplings as well as the sensitivity of the sphaleron transition rate to details of the initial conditions. This includes extending our simulations to SU(3) and to the longitudinally expanding Glasma realized in heavy ion collisions. A further essential improvement to the framework introduced here will include the addition of dynamical fermions to the Glasma dynamics – this will allow us to study the anomaly in real time. Finally, adding an external $U(1)$ electro-magnetic field to the fermion computation will allow us to investigate the Chiral Magnetic Effect in heavy ion collisions from first principles. Calculations including the last two additions discussed here are the subject of the next chapter.

Chapter 3

Real-time lattice QCD and anomaly induced transport

The following chapter is based off of

- M. Mace, N. Mueller, S. Schlichting, S. Sharma. *Non-equilibrium study of the Chiral Magnetic Effect from real-time simulations with dynamical fermions.* Phys. Rev. D 95, 036023 (2017). Copyright (2017) by the American Physical Society

Quantum anomalies are ubiquitous in nature and have lead to many fascinating phenomena in quantum field theories. One of the most prominent examples occurs in the context of electroweak baryogenesis, where the combined effects of anomalous baryon plus lepton number violation and the C and CP violation may provide an explanation for the observed matter/anti-matter asymmetry under suitable out-of-equilibrium conditions [123, 122, 198]. Even though analogous processes exist in QCD, where the conservation of the axial charge j_a^0 is anomalously violated locally, observing such effects is a more subtle issue as QCD by itself does not violate the discrete P and CP symmetries globally.

In recent years, a major discovery is that the combination of QCD and QED effects, expected to occur in a Quark-Gluon Plasma (QGP), can lead to new macroscopic manifestations of real-time quantum anomalies [132], which could potentially be observed in high-energy heavy-ion collision experiments [131]. While several phenomena are presently being discussed in this context (for review, see e.g. [142]), the basic idea can be summarized as follows: topological transitions such as sphalerons [115, 121], which are expected to occur frequently in the QGP [130], and pre-equilibrium (c.f. Chap. 2), can induce a net axial charge asymmetry j_a^0 of light quarks which can fluctuate on an event-by-event basis. Even though this axial charge asymmetry cannot be observed directly, in the presence of the strong electromagnetic $\vec{B}$ field created in off-central heavy-ion collisions it can be converted into an electric current $\vec{j} \propto j_a^0 \vec{B}$ [199]. This phenomenon is called the Chiral Magnetic Effect (CME) (for review, see e.g. [200]) and can lead to observable consequences in heavy-ion experiments [131, 201].

Experimental searches for the CME are ongoing at RHIC and the LHC, and intriguing hints suggestive of the CME have been seen across different experiments [133, 134, 136].

Based on the notion that the CME should lead to a separation of electric charges across the direction of the magnetic field [131], the focus of experimental searches has been to measure the effects of electric charge separation at early times by analyzing charge dependent azimuthal correlations in the final state [202]. However, it turns out that conventional explanations in terms of background effects also exist for the proposed observables and so far it has been a challenge to disentangle signal and background [137, 138, 139, 203, 141, 204, 205]. Experimentally, this question will be addressed in the near future through a proposed isobar run at RHIC [206]. By studying the variation of the charge separation signal for two isobars, this experimental program is specifically designed to separate magnetic field independent backgrounds from the genuine CME signal [207, 208, 209]. Of course, along with the dedicated experimental efforts, there is a simultaneous need for an improved theoretical understanding of the expected magnitude and features of possible CME signals [206].

Over the past few years, a variety of different theoretical approaches have been developed to investigate the real-time dynamics of anomalous transport phenomena such as the CME across different physical systems. In particular, this includes macroscopic descriptions in terms of anomalous hydrodynamics [210, 211, 212, 213] as well as microscopic descriptions based on chiral kinetic theory at weak coupling [214, 215, 216] and holographic methods at strong coupling [217, 218, 219, 220, 221]. Despite all these developments, significant uncertainties remain with regard to a quantitative theoretical description of the CME in heavy-ion collisions [142, 206]. Since the lifetime of the magnetic field is presumably very short[a] [223, 144, 224], a dominant source of uncertainty is an incomplete understanding of the dynamics of axial and vector charges during the early time pre-equilibrium stage [206]. In order to address precisely these uncertainties, we recently advocated the use of a classical-statistical lattice approach which is specifically devised to explore the real time dynamics in far-from-equilibrium situations [225].

Classical-statistical lattice techniques are a commonly used tool in the study of far-from-equilibrium many body systems. In the context of high-energy heavy-ion collisions, a classical-statistical treatment of the early time dynamics can be systematically derived within the Color Glass Condensate effective field theory [48, 49, 9] in the weak-coupling limit ($\alpha_s \ll 1$): Since the phase space occupancies of gluons are non-perturbatively large $f \sim 1/\alpha_s$ at initial times, quantum effects are suppressed by an additional power of α_s and the early time dynamics can be accurately described in terms of an ensemble of classical Yang-Mills fields [186].

Over the past few years classical-statistical lattice techniques have been employed to study various aspects of the early time, non-equilibrium dynamics, starting with the initial state particle production [57, 145, 226, 62] towards the onset of the thermalization process [70, 186, 227, 228, 162]. While so far most works have focused on the dynamics of the gluon fields, which dominate the dynamics in the high-occupancy regime ($f \gg 1$), first attempts have also been made to include dynamical fermions into the description of the early time non-equilibrium dynamics [229, 230, 231, 232, 233, 234].

[a]Even though the lifetime of magnetic field induced by the spectators is extremely short, there is a possibility that a large magnetic field can be induced the QCD medium, which may survive on a somewhat longer time scale [222]. However, the spacetime evolution of the induced magnetic field crucially depends e.g. on the chemical composition of the plasma at very early times and so far no firm conclusions have been reached concerning its actual importance [206].

Based on a classical-statistical lattice gauge theory description of the bosonic degrees of freedom, the real-time quantum dynamics of fermions can be studied from first principles within this approach by numerically solving the operator Dirac equation [235, 236, 237, 238, 239]. While the approach itself is not new as similar techniques have been employed previously e.g. in the context of strong field QED [237, 238, 240], cold electroweak baryogenesis [241, 157] or cold quantum gases [242], we have achieved several improvements which allowed us for the first time to study the 3+1 D dynamics of anomalous transport phenomena in $SU(N_c) \times U(1)$ theories [225].

This chapter is organized as follows: a detailed exposition of the theoretical formalism is provided in Sec. 3.1, including for the first time a real-time formulation of overlap fermions with exact chiral symmetry on the lattice. We then present several new physics results on the real-time dynamics of axial charge production in Sec. 3.2 and anomalous transport processes in Sec. 3.3. Even though our present numerical studies are performed in a minimal setup of a single $SU(2)$ sphaleron transition in a constant external $U(1)$ magnetic field, they provide novel insights into the real-time dynamics of anomalous transport effects and serve as a first important step in extending this approach towards a more realistic description of high-energy heavy-ion collisions. A compact summary of our findings and future perspectives is presented in Sec. 3.4. Supplementary information is provided in the following Appendices.

3.1 Classical-statistical lattice gauge theory with dynamical fermions

We first describe our setup to perform classical-statistical real-time lattice gauge theory simulations with dynamical fermions coupled simultaneously to non-Abelian $SU(N_c)$ and Abelian $U(1)$ gauge fields. Even though we will only consider the $SU(2) \times U(1)$ case in our simulations, the discussion is kept general in anticipation of future applications to the $SU(3) \times U(1)$ case relevant to heavy-ion physics. Our simulations are performed in $3+1$ dimensional Minkowski spacetime ($g^{\mu\nu} = \mathrm{diag}(1,-1,-1,-1)$), and we will denote the spacetime coordinate x^μ as (t,x,y,z).

We employ temporal axial ($A^t = 0$) gauge and work in the Hamiltonian formalism of lattice gauge theory, first formulated by Kogut and Susskind [38], where time t remains a continuous coordinate while the spatial coordinates $\mathbf{x} = (x,y,z)$ are discretized on a lattice of size $N_x \times N_y \times N_z$ with periodic boundary conditions and lattice spacing a_s along each of the three dimensions. We choose a compact U(1) gauge group, such that both the non-Abelian and Abelian gauge fields are represented in terms of the usual lattice gauge link variables $U_{\mathbf{x},i} \in \mathrm{SU(N)}\times\mathrm{U(1)}$, where $\mathbf{x} \in \{0,\ldots,N_x-1\} \times \{0,\ldots,N_y-1\} \times \{0,\ldots,N_z-1\}$ denotes the spatial position and $i = x,y,z$ the spatial Lorentz index.

Since the classical-statistical lattice formulation for gauge fields has been extensively discussed in the literature (see e.g. [227]), we will focus on the practical realization of the fermion dynamics, noting that the foundations of the formalism have been laid out in [235, 238]. Since there are various complications with respect to the realization of continuum symmetries of fermions on the lattice, we have implemented two different discretization schemes for fermions in this work. We will first discuss the real-time lattice formulation with

Wilson fermions and subsequently describe the real-time lattice formulation with overlap fermions.

3.1.1 Wilson Fermions in real time

Our starting point for the real-time lattice formulation with dynamical Wilson fermions is the lattice Hamiltonian operator, which takes the general form[b] [243]

$$\hat{H}_W = \frac{1}{2}\sum_{\mathbf{x}}[\hat{\psi}^\dagger_{\mathbf{x}}, \gamma^0\Big(-i\not{D}^s_W + m\Big)\hat{\psi}_{\mathbf{x}}]. \tag{3.1}$$

Here the fermion fields obey the usual anti-commutation relations

$$\{\hat{\psi}^\dagger_{\mathbf{x},a}, \hat{\psi}_{\mathbf{y},b}\} = \delta_{\mathbf{x},\mathbf{y}}\delta_{a,b}\ , \tag{3.2}$$

where a, b collectively stand for spin and color indices and $-i\not{D}^s_W$ denotes the tree-level improved Wilson Dirac operator

$$\begin{aligned} -i\not{D}^s_W\hat{\psi}_{\mathbf{x}} &= \frac{1}{2}\sum_{n,i} C_n\Big[\Big(-i\gamma^i - nr_w\Big)U_{\mathbf{x},+ni}\hat{\psi}_{\mathbf{x}+n\mathbf{i}} \\ &+ 2nr_w\hat{\psi}_{\mathbf{x}} - \Big(-i\gamma^i + nr_w\Big)U_{\mathbf{x},-ni}\hat{\psi}_{\mathbf{x}-n\mathbf{i}}\Big]\ . \end{aligned} \tag{3.3}$$

By r_w we denote the Wilson coefficient and we introduced the following short hand notation for the connecting gauge links

$$U_{\mathbf{x},+ni} = \prod_{k=0}^{n-1} U_{\mathbf{x}+k\mathbf{i},i}\ , \qquad U_{\mathbf{x},-ni} = \prod_{k=1}^{n} U^\dagger_{\mathbf{x}-k\mathbf{i},i}. \tag{3.4}$$

Based on an appropriate choice of the coefficients up to C_n it is possible to explicitly cancel lattice artifacts $\mathcal{O}(a^{2n-1})$ in the lattice Hamiltonian. By choosing only $C_1 = 1$ and all other coefficients to vanish, one recovers the usual (unimproved) Wilson Hamiltonian, which is only accurate to $O(a)$. With the first two terms $C_1 = 4/3$ and $C_2 = -1/6$ we can achieve an $O(a^3)$ (tree level) improvement, and by including also the third term $C_1 = 3/2$, $C_2 = -3/10$, $C_3 = 1/30$ we get an $O(a^5)$ (tree level) improvement.[c]

Operator decomposition and real-time evolution

While the gauge links $U_{\mathbf{x},i}$ are treated as classical variables, it is important to keep track of the quantum mechanical operator nature of the fermion fields. Evolution equations for the fermion operators are derived from the lattice Hamiltonian, as

$$i\gamma^0\partial_t\hat{\psi}_x = (-i\not{D}^s_W + m)\hat{\psi}_x\ , \tag{3.5}$$

[b] We omit explicit factors of the lattice spacing. Hence all definition are given in dimensionless lattice units.

[c] Note that our improvement procedure parallels that of Ref. [244]. Alternatively one could follow the procedure detailed in Ref. [245], leading to the appearance of the familiar Clover term.

which can be solved on the operator level by performing a mode function expansion [235, 238]. Considering for definiteness an expansion in terms of the eigenstates of the Hamiltonian at initial time ($t = 0$) the mode function decomposition takes the form

$$\hat{\psi}_{\mathbf{x}}(t) = \frac{1}{\sqrt{V}} \sum_{\lambda} \left(\hat{b}_{\lambda}(0) \phi^{u}_{\lambda}(t, \mathbf{x}) + \hat{d}^{\dagger}_{\lambda}(0) \phi^{v}_{\lambda}(t, \mathbf{x}) \right) , \tag{3.6}$$

where $\lambda = 1, \cdots, 2N_c N_x N_y N_z$ labels the energy eigenstates and $\hat{b}(0)/\hat{d}^{\dagger}(0)$ correspond to the (anti) fermion (creation) annihilation operators acting on the initial state ($t = 0$) [235, 238]. By construction the time dependence of the fermion field operator $\hat{\psi}$ is then inherent to the wave-functions $\phi^{u/v}_{\lambda}(t, \mathbf{x})$, whereas the operator nature of $\hat{\psi}$ only appears through the operators $\hat{b}(0)$, $\hat{d}^{\dagger}(0)$ acting in the initial state.

Since for a classical gauge field configuration the Dirac equation (3.5) is linear in the fermion operator, it follows from the decomposition in Eq. (3.6) that the wave-functions $\phi^{u/v}_{\lambda}(t, \mathbf{x})$ satisfy the same equation. One can then immediately compute the time evolution of fermion field operator by solving the Dirac equation for each of the $4N_c N_x N_y N_z$ wave functions. We obtain the numerical solutions using a leap-frog discretization scheme with time step $a_t = 0.02 a_s$.

In practice performing the decomposition in Eq. (3.5) amounts to the diagonalization of the matrix

$$\gamma^0 \Big(- i \not{D}^{s}_{W} + m \Big) \phi^{u/v}_{\lambda}(0, \mathbf{x}) = \pm \epsilon_{\lambda} \phi^{u/v}_{\lambda}(0, \mathbf{x}) , \tag{3.7}$$

at initial time, where $\epsilon_{\lambda} \geq m$ denotes the energy of single particle states. In the simplest case, where the gauge fields vanish at initial time, the eigenfunctions ϕ^{u}_{λ} correspond to plane wave solutions and can be determined analytically as discussed in App. C. However, if we introduce a non-vanishing magnetic field B at initial time (see Sec. 3.1.3), this is no longer the case and we instead determine the eigenfunctions ϕ^{u}_{λ} numerically using standard matrix diagonalization techniques.[d]

Initial conditions and operator expectation values

When computing any physical observable, one has to evaluate the operator expectation values with respect to the initial state density matrix. We will consider for simplicity an initial vacuum state, characterized by a vanishing single particle occupancy of fermions and anti-fermions $n^{u/v}_{\lambda} = 0$ yielding the following operator expectation values

$$\langle [\hat{b}^{\dagger}_{\lambda}, \hat{b}_{\lambda'}] \rangle = +2(n^{u}_{\lambda} - 1/2) \delta_{\lambda, \lambda'} \tag{3.8}$$

$$\langle [\hat{d}_{\lambda}, \hat{d}^{\dagger}_{\lambda'}] \rangle = -2(n^{v}_{\lambda} - 1/2) \delta_{\lambda, \lambda'} \tag{3.9}$$

whereas all other combinations of commutators vanish identically. Specifically for this choice of the initial state, the expectation values of a local operator $\hat{O}(t, \mathbf{x})$ involving a commutator of two fermion fields can be expressed according to

$$\hat{O}(t, \mathbf{x}) = \sum_{\mathbf{y}} O^{ab}_{\mathbf{xy}} \; \frac{1}{2} [\hat{\psi}^{\dagger}_{\mathbf{x},a}(t), \hat{\psi}_{\mathbf{y},b}(t)] \tag{3.10}$$

[d] Despite the fact that well known analytic solutions exist in the continuum in the case of a constant homogenous magnetic field, we are not aware of an equivalent analytic solution to Eq. (3.7) on the lattice.

The expectation value of this bilinear form can be expressed according to

$$\begin{aligned}\langle \hat{O}(t,\mathbf{x})\rangle &= \frac{1}{V}\sum_{\lambda,\mathbf{y}}\Big[\phi^{u\dagger}_{\lambda,a}(t,\mathbf{x})O^{ab}_{\mathbf{xy}}\phi^{u}_{\lambda,b}(t,\mathbf{y})(n^u_\lambda - 1/2) \\ &\quad -\phi^{v\dagger}_{\lambda,a}(t,\mathbf{x})O^{ab}_{\mathbf{xy}}\phi^{v}_{\lambda,b}(t,\mathbf{y})(n^v_\lambda - 1/2)\Big]. \end{aligned} \tag{3.11}$$

as a weighted sum over the matrix elements of all wave-functions.

Vector and axial currents

We will consider vector j^μ_v and axial currents j^μ_a as our basic observables in this study. Since time remains continuous in the Hamiltonian formalism, vector and axial densities are defined in analogy to the continuum as

$$j^0_v(x) = \frac{1}{2}\langle[\hat{\psi}^\dagger_x, \hat{\psi}_x]\rangle\ , \qquad j^0_a(x) = \frac{1}{2}\langle[\hat{\psi}^\dagger_x, \gamma_5\hat{\psi}_x]\rangle\ . \tag{3.12}$$

and no extra terms occur for the time-like components. However, this is different for the spatial components of the currents, where additional terms arise in the lattice definition. By performing the variation of the Hamiltonian with respect to the Abelian gauge field, we obtain the spatial components of the vector currents according to

$$\begin{aligned} j^i_v(x) &= \sum_{n,k=0}^{n-1}\frac{C_n}{4}\Big\langle[\hat{\psi}^\dagger_{\mathbf{x}-k\mathbf{i}}, \gamma^0\Big(\gamma^i - inr_w\Big)U_{\mathbf{x}-k\mathbf{i},ni}\ \hat{\psi}_{\mathbf{x}+(n-k)\mathbf{i}}] \\ &+ [\hat{\psi}^\dagger_{\mathbf{x}+(n-k)\mathbf{i}}, \gamma^0\Big(\gamma^i + inr_w\Big)U_{\mathbf{x}+(n-k)\mathbf{i},-ni}\ \hat{\psi}_{\mathbf{x}-k\mathbf{i}}]\Big\rangle\ . \end{aligned}$$

Since the currents are derived from the improved Hamiltonian, these are by construction improved which is important for reducing discretization effects as we will discuss in more detail in the upcoming section.

Defining the axial currents requires a more careful analysis to recover the correct anomaly relations in the continuum limit. In order to fully appreciate this point, let us first recall that for a naive discretization of the fermion action (obtained e.g. by setting $r_w = 0$) an unphysical cancellation of the anomaly takes place, which can be understood as a consequence of the doubling of fermion modes [246]. Hence the correct realization of the axial anomaly for Wilson fermions relies on lifting the degeneracy between doublers by introducing the Wilson term ($r_w \neq 0$), and achieving an effective decoupling of the fermion doublers in the continuum limit [246]. Defining the spatial components of the axial current as

$$\begin{aligned} j^i_a(x) &= \sum_{n,k=0}^{n-1}\frac{C_n}{4}\Big\langle[\hat{\psi}^\dagger_{\mathbf{x}-k\mathbf{i}}, \gamma^0\gamma^i\gamma_5\ U_{\mathbf{x}-k\mathbf{i},ni}\ \hat{\psi}_{\mathbf{x}+(n-k)\mathbf{i}}] \\ &+ [\hat{\psi}^\dagger_{\mathbf{x}+(n-k)\mathbf{i}}, \gamma^0\gamma^i\gamma_5\ U_{\mathbf{x}+(n-k)\mathbf{i},-ni}\ \hat{\psi}_{\mathbf{x}-k\mathbf{i}}]\Big\rangle. \end{aligned} \tag{3.13}$$

it can easily be shown that the axial current for lattice Wilson fermions satisfies the exact relation

$$\partial_\mu j^\mu_a(x) = 2m\eta_a(x) + r_w W(x), \tag{3.14}$$

where $\partial_i j_a^i(x) = j_a^i(x) - j_a^i(x-i)$ and $\eta_a(x)$ denotes the pseudoscalar density

$$\eta_a(x) = \frac{1}{2}\langle[\hat{\psi}_x^\dagger, i\gamma^0\gamma_5\hat{\psi}_x]\rangle \tag{3.15}$$

and $W(x)$ is the explicit contribution from the Wilson term

$$W(x) = \sum_{n,i} \frac{n \cdot C_n}{4}\Big\langle[\hat{\psi}_{\mathbf{x}}^\dagger, i\gamma_5\gamma_0\big(U_{\mathbf{x},+ni}\hat{\psi}_{\mathbf{x}+n\mathbf{i}} - 2\hat{\psi}_{\mathbf{x}} + U_{\mathbf{x}-n\mathbf{i},+ni}^\dagger\hat{\psi}_{\mathbf{x}-n\mathbf{i}}\big)] + \text{h.c.}\Big\rangle \tag{3.16}$$

Even though the lattice anomaly relation in Eq. (3.14) may appear unfamiliar at first sight, it has been shown in the context of Euclidean lattice gauge theory, that the usual form is recovered in the continuum limit, where the Wilson term gives rise to a non-trivial contribution

$$r_w W(x) \to -\frac{g^2}{8\pi^2}\text{Tr}F_{\mu\nu}(x)\tilde{F}^{\mu\nu}(x), \tag{3.17}$$

$F_{\mu\nu}$ being the field strength tensor and $\tilde{F}^{\mu\nu} = \frac{1}{2}\epsilon^{\mu\nu\rho\sigma}F_{\rho\sigma}$ is it's dual. It can also be shown that the first deviations from the continuum limit appear as an odd function of r_w and improved convergence can be achieved by averaging of positive and negative values of the Wilson parameter [247, 248]. Even though the generalization of these proofs to the non-equilibrium case is non-trivial, explicit numerical verification has been reported in [234] and we will confirm this behavior in Sec. 3.2 based on our own simulations.

3.1.2 Overlap fermions in real time

Constructing the Overlap Hamiltonian

Wilson fermions break the chiral and anomalous $U_A(1)$ symmetries explicitly on the lattice. Explicit chiral symmetry is recovered only in the continuum limit for massless Wilson fermions[e]. With the improvement procedures for the Wilson fermions one can reduce the lattice artifacts responsible for chiral symmetry breaking, however it is still desirable to compare our results with a lattice fermion discretization where the chiral and continuum limits are clearly disentangled. Overlap fermions [32, 33] have exact chiral and flavor symmetries on the lattice and the anomalous $U_A(1)$ symmetry can be realized even for a finite lattice spacing, analogous to the way it happens in the continuum. Even though we will demonstrate that within our simple setup one can obtain comparable results with improved Wilson and Overlap fermions, we point out that the real-time overlap formulation may be important for future real-time simulations that either go beyond classical background fields or involve truly chiral fermions.

[e]Note that mass renormalization effects can render this issue problematic, as a carful tuning of the Wilson bare mass is required in taking the correct continuum limit. However, since we will only consider the dynamics of fermions in a classical background field, such problems are absent in the simulations present in this work.

We will now employ overlap fermions for real-time simulations of the anomaly induced transport phenomena. As we did for the Wilson fermions, we consider a Hamiltonian formulation which for massless overlap quarks,

$$\hat{H}_{ov} = \frac{1}{2}\sum_{\mathbf{x}}[\hat{\psi}^{\dagger}_{\mathbf{x}}, \gamma_0\big(-i\not{D}^{s}_{ov}\big)\hat{\psi}_{\mathbf{x}}] \tag{3.18}$$

Here $-i\not{D}^{s}_{ov}$ is the 3D spatial overlap Dirac operator given by

$$-i\not{D}^{s}_{ov} = M\left(\mathbf{1} + \frac{\gamma_0 H_W(M)}{\sqrt{H_W(M)^2}}\right) \tag{3.19}$$

and $H_W(M)$ is the original Wilson Hamiltonian kernel, defined in Eq. (3.1) but with $C_n = 0$ for $n \geq 2$, and with the fermion mass m being replaced by the negative of the domain wall height M, namely,

$$H_W(M) = \gamma_0(-i\not{D}^{s}_{W} - M). \tag{3.20}$$

The domain wall height takes values $M \in (0, 2]$. In Appendix D we derive the Hamiltonian for the first time in the overlap formalism. We note that it is assuring that this construction is in exact agreement with the ansatz for the overlap Hamiltonian for vector-like gauge theories first discussed in [249]. Furthermore simulating massive overlap quarks is straightforward within this setup, which can be implemented by simply replacing

$$-i\not{D}^{s}_{ov} \to -i\not{D}^{s}_{ov}\left(1 - \frac{m}{2M}\right) + m, \tag{3.21}$$

where m is the quark mass we want to simulate.

The overlap Dirac matrix for massless quarks in three spatial dimensions, $\not{D}^{s}_{ov}$ satisfies the Ginsparg-Wilson relation [250],

$$\{\not{D}^{s}_{ov}, \gamma_5\} = -i\not{D}^{s}_{ov}\gamma_5\not{D}^{s}_{ov} \ . \tag{3.22}$$

Additionally the overlap Dirac operator is γ_0-hermitian, and satisfies a variant of Eq. (3.22),

$$\{\not{D}^{s}_{ov}, \gamma_0\} = -i\not{D}^{s}_{ov}\gamma_0\not{D}^{s}_{ov} \ . \tag{3.23}$$

As a consequence, it was shown in [249] that the Hamiltonian commutes with the operator

$$\hat{Q}_5 = \frac{1}{2}\sum_{\mathbf{x}}\left[\psi^{\dagger}_{\mathbf{x}}, \gamma_5\left(1 - \frac{-i\not{D}^{s}_{ov}}{2}\right)\psi_{\mathbf{x}}\right]. \tag{3.24}$$

This allows one to define $\hat{Q}_5$ as the axial charge within the Hamiltonian formalism, whose time evolution is given by the equation,

$$\frac{d\hat{Q}_5}{dt} = i[\hat{H}_{ov}, \hat{Q}_5] + \frac{\partial\hat{Q}_5}{\partial t} \ . \tag{3.25}$$

Since the first term in the right hand side of Eq. (3.25) is identically zero by construction, the time dependence of the axial charge density operator arises from the explicit real-time evolution of the matter fields in the definition of $\hat{Q}_5$. Hence in the real-time overlap formulation, the axial charge is generated exactly in the same way as in the continuum. While in [249] the definition of the axial charge operator, $\hat{Q}_5$, is motivated from the symmetries of the overlap Hamiltonian, we show below how this definition arises naturally from the spatial integral of the time component of the axial current.

Vector and axial currents in the overlap formalism

Since the overlap operator has exact chiral symmetry on the lattice one can define chiral projectors which project onto fermion states with definite handedness. The left and the right-handed fermion fields can be defined in terms of lattice projection operators $\check{P}_{\pm}$ as

$$\psi_{R/L} = \frac{1}{2}(\mathbf{1} \pm \check{\gamma}_5)\psi \equiv \check{P}_{\pm}\psi, \tag{3.26}$$

where $\check{\gamma}_5 \equiv \gamma_5(\mathbf{1}+i\not{D}^s_{ov})$. In order to satisfy the Ginsparg-Wilson relation, the chiral projectors for the conjugate fields are then

$$\psi^{\dagger}_{R/L} = \psi^{\dagger}\frac{1}{2}(\mathbf{1} \pm \gamma_5) \equiv \psi^{\dagger}P_{\pm}. \tag{3.27}$$

Instead of following the approach to define currents from the variation of the Hamiltonian, we can define vector currents in analogy to the continuum by constructing these quantities in terms of the physical left and right-handed fermion modes [251, 252]. Based on this approach, the vector current for overlap fermions in real-time is constructed as

$$\begin{aligned} j^{\mu}_{v} &= \frac{1}{2}\langle[\hat{\psi}^{\dagger}_{R}, \gamma_0\gamma^{\mu}\hat{\psi}_{R}]\rangle + \frac{1}{2}\langle[\hat{\psi}^{\dagger}_{L}, \gamma_0\gamma^{\mu}\hat{\psi}_{L}]\rangle \\ &= \frac{1}{2}\langle[\hat{\psi}^{\dagger}, \gamma_0\gamma^{\mu}\Big(\mathbf{1} - \frac{-i\not{D}^s_{ov}}{2}\Big)\hat{\psi}]\rangle; \end{aligned} \tag{3.28}$$

similarly the axial current is

$$\begin{aligned} j^{\mu}_{a} &= \frac{1}{2}\langle[\hat{\psi}^{\dagger}_{R}, \gamma_0\gamma^{\mu}\hat{\psi}_{R}]\rangle - \frac{1}{2}\langle[\hat{\psi}^{\dagger}_{L}, \gamma_0\gamma^{\mu}\hat{\psi}_{L}]\rangle \\ &= \frac{1}{2}\langle[\hat{\psi}^{\dagger}, \gamma_0\gamma^{\mu}\gamma_5\Big(\mathbf{1} - \frac{-i\not{D}^s_{ov}}{2}\Big)\hat{\psi}]\rangle \ . \end{aligned} \tag{3.29}$$

Numerical Implementation of the overlap operator

The overlap Hamiltonian consists of a matrix sign function of $H_W(M)$, defined in Eq. (3.19). The inverse square root of $H_W(M)^2$ can be expressed as a Zolotarev rational function [253, 254, 255, 256],

$$\frac{1}{\sqrt{H_W(M)^2}} = \sum_{l=1}^{N_{\mathcal{O}}} \frac{b_l}{d_l + H_W(M)^2}. \tag{3.30}$$

To compute Eq. (3.30), first we compute the coefficients b_l and d_l from the smallest and largest eigenvalues of $H_W(M)^2$ [255]. Once the Zolotarev expansion coefficients d_l are determined, we implement a multi-shift conjugate gradient solver to calculate the inverse of $d_l + H_W(M)^2$. The lowest and the highest eigenvalues for $H_W(M)^2$ are calculated using the Kalkreuter-Simma Ritz algorithm [257] with 20 restarts and a convergence criterion of 10^{-20}. We find that taking $N_{\mathcal{O}} = 20$ terms in the Zolotarev polynomial results in $|\mathrm{sign}(H_W)^2 - \mathbf{1}| < 10^{-9}$. We note that the lowest and highest eigenvalues of $H_W(M)^2$ are sensitive to the choice of the domain wall height M. We have chosen M such that we obtain the best approximation to the sign function as well as the Ginsparg-Wilson relation. For the

sphaleron configuration we studied in this work the optimal choice was $M \in [1.4, 1.6)$ (see App. E for more details).

For the multi-shift conjugate gradient, the convergence of the conjugate gradient is determined by the smallest d_l, and the convergence criterion is set to $|H_W(M)^2| - 1 < 10^{-16}$. For the largest lattice volumes that we consider in this study and for the single $SU(2)$ sphaleron gauge configuration to be introduced in Sec. 3.1.3, the conjugate gradient algorithm reaches the convergence criterion before the maximum number of steps, which we choose to be 2000. We have also checked that the resultant overlap Dirac operator satisfies the Ginsparg-Wilson relation, and found this is satisfied to a precision of $\mathcal{O}(10^{-9})$. We have also carefully studied the M-dependent cut-off effects for the vector and axial-vector currents which we would illustrate in the subsequent sections as well as in the Appendix E. We find that the cut-off effects in the current operators are fairly independent of the choice of M for $M \in [1.4, 1.6)$.

Additionally, we have also implemented the overlap Hamiltonian in the presence an additional static U(1) magnetic field to be introduced in Sec. 3.1.3. For this, we include the $U(1)$ fields in the Wilson Hamiltonian in Eq. (3.19). We find that the sign function is implemented to a precision of 10^{-9} and the overlap Dirac operator in this case satisfies the Ginsparg-Wilson relation to a precision of 10^{-8}.

3.1.3 Non-Abelian and Abelian gauge links

Within the classical-statistical approach, the dynamics of non-Abelian and Abelian fields is usually determined self-consistently by the solution to the classical Yang-Mills and Maxwell equations. In particular, the presence of the fermionic currents in the equations of motion for the gauge fields leads to a back-reaction of fermions, which is naturally included in the approach [235, 236]. Even though it will be desirable to investigate such effects in the long run, in the present study we will limit ourselves to a simpler set-up. Instead of a self-consistent determination of the non-Abelian and Abelian gauge fields, we will treat both of them as classical background fields whose dynamics is a priori prescribed.

$SU(2)$ gauge links

Concerning the $SU(2)$ gauge links, the dynamics is chosen to mimic that of a sphaleron transition by constructing a dynamical transition between topologically distinct classical vacua. Starting from the trivial vacuum solution $U^{SU(2)}_{\mathbf{x},i} = 1$ at initial time $t = 0$, we construct a smooth transition to a topologically non-trivial vacuum $U^{SU(2),G}_{\mathbf{x},i}$ at time $t \geq t_{\rm sph}$ through a constant chromo-electric field, corresponding to the shortest path in configuration space,

$$E^a_{\mathbf{x},i} = \begin{cases} \frac{i}{g a_s t_{\rm sph}} \log_{SU(2)}\big(U^{SU(2),G}_{\mathbf{x},i}\big) & , \quad 0 < t < t_{\rm sph} \\ 0 & , \quad t > t_{\rm sph} \end{cases} \tag{3.31}$$

during which the gauge links are constructed according to

$$U^{SU(2)}_{\mathbf{x},i}(t) = \begin{cases} \mathrm{e}^{-\mathrm{i} g a_s t \mathrm{E}^a_{\mathbf{x},\mathrm{i}} \frac{\sigma^a}{2}} \mathrm{U}^{\mathrm{SU(2)}}_{\mathbf{x},\mathrm{i}}(0) & , \quad 0 < t < t_{\rm sph} \\ U^{SU(2),G}_{\mathbf{x},i} & , \quad t > t_{\rm sph} \end{cases} \tag{3.32}$$

Since the different classical vacua are related to each other by a gauge transformation, we can easily construct a topologically non-trivial vacuum solution

$$U^{SU(2),G}_{\mathbf{x},i} = G_{\mathbf{x}} G^{\dagger}_{\mathbf{x+i}}. \tag{3.33}$$

by specifying a gauge transformation G_x with a non-zero winding number. Based on the usual parametrization of the $SU(2)$ gauge group,

$$G_{\mathbf{x}} = \alpha_0(\mathbf{x})\mathbf{1} + i\alpha_a(\mathbf{x})\sigma^a \ , \tag{3.34}$$

the coordinates $\alpha_a(\mathbf{x})$ of the gauge transformation on the group manifold are obtained by a distorted stereographic projection of the lattice coordinates $\mathbf{x} = (x, y, z)$, which has a non-zero Brouwer degree. By virtue of our construction detailed in App. F, the sphaleron transition profile (i.e all points that map away from the trivial point $G_{\mathbf{x}} = 1$) is localized on a scale r_{sph}, which we will refer to as the characteristic size scale of the sphaleron.

$U(1)$ gauge links

With regard to the Abelian gauge links we have chosen to implement a homogenous magnetic field $\vec{B} = B\hat{z}$ along the z-direction. Since on a periodic lattice the magnetic flux $qa_s^2 BN_xN_y$ is quantized in units of 2π [258], a spatially homogenous magnetic field cannot be varied continuously and we have chosen to keep the magnetic field constant as function of time. By choosing the $U(1)$ components of the gauge links according to [259],

$$U^{\mathrm{U}(1)}_{\mathbf{x},x} = \begin{cases} e^{ia_s^2 qBN_x y} & , \ x = N_x - 1 \\ 1 & , \ \text{otherwise} \end{cases} \tag{3.35}$$

$$U^{\mathrm{U}(1)}_{\mathbf{x},y} = e^{-ia_s^2 qBn_x} \tag{3.36}$$

with $U_{\mathbf{x},z} = 1$ and $a_s^2 qB = \frac{2\pi n_B}{N_x N_y}$ we can then realize different magnetic field strength by varying the magnetic flux quantum number n_B.

3.2 Sphaleron transitions & real-time dynamics of axial charge production in SU(N)

We now turn to the results of our simulations and first study the dynamics of axial charges during a sphaleron transition in the absence of electro-magnetic fields ($B = 0$). Since the realization of the axial anomaly on the lattice is non-trivial a first important cross-check is to verify that the continuum version of the anomaly relation

$$\partial_\mu j^\mu_a(x) = 2m\eta_a(x) - 2\partial_\mu K^\mu(x) \ , \tag{3.37}$$

where $\partial_\mu K^\mu(x) = \frac{g^2}{16\pi^2}\mathrm{tr} F_{\mu\nu}\tilde{F}^{\mu\nu}$ denotes the divergence of the Chern-Simons current, is correctly reproduced in our simulations. If we focus on the volume integrated quantities

$$J^0_a(t) = \int d^3\mathbf{x}\, j^0_a(t, \mathbf{x}) \tag{3.38}$$

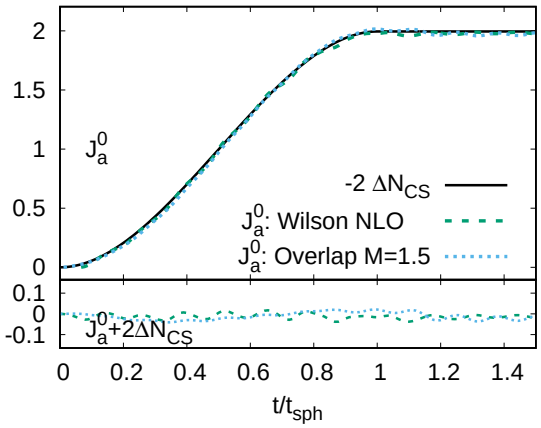

Figure 3.1: A comparison of the net axial charge generated during a sphaleron transition for improved Wilson (NLO) fermions with $mr_{\rm sph} = 1.9 \cdot 10^{-2}$ versus massless overlap fermions on a 16^3 lattice. Top: The net axial charge for both discretizations accurately tracks ΔN_{CS} due to the sphaleron transition. Bottom: Deviations from Eq. (3.39) are shown.

the net axial charge J^0_a can be directly related to the Chern-Simons number difference, according to

$$\Delta J^0_a(t) = -2\Delta N_{CS}(t)\,, \tag{3.39}$$

which changes by an integer amount over the course of the sphaleron transition. Specifically, for the topological transition constructed in Sec. 3.1.3, $\Delta N_{CS}(t \geq t_{\rm sph}) = -1$ and one expects $\Delta J^0_a(t) = 2$ units of axial charge to be created during the transition.

Simulation results for the real-time evolution of the net axial charge $J^0_a(t)$ are compactly summarized in Fig.3.1, where we compare results obtained for massless overlap fermions on a 16^3 spatial lattice with the results obtained for light Wilson fermions ($mr_{\rm sph} = 1.9 \cdot 10^{-2}$). Since the typical size scale of the sphaleron $r_{\rm sph}$ and duration of the sphaleron transition $t_{\rm sph}$ are the only dimensionful parameters in this case, in the following all spatial and temporal coordinates will be normalized in units of $r_{\rm sph}$ and $t_{\rm sph}$ respectively; if not stated otherwise we employ $t_{\rm sph}/r_{\rm sph} = 3/2$.

Since we employ a fermionic vacuum as our initial condition, the axial charge is zero initially, as there are no fermions present. As the sphaleron transition takes place fermions are dynamically produced and an axial imbalance is created. By comparing the evolution of $J^0_a(t)$ with that of the Chern-Simons number, extracted independently from the evolution of the gauge fields[f], it can be clearly seen that the global version of the anomaly relation in Eq. (3.39), is satisfied to good accuracy.

Concerning the comparison of different fermion discretizations, we find that the results for improved Wilson fermions (next to leading order) agree nicely with the ones obtained in the overlap formulation. However, we strongly emphasize that the operator improvements for Wilson fermions are essential to achieve this level of agreement on the relatively small 16^3 lattices. If in contrast one was to consider unimproved Wilson fermions, much finer lattices

[f]We use an an $O(a^2)$ improved lattice definition described in detail in [150, 194].

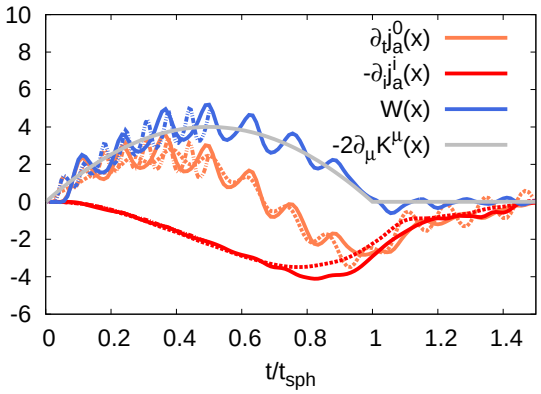

Figure 3.2: The local anomaly budget at the center of the sphaleron transition using improved Wilson (NLO) and overlap fermions. The solid, dash-dotted, and dotted lines represent data for improved Wilson (NLO) on a 16^3 lattice, 32^3 lattice, and overlap fermions on a 16^3 lattice respectively. The gray line represent the local derivative of the Chern Simons current, $-2\partial_\mu K^\mu$.

are needed to correctly reproduce the continuum anomaly and we refer to App. E for further performance and convergence studies.

Even though our present results are obtained for a single smooth gauge field configuration, an important lesson can be inferred for upcoming studies on more realistic gauge fields. Since the computational cost of the simulations scales as $\propto N_x^2 N_y^2 N_z^2$, simulations on fine lattices are often prohibitively expensive and it is therefore of utmost importance to employ improved fermionic operators in real-time lattice simulations with dynamical fermions.

Based on the excellent agreement obtained between different lattice and continuum results for volume integrated quantities, we can now proceed to study the microscopic dynamics of axial charge production in more detail. In Fig. 3.2 we present a breakup of the different contributions, $\partial_t j_a^0, \partial_i j_a^i$ and $-2\partial_\mu K^\mu$, to the local anomaly budget (c.f. Eq. (3.37)) evaluated at the center $(x, y, z) = (N_x/2, N_y/2, N_z/2)$ of the sphaleron transition profile. We have kept the volume fixed in units of $r_{\rm sph}$ and to compare quantities between different lattice spacings and different fermion discretizations we have scaled the observables by appropriate powers of $r_{\rm sph}$. Besides the rate of increase of the axial charge density $\partial_t j_a^0$, a significant fraction of the anomaly budget is compensated by the divergence of the axial current $\partial_i j_a^i$, signaling the outflow of axial charge from the center to the edges of the transition region. Hence, even though an axial charge imbalance is dominantly produced in the center of a sphaleron, axial charge redistributes as a function of time and the axial imbalance at the center again decreases towards later times.

As discussed in Sec. 3.1.1, the lattice anomaly relation for Wilson fermions is realized through the non-trivial continuum limit of the Wilson term $W(x)$ also depicted in Fig. 3.2. Indeed, the evolution of the Wilson term $W(x)$ follows that of the evolution of divergence of the Chern-Simons current $-2\partial_\mu K^\mu$, albeit superseded by fast oscillations. However, the oscillations average out in both space and time yielding a faster convergence for time and/or volume averaged quantities. It also re-assuring that the comparison of the results for almost

massless Wilson and chiral overlap fermions shows good overall agreement, although minor deviations remain on the presently available lattice sizes.

3.2.1 Quark mass dependence

So far we have analyzed the non-equilibrium dynamics of axial charge production for (almost) chiral fermions. We will now vary the quark mass to investigate the effects of explicit chiral symmetry breaking on axial charge production. Before we turn to our physical results a technical remark is in order. Since we find that for Wilson fermions cut-off effects are more pronounced for larger values of the quark mass, we performed r_w averaging of our results, i.e. we performed real-time evolutions with Wilson parameters $r_w = \pm 1$ respectively and calculated observables by averaging the results over each value of r_w. Based on this procedure, a compact summary of our results for massive fermions is compiled in Fig. 3.3, showing freeze-frame profiles of the local anomaly budget for different values of the quark mass. Different panels show profiles of the (four) divergence of the Chern-Simons current $-2\partial_\mu K^\mu$, the pseudoscalar density η, the divergence of the axial current $\partial_i j_a^i$ and the time derivative of the local axial charge density $\partial_t j_a^0$, along one of the spatial directions according to

$$\partial_\mu K^\mu(z,t) = \frac{g^2}{8\pi^2} \int d^2\mathbf{x}_\perp \; E_i^a(x) B_i^a(x) \; , \tag{3.40}$$

and similarly for the other components at three different times $t/t_{\rm sph} = 1/3,\ 2/3,\ 1$ of the sphaleron transition. Different curves in each panel correspond to the results obtained for different values of the fermion mass ranging from almost massless quarks $mr_{\rm sph} = 1.9 \cdot 10^{-2}$ to intermediate values of $mr_{\rm sph} = 1$.

Starting with the dynamics at early times ($t/t_{\rm sph} = 1/3$), the time derivative of the axial charge density shows a clear peak at the center corresponding to the creation of a local imbalance due to the sphaleron transition. While for almost massless quarks $mr_{\rm sph} = 1.9 \cdot 10^{-2}$, the rate of axial charge production $\partial_t j_a^0$ is approximately equal to the divergence of the Chern-Simons current $-2\partial_\mu K^\mu$, for heavier quark masses a significant fraction of the local anomaly budget is balanced by the contribution of the pseudoscalar density $2m\eta$ resulting in a smaller rate of axial charge production, both locally and globally.

Once a local imbalance of axial charge is created at the center, axial currents j_a^i with a negative (positive) divergence $\partial_i j_a^i$ at the center (edges) develop and contribute an outflow of the axial charge density away from the center. Even though the divergence of the Chern-Simons current $-2\partial_\mu K^\mu$ remains positive at times $t/t_{\rm sph} = 2/3$, its contribution to the axial charge production rate j_a^0 at the center is largely compensated by the outward flow of axial currents $\partial_i j^i$. In particular, for massive quarks ($mr_{\rm sph} > 1/2$), the combined effects of axial charge dissipation due to a large pseudoscalar density $2m\eta$ and outflowing currents $\partial_i j^i$ lead to a depletion of axial charge at the center ($\partial_t j_a^0 < 0$) even though the sphaleron transition is still in progress.

Subsequently at even later times, axial charge continues to spread across the entire volume leading to a depletion of axial charge at the center and an increase towards the edges. In the case of massive quarks, the pseudoscalar density contributes towards the dissipation of axial charges, and the global imbalance J_a^0 decreases significantly as a function of time. Our

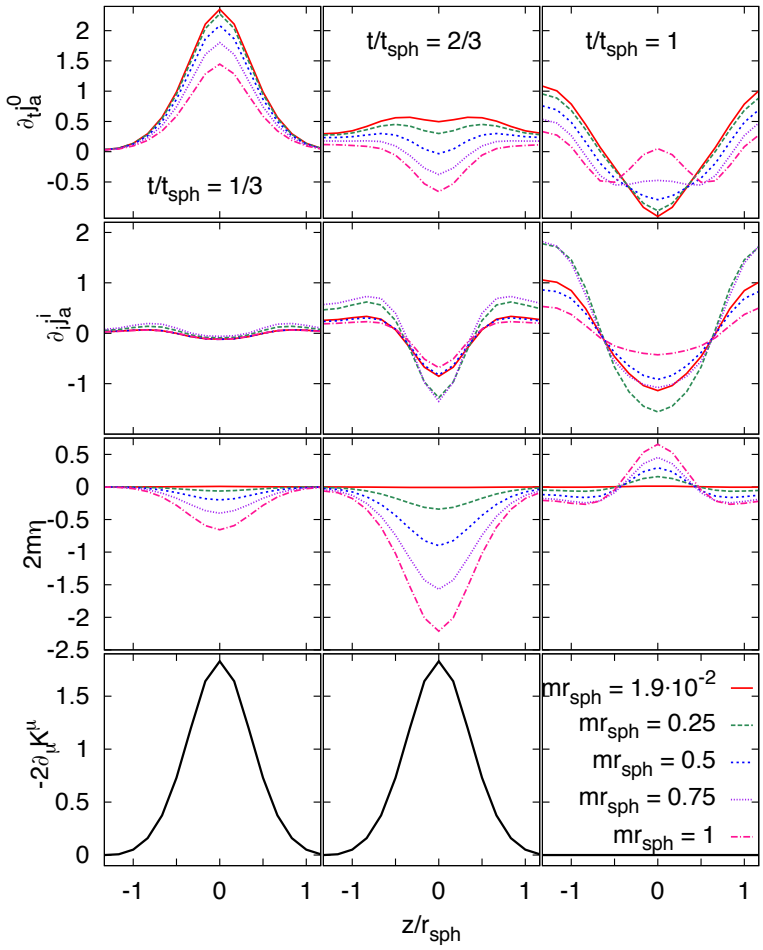

Figure 3.3: One dimensional profiles of the contributions to the anomaly equation for different masses in units of $r_{\rm sph}^{-1}$. As can be seen, the rate of axial charge density production at the center of the sphaleron is reduced due to axial currents carrying charge away and, in the case of a finite quark mass, by the pseudoscalar density, signaling chirality changing fermion-fermion interactions.

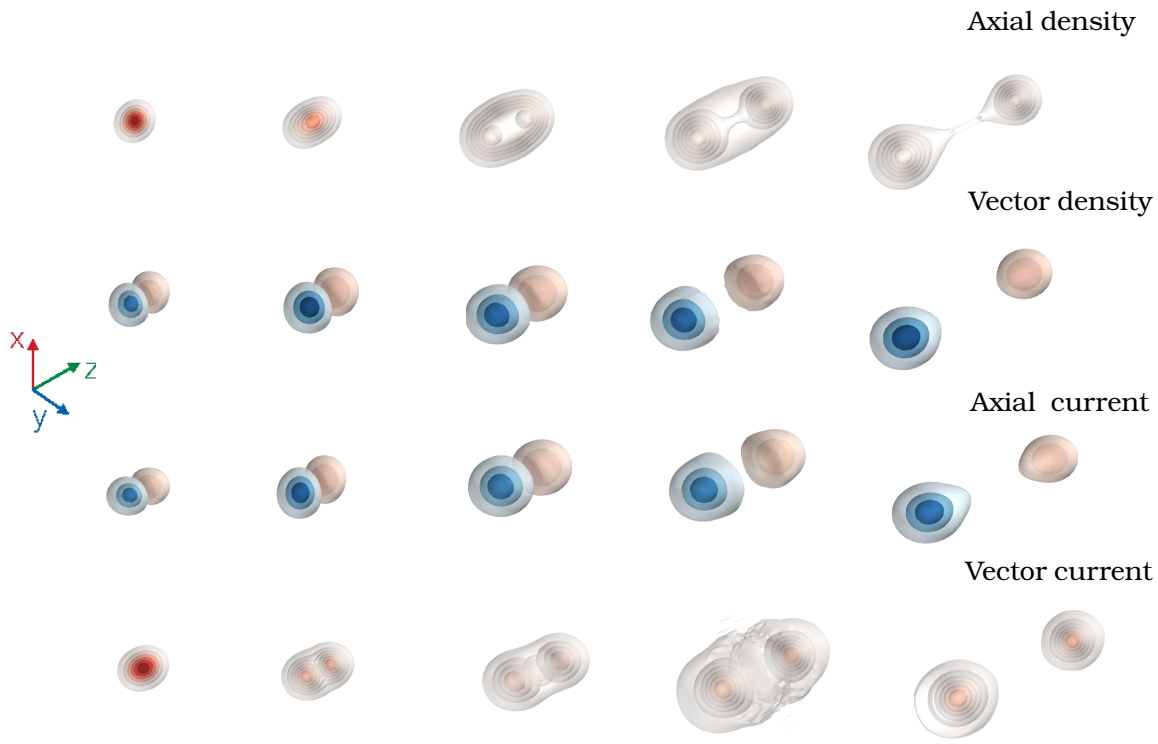

Figure 3.4: Profiles of the axial and vector densities and currents at different times of the real-time evolution for fermions with $mr_{\rm sph} = 1.9 \cdot 10^{-2}$ for strong magnetic fields $qBr_{\rm sph}^{-2} = 7.0$ at times $t/t_{\rm sph} = 0.6, 0.9, 1.1, 1.3, 1.6$.

simulations clearly point to the importance of including such dissipative effects due to a finite quark masses, and we will further elaborate on their influence on the dynamics of axial and vector charges in Sec. 3.3.2.

3.3 Chiral magnetic effect & Chiral magnetic wave in SU(N)×U(1)

We now turn to investigate the real-time dynamics of fermions during a sphaleron transition in the presence of a strong (Abelian) magnetic field. Simulations are performed on larger $24 \times 24 \times 64$ lattices with improved Wilson fermions. We consider a homogenous magnetic field B in the z direction (see Sec. 3.1.3) and prepare the initial conditions as a fermionic vacuum in the presence of the magnetic field. Since the Abelian magnetic field introduces a non-trivial coupling between the dynamics of vector and axial charges due to the Chiral Magnetic Effect (CME) and Chiral Separation Effect (CSE) [260], the SU(N)×U(1) system exhibits interesting dynamics which we addressed previously in [225]. Below we significantly

expand upon our earlier results, concerning in particular the quark mass and magnetic field dependence of the dynamics. Before we address these points in more detail, we will briefly illustrate the general features of the dynamics of vector and axial charges based on simulations for light quarks $mr_{\rm sph} = 1.9 \cdot 10^{-2}$ in a strong magnetic field $qBr_{\rm sph}^{-2} = 7.0$.

The basic features of the dynamics of vector and axial charges are compactly summarized in Fig. 3.4, showing three dimensional profiles of the axial and vector charge ($j^0_{a/v}$) and current ($j^z_{a/v}$) densities at different times ($t/t_{\rm sph} = 0.6, 0.9, 1.1, 1.3, 1.6$) during and after a sphaleron transition. As discussed in the previous section, the SU(N) sphaleron transition leads to the creation of an axial imbalance observed at early times in the top panel of Fig. 3.4. However, in the presence of the $U(1)$ magnetic field, the generation of an axial charge imbalance is now accompanied by the creation of a vector current along the magnetic field direction (CME), which can be observed in the bottom panel of Fig. 3.4. Clearly the spatial profile of the vector current follows that of the axial charge distribution as expected from the constitutive relation $j^z_v \propto j^0_a B^z$ for the Chiral Magnetic Effect.

As seen in the second panel of Fig. 3.4 the vector current leads to a separation of vector charges along the direction of the magnetic field at early times. Over the timescale of the sphaleron transition, positive (red) and negative (blue) charges accumulate at the opposites edges of the sphaleron transition region and give rise to a dipole-like structure of the vector charge distribution. Due to the Chiral Separation Effect (CSE), the presence of a local vector charge imbalance at the edges in turn induces an axial current which is depicted in the third panel of Fig. 3.4 and leads to a separation of axial charge along the direction of the magnetic field. Ultimately the interplay of CME and CSE lead to formation of a Chiral Magnetic Wave, associated with the coupled transport of vector and axial charges along the direction of the magnetic field which can be observed at later times in Fig. 3.4.

Specifically for light fermions in the presence of a strong magnetic field, the emerging wave packets of axial charge and vector current are strongly localized and closely reflect the spacetime profile of the sphaleron. However, as we will see shortly this is no longer necessarily the case for heavier fermions or weaker magnetic fields. We also note that in our present setup, the dynamics at late times is somewhat trivial as the outgoing shock-waves are effectively propagating into the vacuum. While in a more realistic scenario the number of sphaleron transitions at early times is presumably still of $\mathcal{O}(1)$, as we saw in Chapter 2, the chiral shock-waves are created from and move through a hot plasma and it will be interesting to observe how the subsequents dynamics is altered by further interactions with the constituents of the plasma.

Before we analyze the anomalous transport dynamics in more detail, we briefly comment on the comparison of Wilson and Overlap discretizations in the $SU(2) \times U(1)$ case. In order to perform a quantitative comparison of our results with different fermion discretizations, we will focus on the longitudinal profiles of vector and axial charge densities defined as

$$j^0_{a/v}(t, z) = \int d^2\mathbf{x}_\perp \; j^0_{a/v}(t, \mathbf{x}_\perp, z). \tag{3.41}$$

Our results for somewhat smaller magnetic field strength $qB = 3.5 r_{\rm sph}^{-2}$ are compared in Fig. 3.5, showing freeze-frame profiles of the longitudinal vector and axial charge distribution at three different times $t/t_{\rm sph} = 0.34, 1, 1.67$. We observe a striking level of agreement

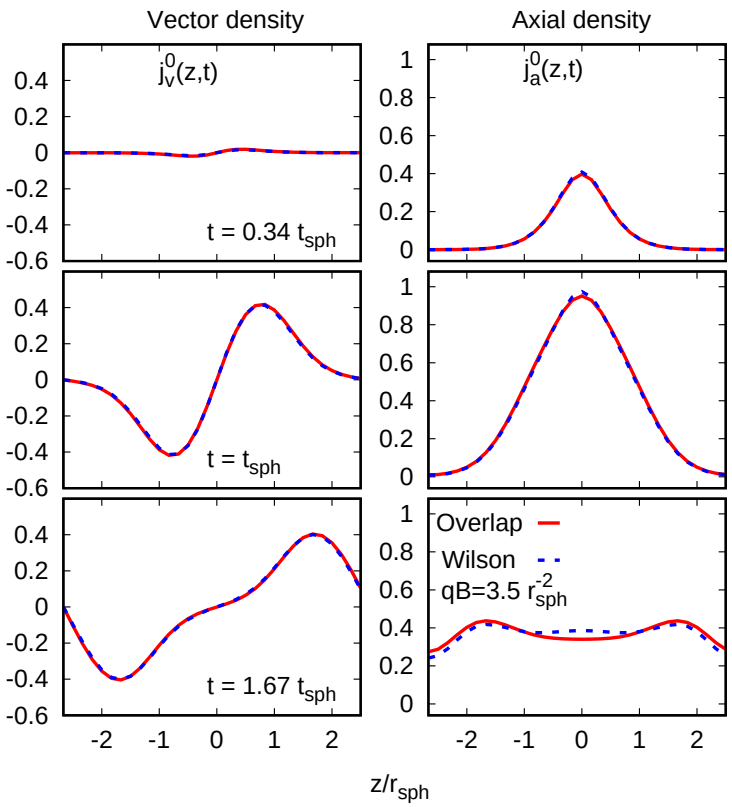

Figure 3.5: Comparison of longitudinal profiles of the vector (left) and axial (right) charge densities for improved Wilson (NLO) fermions and overlap fermions with masses $mr_{\mathrm{sph}} = 1.9 \cdot 10^{-2}$ in an external magnetic field $qB = 3.5 r_{\mathrm{sph}}^{-2}$ at times $t/t_{\mathrm{sph}} = 0.34,\ 1,\ 1.67$ (top to bottom).

between Wilson and Overlap results. Only at late times minor deviations between different discretizations become visible. However, at this point finite volume effects also start to become significant on the smaller $16 \times 16 \times 32$ lattices employed for this comparison.

3.3.1 Magnetic field dependence & comparison to anomalous hydrodynamics

We will now investigate in more detail the magnetic field strength dependence of these anomalous transport phenomena. Even though the basic features of the dynamics of vector and axial charges observed in Fig. 3.4 in the strong field limit remain the same for all values of the magnetic field considered in our study, some interesting changes occur when the magnitude of the magnetic field, qB, becomes comparable to the size of the inverse sphaleron radius squared, r_{sph}^{-2}, which is the other physical scale in our simulations.

Before we turn to the discussion of our simulation results, it is useful to first discuss how the magnetic field dependence enters in a macroscopic description in anomalous hydrodynamics [210]. In anomalous hydrodynamics the dynamics of vector and axial currents (in the chiral limit) is uniquely determined by the (anomalous) conservation of the (axial) vector

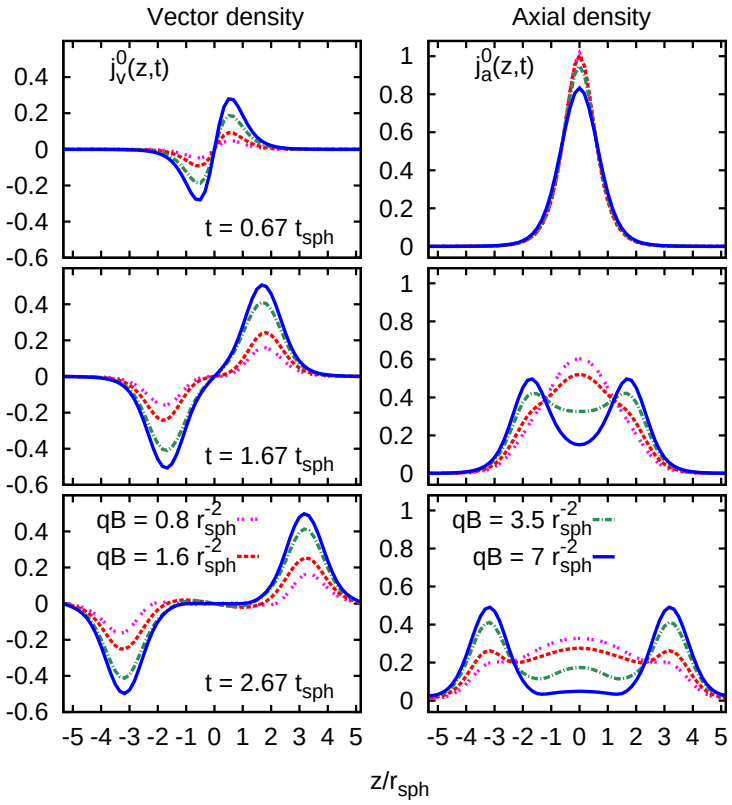

Figure 3.6: Longitudinal profiles of the vector (left) and axial (right) charge density for different magnetic fields qB in units of $r_{\rm sph}^{-2}$ and for $mr_{\rm sph} = 1.9 \cdot 10^{-2}$ at times $t/t_{\rm sph} = 0.67,\ 1.67,\ 2.67$ (top to bottom).

currents

$$\partial_\mu j_v^\mu = 0 \,, \qquad \partial_\mu j_a^\mu = -2\partial_\mu K^\mu \,, \tag{3.42}$$

once the constitutive relations for the currents are enforced. In the ideal limit the constitutive relations take the form [210]

$$j_{v,a}^\mu = n_{v,a} u^\mu + \sigma_{v,a}^B B^\mu \,, \tag{3.43}$$

and the magnetic field dependence enters only via the explicit B dependence of the transport coefficient $\sigma_{v/a}^B$. In the weak field regime ($qB \ll r_{\rm sph}^{-2}$) the conductivity is typically independent of the magnetic field and the CME/CSE currents are linearly proportional to the magnetic field B. In contrast in the strong field limit ($qB \gg r_{\rm sph}^{-2}$), the conductivity of a free fermi gas becomes $\sigma_{v/a}^B = n_{a/v}/B$ [132] for a unit charge and the late time dynamics of vector and axial currents admits a simple analytic solution [225]

$$j_{v,a}^0(t > t_{\rm sph}, z) = \frac{1}{2}\int_0^{t_{\rm sph}} dt' \left[S\big(t', z - c(t-t')\big) \mp S\big(t', z + c(t-t')\big) \right] \tag{3.44}$$

where $S(t,z) = -\frac{g^2}{8\pi^2}\int d^2x_\perp \mathrm{Tr}\; F^{\mu\nu}\tilde{F}_{\mu\nu}$ reflects the spacetime profile of the sphaleron transition. Most remarkably, the solution in Eq. (3.44) shows explicitly that the anomalous transport dynamics becomes independent of the strength of the magnetic field B in the strong field limit. However, this asymptotic scenario is unlikely to be realized in real-world experiments and it is hence important to understand the real-time dynamics of vector and axial charges beyond such simple asymptotic solutions.

Our simulation results for different magnetic field strength $qBr_{\rm sph}^2$ =0.8, 1.6, 3.5, 7.0 are presented in Fig. 3.6, which shows the longitudinal profile of vector and axial charges densities $j_{a/v}^0(z,t)$ defined in Eq. (3.41) for various times during and after the sphaleron transition. Even though the production of axial charge $j_a^0(z,t)$ during the transition ($t < t_{\rm sph}$) is not altered significantly, the subsequent propagation of the chiral shock-waves is clearly affected by the strength of the magnetic field. While for the largest value of $qBr_{\rm sph}^2 = 7.0$, the magnetic field can be interpreted as dominating over all other scales and the late time dynamics is accurately described by the asymptotic solution to anomalous hydrodynamics in Eq. (3.44), significant deviations from the asymptotic behavior occur for smaller values of $qBr_{\rm sph}^2 = 0.8,\ 1.6,\ 3.5$. Specifically, one observes from Fig. 3.6 that a smaller CME current is induced for smaller values of the magnetic field, resulting in a reduced height of the vector charge peaks; in contrast the propagation velocities and profiles of the vector charge distribution are unaffected within this range of parameters.

Since a smaller amount of vector charge imbalance in turn leads to a reduction of the induced axial currents related to the CSE, clear differences emerge for the distribution of axial charges at later times. While for strong magnetic fields essentially all of the axial charge is subject to anomalous transport away from the center, a significant fraction of axial charge remains at the center for weaker magnetic field. Considering for instance the curves for $qBr_{\rm sph}^2 = 1.6$, the axial charge distribution at later times can be thought of as a superposition of the free ($B = 0$) distribution and the Chiral Magnetic Wave contributing clearly visible peaks at the edges.

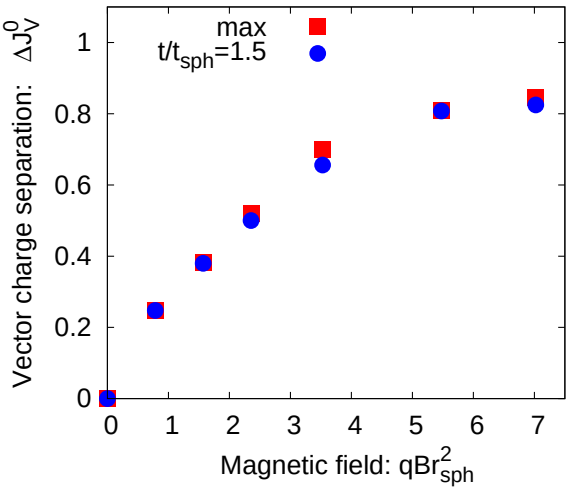

Figure 3.7: Vector charge separation ΔJ_v^0 as a function of the magnetic field strength qB in units of $r_{\rm sph}^{-2}$.

One can further quantify the magnetic field dependence by extracting the amount of vector charge separation achieved for different magnetic field strength. More precisely, we compute

$$\Delta J_v^0(t) = \int_{z\geq 0} dz\ j_v^0(t,z)\ , \tag{3.45}$$

corresponding to integrated the amount of vector charge contained in one of the oppositely charged wave-packets in Fig. 3.6. Simulation results for the magnetic field dependence of the charge separation signal are presented in Fig. 3.7, where different symbols correspond to the value of $\Delta J_v^0(t)$ at $t = 3/2t_{\rm sph}$ and respectively the maximum value of $\Delta J_v^0(t)$ observed over the entire simulation time. In accordance with the expectation that the CME current is linearly proportional to the magnetic field strength in the weak field regime, one observes an approximately linear rise of the charge separation signal at smaller values of the magnetic field strength $qB \lesssim 4/r_{\rm sph}^2$. In contrast for larger magnetic fields, the amount of vector charge separation begins to saturate, asymptotically approaching unity in the strong field limit.

Within our microscopic real-time description we can also attempt to verify directly to what extent the constitutive relations in Eq. (3.43) – assumed in a macroscopic description in anomalous hydrodynamics – are satisfied throughout the dynamical evolution of the system. In order to perform such a comparison, we extract the vector and axial charge $\Delta J_{a/v}^0(t)$ as well as the corresponding current densities $\Delta J_{a/v}^z(t)$ for the left- and right moving wave packets, and investigate the following ratios of net currents to net charges

$$C_{\rm CME}(t) = \frac{\Delta J_v^z(t)}{\Delta J_a^0(t)}\ , \qquad C_{\rm CSE}(t) = \frac{\Delta J_a^z(t)}{\Delta J_v^0(t)}\ . \tag{3.46}$$

If one assumes the validity of the constitutive relations in Eq. (3.43), one can immediately verify that both $C_{\rm CME}$ and $C_{\rm CSE}$ tend towards unity in the strong field limit [132]. In

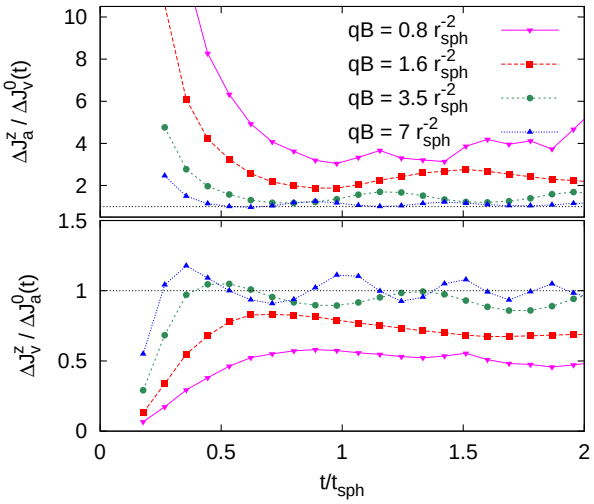

Figure 3.8: (Top panel) Ratio between the axial current along the magnetic field and the electric charge (CSE) as a function of time for different magnetic field strength qB in units of $r_{\rm sph}^{-2}$. Bottom: Ratio between the electric current and the axial charge (CME).

contrast, the weak field regime constitutive relations take the form $\Delta J^z_{v/a} \propto (\Delta J^0_{a/v})^{1/3} qB$ at low temperatures and $\Delta J^z_{v/a} \propto (\Delta J^0_{a/v}) qB$ at high temperatures. Even though the ratios $C_{\rm CME}$ and $C_{\rm CSE}$ are no longer time independent constants in this limit, their numerical values are significantly smaller than unity and decrease as a function of axial/vector charge density [132].

Our results for these ratios are presented in Fig. 3.8, where we show the time evolution of $C^{\rm eff}_{\rm CME}$ and $C^{\rm eff}_{\rm CSE}$ for four different values of the magnetic field strength. Irrespective of the strength of the magnetic field one observes the same characteristic behavior of $C^{\rm eff}_{\rm CME}$ characterized by a rapid rise towards an approximately constant behavior at later times. In contrast for $C^{\rm eff}_{\rm CSE}$, the axial current J^z_a also receives a contribution from the outflow of axial charge that is independent of the vector charge density J^0_v. Since the vector charge imbalance J^0_v is initially small, this contribution dominates over the anomalous transport contribution at early times. Hence the current ratio $C^{\rm eff}_{\rm CSE}$ approaches its asymptotic value from above and can also exhibit asymptotic values larger than unity for small field strength.

Quantitatively the values observed for $C^{\rm eff}_{\rm CME}$ ($C^{\rm eff}_{\rm CSE}$) at later times are close to the strong field limit for $qB = 3.5, 7$ and slightly smaller (larger) for $qB = 0.8, 1.6$ and it is also important to point out that the initial build up of the CME and CSE currents occurs on a shorter time scale for larger magnetic field strength. Oscillations around the constant value are also clearly visible at late times and the oscillation frequency again depends strongly on the strength of the magnetic field. However we can presently not exclude the possibility that the oscillations at late times are due to residual finite volume effects in our simulations and we will therefore not comment further on this behavior.

While the results in Fig. 3.8 nicely confirm the approximate validity of constitutive relations at late times, it is also striking to observe that vector (CME) and axial (CSE) currents are not created instantaneously from the local imbalance of axial or vector charges. Con-

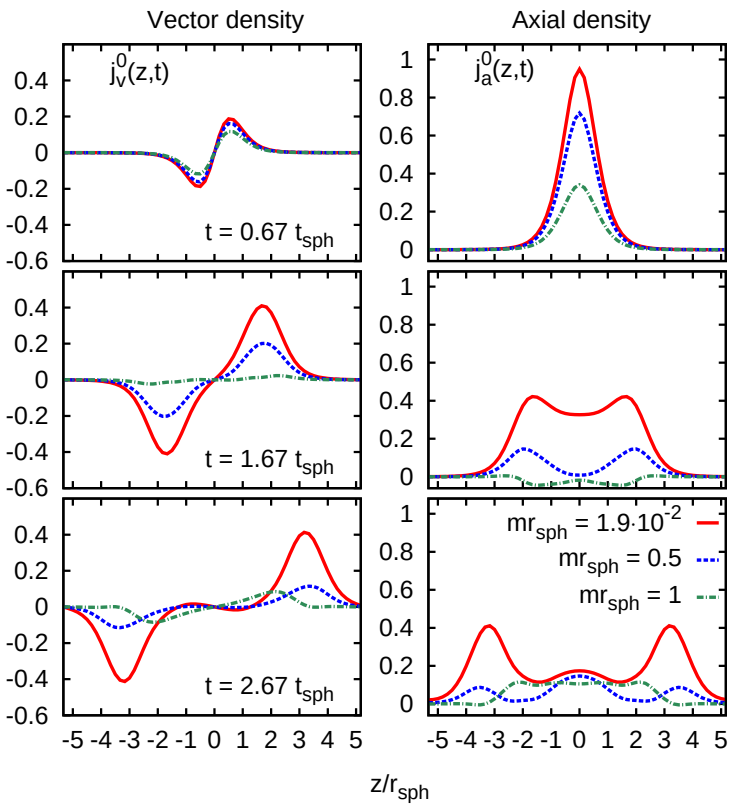

Figure 3.9: Longitudinal profiles of the vector (left) and axial (right) charge densities for different fermion masses in units of $r_{\rm sph}^{-1}$ at times $t/t_{\rm sph} = 0.67,\ 1.67,\ 2.67$ (top to bottom).

versely the results in Fig. 3.8 serve as a clear illustration of the retarded response and strongly suggest that, in order to describe the dynamics on shorter time scales, macroscopic descriptions should be modified to account for a finite relaxation time of anomalous currents. In the context of anomalous hydrodynamics, a natural way to include such effects is to follow the example of Israel and Stewart [97] by promoting the anomalous contribution to the currents to a dynamical variable $\xi^\mu_{v/a}$ that relaxes to the constitutive value $\sigma^B_{v/a}B^\mu$ on a characteristic time scale $\tau_{v/a}$. Since in high-energy heavy-ion collisions the lifetime of the magnetic field is presumably very short, it appears that the introduction of a finite relaxation time could indeed have quite dramatic effects. Hence it would also be important to understand more precisely which elementary processes determine the relevant time scale for the anomalous relaxation times. However, this question is beyond the scope of the present work.

3.3.2 Effects of finite Quark Masses

We discussed in Sec. 3.2.1 how explicit chiral symmetry breaking due to finite quark masses can significantly alter the production of an axial charge imbalance. We will now investigate in more detail the effects of explicit chiral symmetry breaking on the subsequent dynamics, characterized by the anomalous transport of axial and vector charges in the presence of a background magnetic field. Our results for different fermion masses are compactly summa-

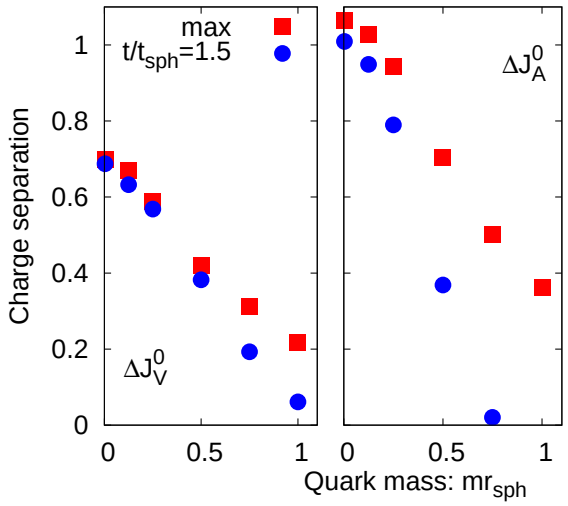

Figure 3.10: Vector (left) and axial (right) charge separation for different quark masses in units of $r_{\rm sph}^{-1}$. The red points denote the maximum amount of charge separation during the entire real-time evolution; the blue points denote the amount of charge separation at a fixed time, $t/t_{\rm sph} = 1.5$, shortly after the sphaleron transition.

rized in Fig. 3.9, where we show again the longitudinal profiles of vector and axial charge densities at different times during and after the sphaleron transition. While the simulations are performed with improved Wilson fermions for a relatively large magnetic field strength, $qBr_{\rm sph}^2 = 7.0$, we vary the masses from almost chiral fermions to fermions with large masses of the order of the inverse sphaleron size, $mr_{\rm sph} = 1$, where dissipative effects clearly become important on the time scales of interest.

In accordance with the discussion in Sec. 3.2.1 one observes from Fig. 3.9 that for heavier fermions ($mr_{\rm sph} = 0.5, 1$) the production of an axial charge imbalance at early times ($t/t_{\rm sph} = 0.67$) is suppressed compared to the almost massless case $mr_{\rm sph} = 1.9 \cdot 10^{-2}$. Since the anomalous vector currents are locally proportional to the axial charge imbalance, a similar suppression of the vector charge density of heavier fermions ($mr_{\rm sph} = 0.5, 1$) can also be observed at early times ($t/t_{\rm sph} = 0.67$). Over the course of the evolution, drastic differences in the distribution of vector and axial charges emerge between light and heavy fermions. One clearly observes from Fig. 3.9, how at times $t/t_{\rm sph} = 1.67, 2.67$ the overall amount of axial and vector charge separation is strongly suppressed for larger values of the fermion mass ($mr_{\rm sph} = 0.5, 1$). Moreover, as one would naturally expect for massive charge carriers, it is also evident from Fig. 3.9 that the propagation velocity of the chiral magnetic shock-waves decreases for larger values of the quark mass.

In order to further quantify the quark mass dependence of the anomalous transport effects, we follow the same procedure outlined in Sec. 3.2.1 and extract the vector and axial charge separation. Our results for the amount of vector/axial charge separation $\Delta J^0_{v/a}$ are presented in Fig. 3.10 as a function of the quark mass. Different symbols in Fig. 3.10 correspond to the vector/axial charge separation observed at a fixed time $t/t_{\rm sph} = 1.5$ and respectively the maximum value throughout the simulation ($0 \leq t/t_{\rm sph} \leq 3$). Most strikingly, one observes from Fig. 3.10 that clear deviations from the (almost) massless case emerge

already for rather modest values of the quark mass. One finds that, for example for $mr_{\rm sph} = 0.25$, the observed vector charge separation signal is readily reduced by approximately 30%. Considering even heavier quarks up to $mr_{\rm sph} = 1$, the vector charge separation signal almost disappears completely as dissipative effects dominate the dynamics.

In view of the significant mass dependence observed in our simulations it would be interesting to compare our microscopic simulation results at finite quark mass to a macroscopic description of anomalous transport. However, we are presently not a aware of a macroscopic formulation that properly includes the effects of explicit chiral symmetry breaking. Even though mass effects might be small for phenomenological applications [212, 213, 261] in the light (u, d) quark sector, they appear to be highly relevant with regard to the phenomenological description of the CME in the strange quark sector. Based on our results in Fig. 3.10, we expect a significant reduction of the possible CME signals for strange quarks, such that overall the situation may be closer to a two-flavor scenario [201].

3.4 Conclusions & Outlook

We presented a real-time lattice approach to study non-equilibrium dynamics of axial and vector charges in the presence of non-Abelian and Abelian fields. Even though the approach itself is by now well known and established in the literature, we pointed out several improvements related to the choice of the fermion discretization which are important to achieve a reliable description of the dynamics of axial charges in particular. Specifically, we pointed out that the use of tree-level improvements and r-averaging for the Wilson operator are essential to accelerate the convergence to the continuum limit and produce physical results on available lattice sizes. We also discussed the advantages and disadvantages of using overlap fermions in real-time lattice simulations and, to the best of our knowledge, performed the first real-time 3+1D lattice simulations with dynamical fermions with exact chiral symmetry.

Based on our real-time non-equilibrium formulation, we studied the dynamics of axial charge production during an isolated sphaleron transition in $SU(2)$ Yang-Mills theory and explicitly verified that the axial anomaly recovered is satisfied to good accuracy at finite lattice spacing for both improved Wilson and overlap fermions. Beyond the dynamics for light fermions, we also investigated dissipative effects due to finite quark mass and reported how the emergence of a pseudoscalar density leads to a significant reduction of the axial charge imbalance created. Even though at present the sphaleron transition in the background gauge field configuration was constructed by hand and does not satisfy the equations of motion for the non-Abelian gauge fields, we emphasize that approximations of this kind made within our exploratory study can be relaxed in the future without any drawbacks on the applicability of our real-time lattice approach.

By introducing a constant magnetic field, we subsequently expand our simulations to a $SU(2) \times U(1)$ setup to study the real-time dynamics of anomalous transport processes such as the Chiral Magnetic and Chiral Separation Effect. We showed how the interplay of CME and CSE lead to the formation of a chiral magnetic shock-wave and demonstrated explicitly the dynamical separation of vector charges along the magnetic field direction. We also investigated in detail the quark mass and magnetic field dependence of these anomalous transport effects. Most importantly, we showed that the amount of vector charge separation

created during this process is linearly proportional to the magnetic field strength (at small qB) and decreases rapidly as a function of the quark mass. Even though for light (u, d) flavors, such quark mass effects are most likely negligible over the typical time scales of a heavy-ion collision, the situation is different with regard to strange quarks, where it appears necessary to take these effects into account in a phenomenological description. Since in contrast to the vector current the axial current is not conserved, it would be extremely important to investigate how creation and dissipation of axial charges, which are accurately described within our microscopic framework, can be accounted for within a macroscopic description. On a similar note, we also studied the onset of the CME and CSE currents and reported first evidence for a finite relaxation time of vector and axial currents. Even though a finite relaxation time may have important phenomenological consequences, given the short lifetime of the magnetic field in high-energy heavy-ion collisions, it is presently unclear which microscopic processes determine the relevant time scale and we intend to return to this issue in a future publication. Our simulations were performed for an isolated sphaleron transition (see Sec. II C 1), allowing us to clearly observe non-perturbative generation and transport of axial charges in a topologically non- trivial background. However, the results presented in this study can only serve as a qualitative benchmark of the real-time dynamics of anomalous transport effects. In a more realistic scenario one expects the quantitative behavior of anomalous transport to be modified through further interactions with the constituents of the plasma, and it will be interesting to explore these effects in more detail in the future by performing analogous studies on more realistic gauge field ensembles.

Despite the fact that our present simulations of anomalous transport phenomena were performed in a drastically simplified setup, our work provides an important step towards a more quantitative theoretical understanding of the CME and associated phenomena in high-energy heavy-ion collisions. Since the life time of the magnetic field in heavy-ion collisions is short, it is important to understand the dynamics of anomalous transport during the early time non-equilibrium phase. However, as we pointed out, the theoretical techniques developed in this work can be used to the address open questions in this context within a fully microscopic description of the early time dynamics. In the future it will be important to extend these studies to include more realistic gauge configurations and a spacetime dependent magnetic field in order to address important phenomenological issues. Besides the applications to high-energy nuclear physics, the theoretical approach advocated in this study has a large variety applications e.g. in the study of cold electroweak baryogenesis [241, 157], strong field QED [237], or cold atomic gases [242]. In this context, the technical developments achieved in this work should also be valuable and we are looking forward to explore further applications of our ideas.

Chapter 4

Multi-particle correlations and collectivity from an initial state parton model

The following chapter is based off of

- K. Dusling, M. Mace, R. Venugopalan. *Multiparticle collectivity from initial state correlations in high energy proton-nucleus collisions.* Phys. Rev. Lett. 120, 042002 (2018); arXiv:1705.00745 [hep-ph]. Copyright (2017) by the American Physical Society
- K. Dusling, M. Mace, R. Venugopalan. *Parton model description of multiparticle azimuthal correlations in pA collisions.* Phys. Rev. D 97, 016014 (2018); arXiv:1706.06260 [hep-ph]. Copyright (2017) by the American Physical Society
- K. Dusling, M. Mace, R. Venugopalan. *What does the matter created in high multiplicity proton-nucleus collisions teach us about the 3-D structure of the proton?* PoS QCDEV2017 (2018) 039 (QCD Evolution 2017 Proceeding) arXiv:1801.09704 [hep-ph]. Copyright (2018) the authors

4.1 Introduction

A remarkable series of recent experiments at CERN's Large Hadron Collider (LHC) and at the Relativistic Heavy Ion Collider (RHIC) at BNL have demonstrated the existence of collective multiparticle dynamics in proton-proton (p+p) and light-heavy ion (h+A) collisions. Collectivity is represented by the behavior of n-th Fourier moments of the cumulants $c_n\{m\}$ of m-particle ($m \geq 4$) azimuthal angular anisotropy correlations; it is observed that corresponding real valued m-th roots of $c_n\{m\}$, the anisotropy coefficients $v_n\{m\}$, have nearly identical values for high multiplicity events. These results are similar to those obtained in peripherally overlapping collisions of heavy nuclei and even exhibit some of the systematics

observed in fully overlapping central heavy-ion collisions. The collective dynamics of the latter is well described by sophisticated hydrodynamic models which presume the creation of a thermalized strongly interacting Quark-Gluon Plasma (QGP).

In this chapter, we demonstrated that a simple initial state parton model gives rise to many of the features of multiparticle azimuthal correlations observed experimentally in small collision systems at both RHIC at BNL and the LHC at CERN. In this model, collinear quarks from the projectile scatter coherently off color sources of the size of the inverse of the saturation scale Q_s in the nuclear target; the scattered quarks are found to be collimated in their relative azimuthal angles. We observed crucially that one obtains a negative value for $c_2\{4\}$, the four-particle azimuthal anisotropy cumulant. This results in a positive definite four-particle Fourier coefficient $v_2\{4\}$. We demonstrated further, in a simpler Abelian version of our model, that one obtains the ordering of m-particle second Fourier harmonics $v_2\{2\} > v_2\{4\} \approx v_2\{6\} \approx v_2\{8\}$. Both of these features were previously believed to be unique signatures of collectivity arising from the hydrodynamic flow of quark-gluon matter. Not least, we demonstrated that so-called symmetric cumulants (mixed four-particle cumulants of different Fourier harmonics) computed in this parton model display the same qualitative features as experimental measurements of symmetric cumulants. We note that symmetric cumulants were designed to probe correlations and fluctuations arising from the hydrodynamic response to different harmonics of the azimuthal structure of the initial geometry.

While the hydrodynamic description of the flow of quark-gluon matter is likely valid in the larger, more central, collisions of heavy-ions (AA), the applicability of this description to more peripheral AA collisions, and to pA and proton-proton (pp) collisions, is less clear [111, 112]. The results of this chapter are therefore a strong hint that the stated measures of hydrodynamic collectivity are not robust in their own right without further corroboration from other distinct measures of collectivity. An example of the latter is the strong jet quenching that is seen in central heavy-ion collisions at RHIC and the LHC [262, 263, 264, 265]. In contrast, jet quenching is either small or absent in peripheral AA collisions and in pA collisions [262, 114, 266].

We further elaborate on this parton model description, which itself is an extension previous work on two-particle azimuthal correlations discussed in [267, 268]. A novel feature is the development of a general algorithm (based on the framework in [269]) to compute expectation values of multi-dipole correlators. These objects encode the physics of multiple eikonal scattering of quarks on a colored target. In particular, the dipole operator is the trace over the product of a lightlike Wilson line appearing in the quark production amplitude at a given transverse position, with its conjugate transpose appearing in the complex-conjugate amplitude at a different spatial location, normalized by the number of colors N_c. We will present a systematic study of azimuthal cumulants and Fourier harmonics as a function of the target saturation scale Q_s and the transverse momentum. Additionally, we will perform a systematic study of the N_c dependence of observables. In particular, we will point to key similarities and differences between the non-Abelian and Abelian versions of the model. We will also make predictions of yet to be measured symmetric cumulants for higher order Fourier harmonics.

Expectation values over the dipole correlators are computed in the McLerran-Venugopalan (MV) model [49, 48]. This model includes coherent multiple scattering of the quarks in the projectile off the nuclear target. If we include at most two scatterings of the quarks, cor-

responding to the expansion of the Wilson lines to lowest nontrivial order, the expectation values correspond to the Glasma graph approximation. This approximation is applicable for $p_\perp > Q_s$. A model including quantum evolution of the Glasma graphs in the Color Glass Condensate (CGC) framework [46, 9] was previously applied to successfully describe key features of azimuthal correlations for $p_\perp \geq Q_s$ [83, 270, 84, 85, 86, 87, 88]. We show that the Glasma graph correlators only produce positive values of the four-particle cumulant $c_2\{4\}$ and therefore do not correspond to a real $v_2\{4\}$. This result demonstrates that coherent multiple scattering, which is significant for $p_\perp \leq Q_s$, is an essential ingredient for the collectivity seen in our initial state framework.

The organization of this chapter is as follow. We begin with the setup of our model in Sec. 4.2. In Sec. 4.3, we discuss the algorithm for the computation of multi-dipole correlators. Results of our computations are presented in Sec. 4.4. In Sec. 4.5, we discuss the dependence of these results on the relative separations of the quarks in the projectile, on the number of color domains for varying $p_\perp$ windows and on the number of colors N_c. We contrast our results to those in the Glasma graph approximation. We briefly discuss the rapidity dependence on correlations in our model. In Sec. 4.6, we conclude and discuss possible future directions of research. Details of the Glasma graph computations are presented in the Appendix.

4.2 Eikonal quark scattering from a nuclear target

We will discuss in this section a simple parton model description of proton-nucleus collisions. The incoming projectile consists of a collection of independent, nearly collinear, quarks that scatter off a dense nuclear target. Spatial correlations within the classical field of the nucleus imprint themselves on the quarks as they scatter, resulting in nontrivial momentum space correlations between the originally uncorrelated quarks. These include correlations in their relative azimuthal angles.

We begin by considering the scattering of a fermion off a classical background field in the high energy limit [271, 272]. The forward scattering amplitude for a fixed background field A^- can be expressed as [273]

$$\langle q(\mathbf{q})_{out}|q(\mathbf{p})_{in}\rangle_{A^-} = \int d^2\mathbf{x}_\perp \left[U(x_\perp) - 1\right] e^{i(\mathbf{q}-\mathbf{p})\cdot\mathbf{x}_\perp} \sim \mathcal{M}(p,q)\,, \tag{4.1}$$

where

$$U(\mathbf{x}_\perp) \;=\; \mathcal{P}\exp\Big(-ig\int dz^+ A^{a-}(\mathbf{x}_\perp, z^+)\, t^a\Big) \tag{4.2}$$

is the Wilson line in the fundamental representation at a transverse position $\mathbf{x}_\perp$ and $\mathcal{P}$ denotes path ordering in the lightcone variable x^+. The -1 in Eq. (4.1) removes the "no scattering" contribution wherein a quark passes through the target nucleus without having its color rotated by an Eikonal phase. As the incoming partons all have transverse momentum of order $\Lambda_{\rm QCD}$, and we are interested in $|\mathbf{p}| \gg \Lambda_{\rm QCD}$, we will ignore this contribution in what follows.

The transverse spatial distribution of collinear quarks with transverse momenta $\mathbf{k}$ in the projectile is represented by the Wigner function $W_q(\mathbf{b},\mathbf{k})$ [267, 268]. The single inclusive

distribution within this model can be expressed as

$$\left\langle \frac{dN}{d^2\mathbf{p}} \right\rangle = \frac{1}{4\pi B_p} \int d^2\mathbf{r} \int d^2\mathbf{b} \int \frac{d^2\mathbf{k}}{(2\pi)^2} \, W_q(\mathbf{b},\mathbf{k}) e^{i(\mathbf{p}-\mathbf{k})\cdot\mathbf{r}} \left\langle D\left(\mathbf{b}+\frac{\mathbf{r}}{2}, \mathbf{b}-\frac{\mathbf{r}}{2}\right)\right\rangle \tag{4.3}$$

where the expectation value denotes an average over fields A^- in the target, as for instance given by the MV model. For simplicity, we assume the Wigner function has the Gaussian form

$$W_q(\mathbf{b},\mathbf{k}) = \frac{1}{\pi^2} e^{-|\mathbf{b}|^2/B_p} e^{-|\mathbf{k}|^2 B_p} \,, \tag{4.4}$$

where both the transverse momentum and spatial location of the quarks is determined by a single nonperturbative scale B_p. Unless otherwise mentioned, we will fix $B_p = 4$ GeV^{-2} [274], obtained from dipole model fits to HERA deep inelastic scattering data. We will discuss later how our results are affected by variations in the value of B_p.

In Eq. (4.6), the function

$$D(x,y) = \frac{1}{N_c} \mathrm{Tr}\left[U(x)U^\dagger(y)\right] \tag{4.5}$$

denotes the dipole operator. This operator encodes all orders in multiple gluon exchanges, as we will explicitly see in the calculations in Sec. 4.3. Performing the integration over the incoming quark momenta $\mathbf{k}$, Eq. (4.6) can be simplified to read,

$$\left\langle \frac{dN}{d^2\mathbf{p}} \right\rangle = \frac{1}{4\pi^3 B_p} \int d^2\mathbf{b} \int d^2\mathbf{r} \; e^{-|\mathbf{b}|^2/B_p} e^{-|\mathbf{r}|^2/4B_p} \; e^{i\mathbf{p}\cdot\mathbf{r}} \langle D\left(\mathbf{b}+\frac{\mathbf{r}}{2}, \mathbf{b}-\frac{\mathbf{r}}{2}\right)\rangle \,. \tag{4.6}$$

The above framework can be extended to multiparticle production. For m incoming quarks in the projectile the m-particle inclusive spectrum can be expressed as

$$\left\langle \frac{d^m N}{d^2\mathbf{p_1}\cdots d^2\mathbf{p_m}} \right\rangle \equiv \left\langle \frac{dN}{d^2\mathbf{p_1}} \cdots \frac{dN}{d^2\mathbf{p_m}} \right\rangle \,, \tag{4.7}$$

where the expectation value denotes an average over classical configurations of the target in a single event and over all events. Since each of the single-particle distributions inside the average here is a gauge-dependent functional of the classical field, we caution the reader that these distributions are qualitatively different from the gauge invariant single-particle distributions employed in hydrodynamic computations. No such simple product of gauge invariant distributions can be written in our case; indeed, as discussed at length in the Appendix, the Feynman diagrams corresponding to Eq. (4.7) are quantum interference diagrams.

On the other hand, the quarks comprising the projectile are uncorrelated, with the m-quark Wigner function of the projectile factorizing into a product of single-quark Wigner functions,

$$W(\mathbf{b_1},\mathbf{k_1},...,\mathbf{b_m},\mathbf{k_m}) = W_q(\mathbf{b_1},\mathbf{k_1}) \cdots\cdots W_q(\mathbf{b_m},\mathbf{k_m}) \,. \tag{4.8}$$

Diagrammatically, this can be represented, as shown in Fig. 4.1, as the multiple scattering between different quarks in the amplitude and complex conjugate amplitude and the target nucleus. In the strict dilute-dense limit in which we work, these Wigner functions are gauge invariant distributions of which the product form is assumed to survive color averaging. From Eq. (4.7) and Eq. (4.8), we arrive at the following compact form for the m-particle inclusive spectra:

$$\left\langle \frac{d^m N}{d^2\mathbf{p_1}\cdots d^2\mathbf{p_m}} \right\rangle = \frac{1}{(4\pi^3 B_p)^m} \prod_{i=1}^{m} \int d^2\mathbf{b_i} \int d^2\mathbf{r_i}\; e^{-|\mathbf{b_i}|^2/B_p} e^{-|\mathbf{r_i}|^2/4B_p} e^{i\mathbf{p_i}\cdot\mathbf{r_i}} \cdot \left\langle \prod_{j=1}^{m} D\left(\mathbf{b_j} + \frac{\mathbf{r_j}}{2}, \mathbf{b_j} - \frac{\mathbf{r_j}}{2}\right) \right\rangle . \tag{4.9}$$

Even though the above expression has a factorized form, it is highly nontrivial. Multiparticle correlations are generated via the expectation value over the classical fields of the target. A primary focus of this work will be computing the correlation between four particles. In this case, the expectation value is over a product of four-dipole operators, each of which, as noted, is a trace of two lightlike Wilson lines. The resulting expectation value is a function of eight transverse coordinates: four coordinates in the amplitude and four in the complex-conjugate amplitude. This expectation value will be evaluated without approximation in the MV model. We will see that large N_c approximations and perturbative expansions (such as the Glasma graph approximation) to such correlators are insufficient to capture the systematics of pA data.

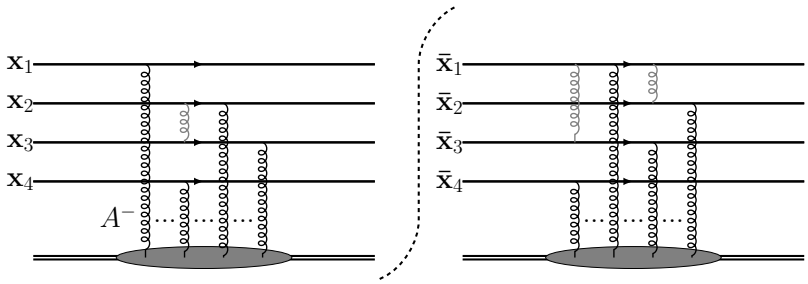

Figure 4.1: Diagrammatic representation of gluon exchanges between quarks in the amplitude (left) and complex-conjugate amplitude (right) and the target nucleus. The light-gray gluons show possible exchanges between quarks that would break the factorization used in Eq. (4.8). Correlations such as these might be generated via quantum evolution of the projectile and are not included in this work. All allowed gluon exchanges between the quarks and the target are fully resummed.

A shortcoming of our model is the oversimplified nature of the projectile. At high energies, gluon radiation dominates the small-x component of the proton's wavefunction. These high parton densities become apparent when $Q_{s,T}/p_T \gtrsim 1$; saturation model fits to HERA data conservatively suggest that these effects become non-negligible around $x = 0.01$ [275]. However, depending on the transverse momentum range studied, the qualitative features we observe could persist to smaller values of x. Furthermore, as the rapidity separation between quarks becomes larger than $\Delta y \gtrsim 1/\alpha_S$, quantum corrections will result in a decorrelation

between partons. A more quantitative discussion of the rapidity dependence is discussed in Sec. 4.5.5.

Quantum evolution will clearly break the factorized form of the Wigner function used in Eq. (4.8). Furthermore, since gluons would dominate the scattering process, their interactions with the target would be represented as adjoint Wilson lines. Multiparticle production, in this dense-dense limit, has been addressed in previous work [276, 277, 61, 62, 81, 278]. Multiparticle distributions can be obtained by solving the classical Yang-Mills equations in the presence of lightlike color sources corresponding to the projectile and the target. These source densities are each drawn from functional distributions of color charges, the evolution with energy of which is described by the JIMWLK equations [279, 47]. However, due to the numerical complexity of the simulations, this has been restricted thus far to two-particle correlations [61, 62]. The success of our simple model in explaining many of the collective signatures seen in light–heavy-ion collisions should stimulate further development of classical Yang-Mills simulations.

One may note that Eq. (4.9) has the structure of an expectation value of a product of functions. If one interpreted these functions as "single-particle" distributions the form of Eq. (4.9) would be markedly similar to a hydrodynamic framework [280]. One may then conjecture that the results we show for $v_2\{4\}$ are simply a consequence of the functional form of Eq. (4.9). This turns out not to be the case. In our discussion of coherent multiple scattering versus Glasma graphs, we will observe that, while both can be expressed in single-particle product form, one obtains negative four-particle azimuthal cumulants in the former case and positive valued cumulants in the latter.

4.3 Expectation values of multi-dipole correlators in the MV model

In this section, we will compute the expectation value of four dipole operators in the MV model [49, 48] of a nucleus at high energies. Although we will only make use of dipole operators, the results also generate all allowed expectation values of eight Wilson lines at no additional computational cost. The algorithm presented here to compute expectation values of lightlike Wilson line correlators can in principle be extended to higher-point functions.

In the MV model, classical gauge fields are described by solutions of the classical Yang-Mills equations,

$$[D_\mu, F^{\mu\nu}] = \delta^{\nu-}\rho(\mathbf{x}, x^+)\,, \tag{4.10}$$

where ρ denotes the classical color charge density in the nucleus. It is determined from the random Gaussian distribution satisfying

$$\langle \rho_a(\mathbf{x}_\perp, x^+)\rho_b(\mathbf{y}_\perp, y^+)\rangle = \delta_{ab}\delta(x^+ - y^+)\delta^{(2)}(\mathbf{x}_\perp - \mathbf{y}_\perp)\,\mu^2(x^+)\,, \tag{4.11}$$

where μ^2 is the squared color charge density per unit area. The above two-point function can also be recast in terms of the gauge fields A_a^- using

$$A_a^-(\mathbf{x}_\perp, x^+) = g\int d^2\mathbf{z}_\perp G(\mathbf{x}_\perp - \mathbf{z}_\perp)\rho_a(\mathbf{z}_\perp, x^+),\ G(\mathbf{x}_\perp) = \int \frac{d^2\mathbf{k}_\perp}{(2\pi)^2}\frac{e^{i\mathbf{k}_\perp\cdot\mathbf{x}_\perp}}{|\mathbf{k}_\perp|^2}\,, \tag{4.12}$$

where $G(\mathbf{x}_\perp)$ is the free gluon propagator in two dimensions [148]. One then obtains,

$$\begin{aligned} g^2\langle A_a^-(\mathbf{x}_\perp, x^+) A_b^-(\mathbf{y}_\perp, y^+) &= g^4\mu^2(x^+)\delta(x^+ - y^+)\delta_{ab}\int d^2\mathbf{z}_\perp G(\mathbf{x}_\perp - \mathbf{z}_\perp)G(\mathbf{y}_\perp - \mathbf{z}_\perp) \\ &\equiv \delta(x^+ - y^+)\delta_{ab}L(\mathbf{x}_\perp, \mathbf{y}_\perp)\,. \end{aligned} \tag{4.13}$$

The integral over the two-dimensional propagator is formally divergent and must be regulated at the nonperturbative scale $\Lambda_{\rm QCD}$ with the result

$$\begin{aligned} L(\mathbf{x}_\perp, \mathbf{y}_\perp) &= (g^2\mu)^2 \int d^2\mathbf{z}_\perp G(\mathbf{x}_\perp - \mathbf{z}_\perp)G(\mathbf{x}_\perp - \mathbf{y}_\perp) \\ &\sim -\frac{(g^2\mu)^2}{16\pi}|\mathbf{x}_\perp - \mathbf{y}_\perp|^2 \log\left(\frac{1}{|\mathbf{x}_\perp - \mathbf{y}_\perp|\Lambda_{\rm QCD}}\right). \end{aligned} \tag{4.14}$$

Expectation values of multiple dipoles can be computed by expanding the path ordered exponential within the Wilson line to second order in the gauge field. All possible pairwise contractions of the gauge fields are evaluated using Eq. (4.13). The result can be re-exponentied resulting in an expression valid to all orders in the gauge field [281, 282]. There is also a formally equivalent graphical method [269, 283], which we will refer to when helpful.

When expanding out the path ordered exponential in the Wilson line, each gauge field represents a single gluon exchange with the target. Each $\langle AA\rangle$ contraction is therefore equivalent to considering two gluon exchanges between two quarks (represented as Wilson lines) and the target nucleus. Gluon exchanges can occur twice on the same quark, or on different quarks, and can also act on anti-quarks in the conjugate amplitude.

Following [269], we will denote as $\mathcal{T}$ contributions arising from two gluon exchanges with the same quark and $\mathcal{N}$ as two-gluon exchange among different quarks. Since exchanges between the same Wilson line in $\mathcal{T}$ are color singlets, these contributions can be considered separately from the $\mathcal{N}$ contributions. The final result for the expectation value of m-dipole operators can be expressed as a product of the two contributions,

$$\langle D\cdots D\rangle = \mathcal{T}\,\mathcal{N}\,. \tag{4.15}$$

4.3.1 Tadpole contribution

Gluon exchanges between the same Wilson line comprise the tadpole contribution $\mathcal{T}$. We take as our starting point eight Wilson lines having transverse positions $\mathbf{x}_1, \bar{\mathbf{x}}_1, \ldots, \mathbf{x}_4, \bar{\mathbf{x}}_4$, where the $\mathbf{x}$ positions refer to quarks and the $\bar{\mathbf{x}}$ positions refer to anti-quarks. These dipoles must be connected in such a way to preserve the flow of color. Namely, quarks can only be connected to anti-quarks and vice versa. Without loss in generality, we connect at $x^+ = -\infty$ quarks at $\mathbf{x}_i$ with anti-quarks at $\bar{\mathbf{x}}_i$, as shown in Fig. 4.2.

This allows us to unambiguously define what we mean as a four-dipole configuration for the given positions[a], as shown in Fig. 4.4a. However, we can consider the $x^+ = +\infty$ ends to be initially open ended. To evaluate the tadpole contribution, we draw a gluon connecting

[a] Physically however these positions are completely arbitrary.

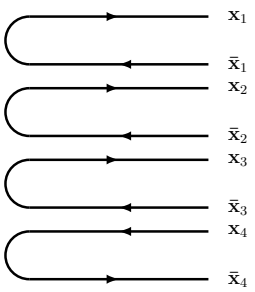

Figure 4.2: Eight fundamental Wilson lines, pairwise connected. Coordinates denote transverse positions.

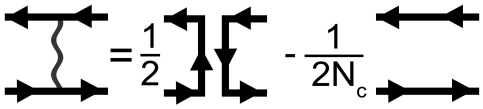

Figure 4.3: The Fierz identity, Eq. (4.16).

at two arbitrary x^+ points on the same Wilson line of Fig. 4.2. We then invoke the Fierz identity,

$$t^a_{ij} t^a_{kl} = \frac{1}{2}\delta_{il}\delta_{jk} - \frac{1}{2N_c}\delta_{ij}\delta_{kl}, \tag{4.16}$$

which is given graphically by Fig. 4.3.

Performing this Fierz-ing, we see that the first term gives us a closed loop, which just is the trace of the identity matrix. This gives a factor of N_c and the dipole again. The second term is just the original dipole. The result is then the original dipole multiplied with the Casimir factor $C_F = \frac{N_c^2-1}{2N_c}$.

For the rest of the result, we must calculate pair-wise contractions of the gauge field A^-_a. As noted, for the MV model, these satisfy Eq. (4.13). Every gluon exchange between the same (anti)-quark (same transverse position Wilson line) results in a factor of $-\frac{C_F}{2}L_{x_i x_i}$, where L was defined in Eq. (4.14), and the $1/2$ is on account of the fact that the two ends of the correlator are ordered in x^+ because they belong to the same Wilson line. The negative sign is from connecting a (anti)-quark with a (anti)-quark.

Summing n such exchanges to the Wilson lines, the tadpole contribution can be expressed as

$$\mathcal{T} = \exp\Big(-\frac{C_F}{2}\sum_{i=1}^{4}\big(L_{x_i x_i} + L_{\bar{x}_i \bar{x}_i}\big)\Big), \tag{4.17}$$

where we now denote the transverse position arguments as subscripts for readability and differentiate between quarks in the amplitude (x_i) and anti-quarks in the complex-conjugate amplitude with an over-bar ($\bar{x}_i$). This tadpole term is a color singlet and commutes with the terms we will derive next.

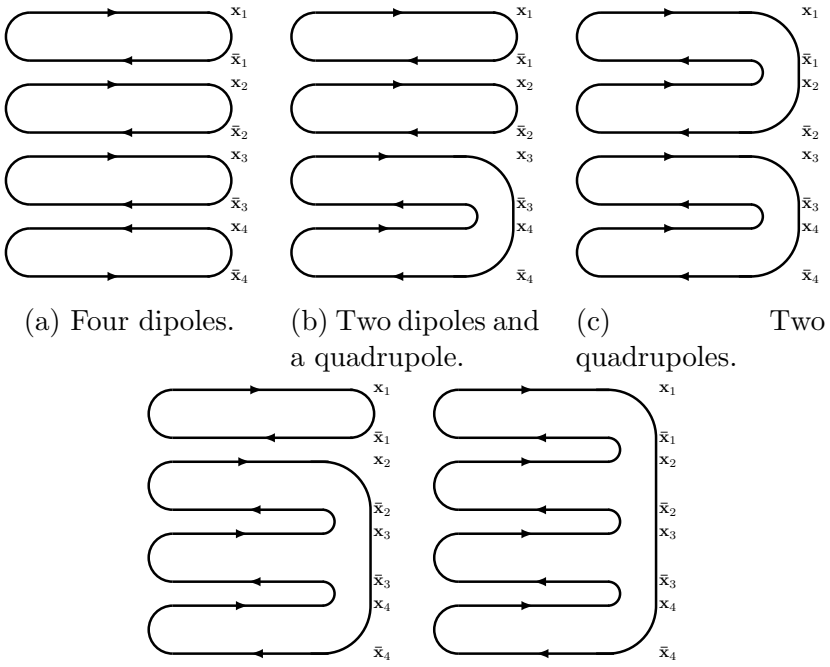

(a) Four dipoles. (b) Two dipoles and a quadrupole. (c) Two quadrupoles.

(d) One dipole and a sextupole. (e) An octupole.

Figure 4.4: The five different topologies possible for eight Wilson lines. All possible permutations with respect to the given transverse coordinates are possible.

4.3.2 Gluon exchange contribution

We shall now consider gluon exchanges between different Wilson lines. Our starting point is again the configuration shown in Fig. 4.2. Closing the ends of the dipoles while preserving the color flow, we find that there are five distinct topologies. Using Fierz ordering as we did previously for the tadpole contribution, a gluon exchange between different Wilson lines in one topology can transform it into a different topology.

We now show how one obtains the five distinct topologies shown in Fig. 4.4. As a concrete example, we start with the four closed dipoles in Fig. 4.4a. Consider a gluon exchange between $\bar{x}_3$ and x_4. From the two terms that result from Fierz ordering, as shown in Fig. 4.3, the first term gives two dipoles and a quadrupole, as depicted in Fig. 4.4b, with a factor of $\frac{1}{2}$. A quadrupole, as depicted, is a distinct topological configuration corresponding to the trace over the product of Wilson lines at two distinct transverse spatial positions in the amplitude and at two such positions in the complex-conjugate amplitude. The second term from Fierz-ing just returns the original four-dipole configuration shown in Fig. 4.4a, but now with the Fierz factor $\frac{1}{2N_c}$. Now taking this dipole-dipole-quadrupole configuration, consider further an exchange between $\bar{x}_1$ and x_2. This creates a quadrupole-quadrupole topology from the first term in the Fierz-ing, as depicted in Fig. 4.4c, and likewise the structure Fig. 4.4b from the second Fierz term, both terms with the appropriate Fierz prefactors.

If instead we had started with the dipole-dipole-quadrupole configuration and considered a gluon exchange between $\bar{x}_2$ and x_3, the first Fierz term would have resulted in a dipole-

sextupole configuration, as depicted in Fig. 4.4d. A sextupole, as depicted in Fig. 4.4d, corresponds to a trace over the product of Wilson lines at three spatial positions in the amplitude and three in the complex-conjugate amplitude. An exchange between $\bar{x}_1$ and x_2 in this dipole-sextupole topology results in an octupole (trace of eight Wilson lines– four in the amplitude and the other four in the complex-conjugate amplitude), depicted in Fig. 4.4e, for the first Fierz term. The second term, as for the previous cases, gives back the original configuration, the dipole-sextupole one, with the appropriate Fierz prefactor. Thus, we see that multiple gluon exchanges continually generate, with each additional exchange, transitions between five topologically distinct configurations: (a) four-dipole, (b) dipole-dipole-quadrupole, (c) quadrupole-quadrupole, (d) dipole-sextupole, (e) octupole.

There is a transverse coordinate permutation degeneracy to these diagrams as well. The four-dipole is the only topology without this permutation degeneracy. For the dipole-dipole-quadrupole topology, there are $\binom{4}{2} = 6$ possible permutations to close the $x^+ = +\infty$ side of the eight pairwise connected Wilson lines we introduced previously. Similarly, there are $\frac{1}{2}\binom{4}{2} = 3$ quadrupole-quadrupole permutations, $2\binom{4}{3} = 8$ dipole-sextupole permutations, and $3! = 6$ octopole permutations. As a sanity check, since we have considered eight Wilson lines connected pairwise at one end ($x^+ = -\infty$), the sum of these permutations degeneracies agrees with the total $4! = 24$ possible different contractions of the $x^+ = +\infty$ side, which is dictated from the fact that quark (anti-quark) Wilson lines can only connect with anti-quark (quark) Wilson lines.

It should be clear from our discussion that we have a closed system of 24 configurations whereby each of these are transformed, through gluon exchanges and Fierz-ing, into other configurations in this system. We can express the 24 possible configurations as elements of a basis characterizing the four-dipole system. Starting with this initial condition, where all other configurations are set to zero, one can construct a 24 by 24 transformation matrix $\mathbf{M}$ that transforms one set of basis elements to another with each gluon exchange and subsequent Fierz-ing. We can then deduce, either analytically [281, 282, 284] or diagramatically [269, 283], what factors (via Fierz) are picked up in going from a basis element α to basis element β, which then define the elements $M_{\alpha\beta}$ of the matrix.

To understand how one fills in the arrays of this matrix, consider a path ordered exponential for the Wilson line

$$U(\mathbf{x}_\perp) \;=\; \mathcal{P}\exp\Big(ig\int^{\xi} dz^+ A^-(z^+,\mathbf{x}_\perp)\Big) \simeq V(\mathbf{x}_\perp)(1+igA_a^-(\xi,\mathbf{x}_\perp)t^a+...)\,, \tag{4.18}$$

where we expanded out the last infinitesimal slice in rapidity, and $V(\mathbf{x}_\perp)$ is a redefinition of the original Wilson line excluding this last infinitesimal slice. Substituting this last expression in the dipole operator, we obtain

$$\begin{aligned}\langle D(\mathbf{x}_\perp,\bar{\mathbf{x}}_\perp)_U\rangle &= \frac{1}{N_c}\langle \mathrm{tr}(U(\mathbf{x}_\perp)U^\dagger(\bar{\mathbf{x}}_\perp)\rangle \\ &= \langle D(\mathbf{x}_\perp,\bar{\mathbf{x}}_\perp)_V\rangle \\ &+ g^2\langle A_a^-(\mathbf{x}_\perp)A_b^-(\bar{\mathbf{x}}_\perp)\rangle\frac{1}{N_c}\langle \mathrm{tr}\left(V(\mathbf{x}_\perp)t^at^bV^\dagger(\bar{\mathbf{x}}_\perp)\right)\rangle\,.\end{aligned} \tag{4.19}$$

Here we have made use of the locality in rapidity of correlators in the MV model.

Using Eq. (4.13), we can express $\langle D_U \rangle$ in the l.h.s in terms of $\langle D_V \rangle$ alone on the r.h.s.. Iterating this expression for each slice in rapidity, one obtains the exponentiated expression

$$\langle D(\mathbf{x}_\perp, \bar{\mathbf{x}}_\perp)_U \rangle \;=\; e^{C_f L(\mathbf{x}_\perp, \bar{\mathbf{x}}_\perp)} \langle D(\mathbf{x}_\perp, \bar{\mathbf{x}}_\perp)_V \rangle \,. \tag{4.20}$$

While this is a simple example, an identical procedure can be followed for multiple dipoles, or any higher order configuration, resulting from an initial four-dipole configuration. Another example is the well-known two-dipole result [269, 283, 281, 282]. In this case, following the procedure outlined above, it is straightforward to show that

$$\begin{aligned} \langle D_{x_1\bar{x}_1} D_{x_2\bar{x}_2} \rangle_U \;&\simeq\; \alpha_{x_1\bar{x}_1 x_2\bar{x}_2} \langle D_{x_1\bar{x}_1} D_{x_2\bar{x}_2} \rangle_V \\ &+\; \beta_{x_1\bar{x}_2 x_2\bar{x}_1} \langle Q_{x_1\bar{x}_2 x_2\bar{x}_1} \rangle_V \end{aligned} \tag{4.21}$$

where $Q = \mathrm{Tr}\left(V(x_1)V^\dagger(\bar{x}_2)V(x_2)V^\dagger(\bar{x}_1)\right)/N_c$ is the quadrupole configuration. Since the only two configurations for two dipoles are the dipole-dipole and quadrupole, we can then write this as a matrix equation:

$$\begin{pmatrix} \langle D_{x_1\bar{x}_1} D_{x_2\bar{x}_2} \rangle \\ \langle Q_{x_1\bar{x}_2 x_2\bar{x}_1} \rangle \end{pmatrix}_U = \begin{pmatrix} \alpha_{x_1\bar{x}_1 x_2\bar{x}_2} & \beta_{x_1\bar{x}_2 x_2\bar{x}_1} \\ \beta_{x_1\bar{x}_1 x_2\bar{x}_2} & \alpha_{x_1\bar{x}_2 x_2\bar{x}_1} \end{pmatrix}_U \begin{pmatrix} \langle D_{x_1\bar{x}_1} D_{x_2\bar{x}_2} \rangle \\ \langle Q_{x_1\bar{x}_2 x_2\bar{x}_1} \rangle \end{pmatrix}_V \tag{4.22}$$

where α and β are simple functions of $L(\mathbf{x}_\perp, \mathbf{y}_\perp)$ given in Ref. [269].

For a further example, if we consider four dipoles, then it is only possible via one gluon exchange to get to the six possible dipole-dipole-quadrupole configurations or stay in the four-dipole configuration. One obtains

$$\begin{aligned} \langle D_{x_1\bar{x}_1} D_{x_2\bar{x}_2} D_{x_3\bar{x}_3} D_{x_4\bar{x}_4} \rangle_U \;&\simeq\; \alpha_{x_1\bar{x}_1 x_2\bar{x}_2 x_3\bar{x}_3 x_4\bar{x}_4} \langle D_{x_1\bar{x}_1} D_{x_2\bar{x}_2} D_{x_3\bar{x}_3} D_{x_4\bar{x}_4} \rangle_V \\ &+\; \beta_{x_1\bar{x}_2 x_2\bar{x}_1} \langle Q_{x_1\bar{x}_2 x_2\bar{x}_1} D_{x_3\bar{x}_3} D_{x_4\bar{x}_4} \rangle_V \\ &+\; \beta_{x_1\bar{x}_2 x_2\bar{x}_1} \langle Q_{x_1\bar{x}_3 x_3\bar{x}_1} D_{x_2\bar{x}_2} D_{x_4\bar{x}_4} \rangle_V \\ &+\; \beta_{x_1\bar{x}_4 x_4\bar{x}_1} \langle Q_{x_1\bar{x}_4 x_4\bar{x}_1} D_{x_2\bar{x}_2} D_{x_3\bar{x}_3} \rangle_V \\ &+\; \beta_{x_2\bar{x}_3 x_3\bar{x}_2} \langle Q_{x_2\bar{x}_3 x_3\bar{x}_2} D_{x_1\bar{x}_1} D_{x_4\bar{x}_4} \rangle_V \\ &+\; \beta_{x_2\bar{x}_4 x_4\bar{x}_2} \langle Q_{x_2\bar{x}_4 x_4\bar{x}_2} D_{x_1\bar{x}_1} D_{x_3\bar{x}_3} \rangle_V \\ &+\; \beta_{x_3\bar{x}_4 x_4\bar{x}_3} \langle Q_{x_3\bar{x}_4 x_4\bar{x}_3} D_{x_1\bar{x}_1} D_{x_2\bar{x}_2} \rangle_V \,. \end{aligned} \tag{4.23}$$

We can repeat this for all topologies to obtain a similar matrix as for the two-dipole case.

For a small number of dipoles, this procedure can be carried out efficiently by hand, and the eigenvalues of the matrix can be even computed analytically. However for larger numbers of dipoles, this becomes cumbersome. For example, for the four dipoles we have been considering, we must compute 7! gluon exchanges for each of the 24 basis elements, totaling 120,960 computations. Fortunately, since the algorithm suggested by our exercises is quite straightforward, it is very tractable to determine the elements of the 24 by 24 matrix and compute their eigenvalues on a computer. This work made extensive use of the GNU Scientific Library [285] and the EXPOKIT software package [286]. The matrix is illustrated schematically by Fig. 4.5; as it indicates, the elements of the matrix are relatively sparse but must nevertheless be diagonalized numerically. Our algorithm can be generalized to a larger number of dipoles of more complex topologies. It is therefore potentially useful for

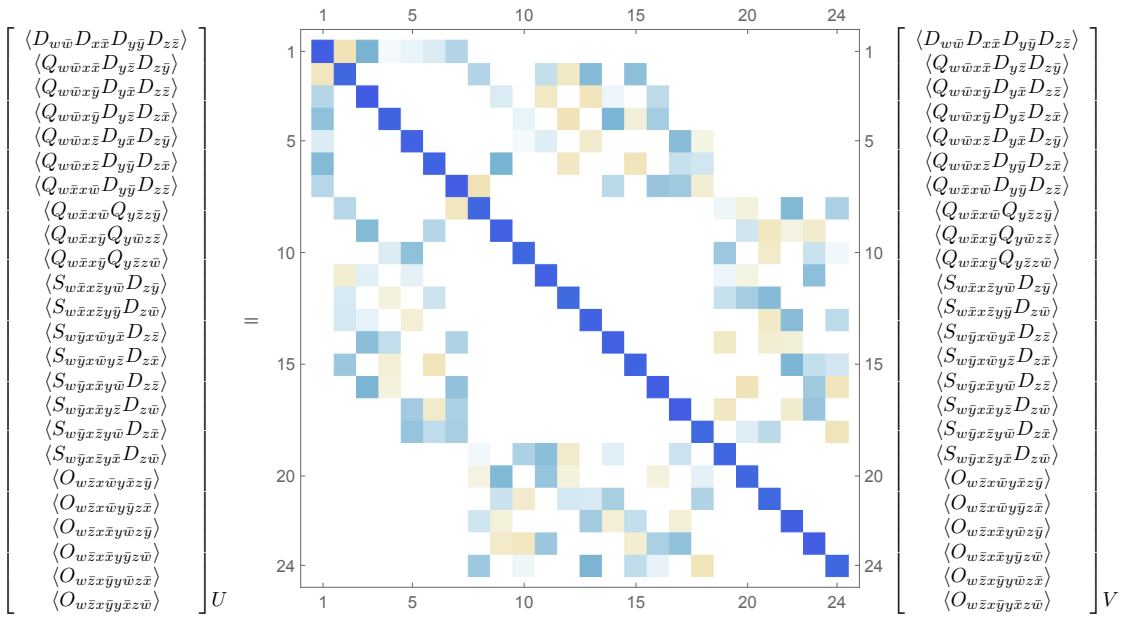

Figure 4.5: The basis of configurations resulting for eight Wilson lines, pairwise connected, resulting in dipoles, quadrupole, sextupoles, and octupoles. Coordinates denote transverse positions.

computations of many-body final states in high energy QCD where n-tupoles of lightlike Wilson lines are ubiquitous.

As a final remark on this matrix computation, we note that in the large N_c limit this problem becomes more tractable [287, 288]. In Ref. [287], it was shown that for large N_c only dipoles and quadrupoles contribute to high energy QCD processes. However the azimuthal cumulants themselves vanish at large N_c, so in order to compute these quantities a finite N_c calculation is necessary.

4.3.3 Result for product of four-dipole correlators

Now that we have explained how to calculate the matrix for one gluon exchange at a single slice in rapidity, we can compute how the basis vector space of configurations evolves after an infinite number of gluon exchanges. More generally, after n gluon exchanges, we have the vector

$$\vec{\mathcal{N}}_n = \mathrm{a}_n \vec{\mathcal{N}}^{(\mathrm{a})} + \mathrm{b}_n \vec{\mathcal{N}}^{(\mathrm{b})} + \ldots + \mathrm{x}_n \vec{\mathcal{N}}^{(\mathrm{x})} \,, \tag{4.24}$$

where $\vec{\mathcal{N}}^{(a)}$ through $\vec{\mathcal{N}}^{(x)}$ refer to individual basis vectors in the 24-dimensional basis space. This then evolves according to

$$\vec{\mathcal{N}}_{n+1} = \mathbf{M} \vec{\mathcal{N}}_n \,. \tag{4.25}$$

One can rewrite this expression as the matrix equation

$$\begin{pmatrix} \mathrm{a}_{n+1} \\ \mathrm{b}_{n+1} \\ \cdots \\ \mathrm{x}_{n+1} \end{pmatrix} = \mathbf{M} \begin{pmatrix} \mathrm{a}_{n} \\ \mathrm{b}_{n} \\ \cdots \\ \mathrm{x}_{n} \end{pmatrix}. \tag{4.26}$$

The setup of the computation thus far is general. However, as previously stated, we wish to begin with an initial condition that is the closed four-dipole configuration. This is done by setting the initial condition $\vec{\mathcal{N}}_0 = \vec{\mathcal{N}}^{(a)}$ (the four-dipole configuration). Since we know how to compute additional gluon exchanges from Eq. (4.26), we need to multiply our initial condition $\vec{\mathcal{N}}_0 = \vec{\mathcal{N}}^{(a)}$ by $\mathbf{M}$ n times. This is, however, just a compact way to write all possible configurations with appropriate factors after n gluon exchanges from the starting point of four closed dipoles. The result, after all orders in gluon exchanges, is simply

$$\vec{\mathcal{N}} = \sum_{n=0}^{\infty} \frac{1}{n!} \vec{\mathcal{N}}_n = \sum_{n=0}^{\infty} \frac{1}{n!} \mathbf{M}^n \vec{\mathcal{N}}_0 = e^{\mathbf{M}} \vec{\mathcal{N}}_0 \,. \tag{4.27}$$

Lastly, to compute the expectation value over the product of four-dipole operators, we need to sum over each of the elements of the 24-dimensional column vector with the respective N_c weights of each of the n-tupoles. The four-dipole configuration in this formulation has weight unity. The dipole-dipole-quadrupole configuration comes with $1/N_c$, both quadrupole-quadrupole and dipole-sextupole configurations with $1/N_c^2$, and octupoles with $1/N_c^3$. The sum over the 24-dimensional basis can then be written as the scalar product of the corresponding row vector and the column vector $\vec{\mathcal{N}}$:

$$\mathcal{N} = (1, 1/N_c, .., 1/N_c, 1/N_c^2, ..., 1/N_c^2, 1/N_c^3, ..., 1/N_c^3)\, \vec{\mathcal{N}} \,. \tag{4.28}$$

Here the $\cdots$ denote the different permutations of each of the five configurations in Fig. 4.4. With this expression for $\mathcal{N}$, the combined gluon exchange and tadpole contributions in Eq. (4.17) can be written as

$$\langle DDDD \rangle \;\; = \;\; \mathcal{T}\, \mathcal{N} \,. \tag{4.29}$$

As we noted, analytical expressions for these quantities are too cumbersome to compute. However, with the procedure outlined, they can be computed numerically and utilized to compute the four-particle correlation functions we shall discuss further in the next section.

4.3.4 Abelian limit

We will consider here the computation of the m-dipole expectation value in an Abelianized version of the MV model. In the $U(1)$ theory, the Wilson line again represents the multiple scattering of a charged particle off a classical field [271]:

$$U(\mathbf{x}_\perp) = \mathcal{P} \exp\left(-ie \int dz^+ A^-(\mathbf{x}_\perp, z^+) \right). \tag{4.30}$$

However, here the Wilson line is a scalar valued function, not an $SU(N_c)$ valued matrix as in the non-Abelian case; this simplifies computations enormously. Expectation values of

multiple Wilson lines can be evaluated analogously to the non-Abelian case by first expanding each exponential to second order in the gauge field, followed by replacing all pairwise contractions of the gauge field with the Gaussian expectation value, as in Eq. (4.13):

$$\begin{aligned} e^2\langle A^-(\mathbf{x}_\perp, x^+)A^-(\mathbf{y}_\perp, y^+)\rangle &= e^4\mu^2\delta(x^+ - y^+)\int d^2\mathbf{z}_\perp G(\mathbf{x}_\perp - \mathbf{z}_\perp)G(\mathbf{y}_\perp - \mathbf{z}_\perp) \\ &\equiv \delta(x^+ - y^+)L(\mathbf{x}_\perp, \mathbf{y}_\perp)\,. \end{aligned} \tag{4.31}$$

The dipole expectation value is then

$$\langle D(\mathbf{x}_\perp, \bar{\mathbf{x}}_\perp)\rangle = \langle U(\mathbf{x}_\perp)U^*(\bar{\mathbf{x}}_\perp)\rangle = \exp\left[L(\mathbf{x}_\perp, \bar{\mathbf{x}}_\perp)\right], \tag{4.32}$$

and the correlator of two dipoles can be expressed as

$$\begin{aligned} \langle D(\mathbf{x}_\perp, \bar{\mathbf{x}}_\perp)D(\mathbf{y}_\perp, \bar{\mathbf{y}}_\perp)\rangle &= \langle U(\mathbf{x}_\perp)U^*(\bar{\mathbf{x}}_\perp)U(\mathbf{y}_\perp)U^*(\bar{\mathbf{y}}_\perp)\rangle \\ &= \exp\left(L_{x,\bar{x}} + L_{y,\bar{y}} + L_{x,\bar{y}} + L_{y,\bar{x}} - L_{x,y} - L_{\bar{x},\bar{y}}\right). \end{aligned} \tag{4.33}$$

Similarly, for four dipoles, one obtains

$$\begin{aligned} &\langle D(\mathbf{x}_\perp, \bar{\mathbf{x}}_\perp)D(\mathbf{y}_\perp, \bar{\mathbf{y}}_\perp)D(\mathbf{z}_\perp, \bar{\mathbf{z}}_\perp)D(\mathbf{w}_\perp, \bar{\mathbf{w}}_\perp)\rangle \\ &\quad = \exp\Big(L_{x,\bar{x}} + L_{y,\bar{y}} + L_{z,\bar{z}} + L_{w,\bar{w}} + L_{x,\bar{y}} + L_{x,\bar{z}} + L_{x,\bar{w}} + L_{y,\bar{x}} \\ &\qquad + L_{y,\bar{z}} + L_{y,\bar{w}} + L_{z,\bar{x}} + L_{z,\bar{y}} + L_{z,\bar{w}} + L_{w,\bar{x}} + L_{w,\bar{y}} + L_{w,\bar{z}} \\ &\qquad - L_{x,y} - L_{x,z} - L_{x,w} - L_{y,z} - L_{y,w} - L_{z,w} - L_{\bar{x},\bar{y}} - L_{\bar{x},\bar{z}} \\ &\qquad - L_{\bar{x},\bar{w}} - L_{\bar{y},\bar{z}} - L_{\bar{y},\bar{w}} - L_{\bar{z},\bar{w}}\Big). \end{aligned}$$

Higher-point correlators can be found similarly by summing over all combinations of two-point functions; a negative sign is introduced for combinations of two quarks or two anti-quarks.

4.4 Results

We will now discuss the calculation of m-particle production using the expression in Eq. (4.9). The inputs into this expression include the parameter B_p representing the transverse area of the projectile and the function $L(\mathbf{x}_\perp, \mathbf{y}_\perp)$ that represents the correlation of gauge field configurations arising from a Gaussian distribution of color sources. In the MV model, the quantity $L(\mathbf{x}_\perp, \mathbf{y}_\perp)$ is related to the expectation value of the dipole operator through the expression

$$\langle D(\mathbf{x}_\perp, \mathbf{y}_\perp)\rangle = e^{C_F L(\mathbf{x}_\perp, \mathbf{y}_\perp)}\,. \tag{4.34}$$

In this work, we will use the functional form

$$L(\mathbf{x}_\perp, \mathbf{y}_\perp) = -\frac{(g^2\mu)^2}{16\pi}|\mathbf{x}_\perp - \mathbf{y}_\perp|^2 \log\left(\frac{1}{|\mathbf{x}_\perp - \mathbf{y}_\perp|\Lambda} + e\right). \tag{4.35}$$

For the infrared cutoff in the model, we will use the value $\Lambda = 0.241$ GeV. This value is obtained from parametrizations of the dipole amplitude used in dipole model computations

of structure functions that are fit to the HERA deep inelastic scattering ep data [289, 290]. We have checked that the results are qualitatively unchanged within a physically reasonable range of values of Λ.

Following Ref. [290], a model independent saturation scale is defined through the relation

$$\left\langle D\left(|\mathbf{x}_\perp - \mathbf{y}_\perp|^2 = 2/Q_s^2\right)\right\rangle = e^{-1/2}\,. \tag{4.36}$$

For the remainder of this work, we will specify values of Q_s^2 rather than $(g^2\mu)^2$. We should point out that the mapping between $(g^2\mu)^2$ and Q_s^2 contains an explicit dependence on C_F, as is transparent from Eq. (4.34). When we compare results at various N_c, this scaling with C_F is taken into account. The exception is the $U(1)$ case, where we take $C_F = 4/3$ when relating Q_s^2 to $(g^2\mu)^2$.

We stress that the saturation scale Q_s here is that of the target nucleus. There is no analogous saturation scale of the projectile in the model we are considering. This is a consequence of the simplicity of our treatment of the projectile's constituents, which are comprised of nearly collinear uncorrelated quarks alone. The corresponding average multiplicity per interaction is unity. This can be seen by explicit integration of Eq. (4.9) and can be contrasted with the expression for the multiplicity found in $k_\perp$-factorization [79]

$$N_{\text{mult}} \sim Q_{s,p}^2 S_\perp \log\left(\frac{Q_{s,T}^2}{Q_{s,p}^2}\right), \tag{4.37}$$

where $Q_{s,p}$ and $Q_{s,T}$ are the saturation scales of the projectile and target respectively. The transverse overlap area $S_\perp$ can be identified with the projectile area B_p in our model. The absence of a projectile saturation momentum is the biggest shortcoming of the above framework. The equivalent scale controlling the momenta of the incoming quarks is $1/B_p$, which is held fixed. While the fact that our model and the experimental data seem to both be independent of the multiplicity (at least qualitatively) may be suggestive of a common physical origin, it is far from clear that this will hold for a more realistic model of the projectile.

In what follows, we will primarily plot quantities as a function of the target saturation scale Q_s. The target saturation scale is a function of both Bjorken x and the impact parameter. As discussed above, the multiplicity is a logarithmic function of Q_s. Instead, Q_s is better thought of as a proxy for the energy of the collision. In the CGC picture of high energy QCD, Q_s grows with the center-of-mass energy.

As a final remark, we stress that we only expect to make a qualitative comparison with data. In addition to the shortcomings of the model addressed above, our final state distributions are for quarks and not for hadrons. Any correlations computed in this model will be reduced through a variety of effects, such as fragmentation, and quantum evolution of parton distributions. They therefore provide an upper limit for azimuthal correlations in initial state frameworks.

4.4.1 Multiparticle azimuthal cumulants and harmonics

Multiparticle correlations carry a wealth of information on the dynamics of the colliding system. For reviews, see for instance, Refs. [291, 292]. Azimuthal correlations, in particular,

are sensitive measures of collective dynamics in heavy-ion collisions. For systems undergoing collective flow, one can define the nth-Fourier harmonic coefficients

$$v_n = \left\langle e^{in(\phi - \Psi_R)} \right\rangle , \tag{4.38}$$

where ϕ is the azimuthal angle of a produced particle and Ψ_R is the angle of a reaction plane determined by the collective geometry of particles produced in the collision. The determination of a suitable reaction plane may be sensitive to a variety of so-called *non-flow* contributions such as resonance decays, to give one example. The effect of these *non-flow* correlations can be minimized using cumulant method [293], which is now widely used in experimental studies of multiparticle correlations. Two- and four-particle cumulants are defined as

$$c_n\{2\} = \langle e^{in(\phi_1 - \phi_2)} \rangle \tag{4.39}$$

$$c_n\{4\} = \langle e^{in(\phi_1 + \phi_2 - \phi_3 - \phi_4)} \rangle - 2\langle e^{in(\phi_1 - \phi_2)} \rangle^2 , \tag{4.40}$$

where the average $\langle \cdots \rangle$ in $c_n\{m\}$ is the average of all possible combinations of m particles in an event, followed by an averaging over all events [293, 294, 295].

The cumulants above can be expressed in terms of the m-particle inclusive distribution by first defining a quantity $\kappa_n\{m\}$ as

$$\kappa_n\{m\} \equiv \int \prod_{i=1}^{m} d^2\mathbf{p_i}\, e^{in(\phi_1 + \cdots + \phi_{m/2-1} - \phi_{m/2} - \cdots - \phi_m)} \left\langle \frac{d^m N}{\prod_{i=1}^{m} d^2\mathbf{p_i}} \right\rangle , \tag{4.41}$$

corresponding to the n^{th} harmonic of the m-particle distribution. The averages can be written as a ratio of the n^{th} azimuthal angle moment of the m-particle inclusive distribution normalized by the zeroth moment (the m-particle inclusive multiplicity):

$$\left\langle e^{in(\phi_1 + \cdots + \phi_{m/2-1} - \phi_{m/2} - \cdots \phi_m)} \right\rangle = \frac{\kappa_n\{m\}}{\kappa_0\{m\}} . \tag{4.42}$$

Fourier coefficients are then defined from the above cumulants as

$$v_n\{2\} = (c_n\{2\})^{1/2} , \tag{4.43}$$

$$v_n\{4\} = (-c_n\{4\})^{1/4} . \tag{4.44}$$

The motivation for the above definitions becomes transparent under the assumption that the m-particle distribution factorizes into a product of single-inclusive distributions correlated with each other only through the event plane angle. This is indeed what one would expect if the system undergoes hydrodynamic flow. In such a framework, the two-particle Fourier harmonic $v_n\{2\}$ would, as above, be the square root of the corresponding two-particle azimuthal angle cumulant, the four-particle Fourier harmonic $v_n\{4\}$, the fourth root of the four particle azimuthal angle cumulant, and so on. The negative sign in the latter case is appropriate because one anticipates intrinsic four-particle angular correlations to be subdominant relative to the square of the two-particle cumulant in Eq. (4.40). While the observation of m-particle Fourier harmonics is suggestive of some form of collective behavior,

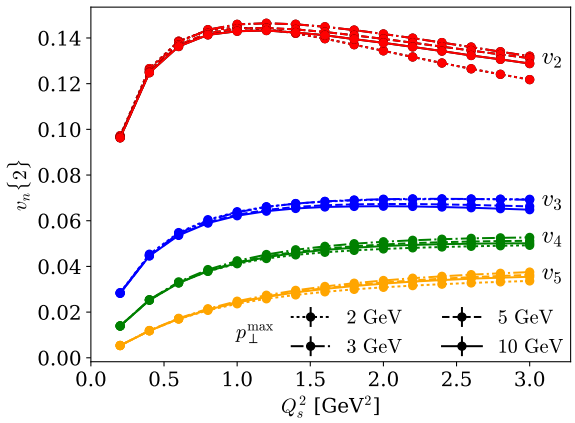

Figure 4.6: Integrated $v_2\{2\}$ as a function of the maximum integrated momenta, $p_\perp^{\max}$, for various Fourier harmonic n, as a function of Q_s^2.

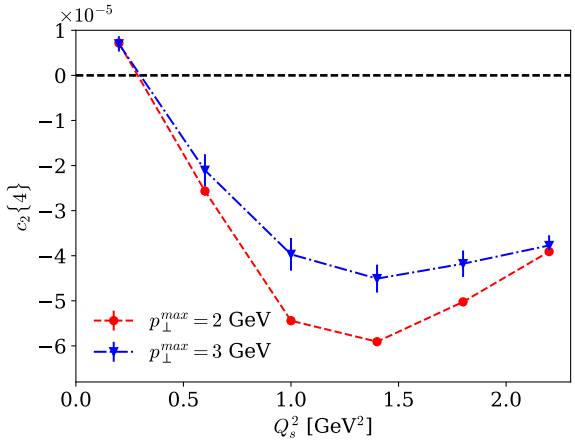

Figure 4.7: $c_2\{4\}$ integrated to $p_\perp^{max} = 2, 3$ GeV as a function of Q_s^2.

we will argue instead that it can result from any physical mechanism where higher cumulants are suppressed relative to the mean and variance of the distribution.

In Fig. 4.6, we show $v_n\{2\}$ as a function of Q_s^2 for Fourier harmonics $n = 2, 3, 4, 5$. For each harmonic, we studied the sensitivity of the result for multiple values of the maximum integrated transverse momentum ($p_\perp^{\max}$). We observe that even for $p_\perp^{\max} = 2$ GeV, the result is insensitive to the high momentum cutoff. Due to the small x evolution of partons in the target, its saturation momentum Q_s will increase with the increasing center-of-mass energy of the collision. Since this is the only energy dependent variable in our framework, our result indicates that the $v_n\{2\}$ are only weakly dependent on the energy. We also observe that the $v_n\{2\}$ have a clear hierarchy with n, similar to what is seen in experiment [296].

The four-particle cumulant $c_2\{4\}$ is shown as a function of Q_s^2 in Fig. 4.7. We clearly see that by $Q_s^2 = 0.3$ GeV^2 that there is a change in the sign of the signal, from positive to negative values, resulting in a real $v_2\{4\} = (-c_2\{4\})^{1/4}$; this is plotted in Fig. 4.8. The magnitude of the signal only weakly depends on the maximum integrated momentum $p_\perp^{\max}$.

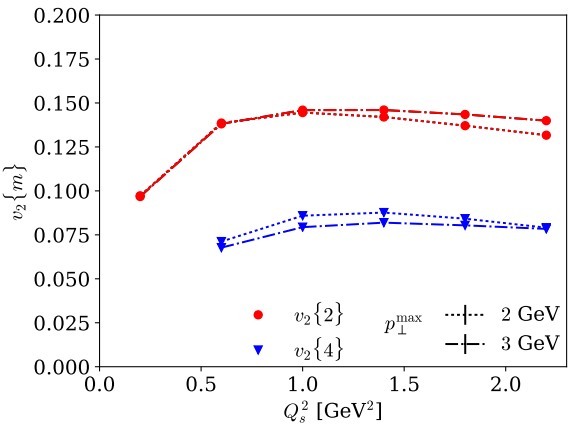

Figure 4.8: $v_2\{4\}$ integrated to $p_\perp^{max} = 2, 3$ GeV as a function of Q_s^2.

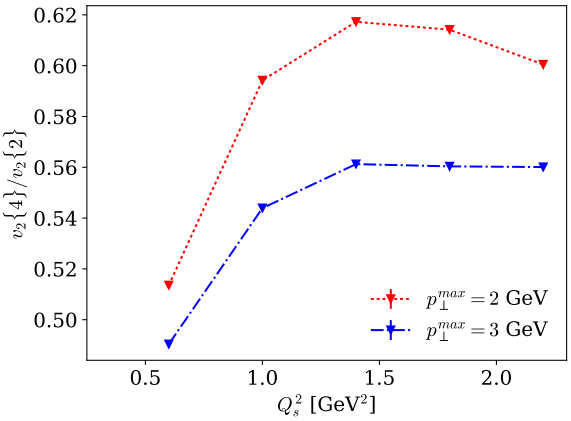

Figure 4.9: The ratio of $v_2\{4\}/v_2\{2\}$ as a function of Q_s^2, for two values for $p_\perp$.

The relatively weak variation in the signal above $Q_s^2 \sim 1$ GeV^2 is in qualitative agreement with the experimental findings on the center-of-mass energy dependence of the four-particle cumulant [297, 298, 295, 299, 300].

As we noted previously, a positive definite value for $v_2\{4\}$ is natural in hydrodynamic models. However, we know of only two 3+1-dimensional numerical hydrodynamic computations of $v_2\{4\}$ in pA collisions [301, 302]. In the case of Ref. [302], while some of the systematics of pA collisions is reproduced, the model is unable to reproduce similar event-by-event systematics of flow in AA collisions.

There also exist qualitative arguments for positive definite $v_2\{4\}$ [294] in an initial state "color domain" model [303, 304, 305, 306, 307]. Though this model provides an intuitive picture of how multiparticle azimuthal cumulants may be generated in an initial state framework, it is unclear how the oriented background color-electric fields are created from first principles [268].

In Fig. 4.9, we plot the ratio of the four- to two-particle integrated $v_2\{m\}$. For both values of $p_\perp^{max}$, this ratio rises with Q_s^2 and saturates above $Q_s^2 \sim 1$ GeV^2. The values obtained

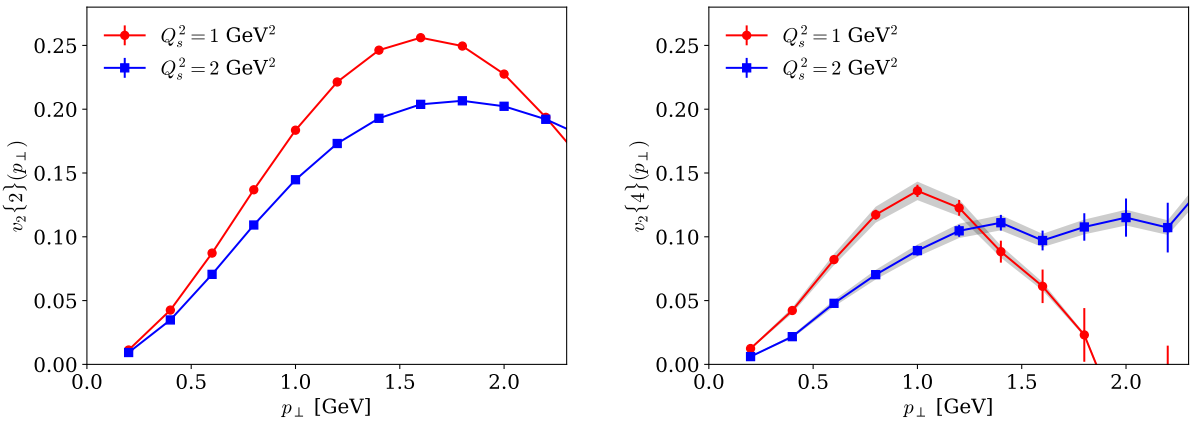

Figure 4.10: The Fourier harmonics $v_2\{2\}$ and $v_2\{4\}$ as a function of $p_\perp$ for two values of Q_s^2.

$v_2\{4\}/v_2\{2\} \sim 0.5$–$0.6$ are remarkably close to those measured by the CMS Collaboration that shows this quantity increasing with centrality from ~ 0.675 to 0.775 [297, 308]. A detailed study of this ratio, and other such ratios, and their centrality dependence, in various models of initial state spatial eccentricities, can be found in Ref. [308].

We now study the multiparticle cumulants differentially in transverse momentum. If we keep the transverse momentum of one particle in Eq. (4.41) fixed and integrate over the momenta of the remaining $m-1$ particles, the two- and four-particle differential Fourier harmonics are defined as [297]

$$v_2\{2\}(p_\perp) = \frac{d_2\{2\}(p_\perp)}{(c_2\{2\})^{1/2}}, \qquad v_2\{4\}(p_\perp) = \frac{-d_2\{4\}(p_\perp)}{(-c_2\{4\})^{3/4}}, \tag{4.45}$$

where $d_n\{m\}$ are the differential analogs of $c_n\{m\}$. Figure 4.10 shows $v_2\{2\}$ (left) and $v_2\{4\}$ (right) as a function of $p_\perp$ for two representative values of the saturation scale $Q_s^2 = 1$ and 2 GeV^2. Note that while the results are differential in $p_\perp$ for one of the particles the remaining particles are integrated up to a $p_\perp^{\max} = 3$ GeV. We note that for $Q_s^2 = 2$ GeV^2 our results exhibit behavior similar to that seen in the experimental p-Pb data data [297, 309]. We know of one other theory computation of $v_2\{4\}(p_\perp)$ in small systems [310].

Event-by-event fluctuations of v_n with $v_{n'}$ for $n \neq n'$ can be captured by symmetric cumulants [311] defined as

$$\mathrm{SC}(n,n') = \langle e^{i(n\phi_1 + n'\phi_2 - n\phi_3 - n'\phi_4)} \rangle - \langle e^{in(\phi_1-\phi_3)} \rangle \langle e^{in'(\phi_2-\phi_4)} \rangle . \tag{4.46}$$

These mixed harmonic angular expectation values are defined analogously to those in Eq. (4.41) and Eq. (4.42). They were originally introduced in hydrodynamic frameworks as a measure of the nonlinear response of the initial geometry of the system [311]. These have been studied mainly in the context of heavy-ion collisions [312]. In these heavy-ion systems, the symmetric cumulants describe how correlations between the initial moments of the eccentricities, which are driven by the overlap geometry and thus the centrality of the collision, are carried to the final state. An example of symmetric cumulants are the correlations between the v_2 and v_3 azimuthal harmonics, denoted by $\mathrm{SC}(2,3)$. From geometrical considerations, there should

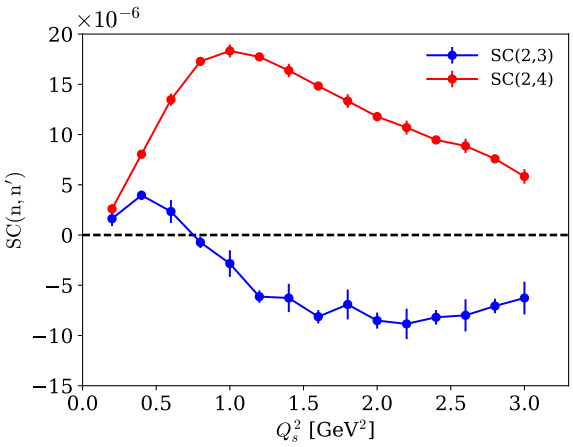

Figure 4.11: Four-particle symmetric cumulants defined in Eq. (4.46), as a function of Q_s^2.

be an anti-correlation between the initial ellipticity and the triangularity. When converted to correlations of final state momentum anisotropies, this results in a negative $\mathrm{SC}(2,3)$. Studies of the symmetric cumulants $\mathrm{SC}(2,3)$ and $\mathrm{SC}(2,4)$ for heavy-ion collisions have been carried out in hydrodynamic simulations [313, 314] and in a hadronic transport model [315].

However, in small systems, this picture should not hold. The initial eccentricities are not believed to be strongly centrality driven, but instead are most likely in response to sub-nucleonic fluctuations [316]. We will touch on the topic of sub-nucleon fluctuations in the next section. In our model, we include sub-nucleon scale fluctuations in sampling the positions of the quarks in the projectile given through our Gaussian Wigner function, Eq. (4.4). Our results for $\mathrm{SC}(2,3)$ and $\mathrm{SC}(2,4)$ are shown in Fig. 4.11 as a function of $Q_{s,T}^2$. We see that $\mathrm{SC}(2,3)$ is negative by $Q_{s,T} = 1$ GeV while $\mathrm{SC}(2,4)$ is positive for all $Q_{s,T}$. This is in qualitative agreement with the data [317]. Our results demonstrate clearly that such patterns are not unique to an interpretation requiring hydrodynamic flow. Results from hydrodynamic computations for these cumulants in light-heavy ion collisions are not yet available. In Fig. 4.12, we show predictions for the behavior of $\mathrm{SC}(2,5)$, $\mathrm{SC}(3,4)$, and $\mathrm{SC}(3,5)$. Results for these symmetric cumulants, for heavy-ion collisions alone, were shown at the Quark Matter 2017 conference [318]. Our results for these cumulants agree qualitatively the results presented. We are unaware of any other theory predictions for these cumulants in light-heavy ion collisions. While not their designated purpose, symmetric cumulants in small systems may be an effective way to access information on initial state sub-nucleon fluctuations.

It is also interesting to consider coherent multiple scattering in the Abelian limit of this model; introduced in Sec. 4.3.4. In this case, the Wilson lines are not matrices in color space, but simply path ordered exponentials [271]. The product of dipoles in Eq. (4.9) is significantly simpler to compute (see Appendix G for explicit expressions), enabling one to extract $v_2\{6\}$ and $v_2\{8\}$ from the corresponding cumulants [293, 295]. Our results, shown in Fig. 4.13, demonstrate that $v_2\{2\} > v_2\{4\} \approx v_2\{6\} \approx v_2\{8\}$, as also seen in the LHC data on multiparticle harmonics [295, 300].

The fact that this behavior is reproduced in a simple initial state model is a proof of principle that it is not unique to interpretations of collectivity arising from the hydrodynamic response of the system to the n-th moments of m particle spatial eccentricities [301, 302, 319,

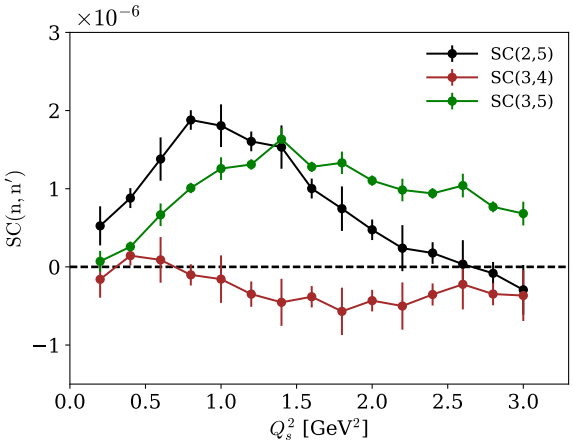

Figure 4.12: Four-particle symmetric cumulants defined in Eq. (4.46) as a function of Q_s^2.

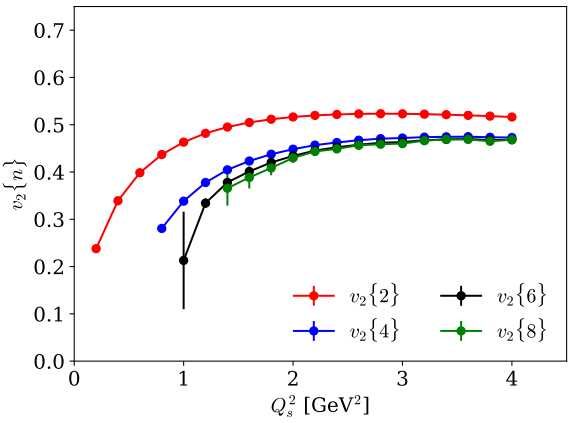

Figure 4.13: Two, four, six and eight particle Fourier harmonics for coherent multiple scattering off Abelian fields plotted as a function of $Q_{s,T}^2$.

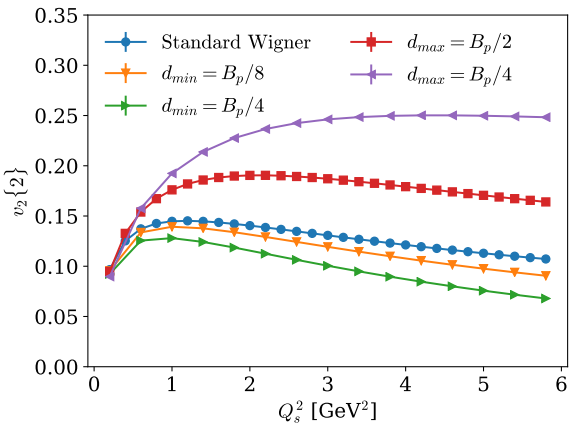

Figure 4.14: $v_2\{2\}$ with minimal and maximal separations between quarks from the projectile. The "standard Wigner" curve imposes no such constraint. The orange and green curves show what happens when the quarks in the projectile are required to be separated by at least d_{min}. The red and purple curves show the result when the quarks are required to be confined to a distance of d_{max} from each other.

308]. For a recent review on hydrodynamic collectivity and relevant references, see [320]. Our results do not necessarily mean that an initial state interpretation of the data is favored. We instead conclude that the $v_n\{m\}$ measurements alone are insufficient to unambiguously distinguish between initial and final state approaches.

4.5 Detailed systematics of the results

4.5.1 Role of the projectile

It is expected that sub-nucleon scale fluctuations play an important role in small systems; hydrodynamic computations including such fluctuations have been performed for pA collisions [65]. Thus it is also interesting to ask what similarities our model bears to a constituent quark model based picture. To mock up this effect, we introduce a hard distance cutoff (either minimum or maximum) between all quarks in the amplitude and similarly between all anti-quarks in the complex-conjugate amplitude. This is in addition to the Gaussian sampling of the quark positions from the Wigner function introduced in Eq. (4.4).

The effect of such a cutoff on $v_2\{2\}$ is shown in Fig. 4.14. Starting with the standard Wigner function in Eq. (4.4) as a reference, we see that by introducing a minimum distance criteria (separating the quarks by at least a distance of $d_{min} = B_p/8$ or $B_p/4$) the correlations decrease. This is to be expected because forcing the transverse positions of the quarks to be farther away from each other ensures that they are less likely to interact with the same color domain in the target. We would then expect, on the same grounds, that if we confined the quarks to be at most a distance $d_{max} = B_p/4$ or $B_p/2$ apart, we would see an increase in the strength of the correlation. This expectation is confirmed by the results shown in Fig. 4.14.

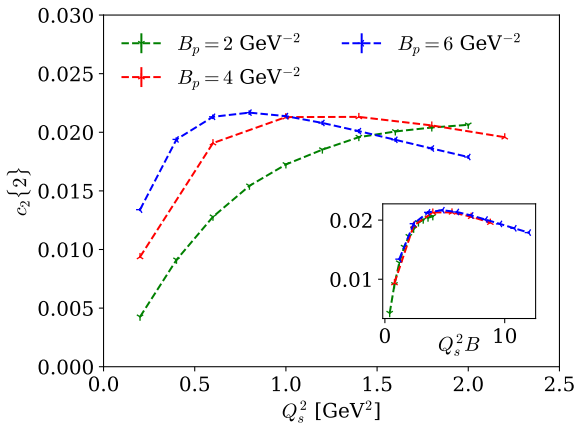

Figure 4.15: The two-particle cumulant $c_2\{2\}$ plotted as a function of Q_s^2 for different values of B_p, the mean transverse area of the projectile. Inset: Same data plotted as a function of the dimensionless ratio $Q_s^2 B_p$, showing the independence of $Q_s^2 B_p$.

4.5.2 $Q_s^2 B_p$ dependence

In our model, the parameter B_p controls the mean transverse area of the projectile, and therefore the transverse overlap area of the scattering off the target. The scale $1/Q_s^2$ sets the scale for the size of color domains in the target. Therefore the dimensionless product $Q_s^2 B_p$ can be interpreted as the number of domains in the target that overlap the projectile. In fact, this dimensionless parameter controls the strength of all correlations. Fig. 4.15 shows $c_2\{2\}$ for three values of B_p for $p_\perp^{\max} = 3$ GeV; note that $B_p = 4$ GeV^{-2} is used elsewhere in this work. The inset in Fig. 4.15 shows the same quantity plotted as a function of the dimensionless scale $Q_s^2 B_p$ demonstrating that all results fall onto a universal curve, as they must.

One might expect that the strength of the correlation should fall with the number of domains $1/(Q_s^2 B_p)$, which is a feature of independent cluster models. However, a falloff that goes like $1/(Q_s^2 B_p)$ is not seen in the results presented above. The reason is that there is another scale, $p_\perp^{\max}$, which controls the maximal momentum kick from the target to the probe. The inverse of $p_\perp^{\max}$ is therefore the smallest distance in the target resolved by the probe. One can therefore construct two dimensionless combinations $Q_s^2 B_p$ and $Q_s^2/(p_\perp^{\max})^2$; the dependence of our results on the number of color domains also depends on what $Q_s^2/(p_\perp^{\max})^2$ is.

For $(p_\perp^{\max})^2 \gtrsim Q_s^2$, the probe resolves a transverse area in the target that is on the order or smaller than the size of a color domain. Because the probe can resolve the structure within individual domains, we expect to see a falloff in correlations to go approximately as $1/(Q_s^2 B_p)$. Fig. 4.16 shows $c_2\{2\}$ for $p_\perp^{\max} = 10, 20, 40$ GeV, all of which satisfy the scaling form $(Q_s^2 B_p)^{-0.95}$ at large Q_s^2. On the other hand, for $(p_\perp^{\max})^2 \leq Q_s^2$, the probe only resolves transverse sizes larger than the typical domain size. For these smaller values of $p_\perp^{\max}$, increasing $Q_s^2 B_p$, and therefore the number of color domains, does not change the signal since the probe cannot resolve the change in the number of color domains. Fig. 4.16 shows that for $p_\perp^{\max} = 3, 5$ GeV we see a rather modest falloff with the number of domains $(Q_s^2 B_p)^{-0.18}$.

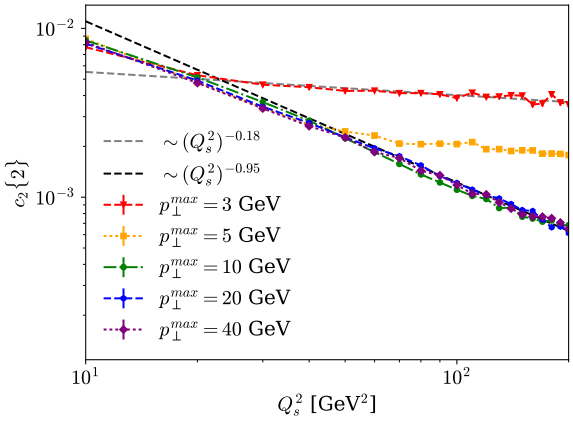

Figure 4.16: Two-particle cumulant $c_2\{2\}$ for various $p_\perp^{max}$ for large values of Q_s^2 for fixed $B_p = 4$ GeV^{-2}. For $p_\perp^{\max} \leq Q_s$, only a weak dependence on $Q_s^2 B_p$ is seen. For larger $p_\perp^{max}$, we can see a falloff in the value of the cumulant that scales approximately with the number of color domains, as $\sim 1/Q_s^2 B_p$.

Our results in Fig. 4.16 suggest more generally that for small values of $p_\perp^{\max}$ relative to the saturation scale Q_s azimuthal cumulants in initial state models are weakly dependent on the number of clusters. This independence of Fourier harmonics on the number of clusters has been interpreted previously as occurring due to the collective response of the system [321]. While coherent multiple scattering may be collective, it is not a final state effect in pA collisions; the interaction with the target is instantaneous and the scattered quarks do not subsequently rescatter.

4.5.3 N_c dependence

In Ref. [322], we showed that an Abelianized version of our model demonstrates the systematics often attributed to collective behavior, $v_2\{4\} \approx v_2\{6\} \approx v_2\{8\}$. Given this finding, it is natural (and of intrinsic interest) to determine the N_c dependence of the two- and four-particle azimuthal correlations. The dependence of $v_2\{2\}(p_\perp)$ for $N_c = 2, 3$ was discussed previously in Ref. [268]. In the left panel of Fig. 4.17, we plot the dependence of integrated $v_2\{2\}$ (up to a $p_\perp^{\max} = 2$ GeV) as a function of Q_s^2 for the Abelian ($N_c = 1$) case and for $N_c = 2 - 5$. For large Q_s^2, we observe a convergence of the results for $N_c \geq 3$. In the right panel of Fig. 4.17, we plot the N_c dependence of $v_2\{4\}$ as a function of Q_s^2. When $v_2\{4\}$ is real and large, we expect the second term in Eq. (4.40) for the four-particle cumulant to dominate. This should then give $v_2\{4\} \sim 1/N_c$. We see from Fig. 4.17 that $N_c\, v_2\{4\}$ begins to converge for $N_c \geq 3$; however, due to limited statistics, the error bars are large.

We previously reported in Ref. [322] on results for the symmetric cumulants for SC$(2,3)$ and SC$(2,4)$ which were in qualitative agreement with experimental results [317]. In Fig. 4.18, we show the N_c dependence of the symmetric cumulants. We find that these symmetric cumulants are extremely sensitive to N_c. (We have chosen here $p_\perp^{\max} = 2$ GeV.) For the Abelian case, the result is an order of magnitude larger than the finite N_c results. Further, SC$(2,3)$ is positive in the Abelian case, which is not observed in any experimental observations.

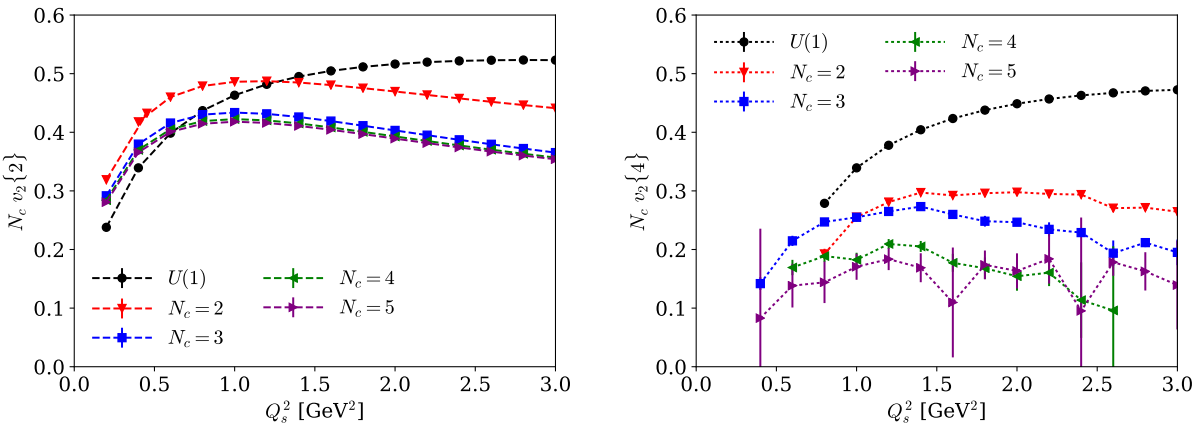

Figure 4.17: The N_c dependence of $v_2\{2\}$ (left panel) and $v_2\{4\}$ (right panel).

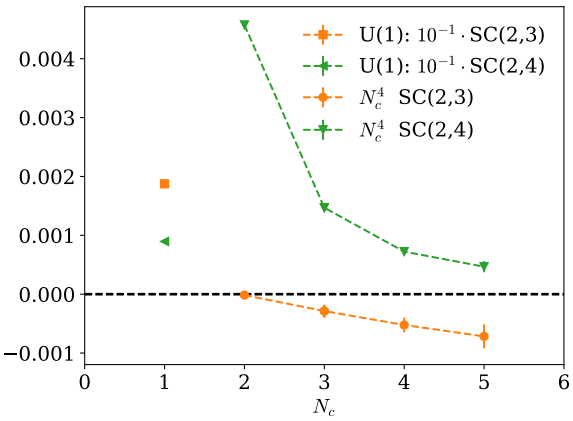

Figure 4.18: N_c dependence of the symmetric cumulants SC(2,3) and SC(2,4) for Q_s^2 = 1 GeV^2.

Interestingly, within the limited number of observables that we have studied, this appears to be the only place where the Abelian version of our model qualitatively differs from the non-Abelian results.

One may infer that there is something specific to the non-Abelian nature of coherent scattering that drives $\mathrm{SC}(2,3)$ to become negative. Going to $N_c = 2$, we find that $\mathrm{SC}(2,3)$ is identically zero. This is not surprising, as for $N_c = 2$, all odd harmonics are identically zero. This is analogous to the absence of odd harmonics for gluons scattering off a target [62]. The underlying reason is that $SU(2)$ representations are real, regardless of whether they are in the fundamental or the in adjoint. For $SU(3)$, only the adjoint representation is real. Thus one expects qualitatively different results for even-odd cumulants for $N_c \geq 3$ relative to the Abelian model and for $N_c = 2$.

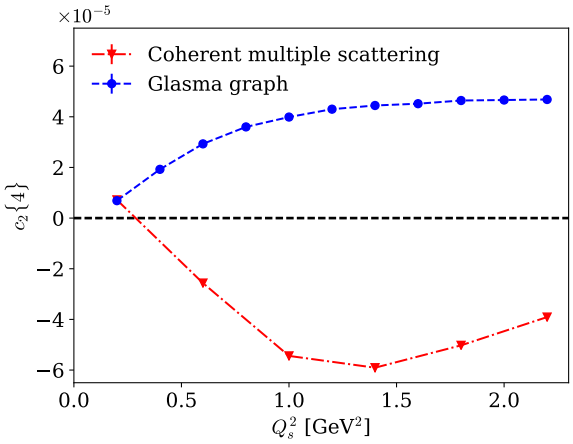

Figure 4.19: Comparison of $c_2\{4\}$ in the model introduced in Sec. 4.3, for coherent multiple scattering compared to the result, given in Eq. (G.11), from the Glasma graph approximation.

4.5.4 Comparison to Glasma graphs

To elucidate the mechanism responsible for the observed negativity of $c_2\{4\}$ for our model, we compare this result to that from the Glasma graph approximation. In this Glasma graph approximation, which is applicable for $p_\perp > Q_s$, the Wilson lines are expanded out to lowest nontrivial order in the gauge fields. The Glasma graph approximation is reviewed in the Appendix, where we also compute the four-dipole correlation function in this approximation. This approximation was used previously to successfully describe two-particle correlations [83, 270, 84, 85, 86, 87, 88], especially near side "ridge" correlations.

Fig. 4.19 shows a comparison of $c_2\{4\}$ in the Glasma graph approximation to our result, which includes all order contributions from the Wilson lines. It is clear that coherent multiple scattering in the MV model computation for $c_2\{4\}$ drives it to become negative. In contrast, the Glasma graph approximation to this full result is always positive.

It is interesting to explore further the physics underlying this striking result. Intrinsic n-particle correlations in the Glasma graph approximation are large. Indeed, the strength of the correlated piece in this distribution relative to the disconnected product of n single-particle distributions is the same for all n; this is close to that of an n-particle Bose distribution [323]. Our results suggest that coherent multiple scattering depletes these higher-point intrinsic correlations. In Eq. (4.40) for instance, this would lead to the second term (the square of $c_2\{2\}$) to dominating over the first term, which comes from intrinsic four-particle correlations.

4.5.5 Rapidity dependence

Before we conclude our discussion of features of the model, it is appropriate to discuss how rapidity correlations manifest themselves in this framework. Since long range rapidity correlations are an essential feature of the experimentally observed ridge-like correlations, it is important to determine whether such correlations are present in this framework. This is particularly so since the hybrid formalism employed in analytical studies of such multiparticle correlations [273, 324, 325] is valid in the forward rapidity region. More precisely, x in the

projectile should be relatively large, with typical values for *large-x* taken to be $x \geq 0.01$. However this does not imply that the resulting correlations are short-range in rapidity. We will show this explicitly by reintroducing rapidity dependence into the single-particle and multi-particle distributions.

We consider an eikonal quark in the projectile traveling in the z^+ direction with initial momentum $k^\mu = (k^+, 0, \mathbf{k}_\perp = \mathbf{0})$ and final momentum $p^\mu = (p^+, 0, \mathbf{p}_\perp)$ after its scattering off the target. In the hybrid framework, the differential multiplicity of the scattered quark with the final state of momentum $\mathbf{p} \equiv (p^+, \mathbf{p}_\perp)$ is given as

$$\frac{dN^{qA\to q+X}}{d^3\mathbf{p}} \equiv \frac{dN^{qA\to q+X}}{dp^+ d^2\mathbf{p}_\perp} = \delta(p^+ - k^+)\frac{dN^{qA\to q+X}}{d^2\mathbf{p}_\perp}\,. \tag{4.47}$$

The above result can be worked out following the formalism of Ref. [273]. (Note though that in Ref. [273], the quark is traveling in the z^- direction.) The expression for $dN/d^2\mathbf{p}_\perp$ is given by Eq. (4.6), where averaging over the target we previously defined is implicitly assumed. Therefore, for single-quark scattering the distribution is a delta function in $\delta(p^+ - k^+)$, which is simply a consequence of the eikonal approximation.

The single inclusive distribution of quarks produced in pA collisions is obtained by convoluting the above expression with the quark parton distribution, which represents the probability of finding a quark in the proton wavefunction:

$$\frac{dN^{pA\to q+X}}{d^3\mathbf{p}} = \int dx_q f(x_q)\frac{dN^{qA\to q+X}}{d^3\mathbf{p}}\,. \tag{4.48}$$

To obtain the single inclusive distribution of hadrons, this expression has to further convoluted with a fragmentation function. This will quantitatively modify the rapidity dependence but will not modify it qualitatively. We will therefore not further consider this point.

The longitudinal momentum carried by the initial quark is $k^+ = \frac{\sqrt{s}}{\sqrt{2}}x_q$, where x_q is the quark's momentum fraction. Likewise, the longitudinal momentum of the final-state quark can be written in terms of its rapidity as $p^+ = \frac{p_\perp}{\sqrt{2}}e^y$. Substituting Eq. (4.47) into Eq. (4.48), we then obtain

$$\frac{dN^{pA\to q+X}}{dyd^2\mathbf{p}_\perp} = x'_q f(x'_q)\frac{dN^{qA\to q+X}}{d^2\mathbf{p}_\perp}\,, \tag{4.49}$$

where x'_q has been set by the δ-function to be

$$x'_q = \frac{p_\perp}{\sqrt{s}}e^y\,. \tag{4.50}$$

In Fig. 4.20a, we show the single-particle inclusive quark distribution using the NNPDF NLO singlet PDF at $Q^2 = 9$ GeV^2 [326]. For $p_\perp = 3$ GeV and $\sqrt{s} = 5.02$ TeV, a value of $x_q = 0.01$ corresponds to a rapidity of $y \simeq 2.8$. Thus, while strictly speaking, our approach is valid for $y \geq 2.8$, we can see that the particle production does extend over a wide range in rapidity and is not peaked in the forward direction.

This can be extended to multiparticle production in the same fashion. For instance, for two particles, we would obtain

$$\frac{d^2N^{pA\to q+X}}{dy_1 d^2\mathbf{p}_{\mathbf{1},\perp} dy_2 d^2\mathbf{p}_{\mathbf{2},\perp}} = x'_{q1} f(x'_{q1}) x'_{q2} f(x'_{q2})\frac{d^2N^{qA\to q+X}}{d^2\mathbf{p}_{\mathbf{1},\perp} d^2\mathbf{p}_{\mathbf{2},\perp}}\,. \tag{4.51}$$

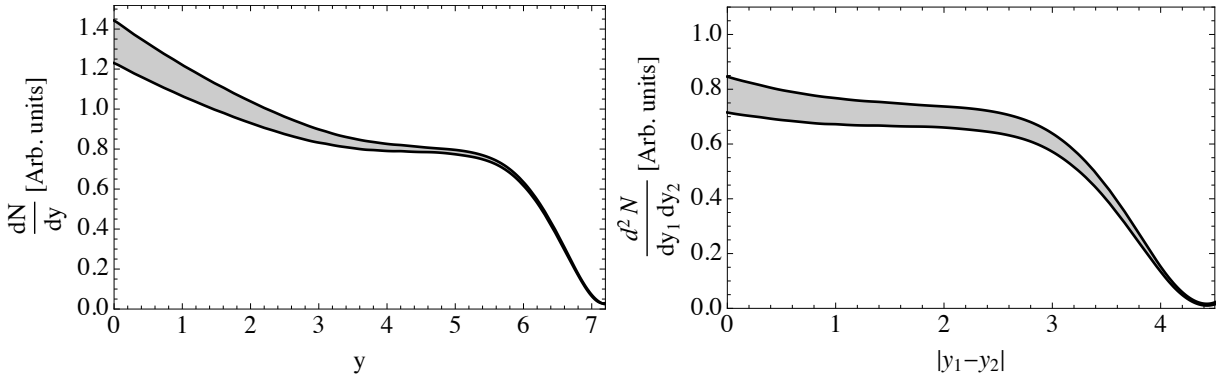

(a) Single particle distribution dN/dy in arbitrary units as a function of rapidity for $p_\perp$ = 3 GeV and $\sqrt{s}$ = 5.02 TeV.

(b) Two-particle distribution d^2N/dy_1dy_2 in arbitrary units as a function of $\Delta y = |y_1 - y_2|$ for $y_1 \simeq 2.8$, which corresponds to $x'_{q1} = 0.01$ in the projectile.

Figure 4.20

This two-particle distribution is shown in Fig. 4.20b. The rapidity of the first quark is fixed at the edge of where the hybrid approach works. We see that the correlation persists out to a Δy of 3 to 4 units as the rapidity of the second quark is varied.

We conclude by pointing out that when the observed correlations are long range in rapidity; a feature we have neglected any discussion of in our model. The factorized form of the rapidity dependence in Eq. (4.51) is then suggestive that the resulting $v_n\{m\}$ will be weakly dependent, or perhaps even constant, as a function of rapidity. We can test this conjecture. In the "hybrid" framework, valid in the forward region, we should consider quarks with relatively large x_q (usually taken to be $x_q \geq 0.01$). These large x_q quarks are most naturally taken to be valence quarks, whereas long-range correlations necessarily probe smaller x_q quarks. This does not preclude long-range correlations in our model. In order to include the quark rapidity dependence, we consider the single quark distribution in Eq. (4.6) and convolve it with the quark distribution function $f(x_q)$ to write (in terms of the rapidity y and quark transverse momentum $p_\perp$) [327]

$$\frac{dN^{pA\to q+X}}{dyd^2\mathbf{p}_\perp} = x_q f(x_q) \frac{dN^{qA\to q+X}}{d^2\mathbf{p}_\perp}\,; \qquad x_q = \frac{p_\perp}{\sqrt{s}} e^y\,. \tag{4.52}$$

For our results, we will employ the quark distribution functions of the NNPDF collaboration [326]. While its straightforward to possible include the fragmentation of the final state quarks into hadrons, this will not qualitatively change the rapidity dependence.

Our computation for the rapidity dependence are shown in Fig. 4.21. We first consider a valence quark at $y = 5.1$; at the top LHC energy of $\sqrt{s} = 5.02$ TeV, this corresponds to an $x_q = 0.1$. Then considering a separation in rapidity of 4 units, which corresponds to a second quark with $x_q \simeq 0.002$, we clearly see that there is no quantitative difference with our previous result that neglected any rapidity dependence. Since it is unlikely a valence quark at this small x can be found in the proton, we can also consider a valence quark with larger $x_q \simeq 0.01$, corresponding to $y = 2.8$. There is no difference in the observed correlations for the two rapidity gaps considered. It is also interesting to consider correlations between valence

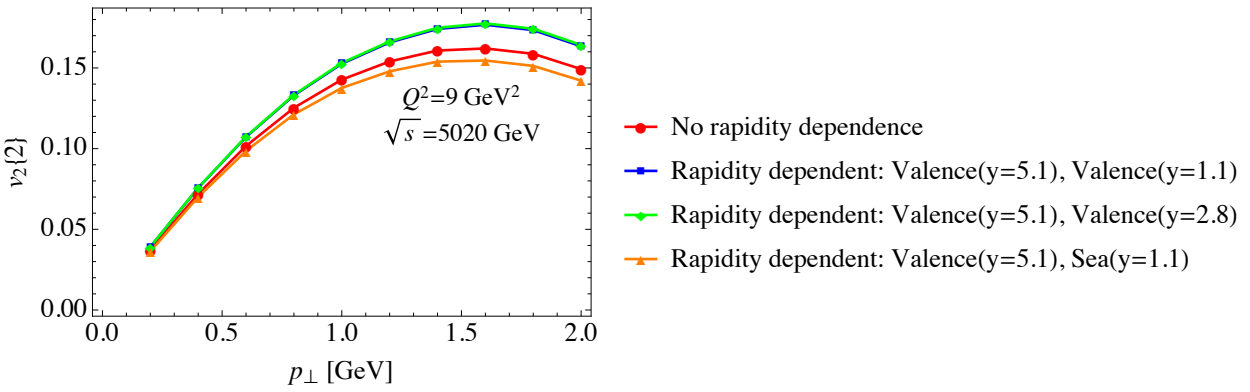

Figure 4.21: Two-particle second Fourier harmonic $v_2\{2\}$ as a function of the momentum of one of the quarks both with and without rapidity dependence introduced via convolution with quark distributions.

and sea quarks. For four-particle correlations, if one does not consider correlations with and amongst gluons, this is the most likely scenario. Fig. 4.21 shows that all the differences are only quantitative, not qualitative. This is because when one takes the ratio of distributions to compute $c_2\{2\}$ (see Eq. (4.39)), the rapidity dependence in our model all but disappears.

4.6 Conclusions

In this chapter, we have discussed the parton model framework for multiparticle correlations that was first presented in Ref. [322, 327, 328]. In this model, collinear partons that are localized in a transverse area B_p in the projectile, scatter off color domains of size $1/Q_s^2$ in the target. The building blocks in this framework are dipole correlators. For a quark projectile, these correspond to a color trace over a path ordered lightlike Wilson line of target fields at a given transverse spatial position in the amplitude multiplied by its adjoint in the complex-conjugate amplitude, normalized by the number of colors, N_c. The azimuthal cumulants of n-particles are proportional to the expectation value over the product of n-dipole correlators. We discussed at length the procedure to compute the expectation value of four-dipole correlators. Gluon exchanges among the dipoles generate distinct quadrupole, sextupole, and octupole topologies and the permutations of their spatial positions, generating a 24 by 24 matrix, that can be exponentiated to determine the expectation value of four-dipole correlators. Our procedure can be extended straightforwardly to compute expectation values of products of an arbitrary number of dipole operators.

We presented results for $v_n\{2\}$ as a function of Q_s^2, demonstrating a clear hierarchy in the $n = 2, 3, 4, 5$ harmonics. These results are only weakly dependent on $p_\perp^{\max}$ upper limit in the integrals. All the harmonics show only a weak dependence on Q_s^2. Since Q_s^2 in the CGC framework increases with increasing energy, and centrality, our results are only weakly dependent on these. Note further that our results, by construction, are independent of the multiplicity. These results for $v_n\{2\}$ exhibit the qualitative features of the data seen in light-heavy ion collisions at RHIC and the LHC.

We next presented results for $c_2\{4\}$ as a function of Q_s^2 for two different values of $p_\perp^{\max}$. For both these values, $c_2\{4\}$ changes sign around $Q_s^2 = 0.3$ GeV^2 and becomes increasingly negative before appearing to saturate. For large Q_s^2, the results are sensitive to $p_\perp^{\max}$. The negative value of $c_2\{4\}$ corresponds to a real $v_2\{4\}$. We computed the ratio of $v_2\{4\}/v_2\{2\}$. In hydrodynamic models, such ratios are sensitive to the initial geometry in the system, motivating experimental extractions of the same. The values we obtained are about 10% lower than the data, which at present have significant error bars.

The dependence of $v_2\{2\}$ and $v_2\{4\}$ as a function of $p_\perp$ increases with $p_\perp$ before saturating and turning over. For both quantities, this saturation occurs later with increasing Q_s^2. In particular, for $v_2\{4\}$, we observed for $Q_s^2 = 2$ GeV^2 that it is quite flat for the $p_\perp$ range between 1 and 2 GeV. These features of our results are also qualitatively similar to data on small-particle systems. To the best of our knowledge, no computations exist in other models for $v_2\{4\}(p_\perp)$.

Symmetric cumulants $\mathrm{SC}(n, n')$, which measure the correlation of nth Fourier harmonics with n' Fourier harmonics, were constructed to understand the nonlinear hydrodynamic response of the system to correlations in the initial spatial geometry. We studied these in our initial state framework as a function of Q_s^2. We showed in Ref. [322] that $\mathrm{SC}(2,3)$ and $\mathrm{SC}(2,4)$ computed are in qualitative agreement with the data presented for heavy-ion collisions and in light-heavy ion collisions. Here, we make predictions for the $\mathrm{SC}(3,4)$, $\mathrm{SC}(2,5)$, and $\mathrm{SC}(3,5)$ cumulants.

Finally, we have shown that our simple initial state model is able to qualitatively reproduce the key signature of multiparticle collectivity, the ordering of the harmonics $v_2\{m\}$ for increasing even particle number such that $v_{\{}2\} > v_2\{4\} \simeq v_2\{6\} \simeq v_2\{8\}$, albeit in the Abelianized version. We however expect that this behavior is not unique to the Abelian version of our model, as the mechanism in our model which is responsible for the reality of the $m \geq 4$ harmonics is coherent multiple scattering, a feature in both the Abelian and non-Abelian versions. When this convergence was first seen in experiment, it was seen by some to be definitive evidence of hydrodynamic collectivity. Fig. 4.13 provides an extremely simple counter example that this pattern, in of itself, is not conclusive to understand the underlying physics.

We examined closely the dependence of our results on $Q_s^2 B_p$ and $Q_s^2/(p_\perp^{\max})^2$, the two dimensionless parameters in our model. The former corresponds to the number of color domains in the target that are encountered by the projectile. The latter corresponds to the resolution of the partons in the projectile to the structure of the color domains. Interestingly, we find that for larger values of $Q_s^2/(p_\perp^{\max})^2$, the two-particle cumulants are only weakly dependent on the number of color domains. In contrast, for smaller values of $Q_s^2/(p_\perp^{\max})^2$, we find that the cumulant behaves approximately as $1/(Q_s^2 B_p)$, as would be anticipated in an independent cluster model. Our results suggest therefore that the $p_\perp^{\max}$ considered is important in any interpretation of the data that may be construed as satisfying or violating an independent cluster model.

We studied next the dependence of our results on N_c. In [322], we showed that the Abelianized treatment of our model reproduced the pattern of $v_2\{2\} > v_2\{4\} \approx v_2\{6\} \approx v_2\{8\}$ seen in the data on pA collisions at the LHC. We studied further the N_c dependence of $v_2\{2\}$ and $v_2\{4\}$ and demonstrated that the both behave as $1/N_c$ for $N_c \geq 3$. There is therefore no ordering in N_c among m-particle cumulants. Practically, it means that N_c suppressed

topologies in products of lightlike Wilson lines must be included in such computations.

Unlike the azimuthal cumulants $c_2\{4\}$, the symmetric cumulants $\mathrm{SC}(n,n')$ (where n and n' denote distinct Fourier harmonics) have a qualitatively different behavior in the Abelian formulation of the model relative to those for the $N_c = 3$ case. This qualitative difference is not unique to $N_c = 1$. It is also seen for $N_c = 2$. In this latter case, the odd harmonics are strictly zero; hence, the corresponding symmetric cumulants are also zero. As we discussed, the underlying reason is that for $SU(2)$ both fundamental and adjoint representations are real. This is responsible for two-particle correlations being symmetric about relative azimuthal angles of zero and π.

To obtain deeper insight into our results, we examined our results within the Glasma graph approximation to our framework. This approximation corresponds to expanding out the Wilson lines in the dipole correlators to lowest nontrivial order. Physically, it corresponds to each quark line interacting at most with two gluons, either in the amplitude, or the complex-conjugate amplitude, or across the cut separating the two. It is justified when $Q_s^2 \ll p_\perp^2$. Remarkably, we find that our results for $c_2\{4\}$ are qualitatively different when we include coherent multiple scattering ($Q_s^2/p_\perp^2$ to all orders) as opposed to the Glasma graph approximation. In the former case, one obtains a real and positive $v_2\{4\}$; in the latter case, one does not. Therefore, the absence of $v_n\{m\}$ multiparticle correlations in previous Glasma graph treatments is an artifact of the approximation and not a genuine feature of initial state frameworks.

We noted that multiparticle correlations are quite strong in the Glasma graph approximation, and are close to those of an m-particle Bose distribution. Indeed, this may be the reason why one does not see signatures of "collectivity", as defined by the $v_n\{m\}$ Fourier harmonics. These assume that the mean and variance dominate the cumulant distribution. Our results suggest that coherent multiple scattering dilutes the contributions from the higher cumulants relative to the mean and the variance, thereby generating the aforementioned signatures of collectivity. In our model, however, the coherent scattering is virtually instantaneous. It takes place on a time scale corresponding to the time it takes partons to cross a Lorentz contracted nucleus. Further, the partons that scatter off the common color field do not rescatter.

The origin of this putative signature of collectivity therefore has little to do with hydrodynamics *per se*. However, our results do not exclude the possible presence of final state interactions, or even hydrodynamics, in the data on light-heavy ion systems. They do provide a clear and simple counterexample to interpretations of these signatures as being of unique origin. Such signatures of collectivity must also be consistent with other signatures of collectivity. In the larger heavy-ion collision systems, jet quenching is seen very clearly, and is an independently robust measure of final state interactions.

It is interesting to consider how this model can be developed further. Gluon degrees of freedom, which are not apparent at lower energies, become important when hadrons are boosted to higher energies. As is well known, a bremsstrahlung cascade develops, which then has a *shock wave* interaction with the nucleus. The partons in the cascade subsequently fragment to hadrons. This picture is implicit in the CGC+PYTHIA model of so-called dense-dense collisions of small systems [329] that combines Yang-Mills dynamics of gluons [62] with Lund fragmentation [330]. Because event-by-event simulations are essential to compute multiparticle cumulants, such computations are computationally intensive. To this end, in

the next chapter, we will follow up on this proof-of-principle model with a more physically motivated, and constrained, framework where we can compute correlations from initial state gluons.

Chapter 5

Gluon correlations and their relation to physics at RHIC

The following chapter is based off of

- M. Mace, V. Skokov, P. Tribedy, R. Venugopalan. *Hierarchy of azimuthal anisotropy harmonics in collisions of small systems from the Color Glass Condensate.* Phys. Rev. Lett. 121, 052301 (2018); arXiv:1805.09342 [hep-ph]. Copyright (2018) by the American Physical Society
- M. Mace, V. Skokov, P. Tribedy, R. Venugopalan. *Systematics of azimuthal anisotropy harmonics in proton-nucleus collisions at the LHC from the Color Glass Condensate* arXiv:1807.00825 [hep-ph].

In this chapter, we will utilize the dilute-dense CGC EFT framework, introduced in Sec. 1.4.1, coupled with realistic nuclear modeling, to study two-particle correlations in small colliding nuclear systems. First, in Sec. 5.1, we consider the "geometry scan" recently performed by the PHENIX collaboration at RHIC. Then in Sec. 5.2 we will use this framework to analytically, and the numerically, study the multiplicity dependence of v_n correlations observed at the LHC.

5.1 RHIC geometry scan

In a recent preprint [7], the PHENIX collaboration presented measurements of the second and third Fourier harmonics (v_2 and v_3 respectively) of two-particle azimuthal correlations in collisions of protons (p), deuterons (d), and helium-3 (^{3}He) ions off gold (Au) nuclei at center-of-mass energies $\sqrt{s}$ = 200 GeV/nucleon. The measurements were performed in the 0-5% centrality class of events in each of the three systems. They significantly improve the precision and reach of previous measurements [331, 332, 333] and strongly confirm the system size dependence of the functions $v_2(p_\perp)$ and $v_3(p_\perp)$, where $p_\perp$ is the measured transverse momentum of charged hadrons.

In [7], the measurements are interpreted as providing strong support to the idea that the collisions of these small systems are producing nature's smallest droplets of a nearly perfect fluid Quark-Gluon Plasma (QGP) [334]. This is in part due to the apparent agreement of the data with two hydrodynamical model computations SONIC [335] and iEBE-VISHNU [336]. Further, while the transport model AMPT [337] reproduces their data, the authors of [7] suggest it is disfavored because model computations do not describe large and small systems with a consistent parameter set. Finally, [7] claims that initial state color correlations in the colliding ions are ruled out as an explanation of the systematics of their data. This claim is however not substantiated by any comparison to initial state models.

In this letter, we will demonstrate that initial state color correlations computed in the Color Glass Condensate [9] effective field theory (CGC EFT) describe the systematics of the PHENIX measurements of $v_{2,3}(p_\perp)$ in light-heavy ion collisions. The essential physics underlying the result was already noted in parton model computations, presented in Chapter 4, wherein quarks from the small sized light ions scatter off domains of strong chromo-electromagnetic fields in the heavy ion target [327, 322, 328]. The size of the color domains in this "toy" model are set by a semi-hard saturation scale Q_S in the target. While this scale plays a critical role in what follows, many features of the phenomena under consideration are universal and related to basic quantum properties of the underlying theory, including Bose-enhancement and Hanbury-Brown–Twiss (HBT) interference effects [83, 325, 338, 339, 340, 341, 342, 343].

Our computations are performed within the dilute-dense power counting of the CGC EFT. Observables are computed in an expansion that includes the leading contribution and the first non-trivial saturation correction [278, 81, 340] to the color charge density of the projectile and to all orders in the corresponding color charge densities of the dense Au nucleus. This saturation correction removes an "accidental" parity symmetry arising from including only the leading order term, and is responsible for the v_3 azimuthal asymmetry in the dilute-dense approximation of the CGC EFT. The accidental nature of this symmetry was known previously from analytical and numerical computations in the full dense-dense (all orders in color charge densities of projectile and target) EFT [61, 62]. However because computations in the latter are numerically intensive, obtaining analytical expressions for the non-trivial saturation correction has proved extremely efficacious [a].

The single particle inclusive gluon distribution in the dilute-dense CGC EFT, expressed as a functional of two-dimensional Fourier transform ρ_p (ρ_t) of the projectile (target) color charge density, $\tilde{\rho}_p$ ($\tilde{\rho}_t$), can be generically decomposed into the parity-even and parity-odd contributions,

$$\frac{dN^{\text{even, odd}}(\mathbf{k}_\perp)}{d^2k dy} = \frac{1}{2}\left(\frac{dN(\mathbf{k}_\perp)}{d^2k dy}\Big[\rho_p, \rho_t\Big] \pm \frac{dN(-\mathbf{k}_\perp)}{d^2k dy}\Big[\rho_p, \rho_t\Big]\right). \tag{5.1}$$

[a] Comparing benchmark results in dense-dense and dilute-dense computations is a good measure of a systematic uncertainty in the latter.

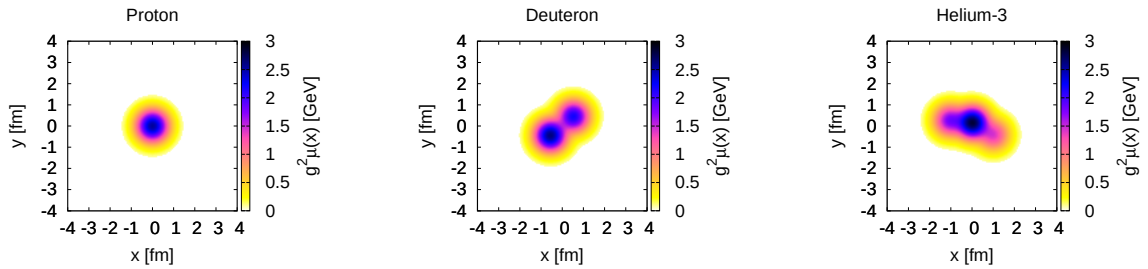

Figure 5.1: Examples of color charge densities determined from Glauber sampling with the IP-Sat model [4, 5] for a single event for p,d, and ^{3}He from high multiplicity events which contribute to the 0-5% centrality class.

Analytical computations [344, 79, 80, 324, 325] provide the compact result [81, 340]

$$\frac{dN^{\rm even}(\mathbf{k}_\perp)}{d^2k dy}\Big[\rho_p,\rho_t\Big] = \frac{2}{(2\pi)^3}\frac{\delta_{ij}\delta_{lm}+\epsilon_{ij}\epsilon_{lm}}{k^2}\Omega^a_{ij}(\mathbf{k}_\perp)\left[\Omega^a_{lm}(\mathbf{k}_\perp)\right]^\star\,, \tag{5.2}$$

$$\begin{aligned}\frac{dN^{\rm odd}(\mathbf{k}_\perp)}{d^2k dy}\Big[\rho_p,\rho_t\Big] = \frac{2}{(2\pi)^3}{\rm Im}\Bigg\{\frac{g}{\mathbf{k}_\perp{}^2}\int\frac{d^2l}{(2\pi)^2}\frac{{\rm Sign}(\mathbf{k}_\perp\times\mathbf{l}_\perp)}{l^2|\mathbf{k}_\perp-\mathbf{l}_\perp|^2}f^{abc}\Omega^a_{ij}(\mathbf{l}_\perp)\Omega^b_{mn}(\mathbf{k}_\perp-\mathbf{l}_\perp)\left[\Omega^c_{rp}(\mathbf{k}_\perp)\right]^\star\\ \times\Big[\left(\mathbf{k}_\perp{}^2\epsilon^{ij}\epsilon^{mn}-\mathbf{l}_\perp\cdot(\mathbf{k}_\perp-\mathbf{l}_\perp)(\epsilon^{ij}\epsilon^{mn}+\delta^{ij}\delta^{mn})\right)\epsilon^{rp}\\ +2\mathbf{k}_\perp\cdot(\mathbf{k}_\perp-\mathbf{l}_\perp)\epsilon^{ij}\delta^{mn}\delta^{rp}\Big]\Bigg\}\,,\end{aligned} \tag{5.3}$$

where

$$\Omega^a_{ij}(\mathbf{k}_\perp) = g\int\frac{d^2p}{(2\pi)^2}\frac{p_i(k-p)_j}{p^2}\rho^b_p(\mathbf{p}_\perp)U_{ab}(\mathbf{k}_\perp-\mathbf{p}_\perp) \tag{5.4}$$

and $\epsilon_{ij}(\delta_{ij})$ denotes the Levi-Civita symbol (Kronecker delta). The adjoint Wilson line U_{ab} is a functional of the target charge density and is the two-dimensional Fourier transform of its coordinate space counterpart: $\tilde{U}(\mathbf{x}_\perp) = \mathcal{P}\exp\left(ig^2\int dx^+\frac{1}{\nabla_\perp{}^2}\tilde{\rho}^a_t(x^+,\mathbf{x}_\perp)T_a\right)$.

Comparing the even and odd contributions in Eqs. (5.2) and (5.3) respectively, one observes that the odd contribution is suppressed in the CGC EFT by $\alpha_S\rho_p$, where $\alpha_S = g^2/4\pi$ is the QCD coupling. This factor arises from the first saturation correction in the interactions with the dilute projectile [81, 340]. This systematic suppression in the power counting is what naturally explains in this framework the relative magnitude of $v_3^2\{2\}$ compared to $v_2^2\{2\}$ observed in the experimental data on small systems.

The m-particle momentum distribution is obtained after performing an ensemble average over the color charge distributions with the weight functionals, $W[\tilde{\rho}_{p,t}]$,

$$\frac{d^mN}{d^2k_1dy_1\cdots d^2k_mdy_m} = \int\mathcal{D}\rho_p\mathcal{D}\rho_t\;W[\rho_p]W[\rho_t]\;\frac{dN}{d^2k_1dy_1}\Big[\rho_p,\rho_t\Big]\cdots\frac{dN}{d^2k_mdy_m}\Big[\rho_p,\rho_t\Big]. \tag{5.5}$$

These have the form described by the McLerran-Venugopalan (MV) model [48, 49]

$$W[\tilde{\rho}_{p,t}] = \mathcal{N}\exp\left[-\int dx^{-,+}d^2x\frac{\tilde{\rho}^a_{p,t}(x^{-,+},\mathbf{x}_\perp)\tilde{\rho}^a_{p,t}(x^{-,+},\mathbf{x}_\perp)}{2\mu^2_{p,t}}\right], \tag{5.6}$$

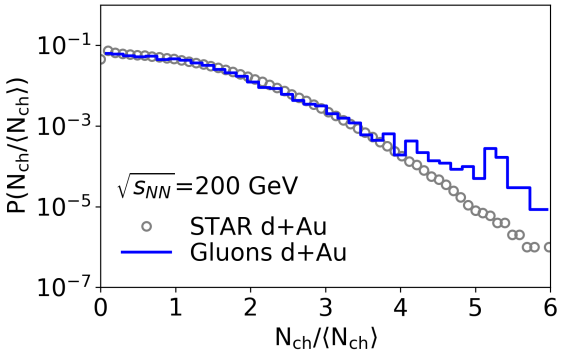

Figure 5.2: The multiplicity distribution of produced particles computed in the dilute-dense CGC framework compared to STAR d+Au data [6].

but are in fact more general because, as a consequence of renormalization group evolution of the color sources in the parton momentum fraction x [345, 277], the color charge squared per unit area $\mu_{p,t}^2$ is a function of x and spatial location of color charges in the transverse plane. Specifically, we follow the same procedure as the phenomenologically constrained IP-Glasma model [5], where the projectile and the target sources are placed using Glauber sampling of nucleons in the transverse plane [346], with position $\mathbf{x}_\perp$ and impact parameter $\mathbf{b}_\perp$, and $g^2\mu(x, \mathbf{x}_\perp, \mathbf{b}_\perp)$ is determined by the IP-Sat model [4]. Examples of the color charge distributions that produce gluons with multiplicities lying in the 0-5% centrality class of the three systems are shown in Fig. 5.1. We will return later to the important message conveyed by this visual depiction.

An essential requirement of a first principles framework is to describe experimental data on the multiplicity distribution in light-heavy ion collisions. This is important to show that the framework captures the underlying physics of correlations and fluctuations. It is also crucial for performing a reliable "apples to apples" centrality selection of events/configurations. It was shown in a remarkable paper [323] that the CGC EFT generates negative binomial distributions (NBD); subsequently, the impact parameter convoluted NBDs from the CGC EFT were employed to describe multiplicity distributions in proton-proton, proton-nucleus, and nucleus-nucleus collisions [347, 226]. Fluctuations of the saturation momentum itself [348] are important to describe high multiplicity tails; the quantitative impact of these is discussed in [349, 350].

Fig. 5.2 shows that the multiplicity distribution as a function of the number of charged hadrons $N_{\rm ch}$ for the rapidity window $|\eta| < 0.5$ in d+Au collisions published by the STAR collaboration at RHIC [6] is well reproduced in the dilute-dense CGC EFT. The details of the numerical computation on two-dimensional lattices are identical to those articulated previously [351, 5, 305, 340]. The free parameters in our framework are fixed by minimizing the deviations from the measured multiplicity distribution. These include the mean of the ratio $Q_S/g^2\mu$ taken to be 0.5, the variance of Gaussian fluctuations of $\ln(Q_S^2)$ [350] taken to be $\sigma = 0.5$, as well as an infrared cutoff scale for color fields taken to be $m = 0.3$ GeV. The effect of variations in these nonperturbative quantities was carefully examined in [349] and contributes to the systematic uncertainties of our computations.

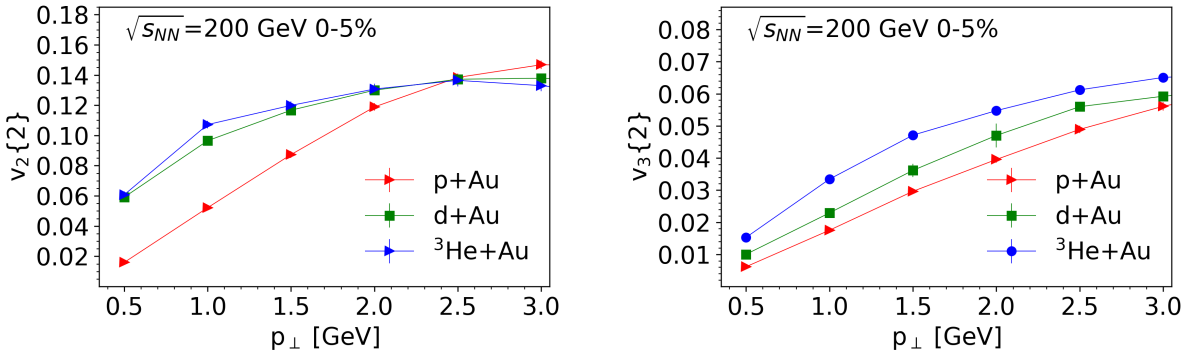

Figure 5.3: Hierarchy of anisotropies $v_{2,3}(p_\perp)$ of gluons produced in the 0-5% centrality class of light-heavy ion collisions computed in the dilute-dense CGC framework

With the parameters thus constrained, we now turn to computing the azimuthal anisotropies in light-heavy ion collisions. Defining for a fixed configuration of color sources, the harmonics for the single particle azimuthal anisotropy as

$$V_n(p_1,p_2) = \frac{\int_{p_1}^{p_2} k_\perp dk_\perp \frac{d\phi}{2\pi} e^{in\phi} \frac{dN(\mathbf{k}_\perp)}{d^2k dy}\Big[\rho_p,\rho_t\Big]}{\int_{p_1}^{p_2} k_\perp dk_\perp \frac{d\phi}{2\pi} \frac{dN(\mathbf{k}_\perp)}{d^2k dy}\Big[\rho_p,\rho_t\Big]}\,, \tag{5.7}$$

the physical two-particle anisotropy coefficients can be simply expressed as

$$v_n^2\{2\}(p_\perp) = \int \mathcal{D}\rho_p \mathcal{D}\rho_t\; W[\rho_p]\; W[\rho_t]\; \times V_n(p_\perp - \Delta/2, p_\perp + \Delta/2) V_n^\star(0,\Lambda_{UV})\,. \tag{5.8}$$

We consider Δ = 0.5 GeV bins in $p_\perp$, similar to what was done in [7]. It is important to note that technically [7] calculates the event plane v_2; however since the event plane resolution is small [b], these two quantities are very similar [352]. Here Λ_{UV} is the ultraviolet $p_\perp$ cutoff, defined by the inverse lattice spacing – our results are insensitive to this cutoff. An identical computation was performed previously in the dense-dense framework to extract v_2 and v_3 [62]. Our dilute-dense framework however has the significant advantage that analytical expressions can be written down and results do not require numerical evaluation of the temporal evolution of the classical Yang-Mills equations.

The results of our computation for the hierarchy of $v_2(p_\perp)$ and $v_3(p_\perp)$ gluon anisotropies for p+Au, d+Au and ^{3}He+Au collisions at $\sqrt{s}$ = 200 GeV/nucleon in the 0-5% centrality class for each of the three systems is shown in Fig. 5.3. A clear hierarchy is observed in the magnitudes of $v_{2,3}(p_\perp)$ for p+Au and those for d+Au and ^{3}He+Au. For most of the $p_\perp$ range plotted, this is opposite to the naive expectation that the anisotropies should be suppressed with an increasing number of color domains. Between d+Au and ^{3}He+Au, this hierarchy is not clearly distinguishable for $v_2(p_\perp)$; it is however clearly visible for $v_3(p_\perp)$. As discussed previously in the toy model computation of Chapter 4, the scaling with inverse number of

[b] The PHENIX experiment has event plane resolution of 6.7% and 5.7% for p+Au and d+Au respectively [7]

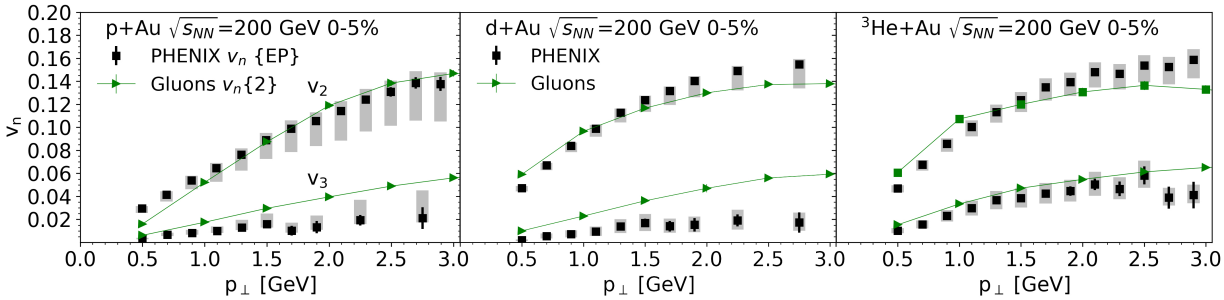

Figure 5.4: Comparision of the results shown in Fig. 5.3 to v_2 and v_3 for charged hadron data from the PHENIX collaboration [7].

color domains is violated primarily because of the interplay of two dimensionful scales: in our case, these are Q_S^p, the saturation scale in the projectile, and a typical gluon resolution scale $\tilde{p}_\perp$. In the toy model of [327, 322, 328], $\tilde{p}_\perp$ is identical to $p_\perp$; in the dilute-dense framework, their relation is less straightforward. Domain scaling holds if $\tilde{p}_\perp > Q_S^p$, because then gluons in the target resolve individual color domains in the projectile. This is clearly seen for $v_2(p_\perp)$ at high $p_\perp$ in Fig. 5.3 and a similar trend is seen for $v_3(p_\perp)$. In contrast, if $\tilde{p}_\perp < Q_S^p$, gluons in the target cannot resolve individual domains any more but interact with $\sim (Q_S^p)^2/\tilde{p}_\perp^2$ of them simultaneously. In Section 4.5.2 ([327]), it was shown that in this case there is no suppression with the number of color domains!

Another important element in understanding the systematics of the data is that 0-5% centrality in ^{3}He+Au collisions corresponds to a significantly higher value of $N_{\rm ch}$ than for p+Au collisions. In the dilute-dense framework, the multiplicity of an event scales with $(Q_S^p)^2$ [79, 60]. Thus for 0-5% centralities, $Q_S^p|_{^3\rm He} > Q_S^p|_{\rm p}$. Hence, as long as $\tilde{p}_\perp < Q_S^p|_{^3\rm He}$, gluons in the target will coherently interact with $(Q_S^p|_{^3\rm He})^2/\tilde{p}_\perp^2$ domains, many more than in p+Au. As shown in simple color domain models [294, 268], the corresponding chromoelectric fields will generate larger anisotropies, but as the similar values of $v_2(p_\perp)$ between d+Au and ^{3}He+Au in Fig. 5.3 indicates, $v_2(p_\perp)$ will saturate at large $N_{\rm ch}$. Because v_3 is due to a higher order $\alpha_S\rho_p$ suppressed effect, this saturation may only occur for larger $N_{\rm ch}$. Our prediction would therefore be that $v_{2,3}(p_\perp)$ for high multiplicity events across small systems should be identical for the same $N_{\rm ch}$.

In Fig. 5.4, we overlay Fig. 5.3 on top of the data for charged hadrons presented by the PHENIX collaboration in [7]. The agreement for $v_2(p_\perp)$ is quite good across systems. This is interesting as $v_2(p_\perp)$ in hydrodynamical models is particularly sensitive to spatial geometry. For $v_3(p_\perp)$, while the agreement for ^{3}He is quite good, the computation overshoots the data in the p,d systems. Since v_3 is fluctuation driven, we speculate this may be related to the fact that our comparison of gluon multiplicities to the $N_{\rm ch}$ multiplicity distribution in Fig. 5.2 also overshoots the data at high multiplicities. A corollary of this statement is that our $P(N_{ch}/\langle N_{ch}\rangle)$ for ^{3}He should agree with the RHIC N_{ch} distribution when available. Nevertheless, our computation and the data share the feature that $v_3(p_\perp)$ for p,d is lower than that for ^{3}He. We note that hydro models show a similar hierarchy for $v_3(p_\perp)$ [336]. We emphasize again that a stronger prediction in our framework is that v_3 in high multiplicity small systems will agree for the same $N_{\rm ch}$. This is indeed what is seen in peripheral A+A

collisions at the LHC and in central $p+A$ collisions at the same $N_{\rm ch}$ [297], a feature of data which in that case is clearly hard to explain by system geometry alone [321].

There are significant systematic uncertainties in the computation. Firstly, within the framework itself, there are higher order color charge density corrections, which may contribute differently for each of the projectile ions. This uncertainty can be benchmarked with numerical dense-dense computations for each species. Secondly, nonperturbative model parameters that are fixed for d+Au collisions by the measured multiplicity distributions may differ for multiplicity distributions of the other light ions. These are not available at present. There are uncertainties due to gluon fragmentation and higher order QCD computations. The technology to estimate the former exists within the CGC+PYTHIA framework [329], whereby gluons produced from the CGC are connected via strings and the latter are fragmented into hadrons with the PYTHIA event generator [353, 354]. Finally, the relative contribution of final-state scattering should be quantified by matching the CGC initial state to transport models at later times [355].

While comparisons to data that progressively reduce the stated theoretical uncertainties are essential to understand the quantitative role of initial state correlations, qualitative trends in data may suffice to assess their dominant role. As our discussion of the physical underpinnings of the anisotropies suggests, CGC EFT computations will generate simple systematics of $v_{2,3}\{2\}$, as a function of $N_{\rm ch}$ and $\sqrt{s}$ which should be straightforward to rule out. Further, multiparticle azimuthal anisotropy correlations $v_n\{m\}$ for $m \geq 4$ can be computed for light-heavy ion collisions and their systematics compared to data; we caution however that universal features of the mathematical structure of CGC EFT n-body distributions and those of hydrodynamic single particle distributions may lead to similar results [356].

A key uncertainty is our knowledge of rare nuclear contributions in high multiplicity events. As suggested by Fig. 5.1, nucleons overlap more closely in such events relative to minimum bias events. In particular, electron scattering experiments at Jefferson Lab have revealed that short-range pairing of nucleons dominates nuclear wavefunctions for momenta larger than the Fermi momentum [357, 358]. It is conceivable therefore that such "clumpy" nucleon configurations may contribute significantly to the ^{3}He nuclear wavefunction, beyond those anticipated from Green's function Monte Carlo computations [359, 360]. This interesting possibility is under active investigation [361].

In summary, we have shown that initial state color correlations in the dilute-dense framework of the CGC EFT provides a competitive explanation for the data presented on azimuthal anisotropy coefficients v_2 and v_3 in small collision systems. Further comparisons to data in different centrality classes, and to multiparticle anisotropies, can help quantify if and where the dominant role of initial state correlations in describing the collectivity observed in small systems breaks down.

5.2 LHC multiplicity dependence

In the previous section, we showed that the dilute-dense framework of the Color Glass Condensate (CGC) Effective Field Theory (EFT) [9] qualitatively describes the hierarchy of $v_{2,3}(p_\perp)$ azimuthal Fourier harmonic coefficients of rapidity separated two-particle "ridge" correlations measured by the PHENIX experiment in collisions of proton/deuterium/helium-

3 ions off gold ions at center-of-mass energy of $\sqrt{s}$ = 200 GeV/nucleon [7]. Within theoretical uncertainties, the CGC EFT computations also provide semi-quantitative agreement with the PHENIX measurements.

The model to data comparison suggests that initial state correlations in the hadron wavefunctions provide a competitive alternative explanation to models that describe the data in terms of hydrodynamic collectivity of the quark-gluon matter produced in the collisions. This conclusion is fortified by the fact that the systematics of m-particle $v_n\{m\}$ harmonics, previously believed to provide an unambiguous signature of hydrodynamic collectivity, are also reproduced in the simple initial state parton model of Chapter 4.

While theory comparisons to measurements across system size are very important for understanding the underlying physical origin of the ridge two-particle correlations, they are at present available only for events characterized by a limited range in $N_{\rm ch}$, the number of charged particles produced. However extensive data on the $N_{\rm ch}$ dependence of ridge yields (and the corresponding v_n coefficients) is available in proton-lead (p+A) collisions at the LHC at $\sqrt{s}$ = 5.02 GeV/nucleon. In addition, p+A collisions have the virtue that modeling the proton wavefunction at high energies is simpler than that of the deuteron or helium-3. Reproducing the systematics of the v_n dependence on $N_{\rm ch}$ in small systems even qualitatively is a challenge for all theory frameworks and can help distinguish between them.

In this note, we will examine the $N_{\rm ch}$ dependence of the azimuthal Fourier harmonics as measured by the ATLAS experiment in p+A collisions at 5.02 TeV/nucleon. We will show that the qualitative features of the data can be deduced very simply from the corresponding equations in the dilute-dense approximation of the CGC. We will go one step further and show that the magnitude of v_2 and v_4, as a function of $N_{\rm ch}$, is reproduced in the CGC EFT within theoretical uncertainties. For reasons we shall discuss, quantitative results for the $N_{\rm ch}$ dependence of v_3 are more challenging numerically – it is outside the scope of the present work.

The dilute-dense approximation [344, 79, 80, 324, 325] of the CGC EFT consists of keeping terms in the solution of the QCD Yang-Mills equations to compute inclusive gluon amplitudes that are to lowest order in the ratio $\rho_p/k_{\perp,p}^2$ in the projectile but to all orders in the ratio $\rho_t/k_{\perp,t}^2$ in the target [c]. Here $\rho_p(\rho_t)$ is color charge density in the proton (lead nucleus) and $k_{\perp,p}$ ($k_{\perp,t}$) is the transverse momentum of the scattered gluon from the proton (lead nucleus). While this dilute-dense approximation may be sufficient to compute the even harmonics v_{2n}, an accidental parity symmetry sets $v_3 = 0$ at this order. This is well known to be an artifact of the leading order in $\rho_p/k_{\perp,p}^2$ approximation. For instance, numerical work in the dense-dense limit of the CGC EFT, where all orders in both $\rho_p/k_{\perp,p}^2$ and $\rho_t/k_{\perp,t}^2$ are kept, clearly recover finite values of v_3 [61, 62].

Indeed, as shown explicitly recently [81, 278, 340], the first nontrivial $\rho_p/k_{\perp,p}^2$ correction breaks the accidental parity symmetry and gives a finite contribution to v_3. Thus a nonzero value for odd azimuthal anisotropies in the CGC EFT can be understood to be a unique signature of the *emerging coherence* of the classical gluon field in the projectile. To quantify these statements, we use the expressions from the previous section, where in Eq. (5.1) we decomposed the single particle inclusive gluon distribution in the dilute-dense CGC EFT

[c] A further glasma graph approximation corresponds to the regime where one expands to lowest order in both $\rho_p/k_{\perp,p}^2$ and $\rho_t/k_{\perp,t}^2$ [83, 270, 85, 86, 87, 88].

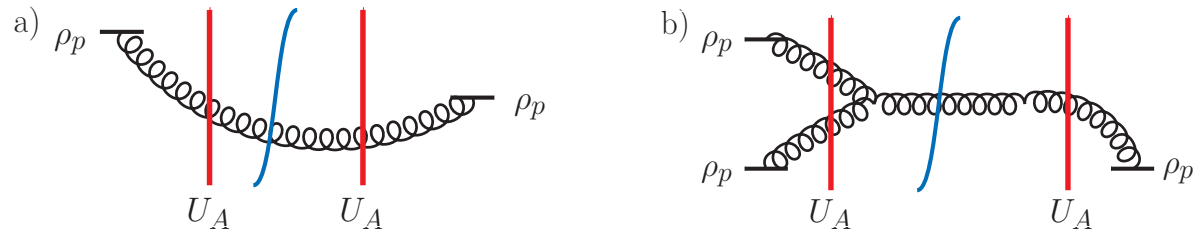

Figure 5.5: Diagrammatic representation of the leading order contributions to the a) P-even and b) P-odd parts of the inclusive gluon production cross section; the straight vertical lines represent multiple scattering in the gluon "shockwave" field of the target. The curved vertical line denotes the cut separating the amplitude from the complex conjugate amplitude.

into parity-even and parity-odd contributions, Eq. (5.2) and Eq. (5.3) respectively [81, 340]. If we compare these even and odd contributions, one observes that the latter is suppressed in the CGC EFT power counting by $\alpha_S \rho_p$, where $\alpha_S = g^2/4\pi$ is the QCD coupling. This is also apparent from the diagrammatic representation of the inclusive single particle distribution depicted in Fig. 5.5.

Defining the harmonics of the even and odd single particle azimuthal momentum anisotropies, for a fixed configuration of ρ_p and ρ_t, respectively as

$$Q_{2n}\left[\rho_p, \rho_t\right] = \frac{\int_{p_1}^{p_2} k_\perp dk_\perp \frac{d\phi}{2\pi} e^{i2n\phi} \frac{dN^{\text{even}}(\mathbf{k}_\perp)}{d^2k dy}\left[\rho_p, \rho_t\right]}{\int_{p_1}^{p_2} k_\perp dk_\perp \frac{d\phi}{2\pi} \frac{dN^{\text{even}}(\mathbf{k}_\perp)}{d^2k dy}\left[\rho_p, \rho_t\right]}, \tag{5.9}$$

$$Q_{2n+1}\left[\rho_p, \rho_t\right] = \frac{\int_{p_1}^{p_2} k_\perp dk_\perp \frac{d\phi}{2\pi} e^{i(2n+1)\phi} \frac{dN^{\text{odd}}(\mathbf{k}_\perp)}{d^2k dy}\left[\rho_p, \rho_t\right]}{\int_{p_1}^{p_2} k_\perp dk_\perp \frac{d\phi}{2\pi} \frac{dN^{\text{even}}(\mathbf{k}_\perp)}{d^2k dy}\left[\rho_p, \rho_t\right]}, \tag{5.10}$$

the physical two-particle anisotropy coefficients can be simply expressed as [d]

$$v_n^2\{2\}(N_{\text{ch}}) = \int \mathcal{D}\rho_p \mathcal{D}\rho_t \; W[\rho_p] \; W[\rho_t] |Q_n\left[\rho_p, \rho_t\right]|^2 \; \delta\left(\frac{dN}{dy}\left[\rho_p, \rho_t\right] - N_{\text{ch}}\right). \tag{5.11}$$

The weight functionals representing the distribution of color sources,

$$W[\tilde{\rho}_{p,t}] = \mathcal{N} \exp\left[-\int dx^{-,+} d^2x \frac{\tilde{\rho}^a_{p,t}(x^{-,+}, \mathbf{x}_\perp)\tilde{\rho}^a_{p,t}(x^{-,+}, \mathbf{x}_\perp)}{2\mu^2_{p,t}(\mathbf{x}_\perp)}\right], \tag{5.12}$$

have the McLerran-Venugopalan (MV) model [48, 49] form, where $\mathcal{N}$ is a normalization factor. However, unlike the MV model, $\mu^2_{p,t}(\mathbf{x}_\perp)$, the color charge squared per unit area, is spatially dependent here due to i) the renormalization group (RG) evolution of the color sources to small Bjorken x for the case of μ_p^2 [345, 277, 5], and ii) both RG evolution and fluctuations in the nucleon positions in the target for μ_t^2.

[d] In the following, for notational simplicity, we will not explicitly write the limits of the momentum integration arguments.

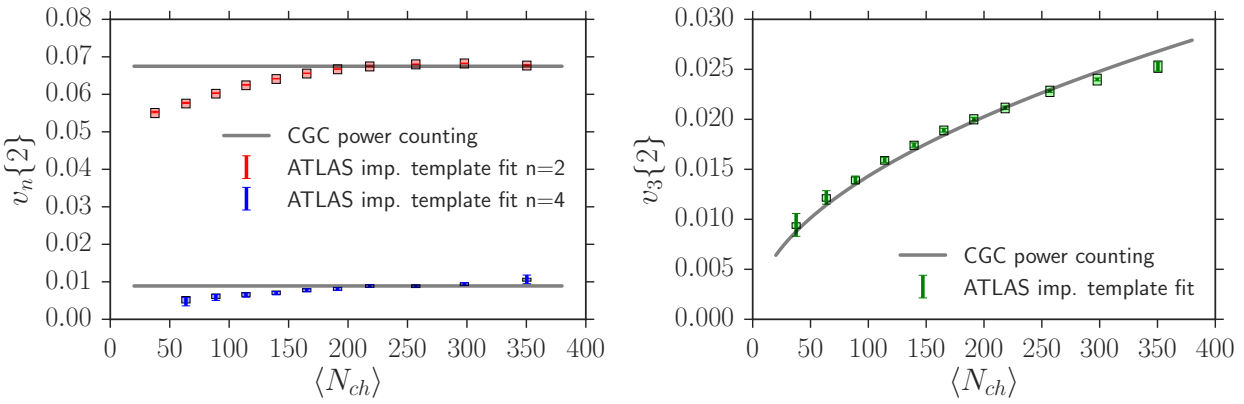

Figure 5.6: Comparison of even and odd harmonics measured in p+Pb collisions from ATLAS improved template fit [8] with the $N_{\rm ch}$ scaling expected in the dilute-dense CGC EFT.

To examine the multiplicity dependence of v_n, let us first rescale $\rho_p \to c\rho_p$, which gives

$$\Omega(\mathbf{k}_\perp) \to c\ \Omega(\mathbf{k}_\perp)\ , \tag{5.13}$$

in Eq. (5.4). This property is obvious physically because $\Omega(\mathbf{k}_\perp)$ represents the covariant gauge classical field of the projectile color rotated by the Wilson line of the target. Hence the "event" multiplicity, for a fixed configuration of ρ_p, ρ_t, transforms as

$$\frac{dN}{dy}\Big[\rho_p,\rho_t\Big] \to c^2\frac{dN}{dy}\Big[\rho_p,\rho_t\Big] + \mathcal{O}(c^3)\,. \tag{5.14}$$

The order c^3 contribution to the multiplicity is P-odd and will vanish after performing the ensemble average. The first nontrivial correction is thus of order c^4 and can be interpreted as the first saturation correction from the proton to single inclusive gluon production [82].

The even "single particle" harmonic is invariant under rescaling

$$Q_{2n}\left[\rho_p,\rho_t\right] \to c^0\ Q_{2n}\left[\rho_p,\rho_t\right]\ , \tag{5.15}$$

because both numerator and denominator scale identically. In contrast, the P-odd contribution appears in the numerator of the odd single particle harmonic, while the normalization in the denominator is dominated by the P-even leading order piece. One therefore obtains,

$$Q_{2n+1}\left[\rho_p,\rho_t\right] \to c\ Q_{2n+1}\left[\rho_p,\rho_t\right]\ . \tag{5.16}$$

Hence these scaling relations Eqs. (5.14)-(5.16) allow us to establish that

$$Q_{2n}\left[\rho_p,\rho_t\right] \propto \left(\tfrac{dN}{dy}\Big[\rho_p,\rho_t\Big]\right)^0, \tag{5.17}$$

$$Q_{2n+1}\left[\rho_p,\rho_t\right] \propto \sqrt{\tfrac{dN}{dy}\Big[\rho_p,\rho_t\Big]}, \tag{5.18}$$

and therefore,

$$v_{2n}\{2\} \propto N_{\rm ch}^0, \qquad v_{2n+1}\{2\} \propto N_{\rm ch}^{1/2}\,. \tag{5.19}$$

This argument is insufficient to fix the coefficients of proportionality. These can however be fixed by data on even and odd harmonics at a given $N_{\rm ch}$. In order to do this, we choose $N_{\rm ch} = 218$ for all v_n. We plot the results of this scaling for the azimuthal Fourier harmonics $v_2\{2\}$, $v_3\{2\}$, $v_4\{2\}$ versus p+Pb ATLAS improved template fit data [8] in Fig. 5.6. We have checked that the results shown are relatively insensitive to the value of $N_{\rm ch}$ used to extract the proportionality coefficient for each harmonic. Note that since this template fit method aims to extract the long-range ridge correlations by cleanly separating them from dijet contribution, it is ideal for theory to data comparisons.

Remarkably, we find that the anticipated scaling of $v_{2,3,4}$ with $N_{\rm ch}$, obtained from the CGC power counting, is in excellent agreement with the ATLAS data. It is unclear at present what the corresponding qualitative expectations are in kinetic and hydrodynamic models for p+A collisions. Studies which include a dense-dense CGC initial state, followed by hydrodynamic evolution [65], also exhibit relative independence on $N_{\rm ch}$ for v_2. However for v_3, they do not see the $\sqrt{N_{\rm ch}}$ dependence but a much flatter behavior. This flatter behavior is also anticipated in the CGC EFT power counting for large $N_{\rm ch}$ because ρ_p from the projectile is promoted to a Wilson line U in the dense-dense limit. It is therefore important to quantify whether the results of [65] are due to the dense-dense IP-Glasma initial dynamics [5, 349, 62, 329] or whether the later (and relatively short) hydrodynamic expansion is also essential in p+Pb collisions.

We will now employ the numerical realization of the dilute-dense framework we developed in the previous section to quantitatively verify whether they corroborate our simple power counting estimates. The parameters in our study are as follows [e]. We take the ratio of the saturation scale to the color charge scale to be $Q_s/g^2\mu = 0.5$; additionally we take the fluctuations of the log of this ratio to be $\sigma = 0.5$ – this quantity is important to account for the large color charge fluctuations in rare events. [350]. Additionally, we employ a regulator mass of $m = 0.3$ GeV for the gauge fields which enters the Poisson equation relating the gauge fields in the projectile and target to their respective color charge densities. As in the previous section, these parameters are determined by minimizing the deviation from the charged particle multiplicity distribution measured by the ATLAS collaboration [362]. Further, following the lattice prescriptions of [351], we take transverse lattices of size $N = 1024$ with lattice spacing $a = 0.0625$ fm, and $N_y = 100$ rapidity slices in the coordinate x^-; we have verified that the continuum limit is obtained for this parameter set.

The extraction of v_4 is especially demanding because very fine lattices are required to extract a robust fourth harmonic. Our results for the convergence of v_4 with increasing lattice size are shown in Fig. 5.7. These results also suggest that a robust extraction of v_4 in the numerically more intensive dense-dense IP-Glasma [62] framework for small systems is very challenging with current resources. The numerical extraction of v_3 in the dilute-dense CGC EFT as a function of $N_{\rm ch}$ is even more formidable than that for $v_{2,4}$. This is evident from Eq. (5.3) because firstly, an additional ρ_p and U have to be sampled; further, one needs to compute an extra momentum integral. For $v_{2,4}$ one needs approximately 10^4 color charge configurations; for v_3 it will require at least an order of magnitude more configurations with each configuration taking N^2 times more operations to compute than for $v_{2,4}$ (due to the extra momentum integral). This is challenging and outside the scope of the present work.

[e] See also [349] for more details on the parameters entering solutions of the QCD Yang-Mills equations.

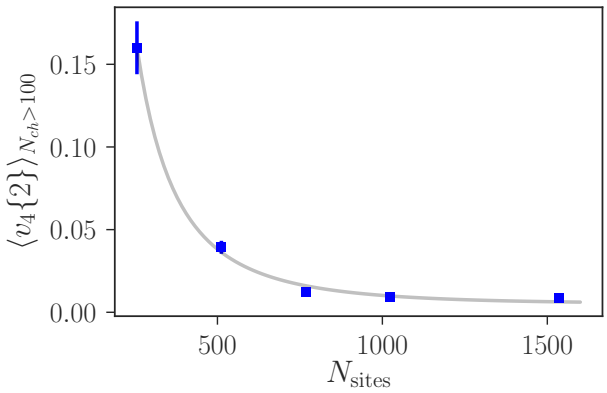

Figure 5.7: Lattice size dependence (for a fixed spacing of a = 0.0625 fm) of the average $v_4\{2\}$ for $N_{\text{ch}} \geq 100$. Excellent convergence is observed for $N \geq 768$ lattice sites.

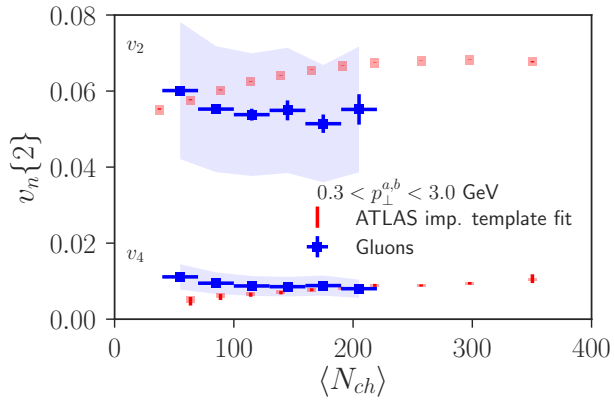

Figure 5.8: Comparison of even and odd harmonics measured in p+Pb collisions from ATLAS improved template fit [8] with the dilute-dense CGC EFT. A 30% systematic uncertainty band is shown.

Our results for $v_{2,4}$ as a function of N_{ch} are shown in Fig. 5.8. Unfortunately, the computational effort required limits our ability to go to larger N_{ch}. Within the systematic uncertainties enumerated below, the agreement of data with the theory is very good. These uncertainties include the dependence on the regulator mass m and on the ratio $Q_s/g^2\mu$ and its fluctuations. Our studies varying these quantities suggest that the uncertainties are less or of order 30%. This is represented by the shaded band around our results; the width of this band also takes into account our estimates of uncertainties from running coupling corrections [62] and from the hadronization of gluons [329], which at this point we are not able to quantify reliably. Some of these uncertainties are somewhat mitigated by the fact that the v_n's are ratios of weighted multiplicities.

It is natural to ask if the correlations in p+Pb collisions have the same origin as those measured in peripheral Pb+Pb collisions at the same N_{ch}. The CMS collaboration [297] observed that the two-particle v_3 in p+Pb and Pb+Pb collisions are nearly identical for the same value of N_{ch} while v_2 is larger in the latter system. The IP-Glasma+MUSIC model [64] (wherein the dense-dense CGC EFT IP-Glasma initial conditions are combined

with hydrodynamic flow [363]) which does a good job of describing Pb+Pb data for central collisions out to at least 60% centrality, does a poor job of describing the p+Pb $v_{2,3}$ data [364]. It was recently shown [65] that including spatial fluctuations of color charge distributions [f] in the model has a big effect leading to good agreement with the p+Pb data. The impact of these studies for peripheral Pb+Pb collisions remains to be quantified. The results of both [364] and [65] rely on hydrodynamic response to an initial spatial geometry and is qualitatively different from our effect which results from initial state momentum anisotropies alone.

Will our dilute-dense framework suffice to describe $v_{2,3}$ in peripheral Pb+Pb collisions? Qualitatively, we anticipate that the $N_{\rm ch}$ dependence of $v_{2,3}$ would be identical for p+Pb and Pb+Pb for partons in the projectile coherently interacting with multiple localized color domains of size $1/Q_s$ [g]. For the values of $N_{\rm ch}$ studied here, v_2 is approximately 25% greater in Pb+Pb than in p+Pb. We plan to examine whether this difference is captured in quantitative studies for Pb+Pb in the dilute-dense and dense-dense frameworks [367]. Alternatively, because the size of the Pb+Pb system is larger, and rescattering is more likely to occur [355, 77], the breakdown of scaling may affect v_2 sooner than it does for v_3. Both of these scenarios for peripheral Pb+Pb collisions, as well as the relative role of initial momentum anisotropy versus enhanced geometry response from shape fluctuations in p+Pb collisions, can be quantified within the CGC EFT framework itself and will be reported in the near future [368].

[f] These fluctuations have been argued to be necessary to describe HERA data on incoherent exclusive J/Ψ production [365, 366].

[g] Interestingly, similar arguments on universal $N_{\rm ch}$ scaling have been advanced in a kinetic theory picture [321].

Chapter 6

Summary and outlook

In this thesis, we have presented original results on a variety of topics related to the dynamics of QCD out of equilibrium. In Chapter 2, we showed for the first time that the pre-equilibrium dynamics of a heavy-ion collisions can produce numerous sphaleron transitions. Additionally, we studied the scaling in time behavior of the characteristic momentum scales, and determined quantitatively that the sphaleron transition rate is controlled by the infrared screening scale. These transitions at early times are essential for the emergence of anomalous transport phenomena like the CME. The search for such effects is currently ongoing with the IsoBar program at RHIC. If detected, this would be the first experimental realization of sphaleron transitions, and a direct probe of the infrared dynamics of non-equilibrium QCD. To gain deeper insights into the real-time dynamics of these sphaleron transitions, in Chapter 3 we developed novel methods for simulating real-time chiral fermion production. This allowed us to directly probe the currents and charge production of anomalous transport phenomena using a first-principles framework. In particular we studied the quark mass dependence and the magnetic field strength dependence, providing insights for phenomenology and modeling for current and future searches for such effects.

We then considered long-range-in-rapidity correlations in small colliding nuclear systems, which necessarily probe the initial infrared dynamics of the system. We made use of a proof-of-principle parton model in Chapter 4 to study up to eight particle correlations in pA collisions. With this simple model, we were able to calculate a large number of experimental observables, including up to eight particle Fourier harmonics. This model provides a strong counterpoint to the conjecture that the multiparticle signatures of collectivity are unique to hydrodynamic response to initial geometry. Along the way, we developed deeper understanding of how such correlations arise in an initial state model; in particular the realization of how the naïve number of domains scaling for correlations emerges, or is obscured, in such initial state models. Using this proof of principle model as motivation, in Chapter 5 we developed a model for initial state correlations based off of the dilute-dense CGC EFT. By coupling the particle production in the CGC EFT to data-constrained nuclear modeling of the initial state, we were able to show that the ordering of two-particle correlations between different small systems recently observed by PHENIX [7] can be understood without hydro-

dynamic flow. We then applied a simple power counting argument in the dilute-dense CGC EFT, fortified by numerical calculations, to explain the multiplicity dependence of azimuthal correlations at the LHC.

Beyond this thesis, a number of timely studies are ongoing or planned. In the study of sphaleron transitions, work is in progress to understand the impact of longitudinal expansion and the gauge group dependence on the rate of these transitions [369]. This will be important for the interpretation of the results of the current IsoBar program. It is also essential we understand the real-time production of chiral fermions from these Glasma fields, however the lattice sizes required are still beyond the scope of what is currently accessible computationally. In the meantime, we are working on understanding the real-time production of chiral fermions from non-equilibrium Abelian fields, both for Schwinger pair production [370] and the chiral plasma instability [371]. These studies will also help us further develop our numerical techniques, which will enable studies of more systems and with a greater degree of theoretical accuracy. Because a strongly interacting fluid is generated during a heavy-ion collision, it is also important to understand how chiral charge is transported macroscopically. To accomplish this, we are employing state-of-the-art magnetohydrodynamic simulations [372], where we study how chiral charges are transported and how they impact the final hadrons spectrum [373]. In the future, we plan to perform simulations of chiral resistive magnetohydrodynamics, which will allow us to study the full macroscopic real-time dynamics of anomalous transport. However, this has many theoretical and numerical challenges, but once accomplished will enable accurate phenomenology for searches for the CME and related effects, and may also be applicable for studying new settings, including neutron stars and Dirac and Weyl semi-metals beyond the ballistic regime.

Small systems represent an exciting domain to understand the initial state dynamics, however a serious quantification of the theoretical uncertainties is necessary. To this end, we plan to conduct a full study, which includes various levels of approximation of the CGC EFT (discussed in Section 1.4.1) and the relative effect of a hydrodynamic stage [368]. We can also look inside our calculations, in hopes of elucidating how different aspects, such as the nucleon positions, drive the initial state "flow". This will be addressed in the near future [367]. We believe that by building off of the work in this thesis, it is possible to fully quantify the correlations produced in the initial state from the CGC EFT. However, greater comparison between all theoretical models is needed to elucidate the true origin of the observed correlations, including the challenging but necessary calculation of higher particle number correlations as well as newer and perhaps more differential observables. We plan to actively participate in this mission.

It will also be important to use the methods presented for calculations of initial state correlations in pA collisions to make predictions for a future Electron Ion Collider (EIC) facility [374]. If built, an EIC would enable the most detailed study ever into the internal QCD dynamics of the nucleons which compose the nuclei. At small-x, the EIC will be a powerful test of the CGC EFT, and if validated, the EIC will likely uncover even richer features of the CGC EFT, and thus QCD. This is something we plan to vigorously pursue in the near future.

Appendix A

Calibrated Cooling

The following appendix is based off of

- M. Mace, S. Schlichting, R. Venugopalan. *Off-equilibrium sphaleron transitions in the Glasma.* Phys.Rev. D93, 074036 (2016). Copyright (2016) by the American Physical Society

We shall describe here further details of our implementation of the "calibrated cooling" method developed in [149, 151] to measure the Chern-Simons number. We focus on the aspects relevant to the practical implementation and refer to Sec 2.2.2 for a more general introduction.

A.1 Cooling

We first perform a cooling of the spatial gauge links $U_\mu(x,t)$ at a given real time t by following the energy gradient flow. We introduce a dimensionless cooling time variable τa^2, which measures the depth of cooling in lattice units and perform a sequence of update steps of the gauge links according to

$$U_\mu(x,t;\tau+\delta\tau) = \exp\big(-igaE^{cool}_\mu(x,t;\tau)\delta\tau\big)U_\mu(x,t,\tau)\,, \tag{A.1}$$

where the "cooling" electric field E^{cool}_μ associated with the change of the gauge links along the cooling path is given by

$$E^{cool,a}_i(x,t;\tau) = -\frac{2}{ga^3}\sum_{j\neq i}\mathrm{ReTr}\big[i\tau^a(U^{\square}_{i,j}-U^{\square}_{i,-j})(x,t;\tau)\big]\,, \tag{A.2}$$

with the elementary plaquettes defined as

$$\begin{aligned} U^{\square}_{i,j}(x) &= U_i(x)U_j(x+\hat{i})U_i^{\dagger}(x+\hat{j})U_j^{\dagger}(x)\,, \\ U^{\square}_{i,-j}(x) &= U_j^{\dagger}(x-\hat{j})U_i(x-\hat{j})U_j(x+\hat{i}-\hat{j})U_i^{\dagger}(x)\,, \\ U^{\square}_{-i,j}(x) &= U_j(x)U_i^{\dagger}(x+\hat{j}-\hat{i})U_j^{\dagger}(x-\hat{i})U_i(x-\hat{i})\,, \\ U^{\square}_{-i,-j}(x) &= U_i^{\dagger}(x-\hat{i})U_j^{\dagger}(x-\hat{i}-\hat{j})U_i(x-\hat{i}-\hat{j})U_j(x-\hat{j})\,. \end{aligned} \tag{A.3}$$

We use a cooling step size of $\delta\tau = a^2/8$ and repeat the update in Eq. (A.1) until reaching the desired cooling depth τ_c. During the course of the real time evolution, the cooling process is repeated after each $t = a/2$. Based on the cooled copies $U_\mu(x,t_1;\tau_c)$ and $U_\mu(x,t_2;\tau_c)$ of the original gauge field configurations at two adjacent times t_1 and t_2 (see Fig. (2.2)) we then compute the change in the Chern-Simons number as detailed below.

A.2 Chern-Simons number

Since we only perform cooling of the spatial gauge links, we first need to re-construct the connection between the cooled configurations $U_\mu(x,t_1;\tau_c)$ and $U_\mu(x,t_2;\tau_c)$ to evaluate the Chern-Simons current. Because the topology measurement does not rely on the exact path connecting the two configurations we do so by simply performing a smooth interpolation between the starting point $U_\mu(x,t_1;\tau_c)$ and end point $U_\mu(x,t_2;\tau_c)$. Explicitly, we choose the cooled analogue of the color electric field

$$E_i^{t_1\to t_2}(x;\tau_c) = \frac{i}{ga(t_2-t_1)}\mathrm{Log}\Big[U_i(x,t_2;\tau_c)U_i^{\dagger}(x,t_1;\tau_c)\Big] \tag{A.4}$$

to be constant between the two adjacent times such that for $t_1 \le t \le t_2$ the gauge links follow the trajectory

$$\begin{aligned} &U_\mu(x,t_1\le t\le t_2;\tau_c) = \\ &\qquad \exp\Big(-igaE_i^{t_1\to t_2}(x;\tau_c)(t-t_1)\Big)U_\mu(x,t_1;\tau_c)\,. \end{aligned} \tag{A.5}$$

We then compute the change in Chern-Simons number between the two configurations by evaluating the space time integral of the Chern-Simons current

$$\begin{aligned} N_{CS}^{\tau_c}(t_2) - N_{CS}^{\tau_c}(t_1) &= \frac{g^2a^3(t_2-t_1)}{8\pi^2}\sum_x E_{i,\mathrm{imp}}^{t_1\to t_2}(x;\tau_c) \\ &\frac{B_i^{\mathrm{imp}}(x,t_1;\tau_c) + 4B_i^{\mathrm{imp}}(x,t_{\mathrm{mid}};\tau_c) + B_i^{\mathrm{imp}}(x,t_2;\tau_c)}{6} \end{aligned} \tag{A.6}$$

where in order to improve the accuracy of the integral over time we construct the magnetic fields at the mid-point $t_{\mathrm{mid}} = (t_1+t_2)/2$ from Eq. (A.5) and use Simpson's rule to approximate

the integral. Similarly, we use an $\mathcal{O}(a^2)$ improved definition of the color electric and color magnetic fields [150], where the electric fields are locally determined at each lattice point according to

$$E^a_{i,\mathrm{imp}}(x) = -\frac{1}{12}U^{ab}_i(x)E^b_i(x+\hat{i}) + \frac{7}{12}U^{\dagger,ab}_i(x-\hat{i})E^b_i(x-\hat{i}) \\ +\frac{7}{12}E^a_i(x) - \frac{1}{12}U^{\dagger,ab}_i(x-\hat{i})U^{\dagger,bc}_i(x-2\hat{i})E^c_i(x-2\hat{i})\,. \tag{A.7}$$

Here $U^{ab} = 2\ \mathrm{tr}\big[t^a U t^b U^\dagger\big]$ denote the adjoint parallel transporters. Similarly, the magnetic fields are constructed from a combination of the four elementary (1x1) plaquettes in Eq. (A.3) and the eight adjacent rectangular (2x1) plaquettes according to

$$B^a_{i,\mathrm{imp}}(x) \;=\; \frac{\epsilon^{ijk}}{ga^2}\ \mathrm{ReTr}\,\Big(i\tau^a\Big[\frac{5}{3}\sum_{4\square}U^{\square}_{\pm j,\pm k}(x) \\ -\frac{1}{3}\sum_{8\square}U^{\square}_{\pm j,\pm k}(x)\Big]\Big), \tag{A.8}$$

with the different lattice operators illustrated in Fig. A.1.

A.3 Calibration

While the successive application of Eq. (A.6) allows us to follow the change of the Chern-Simons number over the course of the real time evolution, it is useful in this process to re-calibrate the measurement occasionally to ensure that residual errors do not accumulate over time. As illustrated in Figure 2.2, we perform additional calibration steps where we cool from τ_c all the way to the vacuum. Since the Chern-Simons number of the associated vacuum configuration is always an integer, we can get an independent estimate of the Chern-Simons number $N^{\tau_c}_{CS}(t)$ of the cooled configuration according to

$$N^{\tau_c,\mathrm{calib}}_{CS}(t) = N^{vac}_{CS}(t) - \Delta N^{\mathrm{coolingpath}}_{CS}(t)\,, \tag{A.9}$$

which can used to re-calibrate the measurement. Here $\Delta N^{\mathrm{coolingpath}}_{CS}(t)$ denotes the change of difference in Chern-Simons number computed along the cooling path from $\tau = \tau_c$ to the vacuum ($\tau \to \infty$)

$$\Delta N^{\mathrm{coolingpath}}_{CS}(t) = \\ \frac{g^2a^3}{8\pi^2}\int_{\tau_c}^{\infty} d\tau \sum_x E^{cool,a}_i(x,t;\tau)B^{cool,a}_i(x,t;\tau)\,. \tag{A.10}$$

Since cooling all the way to the vacuum is computationally expensive, we follow earlier works and use blocking to reduce the numerical cost of the calibration procedure. Each time blocking is performed, neighboring sets of gauge links are combined into new "blocked" links as illustrated in Fig A.2, which reduces the size of the lattice by a factor of 2^3. Since the effective step width $\delta\tau$ of the cooling can also be increased by a factor of 2^2 after blocking, the

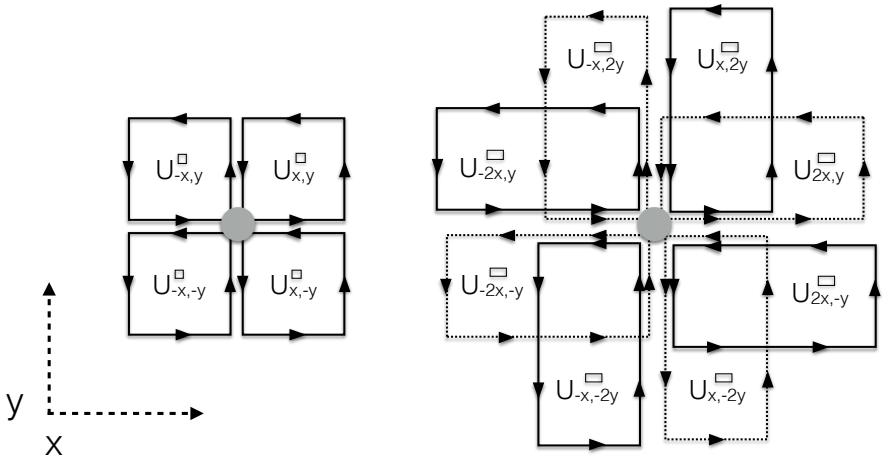

Figure A.1: Illustration of elementary square plaquettes (left) and rectangular plaquettes (right) employed in the computation of the magnetic field strength.

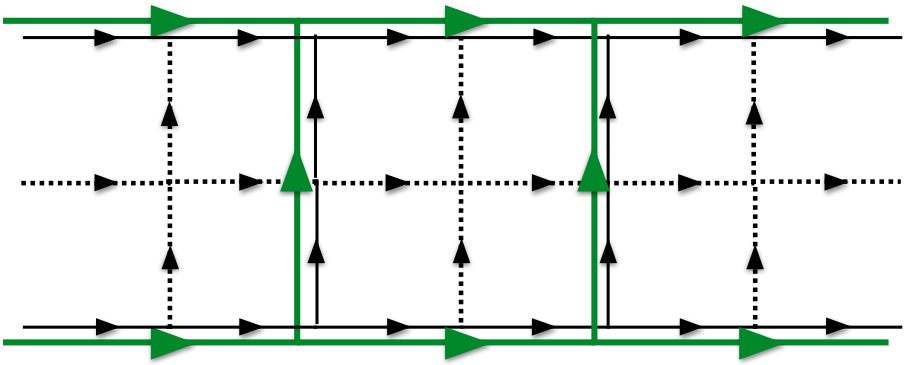

Figure A.2: Illustration of blocking procedure used only during the calibration step. A subset of the original gauge links represented by solid black lines is combined into a coarser lattice of green links.

numerical benefit is enormous and we have used up to two levels of blocking when performing calibration on our largest lattices. When sufficient cooling $\tau a^2 \gtrsim 1$ is performed before each level of blocking we find that the error introduced in the computation of $\Delta N_{CS}^{\text{coolingpath}}(t)$ due to blocking can be kept below the 1% percent level.

By combining the results $\Delta N_{CS}^{\text{coolingpath}}(t_1)$ and $\Delta N_{CS}^{\text{coolingpath}}(t_2)$ of consecutive calibrations with the measurement of the Chern-Simons number difference $N_{CS}^{\tau_c}(t_2) - N_{CS}^{\tau_c}(t_1)$ at the original cooling depth in Eq. (A.6), one can form a trajectory in configuration space which connects the vacuum configurations at t_1 and t_2 such that

$$\begin{aligned} N_{CS}^{vac}(t_2) - N_{CS}^{vac}(t_1) = &-\Delta N_{CS}^{\text{coolingpath}}(t_1) \\ &+N_{CS}^{\tau_c}(t_2) - N_{CS}^{\tau_c}(t_1) + \Delta N_{CS}^{\text{coolingpath}}(t_2)\,. \end{aligned} \tag{A.11}$$

Because the difference in Chern-Simons number of two vacuum configurations $N_{CS}^{vac}(t_1) - N_{CS}^{vac}(t_2)$ on the left hand side is supposed to be an integer, this procedure allows for an

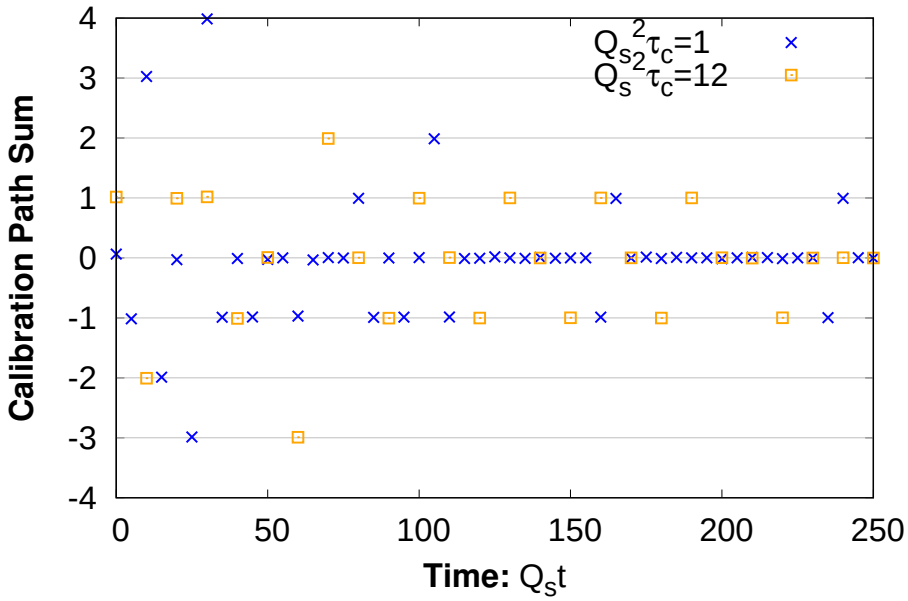

Figure A.3: Space-time integral of the Chern-Simons current computed along a path connecting two vacuum configurations according to the right hand side of Eq. (A.11). Data obtained for a single $N = 96$, $Q_s a = 1$ non-equilibrium configuration.

explicit check of whether the lattice definition of the Chern-Simons current indeed behaves as a total derivative. When evaluating the right hand side of Eq. (A.11), we find that the deviation from integer values is typically less than 2 %. An example of this calibration check is shown Figure A.3, where we plot the values obtained for the right hand side of Eq. (A.11) over the coarse of the non-equilibrium evolution of a single configuration. Excellent agreement with integers can be observed, demonstrating that the measurement is indeed topological.

Appendix B

Slave Field Method

The following appendix is based off of

- M. Mace, S. Schlichting, R. Venugopalan. *Off-equilibrium sphaleron transitions in the Glasma.* Phys.Rev. D93, 074036 (2016). Copyright (2016) by the American Physical Society

We will describe in this appendix the implementation of the slave field method [3]. As discussed in Sec. 2.2.2, it provides an alternative measurement of the integer (topological) part of the Chern-Simons number. The basic philosophy underlying the slave field method is to identify the topological component of the Chern-Simons number with the winding number of the gauge transformation to the topologically trivial sector. The challenge for this method however is to find this gauge transformation at every instance of time and ensure that it is sufficiently slowly varying to allow for a reliable extraction of the winding number.

B.1 Initialization & Slave field dynamics

When performing a slave field measurement, we perform an initial gauge fixing to set the dynamical gauge links and electric field variables such that they satisfy the (minimal) Coulomb gauge condition at initial time $t = 0$. Since after the gauge fixing the configuration is topologically trivial, the initial condition for the slave field then simply becomes $S(x) = \mathbb{1}$. Over the course of the real time evolution of the configuration the Coulomb gauge condition will be violated and one needs to update the slave field to dynamically keep track of the transformation back to Coulomb gauge. We follow the original reference [3] and use an update algorithm based on local lattice gauge fixing techniques to maximize the gauge fixing functional $\sum_x \sum_i \mathrm{ReTr}\; w(x, t+\delta t)$ where

$$w(x,t+\delta t) = S(x,t+\delta t)\sum_i \Big(U_i(x,t+\delta t) S^\dagger(x+\hat{i},t+\delta t) + U_i^\dagger(x-\hat{i},t+\delta t) S^\dagger(x-\hat{i},t+\delta t) \Big), \tag{B.1}$$

Starting from an initial guess $S^{\text{init}}(x, t+\delta t)$ for the slave field $S(x, t+\delta t)$, we perform N_{steps} update steps of the Los Alamos gauge fixing algorithm, setting [375]

$$S(x, t+\delta t) \to S^{\text{new}}(x, t+\delta t) = \tilde{w}^{\dagger}(x, t) S(x, t+\delta t) \ , \tag{B.2}$$

in each step, where $w(x,t)$ is determined from the slave field in the previous step and $\tilde{w}$ denotes the projection of w to $SU(N_c)$, which in the $SU(2)$ case simply takes the form $\tilde{w} = w/\sqrt{det(w)}$.

In order to minimize the number of gauge fixing steps needed to reach acceptable gauge fixing precision, we follow [3] and try to take advantage of the previous update, by setting

$$S^{\text{init}}(x, t+\delta t) = (S(x,t) S^{\dagger}(x, t-\delta t))^m S(x,t) \tag{B.3}$$

with $m = 1 - \delta t/a$ as our initial guess for the slave field, except when the previous step was so large that $\text{ReTr}\big(\mathbb{1} - S(x,t)S^{\dagger}(x,t-\delta t)\big) > 2(1-m)^2$ where we use $S^{\text{init}}(x, t+\delta t) = S(x,t)$ instead. However when the peak-stress

$$PS(t) = \max_x \ \Big(3N_c - \frac{1}{2}\text{ReTr}\ w(x,t)\Big). \tag{B.4}$$

of the previous slave field configuration is above our tolerance $PS(t) > PS_{\max}$, we use $m = (1-\delta t/a)^3$ instead of the above and triple the number of gauge fixing steps N_{steps}. We found that for the small lattices used in our study of the thermal case, we achieve an accurate tracking of the gauge transformation with $N_{steps} = 5$ and $PS_{\max} = 1.2$. However for the larger lattices used in our non-equilibrium study, the local gauge fixing algorithm becomes inefficient and a much larger number of steps is needed. Unfortunately this makes the slave field method computationally too expensive to be of practical use when studying a large number of configurations on large lattices.

Even though the update described above is sufficient to determine the evolution of the slave field, it does not necessarily ensure that (over the course of the real time evolution) the slave field remains sufficiently slowly varying to reliably determine its winding number. However, as pointed out in [3], the smoothness of the slave field can be restored by performing the actual gauge transformation back to Coulomb gauge

$$U_i(x) \to U_i^{(S)}(x) \ , \quad E_i(x) \to E_i^{(S)}(x) \ , \quad S(x) \to \mathbb{1} \ , \tag{B.5}$$

when the peak stress is sufficiently small $PS(t) < PS_{\max}$. In practice, we check after every fifth time step whether this criterion is satisfied and eventually perform the transformation. We also note that, since performing the gauge transformation removes a possible winding, we have to add the winding number of the gauge transformation $S(x,t)$ to all subsequent measurements of the winding number. When the slave field is sufficiently slowly varying, it is then straightforward to determine its winding number using the methodology described in [178, 3].

Appendix C

Eigenmodes of the Dirac Hamiltonian in the helicity basis

The following appendix is based off of

- M. Mace, N. Mueller, S. Schlichting, S. Sharma. *Non-equilibrium study of the Chiral Magnetic Effect from real-time simulations with dynamical fermions.* Phys. Rev. D 95, 036023 (2017). Copyright (2017) by the American Physical Society

In this appendix we derive the eigenmodes for non-interacting fermions in the helicity basis by diagonalizing the Dirac Hamiltonian for Wilson and overlap fermions.

We begin by taking the gamma matrices in the Dirac representation. In the absence of gauge fields ($U = \mathbf{1}$) the eigenfunctions of the Wilson and overlap Dirac equation can be written in the plane wave basis. The spatial momenta and effective mass term for the improved Wilson fermions in this basis are

$$\begin{aligned} p_i^w &= \sum_n \frac{C_n}{a_s} \sin(n a_s q_i) \\ m_{\text{eff}}^w &= m + \sum_{n,i} \frac{2nC_n}{a_s} r_w \sin^2\left(\frac{naq_i}{2}\right) \end{aligned} \tag{C.1}$$

and similarly for massless overlap fermions[a]

$$\begin{aligned} p_i^{ov} &= M \frac{p_i^w}{s} \\ m_{\text{eff}}^{ov} &= M\left(1 + \frac{p_5}{s}\right) \end{aligned} \tag{C.2}$$

[a]For overlap, we always take $r_w = 1$ and the Wilson improvement coefficients $C_1 = 1, C_n = 0$ for $n > 1$.

where

$$\begin{aligned} q_i &= \frac{2\pi n_i}{a_s N_i}, \quad n_i \in 0, ..., N_i - 1 \\ p_5 &= -M + \sum_i \frac{2}{a_s} \sin^2(\frac{a_s q_i}{2}) \\ s &= \sqrt{\sum_i p_i^2 + p_5^2}. \end{aligned} \tag{C.3}$$

With this notation, the eigenvalue problem takes the same form for either discretization; we will we drop the superscript differentiating the two since everything that follows applies equally to both cases. The Hamiltonian in this basis is then

$$H = \begin{pmatrix} m_{\text{eff}} \mathbf{1}_2 & \vec{\sigma} \cdot \vec{p} \\ \vec{\sigma} \cdot \vec{p} & -m_{\text{eff}} \mathbf{1}_2 \end{pmatrix}, \tag{C.4}$$

which has eigenvalues $E_\pm = \pm\sqrt{m_{\text{eff}}^2 + \vec{p}^2}$, where the positive (negative) eigenvalues corresponds to (anti) particles. The corresponding eigenvectors are given as

$$\begin{aligned} u^h(p) &= \frac{E_+ - m_{\text{eff}}}{\sqrt{(E_+ - m_{\text{eff}})^2 + p^2}} \begin{pmatrix} \phi^{(h)}(p) \\ h\frac{E_+ - m_{\text{eff}}}{|p|}\phi^{(h)}(p) \end{pmatrix} \\ v^h(p) &= \frac{E_- - m_{\text{eff}}}{\sqrt{(E_- - m_{\text{eff}})^2 + p^2}} \begin{pmatrix} \phi^{(h)}(-p) \\ h\frac{E_- - m_{\text{eff}}}{|p|}\phi^{(h)}(-p). \end{pmatrix}, \end{aligned} \tag{C.5}$$

Since the Hamiltonian, Eq. (C.4), commutes the helicity operator, the eigenvectors of the Hamiltonian are simultaneously eigenvectors of the helicity operator. We then choose ϕ to be normalized with respect to helicity $\frac{\vec{p}\cdot\vec{\sigma}}{|\vec{p}|}$, so the index h is the helicity and takes values $h = \pm 1$. Now we solve for the ϕ. First, if $(p_x, p_y) \in \{0, N_x/2\} \times \{0, N_y/2\}$, then

$$\phi^+(p) = (1, 0)^T \tag{C.6}$$

$$\phi^-(p) = (0, 1)^T \tag{C.7}$$

otherwise

$$\phi^h(p) = \frac{1}{\sqrt{1 + \frac{(p_z - h|\vec{p}|)^2}{p_x^2 + p_y^2}}} \begin{pmatrix} 1 \\ -\frac{p_z - h\sqrt{p_x^2 + p_y^2 + p_z^2}}{p_x - ip_y} \end{pmatrix} \tag{C.8}$$

For the case $(p_x, p_y, p_z) \in \{0, N_x/2\} \times \{0, N_y/2\} \times \{0, N_z/2\}$, where the linear momentum term vanishes, for $m_{\text{eff}} > 0$

$$u^h(p) = \begin{pmatrix} \phi^h(0) \\ 0 \end{pmatrix}, \quad v^h(p) = \begin{pmatrix} 0 \\ \phi^h(0) \end{pmatrix}, \tag{C.9}$$

while for $m_{\text{eff}} < 0$ we have

$$u^h(p) = \begin{pmatrix} 0 \\ \phi^h(0) \end{pmatrix}, \quad v^h(p) = \begin{pmatrix} \phi^h(0) \\ 0 \end{pmatrix}. \tag{C.10}$$

While this is most obvious in the last case, the orthogonality conditions

$$u^{\dagger}_{q,\lambda} u_{q,\lambda'} = \delta_{\lambda,\lambda'} \tag{C.11}$$

$$v^{\dagger}_{q,\lambda} v_{q,\lambda'} = \delta_{\lambda,\lambda'} \tag{C.12}$$

$$u^{\dagger}_{q,\lambda} v_{q,\lambda'} = v^{\dagger}_{q,\lambda} u_{q,\lambda'} = 0 \tag{C.13}$$

are held for all eigenvectors. We have now constructed the helicity eigenmodes for the free Wilson and overlap Dirac Hamiltonian.

Appendix D

Derivation of the Minkowski overlap Hamiltonian

The following appendix is based off of

- M. Mace, N. Mueller, S. Schlichting, S. Sharma. *Non-equilibrium study of the Chiral Magnetic Effect from real-time simulations with dynamical fermions.* Phys. Rev. D 95, 036023 (2017). Copyright (2017) by the American Physical Society

In this appendix, we outline our construction of the overlap Hamiltonian in 3+1D Minkowski spacetime, applicable for real-time lattice gauge theory simulations. The spatial overlap operator for one massless quark flavor is defined as

$$-i\not{D}_{ov} \;=\; M\Big(\mathbf{1}+\gamma_5\frac{Q}{\sqrt{Q^2}}\Big), \tag{D.1}$$

where a suitable choice of the kernel Q is

$$Q \equiv \gamma_5 \not{D}_W(M), \tag{D.2}$$

with $-i\not{D}_W(M)$ being the massless Wilson Dirac operator in 3+1D Minkowski spacetime. Here the parameter $M \in [0,2)$ can be interpreted as the height of the domain wall or the defect that localizes the chiral fermions on 4D Euclidean spacetime starting from a 5D domain wall formalism [34].

In order to derive the real-time evolution of fermion modes ψ with mass $m = 0$ and at any instant of time t, we solve the overlap Dirac equation on the lattice, $-i\not{D}_{ov}\psi = 0$, where

$$-i\not{D}_{ov}\psi \;=\; M\Big[\mathbf{1}+\frac{-i\not{D}_W(M)}{\sqrt{\gamma_5(-i\not{D}_W(M))\gamma_5(-i\not{D}_W(M))}}\Big]\psi \tag{D.3}$$

In the temporal gauge and furthermore choosing the lattice spacing along temporal direction to be fine enough than the other relevant scales in the operator, such that $a_t \ll M, a_s$, the

dimensionless overlap operator is simply

$$-i\not{D}_{ov} = M\Big[\mathbf{1} + \frac{-i\not{D}^s_W - ia_t\not{\partial}_t - M}{\sqrt{\not{D}^s_W \not{D}^{s\dagger}_W + a_t^2\partial_t^2 + M^2}}\Big]\,. \tag{D.4}$$

If we perform an expansion in powers of a_t and keep terms which are leading order in a_t, we get the RHS of Eq. (D.4) to be,

$$M\Big[\mathbf{1} + \frac{-i\not{D}^s_W - M}{\sqrt{\not{D}^s_W \not{D}^{s\dagger}_W + M^2}} + \frac{-ia_t\not{\partial}_t}{\sqrt{\not{D}^s_W \not{D}^{s\dagger}_W + M^2}}\Big] \tag{D.5}$$

In the denominator of the second term of Eq. (D.5), the domain-wall height scales as $1/a_s$, whereas the spatial Wilson-Dirac operator scales as linear power in a_s, therefore the overlap operator in Eq. (D.5) simply reduces to

$$-i\not{D}_{ov} = -ia_t\not{\partial}_t + M\Big[\mathbf{1} + \frac{-i\not{D}^s_W - M}{\sqrt{\not{D}^s_W \not{D}^{s\dagger}_W + M^2}}\Big] \tag{D.6}$$

The overlap Dirac equation in Eq. (D.3) can be then simply written as a time evolution equation of the form,

$$i\gamma^0\partial_t\psi = -i\not{D}^s_{ov}\psi \tag{D.7}$$

where $-i\not{D}^s_{ov}$ is the spatial overlap operator given by

$$-i\not{D}^s_{ov} \;=\; M\Big[\mathbf{1} + \frac{-i\not{D}^s_W(M)}{\sqrt{\gamma_5(-i\not{D}^s_W(M))\gamma_5(-i\not{D}^s_W(M))}}\Big]. \tag{D.8}$$

Eq. (D.7) is the analogue of the corresponding evolution equation with Wilson fermion discretization given in Eq. (3.5). Using γ_5 and γ_0 hermiticity of $-i\not{D}^s_W$, we can recast Eq. (D.7) as a Hamiltonian equation with the overlap Hamiltonian in 3D Minkowski space for massless fermions defined as,

$$H_{ov} = -i\gamma_0\not{D}^s_{ov} \;=\; M\Big(\gamma^0 + \frac{H_W(M)}{\sqrt{H_W(M)^2}}\Big), \tag{D.9}$$

where H_W is the Wilson Hamiltonian defined in Eq. (3.1) but with $C_n = 0$ for $n \geq 2$ and the mass m being replaced by the negative of the domain wall height M.

Appendix E

Convergence study of net axial charge for Wilson and Overlap fermions

The following appendix is based off of

- M. Mace, N. Mueller, S. Schlichting, S. Sharma. *Non-equilibrium study of the Chiral Magnetic Effect from real-time simulations with dynamical fermions.* Phys. Rev. D 95, 036023 (2017). Copyright (2017) by the American Physical Society

In this appendix we will discuss finite size effects and convergence of our Wilson (see Sec. 3.1.1) and overlap (see Sec. 3.1.2) lattice fermions, as well as compare the properties of two fermion discretizations. In order to be able to concentrate on the chiral properties of the fermions as a function of volume, improvement, and discretization, we will only consider the single sphaleron transition introduced in Sec. 3.1.3. We keep $r_{\rm sph}/a = 6$ fixed for all simulations and consider only isotropic lattices in this section, and will keep the Wilson r-parameter fixed at $r_w = 1$ for all comparisons. In this section we work in the nearly massless limit for the Wilson fermions ($mr_{\rm sph} = 1.9 \cdot 10^{-2}$) and the massless limit for overlap fermions, so the integrated anomaly equation reduces to Eq. (3.39). We have previously shown for Wilson fermions how both the unintegrated (see Fig. 3.3) and integrated (Figure 3 in [225]) anomaly equation are maintained as a function of mass. For the Wilson fermions, we first pick a volume, $N^3 = 16^3$, and study the total axial charge created as a function of time for various levels of operator improvement, as was discussed in Sec. 3.1.1. This is plotted in Fig. E.1. We can clearly see that at Leading Order (LO), the standard unimproved Wilson fermion formulation, there is significant deviation, at the 25% level, from the Chern Simons term $-2\Delta N_{CS}$, which is quantified in the lower panel of Fig. E.1. However, upon going to one level of improvement, Next to Leading Order improvement (NLO), we see that this disagreement disappears. At Next to Next to Leading Order (NNLO) improvement, we see no noticeable difference from NLO, and thus see that our improvement scheme has converged. In practice, we find that in all cases in our current study, NLO is sufficient and nothing additional is gained by going to NNLO.

Now we need to understand how important finite volume effects are in our study. This is shown in Fig. E.2. Here we look at the axial charge generated by NLO improved Wilson

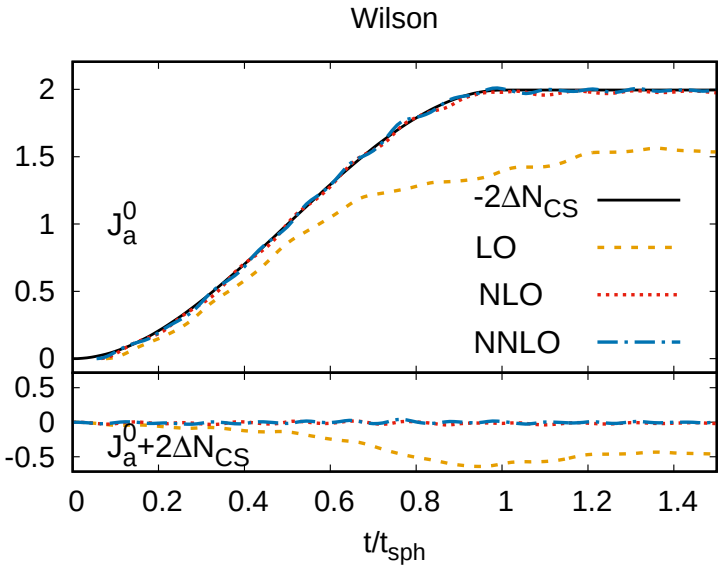

Figure E.1: A comparison of the net axial charge generated during a sphaleron transition for a fixed volume of $N = 16$ using $mr_{\text{sph}} = 1.9 \cdot 10^{-2}$ Wilson fermions with different operator improvements. Top: Already at NLO we see that the net axial charge tracks ΔN_{CS} due to the sphaleron transition. Bottom: Deviations from Eq. (3.39) are shown.

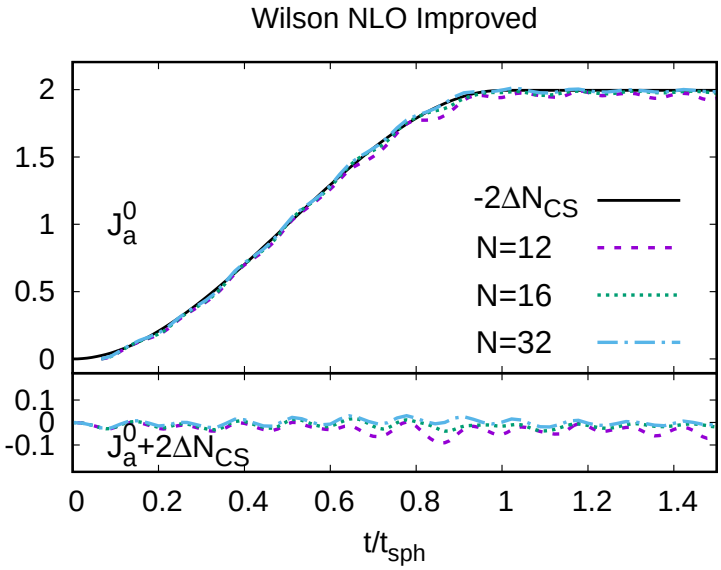

Figure E.2: A comparison of the net axial charge generated during a sphaleron transition using $mr_{\text{sph}} = 1.9 \cdot 10^{-2}$ improved Wilson (NLO) fermions for different lattice volumes. Top: At N=16 and beyond the net axial charge tracks ΔN_{CS} due to the sphaleron transition. Bottom: Deviations from Eq. (3.39) are shown.

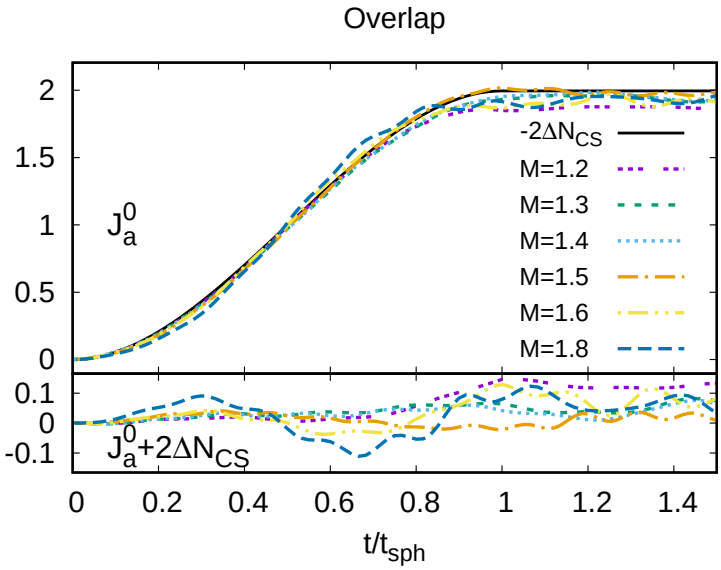

Figure E.3: A comparison of the net axial charge generated during a sphaleron transition using massless overlap fermions for different domain wall heights M at a fixed lattice volume $N = 16$. Top: For $M \in [1.4, 1.6)$, the net axial charge tracks ΔN_{CS} due to the sphaleron transition. Bottom: Deviations from Eq. (3.39) are shown.

fermions for three volumes. It is clear from the lower panel of Fig. E.2 that for $N = 12 = 2r_{\text{sph}}/a$, there are clear finite volume effects that lead to large oscillations of the J^0_a around the sphaleron transition from Eq. (3.39). This is then subsequently improved by going to a volume $N = 16 = 2.67r_{\text{sph}}/a$, where we can see noticeable improvement. To test this convergence, we further look at $N = 32 = 5.34r_{\text{sph}}/a$; here we see that there is no difference in the average deviations from the Chern-Simons term as compared to the $N = 16 = 2.67r_{\text{sph}}/a$.

However, we should note that this is only for resolving the creation of axial charge from a single localized sphaleron transition. To look at charge transport as a function of time, like we studied in Sec 3.3, we need even larger volumes, especially in the magnetic field direction. Typically we choose a spatially anisotropic lattice, where the transverse length is $N_{trans} \geq 2r_{\text{sph}}/a$, while along the direction of the magnetic field $N_z \gg 2r_{\text{sph}}/a$ (a typical choice is $N^3 = 16^2 \times 32 - 24^2 \times 64$). Moreover, the transverse size of the lattice has to be large enough to accommodate the cyclotron orbits of charged particles. In practice this constraint limits the available magnetic field strength to larger magnetic flux quanta.

Next, for the overlap fermions, we proceed in the same manner. Instead of improving the Wilson kernel, we vary the domain wall height M for a fixed isotropic lattice $N = 16$. As we see in Fig. E.3, values in the range of $M \in [1.4, 1.6)$ give the best results; we choose $M = 1.5$. We have verified that the volume dependence of the currents for the overlap is similar to the Wilson fermions with NLO improvement, which is evident from Fig. 3.1.

In summary, for Wilson fermions, NLO improvement is necessary and sufficient to accurately reproduce the anomaly. At this level, we find that it gives comparable results to the overlap fermions, which we find that for a well tuned domain wall mass M we can reproduce the anomaly relation even on reasonably small lattices. Additionally, we find that for spatial lattice sizes of $N = 2\ r_{\text{sph}}/a$, finite volume effects are somewhat noticeable, but seem to be

completely under control for lattice size $N > 2r_{\rm sph}/a$. This will serve also as crucial input for how fine to make one's lattice for future studies with more realistic gauge field configurations, where the size sphalerons is set by physical scales of the problem.

Appendix F

Construction of topologically non-trivial lattice map

The following appendix is based off of

- M. Mace, N. Mueller, S. Schlichting, S. Sharma. *Non-equilibrium study of the Chiral Magnetic Effect from real-time simulations with dynamical fermions.* Phys. Rev. D 95, 036023 (2017). Copyright (2017) by the American Physical Society

Below we describe the construction of a topologically non-trivial gauge transformation, employed in Sec. 3.1.3 for the construction of our handmade sphaleron transition. We first note that in the continuum, gauge transformations $G : \mathbb{R}^3 \cup \{\infty\} \to SU(2) \simeq S^3$ parametrized according to

$$G_{\mathbf{x}} = \alpha_0(\mathbf{x})\mathbf{1} + i\alpha^a(\mathbf{x})\sigma^a, \qquad \alpha_0^2 + \alpha^2 = 1\ . \tag{F.1}$$

where $a = 1, \cdots, 3$ and $\alpha^2 = \alpha_a\alpha^a$ can be classified according to the homotopy classes $\pi_3(\mathbb{R}^3 \cup \{\infty\}) \simeq \mathbb{Z}$ characterized by the topological winding number or Brouwer degree $deg(G)$ of the map. Even though on a lattice with periodic boundary conditions the corresponding map is from the three torus $\mathbb{T}^3$ to the gauge group, the homotopy classes $\pi_3(\mathbb{R}^3 \cup \{\infty\}) \simeq Z$ and $\pi_3(\mathbb{T}^3) \simeq \mathbb{Z}$ are identical and the same classification scheme applies. Our strategy to construct a topologically non-trivial lattice map is to perform a multi-step mapping; first from the set of lattice points to the three torus, then to one-point compactified real space, and finally to the gauge group, such that

$$\mathbf{x} \to \mathbf{x}_T \to \mathbf{x}_{\mathbb{R}} \to \alpha \tag{F.2}$$

with $\mathbf{x} \in \{0, \cdots, N_x - 1\} \times \{0, \cdots, N_y - 1\} \times \{0, \cdots, N_z - 1\}$, $\mathbf{x}_T \in T^3$, $\mathbf{x}_{\mathbb{R}} \in \mathbb{R}^3 \cup \{\infty\}$ and $\alpha \in S^3 \simeq SU(2)$. Since we wish to obtain a non-trivial result ($G_{\mathbf{x}} \neq 1$) only on a characteristic scale r_{sph} around the center $(x, y, z) = (N_x/2, N_y/2, N_z/2)$, we perform a distorted map of the lattice points to real space, given explicitly by the following steps

$$x_T^i = 2\pi \frac{\arctan\left(\frac{x^i - N^i/2}{r_{\text{sph}}}\right) - \arctan\left(\frac{-N^i/2}{r_{\text{sph}}}\right)}{\arctan\left(\frac{N^i/2}{r_{\text{sph}}}\right) - \arctan\left(\frac{-N^i/2}{r_{\text{sph}}}\right)}, \tag{F.3}$$

where the denominator explicitly ensures a smooth profile at the periodic edges, and subsequently

$$x^i_{\mathbb{R}} = \tan\left[\frac{1}{2}\left(x^i_T - \pi\right)\right], \tag{F.4}$$

which identifies a unique point in $\mathbb{R}^3 \cup \{\infty\}$ with each lattice site. Since, in order to ensure that the final map between $\mathbb{R}^3 \cup \{\infty\}$ and $\alpha \in S^3 \simeq SU(2)$ has a non-vanishing degree, it is sufficient to require the map to be surjective; we simply choose the final mapping to be given by a stereographic projection, such that

$$\begin{aligned} \alpha_0 &= \frac{\mathbf{x}^2_{\mathbb{R}} - 1}{\mathbf{x}^2_{\mathbb{R}} + 1} \\ \alpha^a &= (\alpha_0 - 1) \cdot x^i_{\mathbb{R}} \delta^{ia}. \end{aligned} \tag{F.5}$$

Based on the explicit formula for the Brouwer degree, it is straightforward to verify that this map has topological winding number equal to unity.

Appendix G

Glasma graph approximation

The following appendix is based off of

- K. Dusling, M. Mace, R. Venugopalan. *Parton model description of multiparticle azimuthal correlations in pA collisions.* Phys. Rev. D 97, 016014 (2018); arXiv:1706.06260 [hep-ph]. Copyright (2017) by the American Physical Society

In this section, we show how our present calculation fundamentally differs from the so-called "Glasma graph" result [83, 270, 84, 85, 86, 87, 88]. The Glasma graph approximation is constructed by considering all possible two-gluon exchanges between quarks comprising the projectile and the target nucleus under the assumption of Gaussian statistics. The expectation value of n-Wilson lines in the Glasma graph approximation can be evaluated by expanding the path ordered exponential of the Wilson line to order n in the coupling constant. The resulting expectation value of gauge fields are then evaluated by re-expressing higher order expectation values as a product of two-point functions. This procedure was followed in [268] in order to evaluate the dipole-dipole correlator in the Glasma graph approximation. Here we extend the derivation and results of [268] to higher order correlators but taking a more diagrammatic approach.

Diagrammatically, the Glasma graph approximation amounts to replacing each two-gluon exchange with the expectation value of a single dipole operator. For example, for single quark scattering we find the relation of Fig. G.1. While the tadpole terms are explicitly shown

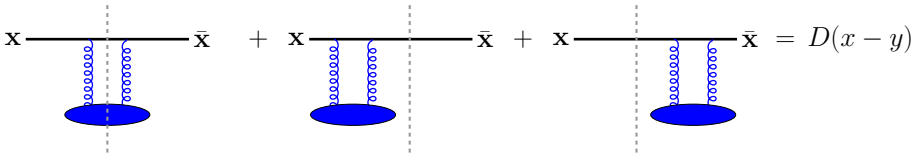

Figure G.1: Single quark multiple-scattering off the target nucleus.

in the single scattering case in Fig. G.1, for higher point functions diagrams containing two gluons on the same quark are power suppressed by either $k_\perp/Q_s \ll 1$ or $1/\left(BQ_s^2\right) \ll 1$. (A line containing two quarks on opposite sides of the cut – corresponding to a gluon connecting

a quark with its conjugate amplitude at a different coordinate – are not suppressed and therefore included in what follows.) While these additional terms are formally higher order and will be ignored in the discussion to follow we should point out that they were found to be important in obtaining a quantitative agreement with experiment [85].

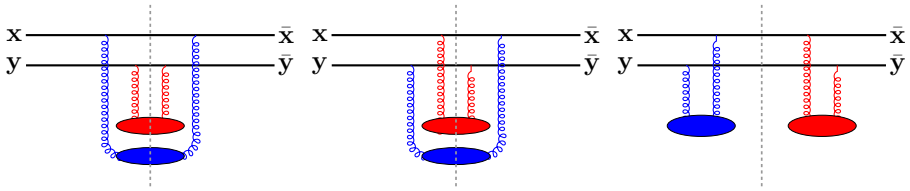

Figure G.2: The three diagrams for two quarks scattering in the Glasma graph approximation. The leftmost diagram is a disconnected contribution and equivalent to the square of single quark scattering.

One can generate all possible Glasma graphs by starting with the completely disconnected diagram whereby each quark multiple-scatters independently off the target. We show an example of this completely disconnected contribution for two quark scattering as the left most diagram of Fig. G.2.

Further diagrams are generated by finding unique exchanges of coordinates (exchanging two gluon endpoints) along with an accompanying (N_c^2-1) suppression for each exchange. There are two unique topologies for two quark scattering as shown in Fig. G.2. The resulting expression for the Glasma graph approximation to the expectation value of two dipole operators is therefore

$$\begin{aligned}\langle D(\mathbf{x},\bar{\mathbf{x}})D(\mathbf{y},\bar{\mathbf{y}})\rangle &= D(\mathbf{x},\bar{\mathbf{x}})D(\mathbf{y},\bar{\mathbf{y}}) \\ &+ \frac{1}{(N_c^2-1)}\left[D(\bar{\mathbf{x}}-\mathbf{y})D(\mathbf{x}-\bar{\mathbf{y}})+D(\bar{\mathbf{x}}-\bar{\mathbf{y}})D(\mathbf{x}-\mathbf{y})\right].\end{aligned} \tag{G.1}$$

Higher point correlators can be found in a similar fashion. For n quarks there are $(n-1)!! \equiv n(n-2)\cdots 3\cdot 1$ diagrams resulting from all possible unique contractions between quark lines. For a correlation among six Wilson lines there are $5\cdot 3\cdot 1 = 15$ pair-wise contractions while for a correlator among eight Wilson lines there are $7\cdot 5\cdot 3\cdot 1 = 105$ pair wise contractions.

As an aside, we remind the reader that the combinatorics discussed above are relevant for a dilute-dense framework. A Glasma graph approximation has also been employed in the dense-dense limit which was shown to have $(n-1)!!^2$ diagrams for n-gluon production. In the dense-dense limit there would be $15^2 = 225$ and $105^2 = 11025$ diagrams for the six- and eight-point functions respectively as shown previously in [376] and [323].

We now come to the expectation value of four dipoles in the Glasma graph calculation following the procedure outlined above. The starting point is the completely disconnected contribution where each of the four quarks scatter independently as shown in the left diagram in Fig. G.3.

Starting from the disconnected diagram there are 12 unique coordinate exchanges that can be made. One example is shown in the right diagram of Fig. G.3 where the coordinates

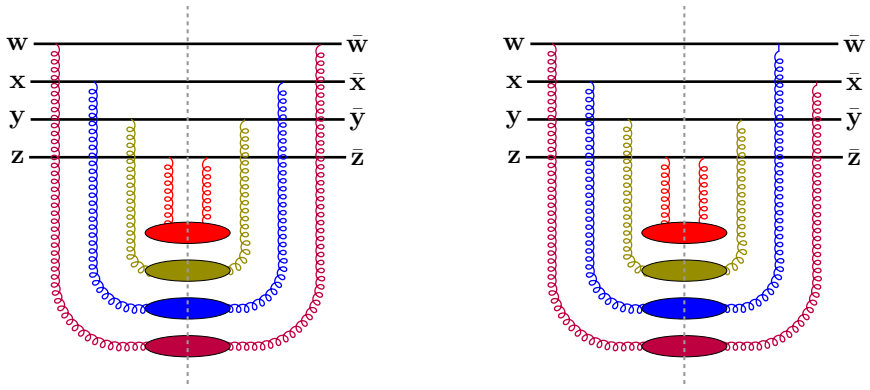

Figure G.3: Left: Completely disconnected Glasma graph for four-quark scattering. Right: Example of one of the 12 diagrams contained within $\mathcal{T}_1$ obtained from an exchange of one pair of coordinates – in this case $\bar{\mathbf{x}}$ and $\bar{\mathbf{w}}$.

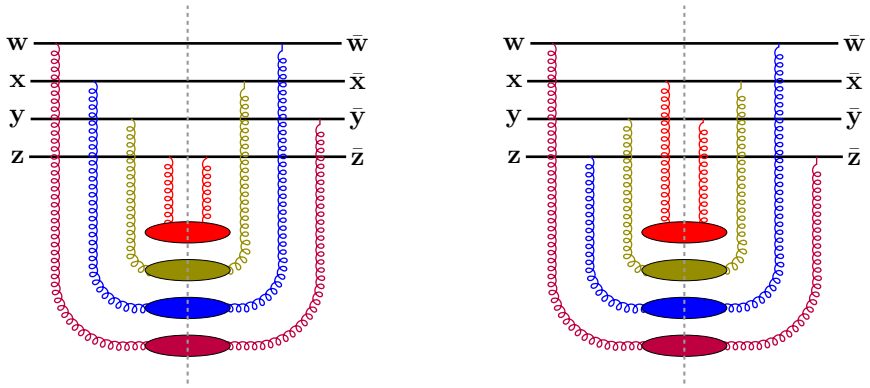

Figure G.4: The diagram on the left is an example of one of 32 diagrams where three-quarks are completely connected and one scatters independently – in this case the quark at x. The diagram on the right shows one of 12 diagrams which factorizes into two two-dipole connected subgraphs.

$\bar{\mathbf{x}}$ and $\bar{\mathbf{w}}$ have been swapped. These 12 diagrams resulting from a single coordinate exchange results in a contribution of $(N_c^2-1)^{-1}\mathcal{T}_1$ where

$$\mathcal{T}_1 = D(\mathbf{w},\bar{\mathbf{x}})D(\mathbf{x},\bar{\mathbf{w}})D(\mathbf{y},\bar{\mathbf{y}})D(\mathbf{z},\bar{\mathbf{z}}) + \cdots . \tag{G.2}$$

We next consider diagrams resulting from unique and non-trivial two coordinate exchanges. There are two classes of diagrams which enter at this order. The first is shown in the left diagram of Fig. G.4. The diagram factorizes into two sub-graphs, one being a completely connected three-quark scattering and the other a single independent quark scattering. There are 32 such diagrams which will contribute with a factor of $(N_c^2-1)^{-2}\mathcal{T}_{2a}$ where

$$\mathcal{T}_{2a} \;=\; D(\mathbf{w},\bar{\mathbf{y}})D(\mathbf{x},\bar{\mathbf{w}})D(\mathbf{y},\bar{\mathbf{x}})D(\mathbf{z},\bar{\mathbf{z}}) + \cdots . \tag{G.3}$$

The second class of diagram is shown in the right of Fig. G.4. It again factorizes into two sub-graphs but in this case each sub-graph is a completely connected two-quark scattering

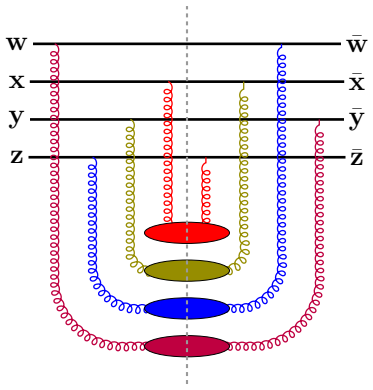

Figure G.5: One of the 48 diagrams completely connected four-quark diagrams included in $\mathcal{T}_3$.

event (*i.e.* one of the two connected graphs shown in Fig. G.2). There are 12 such diagrams which will contribute as $(N_c^2-1)^{-2}\,\mathcal{T}_{2b}$ where

$$\mathcal{T}_{2b} \;=\; D(\mathbf{w},\bar{\mathbf{z}})D(\mathbf{z},\bar{\mathbf{w}})D(\mathbf{x},\bar{\mathbf{y}})D(\mathbf{y},\bar{\mathbf{x}}) + \cdots \tag{G.4}$$

The last set of diagrams correspond to those obtained by three unique and non-trivial coordinate exchanges. An example of such a diagram is shown in Fig. G.5. There are 48 such diagrams which contribute as $(N_c^2-1)^{-3}\,\mathcal{T}_3$ where

$$\mathcal{T}_3 = D(\mathbf{w},\bar{\mathbf{y}})D(\mathbf{z},\bar{\mathbf{w}})D(\mathbf{x},\bar{\mathbf{z}})D(\mathbf{y},\bar{\mathbf{x}}) + \cdots \tag{G.5}$$

Putting all of the diagrams together, we arrive at the final expression for the expectation value of four dipoles in the Glasma graph approximation,

$$\begin{aligned}
\langle D(\mathbf{w},\bar{\mathbf{w}})D(\mathbf{x},\bar{\mathbf{x}})D(\mathbf{y},\bar{\mathbf{y}})D(\mathbf{z},\bar{\mathbf{z}})\rangle \;&=\; D(\mathbf{w},\bar{\mathbf{w}})D(\mathbf{x},\bar{\mathbf{x}})D(\mathbf{y},\bar{\mathbf{y}})D(\mathbf{z},\bar{\mathbf{z}}) \\
&+\; \frac{1}{(N_c^2-1)}\mathcal{T}_1(\mathbf{w},\bar{\mathbf{w}},\mathbf{x},\bar{\mathbf{x}},\mathbf{y},\bar{\mathbf{y}},\mathbf{z},\bar{\mathbf{z}}) \\
&+\; \frac{1}{(N_c^2-1)^2}\mathcal{T}_{2a}(\mathbf{w},\bar{\mathbf{w}},\mathbf{x},\bar{\mathbf{x}},\mathbf{y},\bar{\mathbf{y}},\mathbf{z},\bar{\mathbf{z}}) \\
&+\; \frac{1}{(N_c^2-1)^2}\mathcal{T}_{2b}(\mathbf{w},\bar{\mathbf{w}},\mathbf{x},\bar{\mathbf{x}},\mathbf{y},\bar{\mathbf{y}},\mathbf{z},\bar{\mathbf{z}}) \\
&+\; \frac{1}{(N_c^2-1)^3}\mathcal{T}_3(\mathbf{w},\bar{\mathbf{w}},\mathbf{x},\bar{\mathbf{x}},\mathbf{y},\bar{\mathbf{y}},\mathbf{z},\bar{\mathbf{z}})\,.
\end{aligned} \tag{G.6}$$

We now come to the evaluation of the four-particle cumulant using the above Glasma graph approximation in the four-particle inclusive distribution, where the four-particle cumulant is defined in Eq. (4.40). The Glasma graph approximation implicitly assumes that $(BQ_s^2) \gg 1$ and one must take this power counting into consideration when taking the ratios in the above expression for the cumulants. In order to see this more clearly let us start with

the expression for the double inclusive distribution,

$$\frac{d^2N}{d^2p_1\,d^2p_2} = \frac{1}{(\pi B_p)^2}\frac{1}{(2\pi)^4}\int_{r_1r_2R_1R_2} e^{ip_1\cdot r_1}e^{ip_2\cdot r_2}e^{-r_1^2/4B_p}e^{-R_1^2/B_p}e^{-r_2^2/4B_p}e^{-R_2^2/B_p} \cdot \left\langle D\left(R_1+\frac{r_1}{2},R_1-\frac{r_1}{2}\right)D\left(R_2+\frac{r_2}{2},R_2-\frac{r_2}{2}\right)\right\rangle . \tag{G.7}$$

We can evaluate the single inclusive multiplicity by integrating over d^2p_1 and d^2p_2 resulting in

$$N = \frac{1}{(\pi B_p)^2}\int_{R_1R_2}\langle D(R_1,R_1)\,D(R_2,R_2)\rangle\, e^{-R_1^2/B_p}e^{-R_2^2/B_p} . \tag{G.8}$$

In the full nonlinear theory (without approximation) we know that

$$\langle D(R_1,R_1)\,D(R_2,R_2)\rangle = 1 \tag{G.9}$$

and therefore $N = 1$. However, in the Glasma graph approximation the dipole-dipole correlator is replaced by Eq. (G.2) resulting in the following expression for the total multiplicity,

$$\begin{aligned} N &= 1+\frac{2}{(N_c^2-1)(\pi B_p)^2}\int_{R_1R_2} D(R_1-R_2)^2\, e^{-R_1^2/B_p}e^{-R_2^2/B_p} \\ &= 1+\frac{2}{(N_c^2-1)}\frac{1}{B_pQ^2+1}, \end{aligned} \tag{G.10}$$

violating unitarity by a term of order $1/(BQ_s^2) \ll 1$. When evaluating the cumulant in Eq. (4.40) one should formally only keep the leading order terms in $1/(BQ_s^2)$. In practice this means retaining only the leading disconnected contribution in the two terms $\kappa_0\{4\}$ and $\kappa_0\{2\}$ appearing in the denominators; these terms were defined in Eq. (4.41). For consistency within the Glasma graph approximation we should therefore take $\kappa_0\{4\} = (\kappa_0\{2\})^2 = (\kappa_0\{1\})^4$ where $\kappa_0\{1\}$ is just the single-inclusive distribution.

Now coming to the numerator, due to rotational invariance $\mathcal{T}_1$ and $\mathcal{T}_{2a}$ do not contribute to $\kappa_2\{4\}$. Out of the twelve diagrams in $\mathcal{T}_{2b}$ four vanish by rotational invariance and the remaining eight cancel with the term $2(\kappa_2\{2\}/\kappa_0\{2\})^2$. So within the Glasma graph approximation the cumulant can be evaluated using

$$c_2\{4\} = \frac{\kappa_2\{4\}[\mathcal{T}_3]}{\kappa_0\{1\}^4}, \tag{G.11}$$

where $\kappa_2\{4\}$ is evaluated using the 48 diagrams contained within $\mathcal{T}_3$. With this, we compare this Glasma graph result with the full non-linear result introduced in Sec. 4.3 in Fig. 4.18 in the main text, with accompanying discussion in Sec. 4.5.4.

Bibliography

[1] T. D. N. S. A. Committee, (2008), 0809.3137.

[2] ZEUS, H1, H. Abramowicz *et al.*, Eur. Phys. J. **C75**, 580 (2015), 1506.06042.

[3] G. D. Moore and N. Turok, Phys.Rev. **D56**, 6533 (1997), hep-ph/9703266.

[4] H. Kowalski and D. Teaney, Phys. Rev. **D68**, 114005 (2003), hep-ph/0304189.

[5] B. Schenke, P. Tribedy, and R. Venugopalan, Phys. Rev. Lett. **108**, 252301 (2012), 1202.6646.

[6] STAR, B. I. Abelev *et al.*, Phys. Rev. **C79**, 034909 (2009), 0808.2041.

[7] PHENIX, C. Aidala *et al.*, (2018), 1805.02973.

[8] ATLAS, The ATLAS collaboration, ATLAS-CONF-2018-012 (2018).

[9] F. Gelis, E. Iancu, J. Jalilian-Marian, and R. Venugopalan, Ann. Rev. Nucl. Part. Sci. **60**, 463 (2010), 1002.0333.

[10] J. C. Collins and M. J. Perry, Phys. Rev. Lett. **34**, 1353 (1975).

[11] N. Cabibbo and G. Parisi, Phys. Lett. **59B**, 67 (1975).

[12] B. A. Freedman and L. D. McLerran, Phys. Rev. **D16**, 1169 (1977).

[13] G. Chapline and M. Nauenberg, Phys. Rev. **D16**, 450 (1977).

[14] E. V. Shuryak, Sov. Phys. JETP **47**, 212 (1978), [Zh. Eksp. Teor. Fiz.74,408(1978)].

[15] H. A. Grunder, C. W. Leemann, and F. B. Selph, Relativistic Heavy Ion Accelerators, in *Proceedings: 10th International Conference on High-Energy Accelerators, Protvino, Jul 1977. 1.*, pp. 321–338, 1977.

[16] M. Gell-Mann, Physics Letters **8**, 214 (1964).

[17] G. Zweig, (1964).

[18] E. D. Bloom *et al.*, Phys. Rev. Lett. **23**, 930 (1969).

[19] M. Breidenbach *et al.*, Phys. Rev. Lett. **23**, 935 (1969).

[20] R. P. Feynman, *The Behavior of Hadron Collisions at Extreme Energies* (Springer Netherlands, Dordrecht, 1988), pp. 289–304.

[21] J. D. Bjorken and E. A. Paschos, Phys. Rev. **185**, 1975 (1969).

[22] D. J. Gross and F. Wilczek, Phys. Rev. Lett. **30**, 1343 (1973).

[23] H. D. Politzer, Phys. Rev. Lett. **30**, 1346 (1973).

[24] Particle Data Group, C. Patrignani *et al.*, Chin. Phys. **C40**, 100001 (2016).

[25] LHCb, R. Aaij *et al.*, Phys. Rev. Lett. **115**, 072001 (2015), 1507.03414.

[26] A. Bazavov *et al.*, Phys. Rev. **D95**, 054504 (2017), 1701.04325.

[27] S. Borsanyi *et al.*, (2018), 1805.04445.

[28] M. A. Stephanov, Prog. Theor. Phys. Suppl. **153**, 139 (2004), hep-ph/0402115, [Int. J. Mod. Phys.A20,4387(2005)].

[29] M. Gyulassy and L. McLerran, Nucl. Phys. **A750**, 30 (2005), nucl-th/0405013.

[30] K. G. Wilson, Phys. Rev. **D10**, 2445 (1974), [,319(1974)].

[31] K. G. Wilson, Subnucl. Ser. **13**, 13 (1977).

[32] R. Narayanan and H. Neuberger, Phys. Rev. Lett. **71**, 3251 (1993), hep-lat/9308011.

[33] H. Neuberger, Phys. Lett. **B417**, 141 (1998), hep-lat/9707022.

[34] D. B. Kaplan, Phys. Lett. **B288**, 342 (1992), hep-lat/9206013.

[35] H. B. Nielsen and M. Ninomiya, Nucl. Phys. **B185**, 20 (1981), [,533(1980)].

[36] H. B. Nielsen and M. Ninomiya, Nucl. Phys. **B193**, 173 (1981).

[37] C. Gattringer and C. B. Lang, Lect. Notes Phys. **788**, 1 (2010).

[38] J. B. Kogut and L. Susskind, Phys. Rev. **D11**, 395 (1975).

[39] J. Berges, S. Scheffler, and D. Sexty, Phys. Rev. **D77**, 034504 (2008), 0712.3514.

[40] J. Berges, S. Scheffler, and D. Sexty, Phys. Lett. **B681**, 362 (2009), 0811.4293.

[41] S. Schlichting, *Non-Equilibrium Dynamics and Thermalization of Weakly Coupled Non-Abelian Plasmas*, PhD thesis, Ruperto-Carola University of Heidelberg, 2013.

[42] M. Gyulassy, The QGP discovered at RHIC, in *Structure and dynamics of elementary matter. Proceedings, NATO Advanced Study Institute, Camyuva-Kemer, Turkey, September 22-October 2, 2003*, pp. 159–182, 2004, nucl-th/0403032.

[43] G. Aarts, J. Phys. Conf. Ser. **706**, 022004 (2016), 1512.05145.

[44] L. V. Gribov, E. M. Levin, and M. G. Ryskin, Phys. Rept. **100**, 1 (1983).

[45] Y. V. Kovchegov and E. Levin *Quantum chromodynamics at high energy* Vol. 33 (Cambridge University Press, 2012).

[46] E. Iancu and R. Venugopalan, The Color glass condensate and high-energy scattering in QCD, in *Quark-gluon plasma 4*, edited by R. C. Hwa and X.-N. Wang, pp. 249–3363, 2003, hep-ph/0303204.

[47] E. Iancu, A. Leonidov, and L. D. McLerran, Nucl. Phys. **A692**, 583 (2001), hep-ph/0011241.

[48] L. D. McLerran and R. Venugopalan, Phys. Rev. **D49**, 2233 (1994), hep-ph/9309289.

[49] L. D. McLerran and R. Venugopalan, Phys. Rev. **D49**, 3352 (1994), hep-ph/9311205.

[50] J. Jalilian-Marian, A. Kovner, and H. Weigert, Phys. Rev. **D59**, 014015 (1998), hep-ph/9709432.

[51] A. Kovner, J. G. Milhano, and H. Weigert, Phys. Rev. **D62**, 114005 (2000), hep-ph/0004014.

[52] E. Iancu, A. Leonidov, and L. D. McLerran, Phys. Lett. **B510**, 133 (2001), hep-ph/0102009.

[53] E. Ferreiro, E. Iancu, A. Leonidov, and L. McLerran, Nucl. Phys. **A703**, 489 (2002), hep-ph/0109115.

[54] E. Iancu and D. N. Triantafyllopoulos, Nucl. Phys. **A756**, 419 (2005), hep-ph/0411405.

[55] A. Kovner, L. D. McLerran, and H. Weigert, Phys. Rev. **D52**, 3809 (1995), hep-ph/9505320.

[56] M. Gyulassy and L. D. McLerran, Phys. Rev. **C56**, 2219 (1997), nucl-th/9704034.

[57] A. Krasnitz and R. Venugopalan, Nucl. Phys. **B557**, 237 (1999), hep-ph/9809433.

[58] A. Krasnitz and R. Venugopalan, Phys. Rev. Lett. **84**, 4309 (2000), hep-ph/9909203.

[59] D. Kharzeev, A. Krasnitz, and R. Venugopalan, Phys. Lett. **B545**, 298 (2002), hep-ph/0109253.

[60] A. Krasnitz, Y. Nara, and R. Venugopalan, Nucl. Phys. **A717**, 268 (2003), hep-ph/0209269.

[61] T. Lappi, S. Srednyak, and R. Venugopalan, JHEP **01**, 066 (2010), 0911.2068.

[62] B. Schenke, S. Schlichting, and R. Venugopalan, Phys. Lett. **B747**, 76 (2015), 1502.01331.

[63] B. Schenke and S. Schlichting, Phys. Rev. **C94**, 044907 (2016), 1605.07158.

[64] C. Gale, S. Jeon, B. Schenke, P. Tribedy, and R. Venugopalan, Phys. Rev. Lett. **110**, 012302 (2013), 1209.6330.

[65] H. Mäntysaari, B. Schenke, C. Shen, and P. Tribedy, Phys. Lett. **B772**, 681 (2017), 1705.03177.

[66] T. Lappi and L. McLerran, Nucl. Phys. **A772**, 200 (2006), hep-ph/0602189.

[67] T. Lappi and S. Schlichting, Phys. Rev. **D97**, 034034 (2018), 1708.08625.

[68] J. Berges, B. Schenke, S. Schlichting, and R. Venugopalan, Nucl. Phys. **A931**, 348 (2014), 1409.1638.

[69] J. Berges, (2015), 1503.02907.

[70] J. Berges, K. Boguslavski, S. Schlichting, and R. Venugopalan, Phys. Rev. **D89**, 074011 (2014), 1303.5650.

[71] J. Berges, K. Boguslavski, S. Schlichting, and R. Venugopalan, Phys. Rev. Lett. **114**, 061601 (2015), 1408.1670.

[72] P. B. Arnold, G. D. Moore, and L. G. Yaffe, JHEP **01**, 030 (2003), hep-ph/0209353.

[73] M. C. Abraao York, A. Kurkela, E. Lu, and G. D. Moore, Phys. Rev. **D89**, 074036 (2014), 1401.3751.

[74] N. Tanji and R. Venugopalan, Phys. Rev. **D95**, 094009 (2017), 1703.01372.

[75] A. Kurkela and E. Lu, Phys. Rev. Lett. **113**, 182301 (2014), 1405.6318.

[76] A. Kurkela and Y. Zhu, Phys. Rev. Lett. **115**, 182301 (2015), 1506.06647.

[77] A. Kurkela, A. Mazeliauskas, J.-F. Paquet, S. Schlichting, and D. Teaney, (2018), 1805.00961.

[78] A. Kurkela, A. Mazeliauskas, J.-F. Paquet, S. Schlichting, and D. Teaney, (2018), 1805.01604.

[79] A. Dumitru and L. D. McLerran, Nucl. Phys. **A700**, 492 (2002), hep-ph/0105268.

[80] J. P. Blaizot, F. Gelis, and R. Venugopalan, Nucl. Phys. **A743**, 13 (2004), hep-ph/0402256.

[81] L. McLerran and V. Skokov, Nucl. Phys. **A959**, 83 (2017), 1611.09870.

[82] G. A. Chirilli, Y. V. Kovchegov, and D. E. Wertepny, JHEP **03**, 015 (2015), 1501.03106.

[83] A. Dumitru, F. Gelis, L. McLerran, and R. Venugopalan, Nucl. Phys. **A810**, 91 (2008), 0804.3858.

[84] K. Dusling and R. Venugopalan, Phys. Rev. Lett. **108**, 262001 (2012), 1201.2658.

[85] K. Dusling and R. Venugopalan, Phys. Rev. **D87**, 051502 (2013), 1210.3890.

[86] K. Dusling and R. Venugopalan, Phys. Rev. **D87**, 054014 (2013), 1211.3701.

[87] K. Dusling and R. Venugopalan, Phys. Rev. **D87**, 094034 (2013), 1302.7018.

[88] K. Dusling, P. Tribedy, and R. Venugopalan, Phys. Rev. **D93**, 014034 (2016), 1509.04410.

[89] T. Hayata, Y. Hidaka, T. Noumi, and M. Hongo, Phys. Rev. **D92**, 065008 (2015), 1503.04535.

[90] Rezzolla, L. and Zanotti, O., *Relativistic Hydrodynamics* (Oxford University Press, 2013).

[91] P. Danielewicz and M. Gyulassy, Phys. Rev. **D31**, 53 (1985).

[92] D. Teaney, Phys. Rev. **C68**, 034913 (2003), nucl-th/0301099.

[93] H.-J. Drescher, A. Dumitru, C. Gombeaud, and J.-Y. Ollitrault, Phys. Rev. **C76**, 024905 (2007), 0704.3553.

[94] P. Romatschke and U. Romatschke, Phys. Rev. Lett. **99**, 172301 (2007), 0706.1522.

[95] W. A. Hiscock and L. Lindblom, Phys. Rev. **D31**, 725 (1985).

[96] W. Israel, Annals Phys. **100**, 310 (1976).

[97] W. Israel and J. M. Stewart, Annals Phys. **118**, 341 (1979).

[98] R. Baier, P. Romatschke, D. T. Son, A. O. Starinets, and M. A. Stephanov, JHEP **04**, 100 (2008), 0712.2451.

[99] G. S. Denicol, E. Molnr, H. Niemi, and D. H. Rischke, Eur. Phys. J. **A48**, 170 (2012), 1206.1554.

[100] P. Kovtun, D. T. Son, and A. O. Starinets, Phys. Rev. Lett. **94**, 111601 (2005), hep-th/0405231.

[101] H. B. Meyer, Phys. Rev. **D76**, 101701 (2007), 0704.1801.

[102] H. B. Meyer, Nucl. Phys. **A830**, 641C (2009), 0907.4095.

[103] N. Christiansen, M. Haas, J. M. Pawlowski, and N. Strodthoff, Phys. Rev. Lett. **115**, 112002 (2015), 1411.7986.

[104] A. Dubla *et al.*, (2018), 1805.02985.

[105] J.-Y. Ollitrault, Phys. Rev. **D46**, 229 (1992).

[106] F. Cooper and G. Frye, Phys. Rev. **D10**, 186 (1974).

[107] S. A. Bass *et al.*, Prog. Part. Nucl. Phys. **41**, 255 (1998), nucl-th/9803035, [Prog. Part. Nucl. Phys.41,225(1998)].

[108] M. Bleicher *et al.*, J. Phys. **G25**, 1859 (1999), hep-ph/9909407.

[109] CMS Collaboration, C. Collaboration, CERN Report No. CMS-PAS-HIN-18-001, 2018 (unpublished).

[110] C. Shen and B. Schenke, Phys. Rev. **C97**, 024907 (2018), 1710.00881.

[111] A. Bzdak, B. Schenke, P. Tribedy, and R. Venugopalan, Phys. Rev. **C87**, 064906 (2013), 1304.3403.

[112] H. Niemi and G. S. Denicol, (2014), 1404.7327.

[113] W. Florkowski, M. P. Heller, and M. Spalinski, Rept. Prog. Phys. **81**, 046001 (2018), 1707.02282.

[114] ALICE, J. Adam *et al.*, Phys. Lett. **B760**, 720 (2016), 1601.03658.

[115] F. R. Klinkhamer and N. S. Manton, Phys. Rev. **D30**, 2212 (1984).

[116] N. S. Manton, Phys. Rev. **D28**, 2019 (1983).

[117] R. F. Dashen, B. Hasslacher, and A. Neveu, Phys. Rev. **D10**, 4138 (1974).

[118] V. Soni, Phys. Lett. **B93**, 101 (1980).

[119] J. Boguta, Phys. Rev. Lett. **50**, 148 (1983).

[120] V. A. Kuzmin, V. A. Rubakov, and M. E. Shaposhnikov, Phys. Lett. **B155**, 36 (1985).

[121] P. B. Arnold and L. D. McLerran, Phys. Rev. **D36**, 581 (1987).

[122] A. G. Cohen, D. B. Kaplan, and A. E. Nelson, Ann. Rev. Nucl. Part. Sci. **43**, 27 (1993), hep-ph/9302210.

[123] A. D. Sakharov, Pisma Zh. Eksp. Teor. Fiz. **5**, 32 (1967), [Usp. Fiz. Nauk161,61(1991)].

[124] L. D. McLerran, E. Mottola, and M. E. Shaposhnikov, Phys. Rev. **D43**, 2027 (1991).

[125] L. D. McLerran, M. E. Shaposhnikov, N. Turok, and M. B. Voloshin, Phys. Lett. **B256**, 451 (1991).

[126] D. Yu. Grigoriev, V. A. Rubakov, and M. E. Shaposhnikov, Nucl. Phys. **B326**, 737 (1989).

[127] P. B. Arnold, D. Son, and L. G. Yaffe, Phys.Rev. **D55**, 6264 (1997), hep-ph/9609481.

[128] D. Bodeker, Phys. Lett. **B426**, 351 (1998), hep-ph/9801430.

[129] D. Bodeker, G. D. Moore, and K. Rummukainen, Phys. Rev. **D61**, 056003 (2000), hep-ph/9907545.

[130] G. D. Moore and M. Tassler, JHEP **02**, 105 (2011), 1011.1167.

[131] D. E. Kharzeev, L. D. McLerran, and H. J. Warringa, Nucl. Phys. **A803**, 227 (2008), 0711.0950.

[132] K. Fukushima, D. E. Kharzeev, and H. J. Warringa, Phys.Rev. **D78**, 074033 (2008), 0808.3382.

[133] STAR, B. I. Abelev *et al.*, Phys. Rev. Lett. **103**, 251601 (2009), 0909.1739.

[134] ALICE, B. Abelev *et al.*, Phys. Rev. Lett. **110**, 012301 (2013), 1207.0900.

[135] STAR, L. Adamczyk *et al.*, Phys. Rev. Lett. **113**, 052302 (2014), 1404.1433.

[136] STAR, L. Adamczyk *et al.*, Phys. Rev. Lett. **114**, 252302 (2015), 1504.02175.

[137] S. Schlichting and S. Pratt, (2010), 1005.5341.

[138] S. Schlichting and S. Pratt, Phys. Rev. **C83**, 014913 (2011), 1009.4283.

[139] S. Pratt, S. Schlichting, and S. Gavin, Phys. Rev. **C84**, 024909 (2011), 1011.6053.

[140] V. Koch, A. Bzdak, and J. Liao, Acta Phys. Polon. Supp. **5**, 773 (2012).

[141] Y. Hatta, A. Monnai, and B.-W. Xiao, Nucl. Phys. **A947**, 155 (2016), 1507.04690.

[142] D. E. Kharzeev, J. Liao, S. A. Voloshin, and G. Wang, Prog. Part. Nucl. Phys. **88**, 1 (2016), 1511.04050.

[143] W.-T. Deng and X.-G. Huang, Phys. Rev. **C85**, 044907 (2012), 1201.5108.

[144] L. McLerran and V. Skokov, Nucl. Phys. **A929**, 184 (2014), 1305.0774.

[145] T. Lappi, Phys. Rev. **C67**, 054903 (2003), hep-ph/0303076.

[146] P. Romatschke and R. Venugopalan, Phys. Rev. Lett. **96**, 062302 (2006), hep-ph/0510121.

[147] T. Epelbaum and F. Gelis, Phys. Rev. **D88**, 085015 (2013), 1307.1765.

[148] F. Gelis, T. Lappi, and R. Venugopalan, Phys. Rev. **D78**, 054019 (2008), 0804.2630.

[149] J. Ambjorn and A. Krasnitz, Nucl. Phys. **B506**, 387 (1997), hep-ph/9705380.

[150] G. D. Moore, Nucl.Phys. **B480**, 689 (1996), hep-lat/9605001.

[151] G. D. Moore, Phys. Rev. **D59**, 014503 (1998), hep-ph/9805264.

[152] J. Smit and A. Tranberg, JHEP **12**, 020 (2002), hep-ph/0211243.

[153] A. Tranberg and J. Smit, JHEP **11**, 016 (2003), hep-ph/0310342.

[154] M. van der Meulen, D. Sexty, J. Smit, and A. Tranberg, JHEP **02**, 029 (2006), hep-ph/0511080.

[155] A. Tranberg and J. Smit, JHEP **08**, 012 (2006), hep-ph/0604263.

[156] A. Tranberg, J. Smit, and M. Hindmarsh, JHEP **01**, 034 (2007), hep-ph/0610096.

[157] P. M. Saffin and A. Tranberg, JHEP **02**, 102 (2012), 1111.7136.

[158] M. D'Onofrio, K. Rummukainen, and A. Tranberg, JHEP **08**, 123 (2012), 1207.0685.

[159] J.-P. Blaizot, F. Gelis, J. Liao, L. McLerran, and R. Venugopalan, Nucl.Phys. **A873**, 68 (2012), 1107.5296.

[160] A. Kurkela and G. D. Moore, JHEP **1112**, 044 (2011), 1107.5050.

[161] S. Schlichting, Phys. Rev. **D86**, 065008 (2012), 1207.1450.

[162] A. Kurkela and G. D. Moore, Phys. Rev. **D86**, 056008 (2012), 1207.1663.

[163] G. 't Hooft, Phys. Rev. Lett. **37**, 8 (1976), [,226(1976)].

[164] Y. Akamatsu and N. Yamamoto, Phys. Rev. Lett. **111**, 052002 (2013), 1302.2125.

[165] Y. Akamatsu and N. Yamamoto, Phys. Rev. **D90**, 125031 (2014), 1402.4174.

[166] Y. Akamatsu, A. Rothkopf, and N. Yamamoto, JHEP **03**, 210 (2016), 1512.02374.

[167] F. Lenz, Lect.Notes Phys. **659**, 7 (2005), hep-th/0403286.

[168] P. B. Arnold and L. D. McLerran, Phys. Rev. **D37**, 1020 (1988).

[169] S. Yu. Khlebnikov and M. E. Shaposhnikov, Nucl. Phys. **B308**, 885 (1988).

[170] J. Ambjørn and A. Krasnitz, Phys.Lett. **B362**, 97 (1995), hep-ph/9508202.

[171] J. Ambjorn, T. Askgaard, H. Porter, and M. E. Shaposhnikov, Phys. Lett. **B244**, 479 (1990).

[172] D. T. Son and A. O. Starinets, JHEP **09**, 042 (2002), hep-th/0205051.

[173] P. B. Arnold, D. T. Son, and L. G. Yaffe, Phys. Rev. **D59**, 105020 (1999), hep-ph/9810216.

[174] P. B. Arnold and L. G. Yaffe, Phys. Rev. **D62**, 125013 (2000), hep-ph/9912305.

[175] G. D. Moore, C.-r. Hu, and B. Muller, Phys. Rev. **D58**, 045001 (1998), hep-ph/9710436.

[176] G. D. Moore and K. Rummukainen, Phys. Rev. **D61**, 105008 (2000), hep-ph/9906259.

[177] D. Bodeker, G. D. Moore, and K. Rummukainen, Nucl. Phys. Proc. Suppl. **83**, 583 (2000), hep-lat/9909054.

[178] P. Woit, Nucl.Phys. **B262**, 284 (1985).

[179] M. Garcia Perez and P. van Baal, Nucl. Phys. **B429**, 451 (1994), hep-lat/9403026.

[180] P. de Forcrand, M. Garcia Perez, and I.-O. Stamatescu, Nucl. Phys. **B499**, 409 (1997), hep-lat/9701012.

[181] M. Garcia Perez, O. Philipsen, and I.-O. Stamatescu, Nucl. Phys. **B551**, 293 (1999), hep-lat/9812006.

[182] S. Durr, Z. Fodor, C. Hoelbling, and T. Kurth, JHEP **04**, 055 (2007), hep-lat/0612021.

[183] M. Luscher, PoS **LATTICE2010**, 015 (2010), 1009.5877.

[184] G. Parisi and F. Rapuano, Phys.Lett. **B152**, 218 (1985).

[185] G. D. Moore, Nucl. Phys. **B480**, 657 (1996), hep-ph/9603384.

[186] J. Berges, K. Boguslavski, S. Schlichting, and R. Venugopalan, Phys. Rev. **D89**, 114007 (2014), 1311.3005.

[187] R. Baier, A. H. Mueller, D. Schiff, and D. T. Son, Phys. Lett. **B502**, 51 (2001), hep-ph/0009237.

[188] P. B. Arnold and L. G. Yaffe, Phys. Rev. **D52**, 7208 (1995), hep-ph/9508280.

[189] A. Dumitru, T. Lappi, and Y. Nara, Phys. Lett. **B734**, 7 (2014), 1401.4124.

[190] F. J. Wegner, J. Math. Phys. **12**, 2259 (1971).

[191] K. Becker, M. Becker, and J. H. Schwarz, *String theory and M-theory: A modern introduction* (Cambridge University Press, 2006).

[192] C. Rovelli, *Quantum gravity*Cambridge Monographs on Mathematical Physics (Univ. Pr., Cambridge, UK, 2004).

[193] Y. Aoki, G. Endrodi, Z. Fodor, S. D. Katz, and K. K. Szabo, Nature **443**, 675 (2006), hep-lat/0611014.

[194] M. Mace, S. Schlichting, and R. Venugopalan, Phys. Rev. **D93**, 074036 (2016), 1601.07342.

[195] J. Berges, A. Rothkopf, and J. Schmidt, Phys. Rev. Lett. **101**, 041603 (2008), 0803.0131.

[196] J. Berges, D. Gelfand, S. Scheffler, and D. Sexty, Phys. Lett. **B677**, 210 (2009), 0812.3859.

[197] D. J. Gross, R. D. Pisarski, and L. G. Yaffe, Rev. Mod. Phys. **53**, 43 (1981).

[198] V. A. Rubakov and M. E. Shaposhnikov, Usp. Fiz. Nauk **166**, 493 (1996), hep-ph/9603208, [Phys. Usp.39,461(1996)].

[199] A. Vilenkin, Phys. Rev. **D22**, 3080 (1980).

[200] D. E. Kharzeev, Prog. Part. Nucl. Phys. **75**, 133 (2014), 1312.3348.

[201] D. E. Kharzeev and D. T. Son, Phys. Rev. Lett. **106**, 062301 (2011), 1010.0038.

[202] S. A. Voloshin, Phys. Rev. **C70**, 057901 (2004), hep-ph/0406311.

[203] A. Bzdak, V. Koch, and J. Liao, Phys. Rev. **C83**, 014905 (2011), 1008.4919.

[204] X.-G. Huang, Y. Yin, and J. Liao, Nucl. Phys. **A956**, 661 (2016), 1512.06602.

[205] CMS, V. Khachatryan *et al.*, Phys. Rev. Lett. **118**, 122301 (2017), 1610.00263.

[206] V. Koch *et al.*, Chin. Phys. **C41**, 072001 (2017), 1608.00982.

[207] S. A. Voloshin, Phys. Rev. Lett. **105**, 172301 (2010), 1006.1020.

[208] S. Chatterjee and P. Tribedy, Phys. Rev. **C92**, 011902 (2015), 1412.5103.

[209] W.-T. Deng, X.-G. Huang, G.-L. Ma, and G. Wang, Phys. Rev. **C94**, 041901 (2016), 1607.04697.

[210] D. T. Son and P. Surowka, Phys. Rev. Lett. **103**, 191601 (2009), 0906.5044.

[211] A. V. Sadofyev and M. V. Isachenkov, Phys. Lett. **B697**, 404 (2011), 1010.1550.

[212] Y. Hirono, T. Hirano, and D. E. Kharzeev, (2014), 1412.0311.

[213] Y. Yin and J. Liao, Phys. Lett. **B756**, 42 (2016), 1504.06906.

[214] D. T. Son and N. Yamamoto, Phys. Rev. Lett. **109**, 181602 (2012), 1203.2697.

[215] M. A. Stephanov and Y. Yin, Phys. Rev. Lett. **109**, 162001 (2012), 1207.0747.

[216] J.-H. Gao, Z.-T. Liang, S. Pu, Q. Wang, and X.-N. Wang, Phys. Rev. Lett. **109**, 232301 (2012), 1203.0725.

[217] H.-U. Yee, JHEP **11**, 085 (2009), 0908.4189.

[218] I. Amado, K. Landsteiner, and F. Pena-Benitez, JHEP **05**, 081 (2011), 1102.4577.

[219] S. Lin and H.-U. Yee, Phys. Rev. **D88**, 025030 (2013), 1305.3949.

[220] I. Iatrakis, S. Lin, and Y. Yin, Phys. Rev. Lett. **114**, 252301 (2015), 1411.2863.

[221] I. Iatrakis, S. Lin, and Y. Yin, JHEP **09**, 030 (2015), 1506.01384.

[222] U. Gursoy, D. Kharzeev, and K. Rajagopal, Phys. Rev. **C89**, 054905 (2014), 1401.3805.

[223] V. Skokov, A. Yu. Illarionov, and V. Toneev, Int. J. Mod. Phys. **A24**, 5925 (2009), 0907.1396.

[224] K. Tuchin, Phys. Rev. **C91**, 064902 (2015), 1411.1363.

[225] N. Mueller, S. Schlichting, and S. Sharma, Phys. Rev. Lett. **117**, 142301 (2016), 1606.00342.

[226] B. Schenke, P. Tribedy, and R. Venugopalan, Phys. Rev. **C86**, 034908 (2012), 1206.6805.

[227] J. Berges, S. Schlichting, and D. Sexty, Phys. Rev. **D86**, 074006 (2012), 1203.4646.

[228] T. Epelbaum and F. Gelis, Phys. Rev. Lett. **111**, 232301 (2013), 1307.2214.

[229] F. Gelis, K. Kajantie, and T. Lappi, Phys. Rev. Lett. **96**, 032304 (2006), hep-ph/0508229.

[230] F. Hebenstreit, J. Berges, and D. Gelfand, Phys. Rev. **D87**, 105006 (2013), 1302.5537.

[231] N. Tanji, Phys. Rev. **D92**, 125012 (2015), 1506.08442.

[232] F. Gelis and N. Tanji, Prog. Part. Nucl. Phys. **87**, 1 (2016), 1510.05451.

[233] D. Gelfand, F. Hebenstreit, and J. Berges, Phys. Rev. **D93**, 085001 (2016), 1601.03576.

[234] N. Tanji, N. Mueller, and J. Berges, Phys. Rev. **D93**, 074507 (2016), 1603.03331.

[235] G. Aarts and J. Smit, Nucl. Phys. **B555**, 355 (1999), hep-ph/9812413.

[236] G. Aarts and J. Smit, Phys. Rev. **D61**, 025002 (2000), hep-ph/9906538.

[237] N. Mueller, F. Hebenstreit, and J. Berges, Phys. Rev. Lett. **117**, 061601 (2016), 1605.01413.

[238] V. Kasper, F. Hebenstreit, and J. Berges, Phys. Rev. **D90**, 025016 (2014), 1403.4849.

[239] K. Fukushima, Phys. Rev. **D92**, 054009 (2015), 1501.01940.

[240] P. V. Buividovich and M. V. Ulybyshev, Phys. Rev. **D94**, 025009 (2016), 1509.02076.

[241] P. M. Saffin and A. Tranberg, JHEP **1107**, 066 (2011), 1105.5546.

[242] V. Kasper, F. Hebenstreit, M. Oberthaler, and J. Berges, Phys. Lett. **B760**, 742 (2016), 1506.01238.

[243] W. Greiner, B. Muller, and J. Rafelski, *Quantum Electrodynamics of Strong Fields* (Springer, 1985).

[244] T. Eguchi and N. Kawamoto, Nucl. Phys. **B237**, 609 (1984).

[245] B. Sheikholeslami and R. Wohlert, Nucl. Phys. **B259**, 572 (1985).

[246] L. H. Karsten and J. Smit, Nucl. Phys. **B183**, 103 (1981), [,495(1980)].

[247] S. Aoki, Phys. Rev. **D30**, 2653 (1984).

[248] A. K. De, A. Harindranath, and S. Mondal, JHEP **07**, 117 (2011), 1105.0762.

[249] M. Creutz, I. Horvath, and H. Neuberger, Nucl. Phys. Proc. Suppl. **106**, 760 (2002), hep-lat/0110009.

[250] P. H. Ginsparg and K. G. Wilson, Phys. Rev. **D25**, 2649 (1982).

[251] R. V. Gavai and S. Sharma, Phys. Lett. **B716**, 446 (2012), 1111.5944.

[252] R. Narayanan and S. Sharma, JHEP **10**, 151 (2011), 1108.2667.

[253] R. G. Edwards, U. M. Heller, and R. Narayanan, Nucl. Phys. **B540**, 457 (1999), hep-lat/9807017.

[254] J. van den Eshof, A. Frommer, T. Lippert, K. Schilling, and H. A. van der Vorst, Comput. Phys. Commun. **146**, 203 (2002), hep-lat/0202025.

[255] T.-W. Chiu, T.-H. Hsieh, C.-H. Huang, and T.-R. Huang, Phys. Rev. **D66**, 114502 (2002), hep-lat/0206007.

[256] R. V. Gavai, S. Gupta, and R. Lacaze, Comput. Phys. Commun. **154**, 143 (2003), hep-lat/0207005.

[257] T. Kalkreuter and H. Simma, Comput. Phys. Commun. **93**, 33 (1996), hep-lat/9507023.

[258] M. H. Al-Hashimi and U. J. Wiese, Annals Phys. **324**, 343 (2009), 0807.0630.

[259] G. S. Bali *et al.*, JHEP **02**, 044 (2012), 1111.4956.

[260] D. E. Kharzeev and H.-U. Yee, Phys. Rev. **D83**, 085007 (2011), 1012.6026.

[261] Y. Jiang, S. Shi, Y. Yin, and J. Liao, Chin. Phys. **C42**, 011001 (2018), 1611.04586.

[262] STAR, J. Adams *et al.*, Phys. Rev. Lett. **91**, 072304 (2003), nucl-ex/0306024.

[263] STAR, J. Adams *et al.*, Phys. Rev. Lett. **91**, 172302 (2003), nucl-ex/0305015.

[264] ALICE, B. Abelev *et al.*, Phys. Lett. **B720**, 52 (2013), 1208.2711.

[265] CMS, S. Chatrchyan *et al.*, Eur. Phys. J. **C72**, 1945 (2012), 1202.2554.

[266] PHENIX, D. McGlinchey, Nucl. Phys. **A967**, 19 (2017), 1704.04568.

[267] T. Lappi, Phys. Lett. **B744**, 315 (2015), 1501.05505.

[268] T. Lappi, B. Schenke, S. Schlichting, and R. Venugopalan, JHEP **01**, 061 (2016), 1509.03499.

[269] J. P. Blaizot, F. Gelis, and R. Venugopalan, Nucl. Phys. **A743**, 57 (2004), hep-ph/0402257.

[270] A. Dumitru *et al.*, Phys. Lett. **B697**, 21 (2011), 1009.5295.

[271] J. D. Bjorken, J. B. Kogut, and D. E. Soper, Phys. Rev. **D3**, 1382 (1971).

[272] A. H. Mueller, Nucl. Phys. **B437**, 107 (1995), hep-ph/9408245.

[273] A. Dumitru and J. Jalilian-Marian, Phys. Rev. Lett. **89**, 022301 (2002), hep-ph/0204028.

[274] H. Kowalski, L. Motyka, and G. Watt, Phys. Rev. **D74**, 074016 (2006), hep-ph/0606272.

[275] A. H. Rezaeian, M. Siddikov, M. Van de Klundert, and R. Venugopalan, Phys. Rev. **D87**, 034002 (2013), 1212.2974.

[276] F. Gelis, T. Lappi, and R. Venugopalan, Phys. Rev. **D78**, 054020 (2008), 0807.1306.

[277] K. Dusling, F. Gelis, T. Lappi, and R. Venugopalan, Nucl. Phys. **A836**, 159 (2010), 0911.2720.

[278] A. Kovner, M. Lublinsky, and V. Skokov, Phys. Rev. **D96**, 016010 (2017), 1612.07790.

[279] J. Jalilian-Marian, A. Kovner, A. Leonidov, and H. Weigert, Phys. Rev. **D59**, 014014 (1998), hep-ph/9706377.

[280] H. Grönqvist, J.-P. Blaizot, and J.-Y. Ollitrault, Phys. Rev. **C94**, 034905 (2016), 1604.07230.

[281] A. Kovner and U. A. Wiedemann, Phys. Rev. **D64**, 114002 (2001), hep-ph/0106240.

[282] H. Fujii, Nucl. Phys. **A709**, 236 (2002), nucl-th/0205066.

[283] F. Dominguez, C. Marquet, and B. Wu, Nucl. Phys. **A823**, 99 (2009), 0812.3878.

[284] K. Fukushima and Y. Hidaka, JHEP **06**, 040 (2007), 0704.2806.

[285] Gough, Brian, *GNU Scientific Library Reference Manual - Third Edition*, 3rd ed. (Network Theory Ltd., 2009).

[286] R. B. Sidje, ACM Trans. Math. Softw. **24**, 130 (1998).

[287] F. Dominguez, C. Marquet, A. M. Stasto, and B.-W. Xiao, Phys. Rev. **D87**, 034007 (2013), 1210.1141.

[288] Y. Shi, C. Zhang, and E. Wang, Phys. Rev. **D95**, 116014 (2017), 1704.00266.

[289] J. L. Albacete, N. Armesto, J. G. Milhano, P. Quiroga-Arias, and C. A. Salgado, Eur. Phys. J. **C71**, 1705 (2011), 1012.4408.

[290] T. Lappi and H. Mntysaari, Phys. Rev. **D88**, 114020 (2013), 1309.6963.

[291] K. Dusling, W. Li, and B. Schenke, Int. J. Mod. Phys. **E25**, 1630002 (2016), 1509.07939.

[292] S. Schlichting and P. Tribedy, Adv. High Energy Phys. **2016**, 8460349 (2016), 1611.00329.

[293] N. Borghini, P. M. Dinh, and J.-Y. Ollitrault, Phys. Rev. **C64**, 054901 (2001), nucl-th/0105040.

[294] A. Dumitru, L. McLerran, and V. Skokov, Phys. Lett. **B743**, 134 (2015), 1410.4844.

[295] CMS, V. Khachatryan *et al.*, Phys. Rev. Lett. **115**, 012301 (2015), 1502.05382.

[296] ATLAS, G. Aad *et al.*, Phys. Rev. **C90**, 044906 (2014), 1409.1792.

[297] CMS, S. Chatrchyan *et al.*, Phys. Lett. **B724**, 213 (2013), 1305.0609.

[298] ALICE, B. B. Abelev *et al.*, Phys. Rev. **C90**, 054901 (2014), 1406.2474.

[299] PHENIX, R. Belmont, Nucl. Phys. **A967**, 341 (2017), 1704.04570.

[300] ATLAS, M. Aaboud *et al.*, Eur. Phys. J. **C77**, 428 (2017), 1705.04176.

[301] P. Bozek and W. Broniowski, Phys. Lett. **B718**, 1557 (2013), 1211.0845.

[302] I. Kozlov, M. Luzum, G. Denicol, S. Jeon, and C. Gale, (2014), 1405.3976.

[303] A. Kovner and M. Lublinsky, Phys. Rev. **D83**, 034017 (2011), 1012.3398.

[304] A. Dumitru and A. V. Giannini, Nucl. Phys. **A933**, 212 (2015), 1406.5781.

[305] A. Dumitru and V. Skokov, Phys. Rev. **D91**, 074006 (2015), 1411.6630.

[306] A. Dumitru, A. V. Giannini, and V. Skokov, (2015), 1503.03897.

[307] V. Skokov, Phys. Rev. **D91**, 054014 (2015), 1412.5191.

[308] G. Giacalone, J. Noronha-Hostler, and J.-Y. Ollitrault, Phys. Rev. **C95**, 054910 (2017), 1702.01730.

[309] ATLAS, G. Aad *et al.*, Phys. Lett. **B725**, 60 (2013), 1303.2084.

[310] E. Iancu and A. H. Rezaeian, Phys. Rev. **D95**, 094003 (2017), 1702.03943.

[311] A. Bilandzic, C. H. Christensen, K. Gulbrandsen, A. Hansen, and Y. Zhou, Phys. Rev. **C89**, 064904 (2014), 1312.3572.

[312] ALICE, J. Adam *et al.*, Phys. Rev. Lett. **117**, 182301 (2016), 1604.07663.

[313] G. Giacalone, L. Yan, J. Noronha-Hostler, and J.-Y. Ollitrault, Phys. Rev. **C94**, 014906 (2016), 1605.08303.

[314] X. Zhu, Y. Zhou, H. Xu, and H. Song, Phys. Rev. **C95**, 044902 (2017), 1608.05305.

[315] Y. Zhou, K. Xiao, Z. Feng, F. Liu, and R. Snellings, Phys. Rev. **C93**, 034909 (2016), 1508.03306.

[316] K. Welsh, J. Singer, and U. W. Heinz, Phys. Rev. **C94**, 024919 (2016), 1605.09418.

[317] CMS, C. Collaboration, (2017).

[318] o. b. o. A. c. Zhou, You, Probing non-linearity of higher harmonic flow in Pb-Pb collisions, Quark Matter, 2017.

[319] A. Bzdak, P. Bozek, and L. McLerran, Nucl. Phys. **A927**, 15 (2014), 1311.7325.

[320] H. Song, Y. Zhou, and K. Gajdosova, Nucl. Sci. Tech. **28**, 99 (2017), 1703.00670.

[321] G. Başar and D. Teaney, Phys. Rev. **C90**, 054903 (2014), 1312.6770.

[322] K. Dusling, M. Mace, and R. Venugopalan, Phys. Rev. Lett. **120**, 042002 (2018), 1705.00745.

[323] F. Gelis, T. Lappi, and L. McLerran, Nucl. Phys. **A828**, 149 (2009), 0905.3234.

[324] A. Kovner and M. Lublinsky, Int. J. Mod. Phys. **E22**, 1330001 (2013), 1211.1928.

[325] Y. V. Kovchegov and D. E. Wertepny, Nucl. Phys. **A906**, 50 (2013), 1212.1195.

[326] NNPDF, R. D. Ball *et al.*, JHEP **04**, 040 (2015), 1410.8849.

[327] K. Dusling, M. Mace, and R. Venugopalan, Phys. Rev. **D97**, 016014 (2018), 1706.06260.

[328] K. Dusling, M. Mace, and R. Venugopalan, PoS **QCDEV2017**, 039 (2018), 1801.09704.

[329] B. Schenke, S. Schlichting, P. Tribedy, and R. Venugopalan, Phys. Rev. Lett. **117**, 162301 (2016), 1607.02496.

[330] B. Andersson, G. Gustafson, G. Ingelman, and T. Sjostrand, Phys. Rept. **97**, 31 (1983).

[331] C. Aidala *et al.*, Phys. Rev. **C95**, 034910 (2017), 1609.02894.

[332] PHENIX, C. Aidala *et al.*, Phys. Rev. **C96**, 064905 (2017), 1708.06983.

[333] PHENIX, A. Adare *et al.*, Phys. Rev. Lett. **115**, 142301 (2015), 1507.06273.

[334] J. L. Nagle and W. A. Zajc, (2018), 1801.03477.

[335] M. Habich, J. L. Nagle, and P. Romatschke, Eur. Phys. J. **C75**, 15 (2015), 1409.0040.

[336] C. Shen, J.-F. Paquet, G. S. Denicol, S. Jeon, and C. Gale, Phys. Rev. **C95**, 014906 (2017), 1609.02590.

[337] Z.-W. Lin, C. M. Ko, B.-A. Li, B. Zhang, and S. Pal, Phys. Rev. **C72**, 064901 (2005), nucl-th/0411110.

[338] T. Altinoluk, N. Armesto, G. Beuf, A. Kovner, and M. Lublinsky, Phys. Lett. **B751**, 448 (2015), 1503.07126.

[339] B. Blok, C. D. Jäkel, M. Strikman, and U. A. Wiedemann, JHEP **12**, 074 (2017), 1708.08241.

[340] Y. V. Kovchegov and V. V. Skokov, Phys. Rev. **D97**, 094021 (2018), 1802.08166.

[341] A. Kovner and A. H. Rezaeian, Phys. Rev. **D97**, 074008 (2018), 1801.04875.

[342] T. Altinoluk, N. Armesto, and D. E. Wertepny, (2018), 1804.02910.

[343] T. Altinoluk, N. Armesto, A. Kovner, and M. Lublinsky, (2018), 1805.07739.

[344] Y. V. Kovchegov and A. H. Mueller, Nucl. Phys. **B529**, 451 (1998), hep-ph/9802440.

[345] A. Dumitru, J. Jalilian-Marian, T. Lappi, B. Schenke, and R. Venugopalan, Phys. Lett. **B706**, 219 (2011), 1108.4764.

[346] C. Loizides, J. Nagle, and P. Steinberg, SoftwareX **1-2**, 13 (2015), 1408.2549.

[347] P. Tribedy and R. Venugopalan, Phys. Lett. **B710**, 125 (2012), 1112.2445, [Erratum: Phys. Lett.B718,1154(2013)].

[348] E. Iancu and L. McLerran, Nucl. Phys. **A793**, 96 (2007), hep-ph/0701276.

[349] B. Schenke, P. Tribedy, and R. Venugopalan, Phys. Rev. **C89**, 024901 (2014), 1311.3636.

[350] L. McLerran and P. Tribedy, Nucl. Phys. **A945**, 216 (2016), 1508.03292.

[351] T. Lappi, Eur. Phys. J. **C55**, 285 (2008), 0711.3039.

[352] M. Luzum and J.-Y. Ollitrault, Phys. Rev. **C87**, 044907 (2013), 1209.2323.

[353] T. Sjostrand, Nucl. Phys. **B248**, 469 (1984).

[354] T. Sjöstrand *et al.*, Comput. Phys. Commun. **191**, 159 (2015), 1410.3012.

[355] M. Greif, C. Greiner, B. Schenke, S. Schlichting, and Z. Xu, Phys. Rev. **D96**, 091504 (2017), 1708.02076.

[356] L. Yan and J.-Y. Ollitrault, Phys. Rev. Lett. **112**, 082301 (2014), 1312.6555.

[357] O. Hen, G. A. Miller, E. Piasetzky, and L. B. Weinstein, Rev. Mod. Phys. **89**, 045002 (2017), 1611.09748.

[358] R. Cruz-Torres *et al.*, (2017), 1710.07966.

[359] J. Carlson and R. Schiavilla, Rev. Mod. Phys. **70**, 743 (1998).

[360] J. L. Nagle *et al.*, Phys. Rev. Lett. **113**, 112301 (2014), 1312.4565.

[361] O. Hen, M. Mace, A. Schmidt, and R. Venugopalan, in progress (2018).

[362] ATLAS, M. Aaboud *et al.*, Phys. Rev. **C95**, 064914 (2017), 1606.08170.

[363] B. Schenke, S. Jeon, and C. Gale, Phys. Rev. Lett. **106**, 042301 (2011), 1009.3244.

[364] B. Schenke and R. Venugopalan, Phys. Rev. Lett. **113**, 102301 (2014), 1405.3605.

[365] H. Mäntysaari and B. Schenke, Phys. Rev. Lett. **117**, 052301 (2016), 1603.04349.

[366] H. Mäntysaari and B. Schenke, Phys. Rev. **D94**, 034042 (2016), 1607.01711.

[367] M. Mace, V. Skokov, P. Tribedy, and R. Venugopalan, in progress (2018).

[368] M. Mace *et al.*, in progress (2018).

[369] M. Mace and R. Venugopalan, in progress (2018).

[370] M. Mace, S. Schlichting, and S. Sharma, in preparation (2018).

[371] M. Mace, N. Mueller, S. Schlichting, and S. Sharma, in progress (2018).

[372] L. Del Zanna *et al.*, Eur. Phys. J. **C73**, 2524 (2013), 1305.7052.

[373] G. Inghirami *et al.*, in preparation (2018).

[374] A. Accardi *et al.*, Eur. Phys. J. **A52**, 268 (2016), 1212.1701.

[375] A. Cucchieri and T. Mendes, Nucl. Phys. **B471**, 263 (1996), hep-lat/9511020.

[376] K. Dusling, D. Fernandez-Fraile, and R. Venugopalan, Nucl. Phys. **A828**, 161 (2009), 0902.4435.